Estimation of Landscape Carbon Budgets: Combining Geostatistical and Data Assimilation Approaches

Luke Spadavecchia

PhD by Research The University of Edinburgh 2008

Declaration

This thesis is a presentation of my original research work. Wherever contributions of others are involved, every effort is made to indicate this clearly, with due reference to the literature, and acknowledgement of collaborative research and discussions. Contributions from other authors are acknowledged prior to the relevant sections. The work was done under the supervision of Mathiew Williams at the University of Edinburgh.

Luke Spadavecchia

Date: 29-01-2009

Acknowledgements

I would like to thank all of my friends and family for their patience over the last few years; without their support this would never have been possible. In particular I would like to thank my parents, whose love and encouragement kept me going. I would like to thank Tim Hill and Casey Ryan for good company, organizing me when I was hopeless, and providing a sympathetic ear for a good moan. I owe a huge debt of gratitude to Mat Williams, my supervisor, who tolerated my somewhat erratic work methods and kept me on track when I was distracted. Much of the quality of my work is due to his guidance and without him I never would have achieved this. Throughout my PhD I benefited from the friendship and expertise of everyone at the Centre for Terrestrial Carbon Dynamics (CTCD), and was lucky to be surrounded by such talented and stimulating people: In particular Martin De Kauwe and Steve Hancock. I benefited from the hospitality and kindness of many people at Oregon State University, particularly James and Kathryn Irvine and Bev Law. Finally I would like to thank my wonderful girlfriend Danielle, for putting up with me at my worst, and helping me forget work when things were tough.

Contents

1. Abstract

Carbon fluxes at the site scale (~ 1km^2) are well quantified by continuous monitoring with eddy flux covariance instruments, whilst national to continental scale fluxes may be measured by tall towers or flask measurements. Quantification of carbon (C) budgets at the landscape or catchment scale is more problematic, and is generally achieved using process-based models as scaling tools. Such models require some metric of the exchange surface capability (e.g., Leaf Area Index, LAI) and a set of rate parameters for C processing. The net C exchange is then determined by driving the model with meteorological observations. Regional fields of parameters and drivers may be derived by upscaling site level measurements, constrained using Earth Observation (EO) data such as radiance derived vegetation indices and digital elevation models (DEMs). I explore issues of error and uncertainty when upscaling C model parameters and drivers, and the effect of these uncertainties on the final analysis of the carbon budget. Two study areas, with excellent research infrastructure, focus the research: a region of tundra in Arctic Sweden and a ponderosa pine stand in Oregon. I use geostatistical techniques to develop fields of LAI and meteorology, complete with error statistics, whilst the distributions of rate parameters for a C model are derived *via* the Ensemble Kalman filter (EnKF). I report that the use of DEM data can provide LAI fields with an r^2 ~50% greater than those derived from EO data alone. In particular I find strong relationships between LAI, elevation and topographic exposure. I explore the use of spatio-temporal geostatistics to improve meteorological fields, but report a better interpolation skill when temporal autocorrelations are ignored. I employ simulation techniques to propagate parameter and driver uncertainty through a simple carbon dynamics model, finding that variation in parameters has a much larger effect on

the uncertainty of the carbon budget (~50%) than driver uncertainty (<10%). Whilst driver uncertainty is related to the quantity and spatio-temporal arrangement of the conditioning data, we find this result to be stable in cases of extreme data scarcity (max driver uncertainty <20%). The combined uncertainty in parameterisation and meteorology may result in a 53% uncertainty in total C uptake. I conclude that improved methods to constrain vegetation surface characteristics on the regional scale should take precedence over improvements to model drivers: It is likely that data assimilation of high quality EO products may go some way to providing such constraint.

2. Introduction

In the past, carbon cycle research depended on site level experiments or observational studies of ecosystems to make local assertions about carbon budgets (Grace 2004). Typically these were based around micro-meteorological eddy flux covariance methods (Baldocchi et al. 1988, Grace et al. 1995a, Grace et al. 1995b, Moncrieff et al. 1997) at the stand to forest scale, or flask sampling giving information at the continental to global scale (Keeling et al. 1996a, Keeling et al. 1996b). Later attempts to formalise this knowledge for hypothesis testing led to increasing focus on modelling studies to understand ecosystem dynamics on a global scale and typically over long time periods *via* Dynamic Global Vegetation Models (DGVMs) (Woodward et al. 1995, Sitch et al. 2003).

DGVMs are generally heuristic, and do not aim to match site level data accurately, but rather describe likely system behaviour in the event of various scenarios (e.g. IPCC 2007). As such, the system can be 'spun up', typically with synthetic meteorology generated within the model, to generate surface vegetation characteristics. This approach assumes an ecosystem in equilibrium, with vegetation settled at some 'climax community', in accordance with Clement's view of succession and plant community structure (Clements 1916, 1936): Such notions of climax communities have been challenged, and 'non-equilibrium' concepts associated with Gleason (Gleason 1927) are generally considered to be more appropriate at the regional scale. Large-scale models have been useful tools for predictions of future climate and vegetation states, and for exploring system behaviour under different sets of assumptions (Cox et al. 2000, Cramer et al. 2001), but have caveats due to the omission of key feedbacks; particularly

in terms of soil nutrient dynamics, e.g. the relationship between the decomposition rate of soil organic carbon and soil nitrogen availability (Henriksen and Breland 1999).

More recently, modelling studies have focused on regional to catchment scale studies of the carbon balance (Running 1994, Williams et al. 2001). These models may be simpler in terms of the number of processes represented in the model structure, but tend to be better at matching site level observations over fairly short time periods (~3 years). At the regional scale, these models are used as a scaling tool to implement knowledge gained at the site level to a larger region of interest. Interest in local ecosystem potential as C sinks and their behaviour in response to climatic variability is increasing, particularly with a view towards sequestration and climate change mitigation.

Regional scale modelling presents a different set of challenges to global scale modelling: Local scale models must accurately reproduce the C fluxes observed at the site level, to provide both diagnostic and prognostic information on regional dynamics of C. Furthermore, at the regional scale, effects of micro-topography and vegetation surface heterogeneity which are irrelevant at the global scale have an appreciable effect on the C balance. As such the synthetic 'spin-up' methods employed in DGVMs are inappropriate; we therefore require a set of meteorological driving variables, and some conception of the vegetative surface at an appropriate scale to derive estimates of C dynamics. Typically we utilise a combination of site level observational data and earth observation (EO) products to parameterise the vegetation surface and derive fields of meteorological drivers. There are unavoidable errors inherent in the up/downscaling of observational data sources, which are often poorly quantified, or not considered in regional modelling studies (Fuentes et al. 2006).

Quantification of errors is becoming increasingly important for C modelling. Current trends in research towards data assimilation (DA) and data fusion techniques

(e.g. Williams et al. 2005, Quaife et al. 2008) require some knowledge of model and data uncertainty, which are often difficult to quantify. DA techniques are the next logical step in the development of our understanding of the C cycle, as they allow the use of formalised knowledge in the form of a model to flag and correct aberrant observational data, whilst allowing better integration of site level and satellite derived ecological observations into such models in a way which optimally balances the errors of each. Such methods effectively bridge the gap between field ecologists and modellers, and provide a better analysis than either model or data alone (Maybeck 1979, Williams et al. 2005). In order to achieve an unbiased estimate of the system state, DA requires an accurate estimate of model variability, without which the results may be highly questionable (Quaife et al. 2008). It is the goal of accurate model uncertainty analysis that motivates this thesis.

Quantification of regional model errors is not only an academic exercise. Political decisions to achieve binding emission reduction targets (Kyoto protocol) through offsetting have led to a growing C trading market (Grace 2004); reflected in the recent restructuring of the National Environmental Research Councils (NERC) Earth observation centres to the National Centre for Earth Observation (NCEO), which has an objective towards developing commercial deliverables to customers from research. To be truly useful, such products must have some form of error quantification (Kennedy et al. 2008), and this is likely to be a profitable area of research in the future.

In this thesis I aim to quantify and reduce the errors associated with the production of regionalised data sources for the parameterisation and driving of models. I employ geostatistical techniques to the problem of upscaling, which confer the considerable advantage of providing estimates of uncertainty to estimated fields. Furthermore, I aim to examine the effects of these errors on the state vector when

propagated through a simple carbon dynamics model (DALEC). Issues related to parameterisation of the vegetation surface are tackled in chapters 3 and 4, whilst issues related to the estimation of driver fields are addressed in chapters 5 to 6. An examination of error propagation is undertaken in chapter 6.

Chapter three was published as a paper in *Global Change Biology* (Williams et al. 2008), and aims to quantify the errors associated with upscaling leaf area index (LAI) from site level harvest data to the regional scale in an arctic tundra ecosystem. Correctly specifying LAI is critical to the quantification of the carbon balance (Sitch et al. 2003) because (along with foliar nitrogen content) it dictates the rate of exchange of mass and energy between the land and atmosphere by defining the total exchange surface. LAI can be inferred from EO reflectance data *via* vegetation indices such as the Normalised Difference Vegetation Index (NDVI) (Lillesand et al. 2004). Issues of scale invariance for relationships of NDVI and LAI are explored. We found that for a relatively large range of spatial scales, the same relationship between LAI and NDVI held, with similar prediction error. However, we are only able to capture ~ 17% of the LAI variation with EO data sources, indicating the use of EO data alone may be insufficient to parameterise the vegetation surface in highly heterogeneous areas. This result motivated the chapter four, in which we attempted to find suitable topographic predictors of LAI to support or supplant the use of EO data for vegetation surface parameterisation.

Chapter four was submitted as a paper to the *Journal of Ecology*, and explores the spatial relationships between topography and variation in LAI in an arctic tundra ecosystem. We report significant scale dependent relationships between LAI, elevation and topographic position, indicating that at larger spatial scales LAI is constrained by elevation (perhaps due to temperature variation), whilst topographic exposure dominates the spatial patterns of vegetation at smaller scales. The effect of topographic

exposure on LAI is likely due to wind shear, and shelter effects on snow accumulation and melt. Geostatistical techniques were used to build simple spatially explicit models of LAI variation with relevant topographical characteristics, better replicating the observed vegetation characteristics than EO sources ($r^2 \sim 30\%$). Future development in this area may integrate EO derived NDVI and vegetation classifications with data on surface topography to provide more accurate LAI parameterisations complete with error statistics.

Chapter five was submitted as a paper to *Agricultural and Forest Meteorology*, and aims to address the issue of spatio-temporal autocorrelation in meteorological data sources, and how this information can be potentially exploited to improve estimation of model driver fields for a moderately large region of central Oregon, USA. The paper also explores the effects of temporal aggregation on error magnitude and bias. We employ the product-sum representation of spatiotemporal covariance (De Cesare et al. 2001) to meteorological upscaling problems for the first time. Interestingly, incorporation of temporal autocorrelation did not improve the accuracy of driver fields over utilisation of spatial data sources alone. However, we report that *post hoc* temporal aggregation of high-resolution estimates tends to reduce their bias and error. The likely consequences of this in terms of model error propagation are uncertain, as some model processes react instantaneously to driving variable, whilst others act as capacitors, integrating driver error over longer time periods. These results provide the motivation for chapter six.

Chapter six is intended for submission to *Global Change Biology*, and aims to quantify and compare model uncertainties resultant from parameter and driver uncertainties respectively. The paper utilises DA techniques to parameterise a simple model of C dynamics for an intensive observation site at Metolius, central Oregon.

Parameters are derived *via* the Ensemble Kalman filter (ENKF) (Evensen 2003), to construct optimal parameter distributions. The variation in C fluxes due to parameter uncertainty is derived, and compared with the uncertainties resultant from meteorological driver uncertainty. Driver uncertainty is quantified using geostatistical simulation techniques (Sequential Gaussian Simulation, SGS) (Goovaerts 2001), whereby an ensemble of 1000 weather scenarios is produced. We also undertake a series of experiments to disaggregate the errors resultant from temperature and precipitation uncertainty.

We find that parameter error dominates the total C sink strength uncertainty, despite the considerable uncertainties associated with upscaling meteorology. In order to assess the robustness of this conclusion we examine the effect of conditioning the simulated meteorology on increasingly remote sets of stations. We report that in cases of extreme data sparsity, conditioning the meteorology on stations over 100km from the study site, the effect parameter uncertainty still exceeds the effect of meteorological uncertainty on NEE by ~50%. Disaggregation of the driver uncertainty reveals that temperature variability has a larger impact on total C sink uncertainty than precipitation. Interestingly we find that biases in simulated meteorological drivers appear to cancel out over model runs, although further research at other sites is needed to rule out the possibility of this occurring by chance. We conclude that producing reasonable parameterisations over the study area is of greater importance than reducing driver uncertainty.

All geostatistical analyses presented in this thesis were conducted using a set of software tools developed specifically for this thesis. This set of software tools, the *Edinburgh Spatio-Temporal Geostatistics* package is documented in chapter seven, which serves as a technical paper and manual for the software, and also provides an exposition

and justification of some of the modelling choices made in the thesis. The Fortran 90 code is provided in the appendix in digital format.

2.1 References

Baldocchi, D. D., B. B. Hincks, and T. P. Meyers. 1988. Measuring biosphere-atmosphere exchanges of biologically related gases with micrometeorological methods. Ecology 69:1331-1340.

Clements, F. E. 1916. Plant Succession: An analysis of the development of vegetation. Carnegie Institute Washington Publication 242, Washington D.C.

Clements, F. E. 1936. Nature and structure of the climax. The Journal of Ecology 24:252-284.

Cox, P. M., R. A. Betts, C. D. Jones, S. A. Spall, and I. J. Totterdell. 2000. Acceleration of global warming due to carbon-cycle feedbacks in a coupled climate model. Nature 408:184-187.

Cramer, W., A. Bondeau, F. I. Woodward, I. C. Prentice, R. A. Betts, V. Brovkin, P. M. Cox, V. Fisher, J. Foley, A. D. Friend, C. Kucharik, M. R. Lomas, N. Ramankutty, S. Sitch, B. Smith, A. White, and C. Young-Molling. 2001. Global response of terrestrial ecosystem structure and function to CO2 and climate change: results from six dynamic global vegetation models. Global Change Biology 7 357-373.

De Cesare, L., D. E. Myers, and D. Posa. 2001. Estimating and modeling space-time correlation structures. Statistics & Probability Letters 51:9-14.

Evensen, G. 2003. The ensemble Kalman filter: theoretical formulation and practical implementation. Ocean Dynamics 53:343-367.

Fuentes, M., T. G. F. Kittel, and D. Nychka. 2006. Sensitivity of ecological models to their climate drivers: Statistical ensembles for forcing. Ecological Applications 16:99-116.

Gleason, H. A. 1927. Further views on the succession-concept. Ecology 8:299-326.

Goovaerts, P. 2001. Geostatistical modelling of uncertainty in soil science. Geoderma 103:3-26.

Grace, J. 2004. Understanding and managing the global carbon cycle. Journal of Ecology 92:189-202.

Grace, J., J. Lloyd, J. Mcintyre, A. Miranda, P. Meir, H. Miranda, J. Moncrieff, J. Massheder, I. Wright, and J. Gash. 1995a. Fluxes of Carbon-Dioxide and Water-Vapor over an Undisturbed Tropical Forest in South-West Amazonia. Global Change Biology 1:1-12.

Grace, J., J. Lloyd, J. Mcintyre, A. C. Miranda, P. Meir, H. S. Miranda, C. Nobre, J. Moncrieff, J. Massheder, Y. Malhi, I. Wright, and J. Gash. 1995b. Carbon-Dioxide Uptake by an Undisturbed Tropical Rain-Forest in Southwest Amazonia, 1992 to 1993. Science 270:778-780.

Henriksen, T. M., and T. A. Breland. 1999. Nitrogen availability effects on carbon mineralization, fungal and bacterial growth, and enzyme activities during decomposition of wheat straw in soil. Soil Biology and Biochemistry 31:1121-1134.

IPCC. 2007. IPCC Fourth Assessment Report: Climate Change 2007. Published for the Intergovernmental Panel on Climate Change [by] Cambridge University Press, Cambridge.

Keeling, C. D., J. F. S. Chin, and T. P. Whorf. 1996a. Increased activity of northern vegetation inferred from atmospheric CO2 measurements. Nature 382:146-149.

Keeling, R. F., S. C. Piper, and M. Heimann. 1996b. Global and hemispheric CO2 sinks deduced from changes in atmospheric O-2 concentration. Nature 381:218-221.

Kennedy, M., C. Anderson, A. O'Hagan, M. Lomas, I. Woodward, J. P. Gosling, and A. Heinemeyer. 2008. Quantifying uncertainty in the biospheric carbon flux for England and Wales. Journal of the Royal Statistical Society Series a-Statistics in Society 171:109-135.

Lillesand, T. M., R. W. Kiefer, and W. Chipman Jonathan. 2004. Remote sensing and image interpretation, 5th edition. John Wiley & Sons, New York.

Maybeck, P. S. 1979. Stochastic Models, Estimation and Control. Academic Press, New York.

Moncrieff, J. B., J. M. Massheder, H. deBruin, J. Elbers, T. Friborg, B. Heusinkveld, P. Kabat, S. Scott, H. Soegaard, and A. Verhoef. 1997. A system to measure surface fluxes of momentum, sensible heat, water vapour and carbon dioxide. Journal of Hydrology 189:589-611.

Quaife, T., P. Lewis, M. D. Kauwe, M. Williams, B. E. Law, M. Disney, and P. Bowyer. 2008. Assimilating canopy reflectance data into an ecosystem model with an ensemble Kalman filter. Remote Sensing of Environment 112:1347-1364.

Running, S. W. 1994. Testing forest-bgc ecosystem process simulations across a climatic gradient in Oregon. Ecological Applications 4:238-247.

Sitch, S., B. Smith, I. C. Prentice, A. Arneth, A. Bondeau, W. Cramer, J. Kaplan, S. Levis, W. Lucht, M. Sykes, K. Thonicke, and S. Venevsky. 2003. Evaluation of ecosystem dynamics, plant geography and terrestrial carbon cycling in the LPJ dynamic vegetation model. Global Change Biology 9:161–185.

Williams, M., R. Bell, L. Spadavecchia, L. E. Street, and M. T. van Wijk. 2008. Upscaling leaf area index in an Artctic landscape using multi-scale reflectance observations. Global Change Biology: DOI: 10.1111/j.1365-2486.2008.01590.x.

Williams, M., E. B. Rastetter, G. R. Shaver, J. E. Hobbie, E. Carpino, and B. L. Kwiatkowski. 2001. Primary production of an arctic watershed: An uncertainty analysis. Ecological Applications 11:1800-1816.

Williams, M., P. A. Schwarz, B. E. Law, J. Irvine, and M. R. Kurpius. 2005. An improved analysis of forest carbon dynamics using data assimilation. Global Change Biology 11:89-105.

Woodward, F. I., T. M. Smith, and W. R. Emanuel. 1995. A global primary productivity and phytogeography model. Global Biogeochemical Cycles 9:471–490.

3. Upscaling leaf area index in an Arctic landscape through multi-scale observations

Running title: Upscaling LAI in Arctic tundra

M. Williams[1*], R. Bell[1], L. Spadavecchia[1], L.E. Street[1] and M.T. van Wijk[2]

[1]Institute of Atmospheric and Environmental Sciences, School of GeoSciences, University of Edinburgh, Edinburgh EH9 3JN, UK.

[2] Plant Production Systems, Wageningen University, Plant Sciences, Haarweg 333, 6709 RZ Wageningen, Netherlands.

* Correspondence to Mathew Williams, mat.williams@ed.ac.uk.

KEY WORDS: LAI, tundra, NDVI, Landsat, remote sensing, semi-variogram, Kriging, data assimilation, geostatistics, Arctic.

* Corresponding author

3.1 Declaration

The following chapter was submitted as a paper to *Global Change Biology*. Although the main body of the text is attributable to M. Williams, I contributed significantly to content of the paper. Specifically I collated and manipulated the EO data and extracted the NDVI values to the sample locations. I analysed the relationship between the EO (Landsat) dervided LAI and the ground observations, and calculated the semivariograms. I also implemented the geostatistical analysis used for the extrapolation sections of the paper. I provided the text for the sections entitled *remote sensing* (3.4.3) and *geospatial methods* (3.4.4). M. Williams produced all the figures, with the exception of Figure 3.9, which I produced.

3.2 Abstract

Monitoring and understanding global change requires a detailed focus on upscaling, the process for extrapolating from the site-specific scale to the smallest scale resolved in regional or global models or earth observing systems. Leaf area index (LAI) is one of the most sensitive determinants of plant production and can vary by an order of magnitude over short distances. The landscape distribution of LAI is generally determined by remote sensing of surface reflectance (e.g. normalised difference vegetation index, NDVI) but the mismatch in scales between ground and satellite measurements complicates LAI upscaling. Here, we describe a series of measurements to quantify the spatial distribution of LAI in a sub-Arctic landscape and then describe the upscaling process and its associated errors. Working from a fine-scale harvest LAI-NDVI relationship, we collected NDVI data over a 500 x 500 m catchment in the Swedish Arctic, at resolutions from 0.2 – 9.0 m in a nested sampling design. NDVI scaled linearly, so that NDVI at any scale was a simple average of multiple NDVI measurements taken at finer scales. The LAI-NDVI relationship was scale invariant from 1.5 – 9.0 m resolution. Thus, a single exponential LAI-NDVI relationship was valid at all these scales, with similar prediction errors. Vegetation patches were of a scale of ~0.5 m, and at measurement scales coarser than this there was a sharp drop in LAI variance. Landsat NDVI data for the study catchment correlated significantly, but poorly, with ground based measurements. A variety of techniques were used to construct LAI maps, including interpolation by inverse distance weighting, ordinary Kriging, Kriging with an External Drift using Landsat data, and direct estimation from a Landsat NDVI-LAI calibration. All methods produced similar LAI estimates and overall errors. However, Kriging approaches also generated maps of LAI estimation error

based on semi-variograms. The spatial variability of this arctic landscape was such that local measurements assimilated by Kriging approaches had a limited spatial influence. Over scales >50 m, interpolation error was of similar magnitude to the error in the Landsat NDVI calibration. The characterisation of LAI spatial error in this study is a key step towards developing spatio-temporal data assimilation systems for assessing C cycling in terrestrial ecosystems by combining models with field and remotely sensed data.

3.3 Introduction

Leaf area index (LAI) is a vegetation characteristic with a dominant role in controlling primary production, evapotranspiration, surface energy balance, and biogeochemical cycling. LAI is thus a critical part of many global change studies, including those focussing on identifying recent changes in plant growth (Jia et al., 2006; Myneni et al., 1997) or interpreting measurements of net carbon fluxes from global networks (Owen et al., 2007). LAI is also a key variable in vegetation/biogeochemical models (Sitch et al., 2003) and land surface schemes in general circulation models (Essery et al., 2001), and its variation across space must be determined to improve model predictions.

LAI can be highly heterogeneous. For instance, LAI in Arctic ecosystems can vary by an order of magnitude over landscapes (Williams & Rastetter, 1999) due to the patchiness of vegetation. The size of vegetation patches, and the range and statistical distribution of LAI in the landscape, are generally poorly recorded worldwide. The patchiness of ecosystem structure and function thus represents a major challenge in

upscaling LAI (Boelman et al., 2005; Williams et al., 2001). In the Arctic, changes in LAI are already occurring, and resulting in feedbacks to regional climate (Chapin et al., 2005).

Upscaling can be defined as the process for extrapolating from the site-specific scale, at which direct observations are made, to the smallest scale resolved in regional or global models or earth observing systems (Harvey, 2000). Because the terrestrial biosphere is characterised by spatial heterogeneity and non-linear processes, it is important to determine whether the relationships determined at fine scales in field research are applicable directly at coarser scales. Without proper care, significant errors can be introduced in the upscaling process.

Because LAI is related to the surface energy balance, satellite and airborne instruments provide a means to monitor LAI remotely (Tian et al., 2002). Remote sensing does not, however, measure LAI directly. Observations of surface reflectance (e.g. the normalized difference vegetation index (NDVI); the normalized ratio between the red and infrared bands) are generally calibrated against direct observations of LAI from field measurements (Boelman et al., 2003; Van Wijk & Williams, 2005). A particular source of error is caused by differences in spatial scale between remote observations and direct measurements (Woodcock & Strahler, 1987). Williams et al. (2001) showed a poor correlation between LAI measured in destructive harvests in arctic tundra in 0.2 x 0.2 m quadrats versus NDVI data from satellites at 1 km^2 resolution.

Here, we describe a series of measurements to map and quantify the spatial distribution of LAI in a sub-Arctic landscape. Our overall objective is to test an upscaling approach so that uncertainty in landscape LAI can be directly determined. The landscape scale selected (500 x 500 m) is highly relevant as it represents the approximate scale of sampling by eddy flux instrumentation used to monitor C fluxes, and it is also

spans the scale of key earth observation sensors, such as Landsat ETM+ and MODIS. With a detailed knowledge of LAI at this scale it should be possible to interpret flux data and satellite information more effectively for global change research.

In a microscale study (spatial resolutions from 0.2-9 m), determinations of LAI from harvests were linked to a series of scaled observations of NDVI collected with hand-held instruments. We tested the hypothesis (H1) that NDVI averaged linearly at resolutions from 0.2-9 m. If proven, this relationship simplifies up-scaling. We then tested the hypothesis (H2) that LAI-NDVI relationships were scale-invariant. Scale-invariance means that an NDVI-LAI relationship developed at a fine scale can be applied at a coarser scale. We hypothesised (H3) that the range of LAI data estimated for a sample area would increase at finer sensor resolutions. We expected that the distribution of estimated LAI would be increasingly skewed at finer resolutions, because much of the Arctic land surface has low LAI values and is patchy at fine scales (Street et al., 2007; Williams & Rastetter, 1999). Any shift in the distribution of estimated LAI will have important implications for any process non-linearly associated with LAI.

We then determined the capacity of satellite remote sensing approaches to retrieve information on spatial distribution of LAI. In a macroscale study (spatial resolutions from 10-500 m) overlaid on the microscale measurement area, we compared collocated ground-based estimates of NDVI (9 m resolution) to satellite data (30 m resolution). Our first objective was to test the quality of space-borne observations of NDVI. Our second objective was to construct maps of LAI using a variety of methods, including interpolation of ground data, direct application of calibrated remotely sensed data, and a combination of the two. We hypothesised (H4) that geostatistical interpolations of ground data combined through Kriging with remotely sensed NDVI

data, would produce better maps than either interpolation or satellite-based approaches alone.

There is an increasing interest in data assimilation approaches (Raupach et al., 2005; Williams et al., 2005) for modelling studies, whereby models and multiple observations are combined to produce an analysis of a system with quantified confidence levels. For regional data assimilation, provision of estimation errors and their spatial structure is vital, so we generated maps of LAI estimation error. We conclude by discussing how studies of this type can guide the process of assimilating remote sensing observations into ecosystem C models.

Previous studies have correlated ground measurements of LAI against satellite NDVI (Turner et al., 1999) in temperate and boreal ecosystems. But these studies have not taken explicit account of the difference in scales between satellite pixels and ground data collections, nor assessed NDVI at ground level for direct comparison to satellite data. Our study is novel in that, for the first time, a nested design has been used to upscale direct, harvest measurements of LAI to the landscape scale, with the same sensor approach (NDVI) employed at all scales from ground to satellite. This experimental design means it is possible to track the development of errors throughout the upscaling and properly quantify canopy heterogeneity.

3.4 Methods

3.4.1 The study area

This study was carried in a 500 x 500 m area located within the sub-Arctic zone of Fennoscandia; an ecotone between taiga and tundra characterised by deciduous birch forests with low altitudinal tree lines, above which heath and mire communities

predominate (Callaghan & Karlsson, 1996). The study area was located above the tree line near Abisko, Sweden (68° 18'N, 18° 50'E) at an average elevation of 580 m at the centre of a shallow valley draining northwards, hereafter known as the intensive valley (IV). At Abisko the average rainfall is 400 mm per annum and average temperatures are –1°C (Anderson et al., 1996). A stream running through the centre of the area was bordered by shrubby riparian vegetation characterised by Betula nana and Salix species. Elsewhere vegetation was dominated by a low heath characterised by Empetrum nigrum, with Betula nana growing in more sheltered dips. There were some scattered wooded areas characterised by Betula pubescens usually with a Vaccinium understory.

3.4.2 Skye NDVI and LAI measurements

Measurements were carried out at two scales within the IV. The 'microscale' study (testing H1-H3) focussed on detailed measurements within a 40 x 40 m area straddling the stream and foot-slopes of the IV. The 'macroscale' study (testing H4) involved estimates of NDVI from a 500 m x 500 m area spanning the upper slopes and valley floor of the IV, and including the microscale site at its centre (Figure 3.1).

The microscale study involved measurements in nine 10 x 10 m plots laid out in a regular grid at 5 m spacing in the 40 m x 40 m domain, collected between the 10th and 31st July, 2002 (Van Wijk & Williams, 2005). In each 10 x 10 m plot, direct harvest measurements of LAI (harvest LAI) were determined in nine 0.2 m x 0.2 m quadrats (Williams & Rastetter, 1999). A series of indirect LAI measurements were also obtained on each quadrat pre-harvest using (1) NDVI obtained with a Skye Instruments 2 Channel Sensor SKR1800 (Skye Instruments, Powys, UK, channel 1 = 0.56-0.68 μm, channel 2 = 0.725-1.1 μm) with the diffuser off (Skye NDVI), and (2) a LI-COR LAI-2000 Canopy Analyzer (LI-COR, Lincoln, NE, USA), collecting one above and one

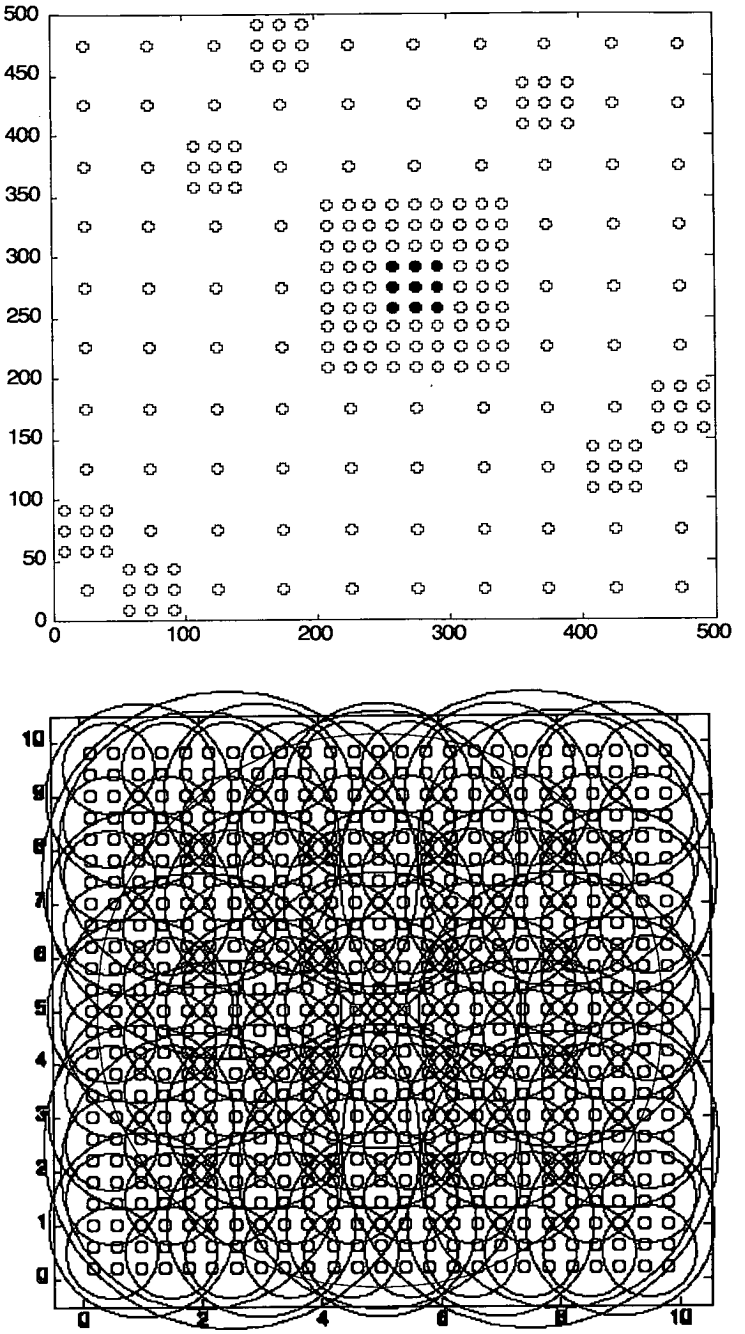

Figure 3.1.The top panel shows the 500 x 500 m macroscale experimental design, and its approximate orientation. The circles show the locations and sampling area of 9 m resolution Skye NDVI observations. The filled circles indicate the location of the microscale study area. The bottom panel shows the nested multi-scale experimental design for one of the nine microscale 10 m x 10 m plots. The circles show the locations and approximate sampling area of Skye NDVI, with scales ranging from 0.2 m (smallest circles, n = 625) to ~9 m (the largest circle, n = 1). LAI-2000 data were also collected at the points indicated by the smallest circles. Both figures have scales in m.

Table 3.1: The design of multiscale NDVI measurements on 10 x 10 m microscale plots. Nine 10 m x 10 m plots were sampled in this way.

Measurement height (m)	Area (m^2)	Diameter (m)	N‡
0.9*	0.03	0.2	525
0.5	1.77	1.5	100
1.0	7.07	3.0	25
1.5	15.9	4.5	9
2.0	28.3	6.0	5
3.0	63.6	9.0	1

All units in meters
* indicates the diffuser was not used, so field of view was reduced.
‡ Number of samples in aerial unit

below-canopy measurement (LAI-2000 LAI). The harvest LAI data were used to calibrate the indirect sensors, see Van Wijk and Williams (2005) for full details.

The spatial variability of LAI within the nine microscale plots was determined by performing paired LAI-2000 and NDVI measurements, each giving an estimated resolution of 0.2 m, in each plot in a regular grid at 0.4 m intervals. 625 measurements for each instrument were collected in each plot, giving 5625 measurements at 0.2 m resolution for the microscale study. Harvest LAIs in the microscale study were closely related to Skye NDVI values, but the best estimates of LAI were generated by combining information from co-located LAI-2000 and Skye NDVI data, with parameters estimated by maximum likelihood methods (Van Wijk & Williams, 2005).

Besides estimating the NDVI at 0.2 m resolution on a regular grid of 0.4 m, we also estimated the Skye NDVI of larger surface areas on successively coarser grids (Figure 3.1). A diffuser cap extended the field-of-view of the Skye sensor to 113°, and the area of reflectance measurement was further increased by raising the sensor height using light-weight poles. The sensor heights, the area measured, the pixel resolution and the number of measurements taken at coarser scales are shown in Table 3.1. The

experimental design meant that measurements at a coarse resolution could be directly compared with multiple fine resolution data collected within the coarse pixel.

The macroscale study was undertaken between the 14th and 25th of August, 2004. A 500 m x 500 m area was set up centred on the microscale study (Figure 3.1). The macroscale area was divided into one hundred 50 x 50 m plots on a 10 x 10 grid (Figure 3.1). Sixteen of the 50 x 50 m plots were subdivided into nine 10 x 10 m intensive plots on a 3 x 3 grid with 5 m spacing to generate a nested sampling design with 228 plots. The central intensive 50 x 50 m plot corresponded with, and resampled, the microscale study of 2002. At the centre of each plot (whether 50 x 50 m, or 10 x 10 m) a Skye NDVI reading was recorded with the sensor suspended 3 m above the ground (Table 3.1) with a nominal resolution of 9 m. The location of each plot centre was determined using GPS, with spatial error estimated at ~6 m. Some plots had a covering of birch trees (>2 m tall) which precluded the use of the Skye sensor. These locations (n = 31) were excluded from the sampling analysis, so that the focus was purely on tundra vegetation in the remaining 197 macroscale plots.

3.4.3 Remote sensing

Remote sensing observations for the Abisko region were generated from Landsat 7 ETM+ data, with a nominal resolution of 30 m, collected from an overpass on 20 August 2001. The image belonged to the NASA's orthorectified data-set and was geo-referenced to a root-mean-square error (RMSE) of 50 m (Tucker et al., 2004). In order to confirm this claim and improve the accuracy, further geo-referencing was carried out using a 1:100,000 scale map belonging to the Lantmäteriet series. Twelve ground control points were used to give an image with a final RMSE of <35 m. We used bands 1 (red) and 4 (near infra-red) to determine Landsat NDVI. Landsat NDVI

values were then extracted by distance weighted averaging (ArcInfo software, ESRI, Redlands, USA) for each macroscale plot for comparison with Skye NDVI measurements and LAI estimates for these locations.

Airborne remote sensing was undertaken using a helicopter, with the Skye NDVI sensor mounted externally on a boom. The macroscale area was located from the air using GPS, and the helicopter hovered over the centre of the study area at a height of 235 m above the ground surface. Given the field of view with the cosine diffuser, the ground resolution (i.e. diameter) of the single NDVI observations was ~700 m.

3.4.4 Geospatial methods

To identify pattern in spatial measurements of the microscale and macroscale areas, and also the remote sensing data, we generated semi-variograms, a description of the spatial autocorrelation structure of the data (Cressie, 1993). For a stationary process, there is generally an increase in semivariance with increased separation vector, up to some threshold distance, referred to as the range. At separation distances greater than the range, the semivariance remains at a constant 'sill' value. The semivariance at zero separation is known as the nugget.

We fitted an exponential model of semivariance

$$g(h) = \tau + c\left(1 - \exp\left(\frac{-3h}{\phi}\right)\right) \qquad \textbf{(3.1)}$$

where τ is the 'nugget' variance, c is the contribution of the exponential structure, and ϕ is the effective range, interpreted as the distance at which $g(h)$ reaches 95% of the asymptotic 'sill' variance ($\tau + c$). The factor of 3 in the numerator solves for

Table 3.2. Testing different techniques of LAI extrapolation. All techniques used ground LAI estimates, but only some used Landsat NDVI data. Root-mean-square-error and mean absolute error of the jackknife test are shown.

Technique	Ground LAI	Landsat NDVI	RMSE	MAE
Inverse distance weighting (IDW)	Yes	no	0.27	0.21
Linear correlation model (LCM)	Yes	yes	0.28	0.21
Ordinary Kriging (OK)	Yes	no	0.28	0.21
Kriging with external drift (KED)	Yes	yes	0.29	0.22

effective range. The model was fit to the data by minimising the sum of squares differences.

3.4.5 Generating LAI maps

We used a variety of methods, from relatively simple to more complex, to generate maps of LAI for the macroscale area, using various combinations of ground and satellite observations (Table 3.2). Inverse distance weighting (IDW) makes use of estimates of LAI, derived from Skye NDVI, and information on their spatial arrangement. LAI values across the macroscale domain were generated through interpolation of the 197 macroscale plots, with weights determined according to distance. The linear correlation model (LCM) approach used the linear regression of Landsat NDVI (30 m resolution) against ground-based estimates of LAI (9 m resolution, from Skye NDVI data) for the same locations. The linear regression was then used to estimate LAI for all Landsat NDVI pixels over the intensive valley.

Kriging refers to a set of multiple linear regression procedures by which the best linear unbiased estimate of an unobserved datum value is arrived at by the weighted linear combination of surrounding observations, such that the prediction error is minimized (Goovaerts, 1999; Isaaks & Srivastava, 1990). The weights ascribed to each observation are arrived at by taking into consideration the clustering of the data locations (with points from over-sampled locations being down-weighted), and the proximity of each observation to the prediction location. These spatial effects are included via reference to the autocorrelation structure of the data set, as summarized by the semi-variogram. Ordinary Kriging (OK) involved generating an interpolated LAI map using ground based LAI data and their semi-variograms. An additional output from Kriging is a prediction of interpolation error, provided by the geostatistics of the semi-variograms.

More complex spatial regression models partition the spatial information into a large-scale trend component, and a stationary, spatially autocorrelated residual component (i.e., non-stationary geostatistics). In Kriging with an External Drift (KED) we used a secondary covariate 'external' to the calculation of semivariance for our data as extra spatial information (Deutsch & Journel, 1998). Here we require that the variation of the secondary data, in this case Landsat NVDI data, be smoothly and linearly related to the local variable, the estimates of LAI. The covariate must be sampled at all observation and all prediction locations. The extra covariate informs the interpolation, so that the more spatially complete remote sensing observations improve interpolation skill.

The interpolation skill of each technique was assessed by statistical resampling. The jackknife approach involved systematically recomputing the interpolations, leaving out one observation at a time. The ability of the interpolation routine to predict the

missing observations can then be used to construct statistics, such as a RMSE and mean absolute error (MAE).

3.5 Results

3.5.1 Microscale study

3.5.1.i Microscale NDVI

The mean microscale site NDVI estimated by averaging 0.2 x 0.2 m NDVI observations was 0.68, and was identical at all scales from 1.5 – 9 m (Table 3.3), and very similar to the median values. The mean NDVI estimated for the same range of scales using individual, coarser samplings (Table 3.2) was slightly larger, 0.73, but also did not vary across the pixel resolution from 1.5 - 9 m (Table 3.3). Again, the median values were very similar (0.74). NDVI generated by averaging the finest resolution data (0.2 m) plotted against single observations at increasingly coarser resolution showed a strong linear relationship across the range of scales (Figure 3.2). The slopes and intercepts of the linear regressions fitted to the NDVI comparisons were very similar in all cases.

3.5.1.ii Microscale LAI

The fine scale estimates of LAI (0.2 m resolution), derived from co-located Skye NDVI and LAI-2000 observations, were aggregated at various scales (1.5 – 9.0 m resolution) and compared to corresponding single Skye NDVI estimates at those scales (Figure 3.3). A simple exponential fit of NDVI-LAI using maximum likelihood approaches with an assessment of LAI estimation error (Van Wijk & Williams, 2005) was successful (i.e. acceptable parameter combinations were identified, $P<0.05$) at each scale of comparison

(Figure 3.3). This successful fit was in contrast to the case at 0.2 x 0.2 m reported in Van Wijk and Williams (2005), which required the combination of Skye NDVI and LAI-2000 data to generate an acceptable estimation of LAI.

The exponential fits are able to explain 80-94% of the variability in LAI from NDVI data. The parameters for the exponential relationships were similar across all scales (Figure 3.3). The RMSE of the LAI-NDVI relationships varied from 0.18 at 1.5 m resolution to 0.08 at 9 m resolution (Figure 3.3). As the range of LAI and NDVI variability declined with coarsening resolution, linear fits became increasingly acceptable, although the exponential models were always better.

The mean LAI for the microscale site generated using 0.2 m resolution data was 0.69, and the median was 0.65. Both the NDVI data (Table 3.3) and the LAI estimates derived from NDVI and LAI-2000 (Figure 3.4) show decreasing ranges with spatial aggregation. At the finest scales, some sites had LAI values very close to zero, but the minimum LAI (L_{min}) estimate increased linearly with resolution, (L_{min} = 0.0371 r = 0.0108, where r is resolution in m, r^2 = 0.99, n = 6). The maximum LAI dropped sharply in the aggregation from 0.2 m (L_{max} = 3.68) to 1.5 m (L_{max} = 1.75), but thereafter declined slowly. The distribution of LAI at 0.2 m resolution was highly skewed, but tended towards normality at coarser aggregations (Figure 3.4).

Table 3.3 Comparison of Skye NDVI generated across a range of scales in the microscale plots. At each pixel resolution, there are two methods for determination of NDVI, classified by whether the NDVI is the average of several fine-scale NDVI measurements (n>1), or is determined by a single measurement (n=1). The number of replicates (n') indicates the number of pixels at each resolution, which are then used to generate statistics of NDVI at different scales and generated with different numbers of observations (n), in the columns below.

Resolution (m)	1.5		3		4.5		6		9	
Observations in pixel (n)	6	1	25	1	69	1	125	1	625	1
Number of replicates (n')	900		225		81		45		9	
minimum	0.36	0.5	0.47	0.56	0.51	0.61	0.53	0.62	0.59	0.67
median	0.69	0.75	0.69	0.74	0.68	0.73	0.68	0.73	0.68	0.74
maximum	0.83	0.85	0.8	0.83	0.79	0.8	0.78	0.83	0.76	0.78
mean	0.68	0.73	0.68	0.73	0.68	0.73	0.68	0.73	0.68	0.73
standard deviation	0.08	0.061	0.07	0.054	0.062	0.047	0.055	0.046	0.052	0.04
variance	0.0063	0.0037	0.0049	0.0029	0.0039	0.0022	0.0031	0.0021	0.0027	0.0015
skew	-0.95	-0.89	-0.72	-0.85	-0.55	-0.88	-0.29	-0.27	-0.29	-0.29
kurtosis	3.73	3.62	3.15	3.42	3.06	3.21	2.74	2.52	2.3	1.75

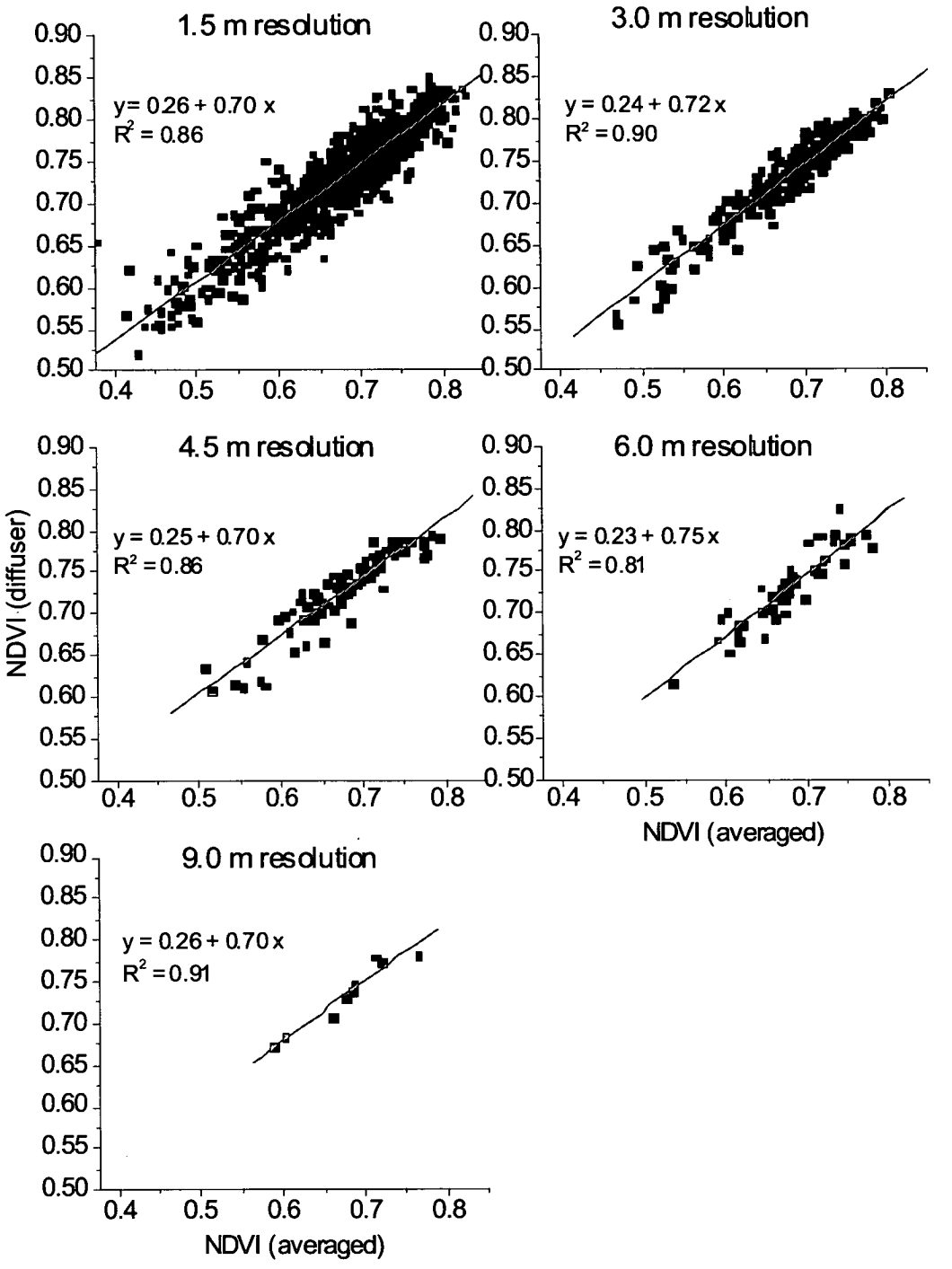

Figure 3.2. Linear averaged Skye NDVIs (collected at 0.2 x 02 m resolution with diffuser off) versus measured NDVIs at coarser spatial scales with diffuser on. Linear regression equations and r^2 values are shown.

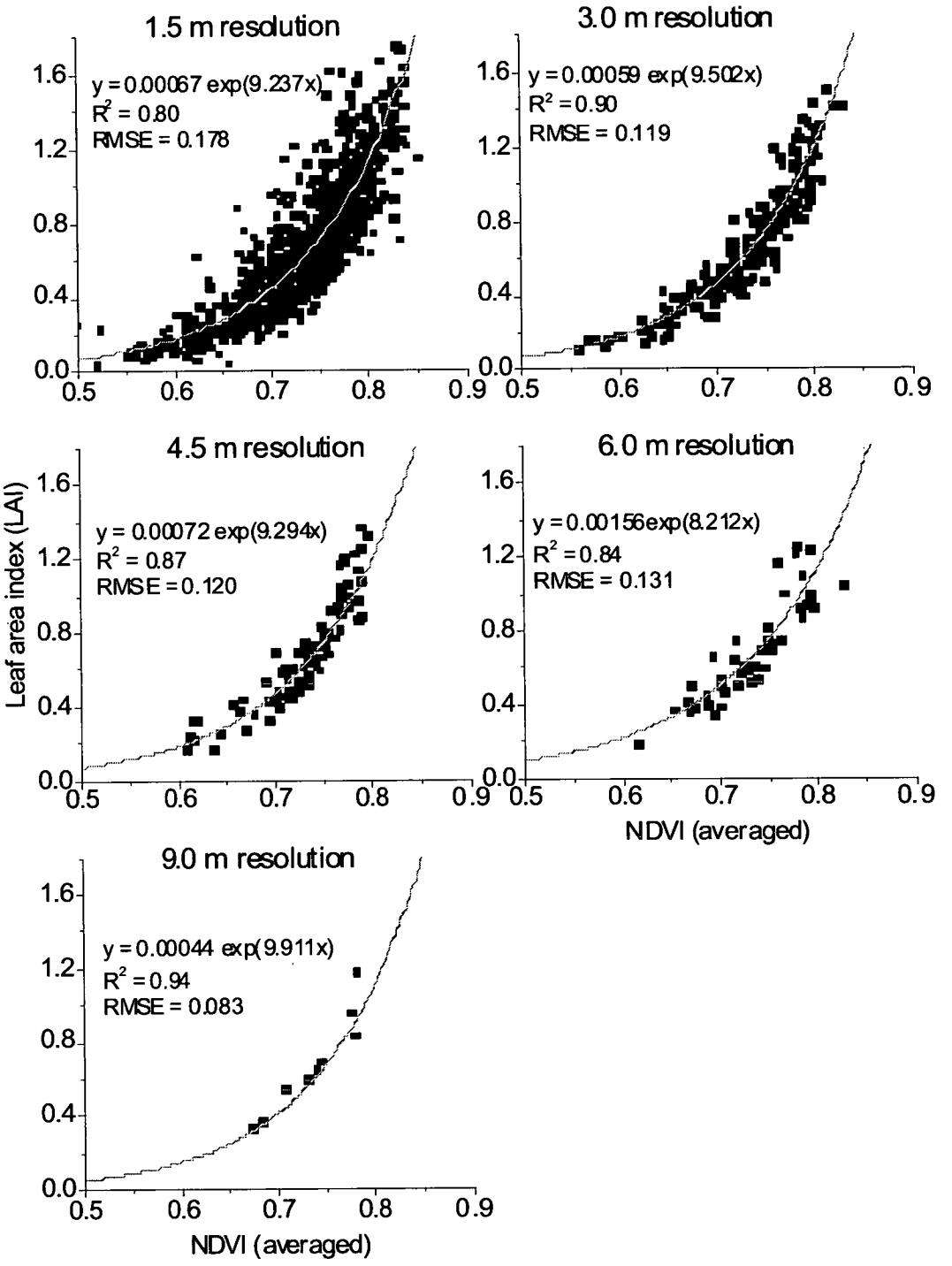

Figure 3.3 Relationships between estimated LAI (using both Skye NDVI and LI-COR LAI-2000 observations at 0.2 m resolution, linearly averaged for upscaling) versus Skye NDVI at different spatial scales. Exponential model equations, R^2 and root mean square error are shown.

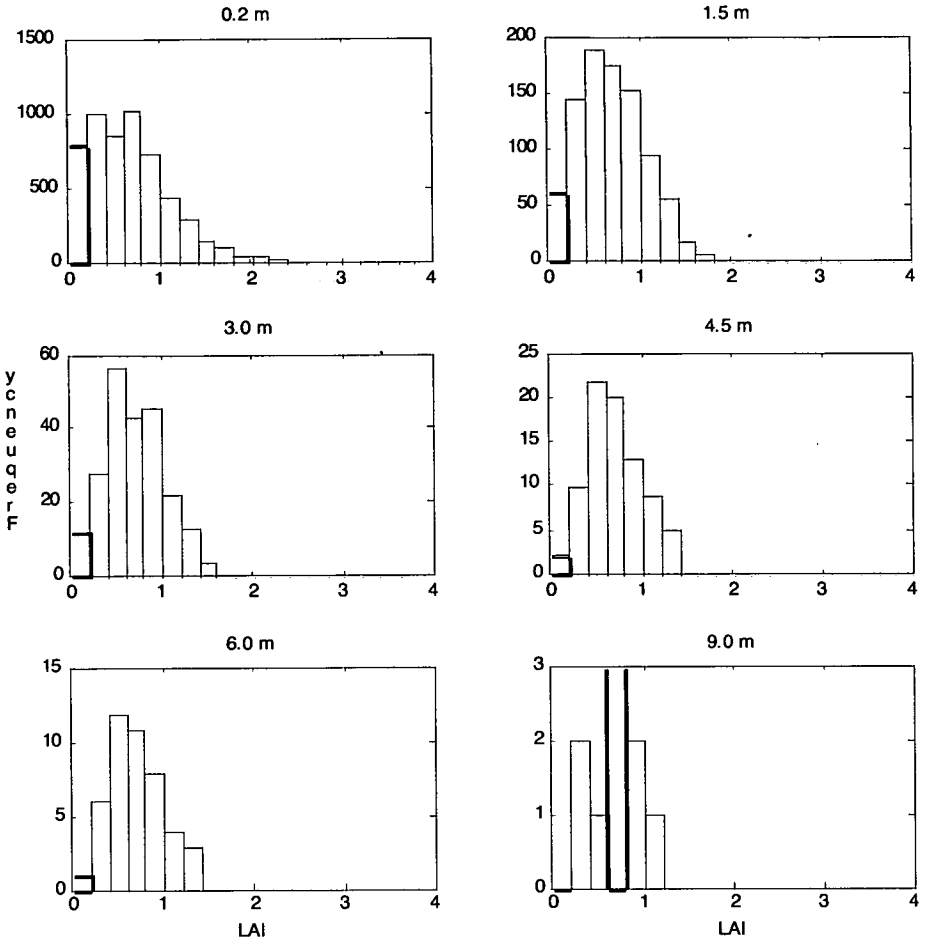

Figure 3.4. Frequency histograms for LAI estimates in the microscale site at a range of resolutions. LAI was derived from the calibrated NDVI and LAI-2000 relationship at 0.2 m resolution. The complete 5625 estimates are shown in the top left panel. In succeeding panels the data are aggregated into coarser pixels by linear averaging.

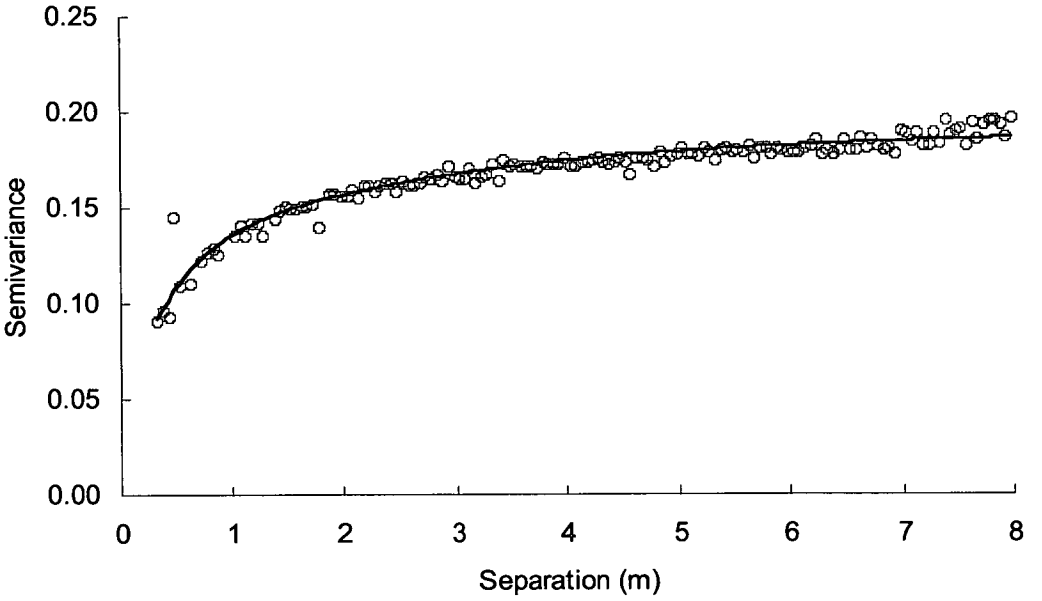

Figure 3.5. Semi-variogram for LAI in the microscale study. The plot demonstrates the increase in spatial variance with separation distance using all paired measurements from 5625 LAI estimates (symbols). An exponential model (solid line) is fitted to the observations. The nugget variance is 0.03, the range for the first exponential model is 1.2 m, and for the second is 8.0 m, where the sill is 0.19.

3.5.1.iii Spatial autocorrelation

There was clear spatial autocorrelation in the microscale estimates of LAI, as indicated in the semi-variogram (Figure 3.5). However, the autocorrelation dropped rapidly at distances beyond 1.2 m. A more gentle decline followed, with the sill value reached at 8 m. The discontinuity at the origin of the semi-variogram (the 'nugget') is a combination of noise and the interaction of the discrete nature of plants with the sampling scale. So the nugget represents a fundamental uncertainty in observed LAI. The nugget value of 0.03 suggested that the standard deviation on LAI uncertainty was 0.17.

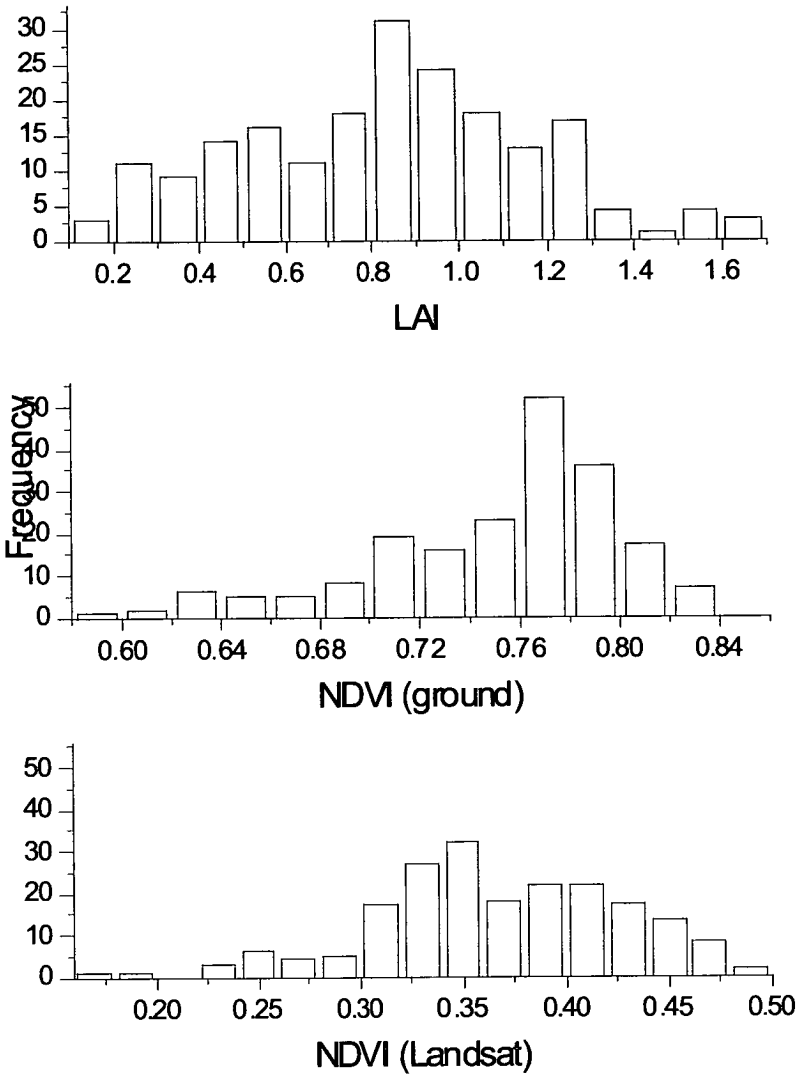

Figure 3.6. Histograms showing the variation in NDVI/LAI recorded in the macroscale study, at the 197 tundra sampling points (Figure 1). The panels show a comparison between Landsat ETM+ NDVI data (lower panel), NDVI recorded in the field at 9 m resolution (middle panel), and LAI (upper panel) estimated using the 9 m resolution data using the equation from Figure 3.3.

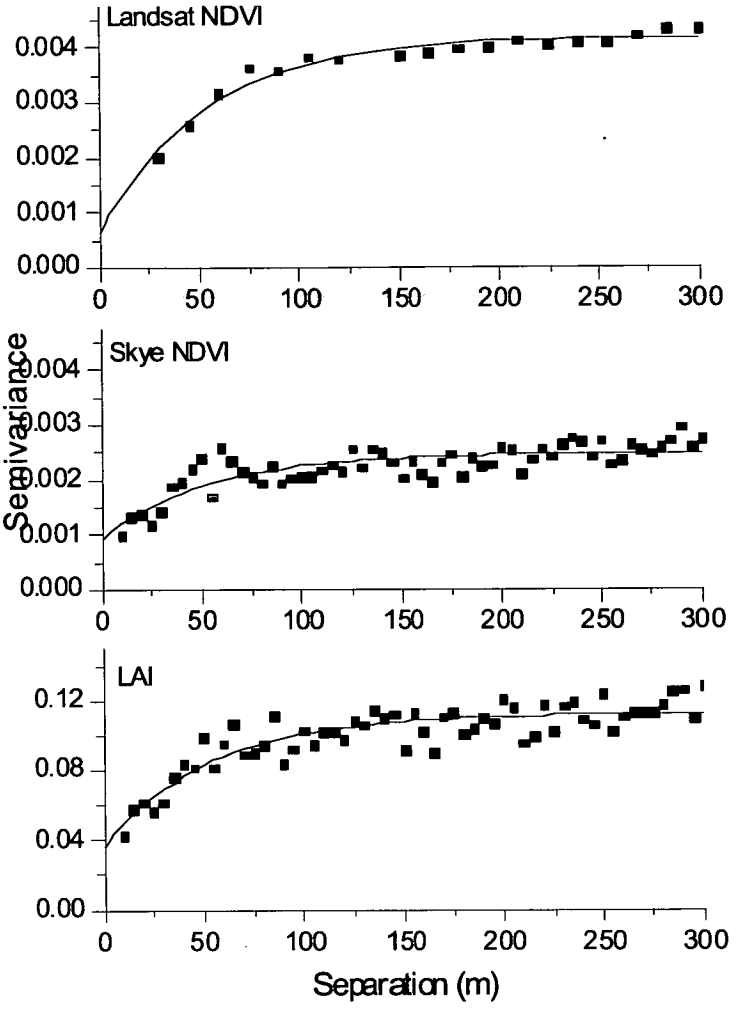

Figure 3.7. Semi-variograms for LAI and NDVI in the macroscale study of the intensive valley. The middle panel was generated from Skye NDVI, and the lower panel from associated estimates of LAI. The top panel was generated from Landsat NDVI for the same locations. Exponential models (solid lines) are fitted to the observations (symbols).

3.5.2 Macroscale study

3.5.2.i Macroscale NDVI and LAI

The mean NDVI recorded across the 197 tundra sample locations at a resolution of 9 m was 0.75, close to the mean value of 0.73 recorded using the same sampling approach at the microscale site (Table 3.3). The distribution of measured NDVI was skewed towards higher values (Figure 3.6). Using the relationship between LAI and NDVI generated using microscale data at 9 m resolution (Figure 3.3), LAI was estimated for all macroscale locations. The mean estimated LAI was 0.84 with a range from 0.14 to 1.60, and a distribution without skew (Figure 3.6), similar to the distributions of LAI determined at ≥3.0 m resolution in the microscale study (Figure 3.4). We tested deriving macroscale LAI estimates using the LAI-NDVI relationships from the other microscale resolutions, 1.5 – 6.0 m (Figure 3.3). The mean LAI (n = 197) using all relationships was 0.82, and the individual relationships differed from the mean by 1-7%, so there is little difference between the relationships.

The NDVI estimated by airborne sampling of the entire macroscale area was 0.74, close to the mean value of the macroscale field measurements. Using the upscaled NDVI-LAI relationship (Figure 3.3) resulted in estimate of LAI of 0.70 at 700 m resolution for the intensive valley, 17% less than the estimate summed from 9 m resolution ground data. This error is what might be expected, given the RMSE of the LAI-NDVI relationship from the microscale study.

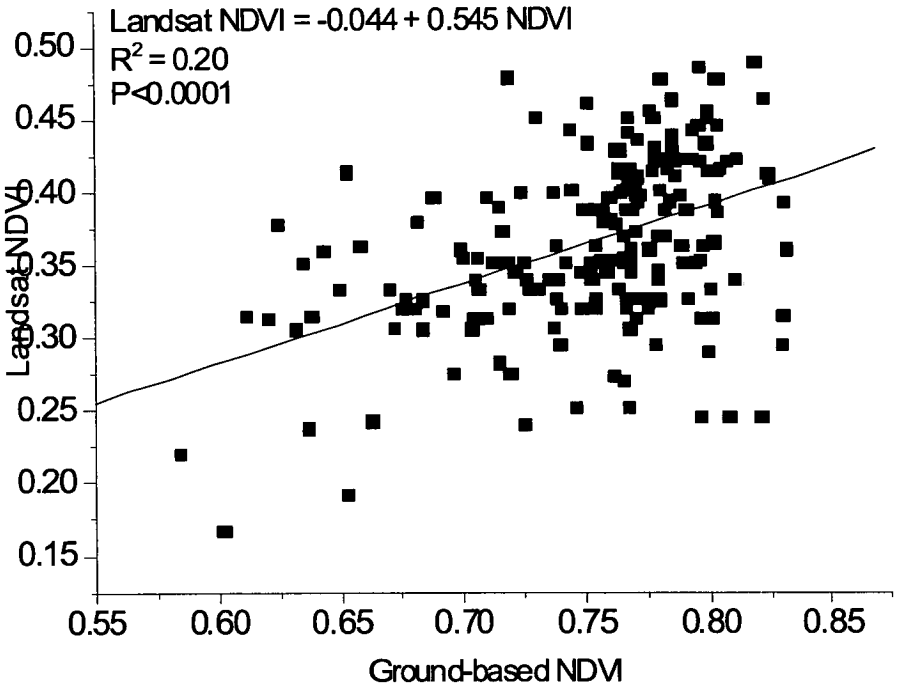

Figure 3.8. A comparison across the macroscale area of the intensive valley of ground-based NDVI using 9 m resolution measurements and LandSat NDVI measurements for the same locations. The line indicates the linear regression.

3.5.2.ii Macroscale geostatistics

Semi-variograms for the macroscale observations of LAI and NDVI in the intensive valley, and also the LandSat observations of NDVI for the same locations, indicated clear spatial autocorrelation (Figure 3.7). Pairs of data observations separated by <160 m showed clear autocorrelation in both analyses. The sill values (i.e. maximum semivariance) for the satellite NDVI analysis were larger than those for the ground-based NDVI, and this was likely due to the effect of atmospheric interference and differences in viewing angle (Lillesand et al., 2003). The nugget value was 50% greater for the Skye NDVI than for the Landsat data, but the ground-based values require less

extrapolation and thus are more trustworthy. The nugget on the macroscale semi-variogram was the same as that determined on the microscale data, again indicating an uncertainty in LAI estimates of 0.17. At distances of 50 m, the standard deviation in LAI increased by >50% to 0.26.

3.5.2.iii Satellite data

The comparison of ground-based NDVI with LandSat NDVI revealed a highly significant linear relationship (Figure 3.8, $r^2 = 0.20$, $P < 0.0001$). The intercept was not significantly different from zero ($P = 0.446$) but the slope of the relationship (0.55) was significantly different from one ($P<0.001$). A simple linear correlation model (LCM) between Landsat NDVI and ground-based LAI at the macroscale sites was developed ($r^2 = 0.17$, LAI =-0.004 + 2.1 NDVI, data not shown). The LCM predictions of LAI had an RMSE of 0.28 for the macroscale plots. Semi-variograms of NDVI from Skye and Landsat showed a very similar form (Figure 3.7), suggesting a detection of the same underlying spatial pattern. However, the frequency distribution of Landsat NDVI values was quite different to Skye NDVI measurements (Figure 3.6). The satellite data showed a peak in frequency towards the low end of the measurement range, while the ground data showed a peak towards the high end of the range.

3.5.2.iv Extrapolation of LAI

Extrapolation with the linear correlation model (LCM, Figure 3.9), inverse distance weighting (IDW), ordinary Kriging (OK, not shown) and Kriging with an External Drift (KED,) generated maps with some clear commonalities, but also differences. All approaches predicted an increase in LAI towards the north of the IV, matching the local drop in elevation. There was a smoother LAI distribution with IDW and OK compared to LCM and KED.

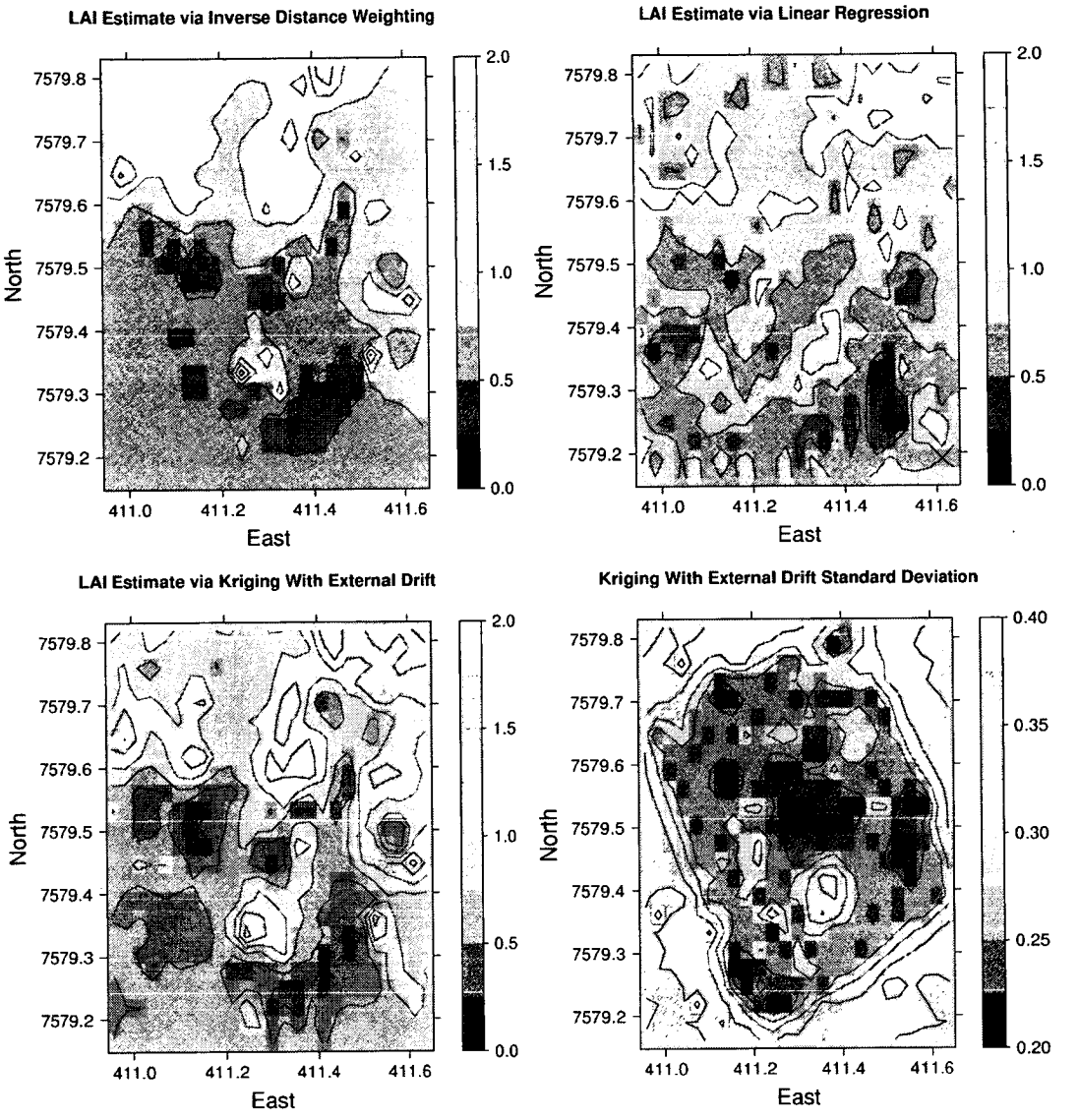

Figure 3.9. Maps of LAI for the intensive valley for late August, using inverse distance weighting of ground-based NDVI data (upper left); a simple correlation model of ground-based LAI versus Landsat NDVI data (upper right); Kriging of ground-based NDVI data with external drift from Landsat NDVI data (lower left). The variances of the Kriging estimates are shown in the lower right panel. Contour lines are overlaid on the pixels. The units of the axes are in kilometers, based on the UTM coordinate system.

The four methods showed similar overall skill, as determined in the jackknifing of predicted LAI against LAI estimates from Skye NDVI (Figure 3.9). These techniques make use of different data sets and assumptions, so this similarity is unexpected. The Kriging methods have the advantage of producing spatial error estimates, which clearly were minimised around ground sampling points, and maximised in areas with sparse

sampling (Figure 3.9, lower right panel). Some ground sampling points were missed out if there was tree cover, and this explains some of the largest concentrations of error. In Kriging the growth of error with distance from ground sampling points is determined by the semi-variograms (Figure 3.7).

3.6 Discussion

3.6.1 Comparing NDVI measurements across scales

The microscale multi-resolution data were consistent with the hypothesis (H1) that NDVI averaged linearly at resolutions from 0.2-9 m (Figure 3.2). The coarse measurements of NDVI were slightly offset from the fine-scale averages, probably due to the presence of the cosine diffuser on the sensor during the coarse measurements. However, at all scales of averaging up to 9 m, the linear regression parameters were very similar. These sensor resolutions are estimates only, because the instrumental field of view does not have sharp boundaries, but rather a weighting towards 113°. Furthermore, there was some error associated with the location of each sensor reading, particularly those where the sensor was suspended over the land-surface at heights of 2 or 3 m. The landscape is heterogeneous, with a highly skewed distribution in NDVI at fine (0.2 m) scales. Nevertheless, the results here show that single, coarse pixel measurements capture the mean properties of surface reflectance accurately. The lack of falsification for H1 is a powerful support for the subsequent scaling exercises.

3.6.2 Scale invariance in LAI-NDVI relationships

In support of hypothesis (H2), we found that LAI-NDVI relationships were scale-invariant in the microscale study (Figure 3.3). At all resolutions, from 1.5 – 9 m, a

simple exponential relationship linked upscaled LAI with Skye NDVI measured directly at the relevant resolution. While these LAI-NDVI relationships were all similar (in terms of parameters), they differed from the LAI-NDVI relationship at 0.2 m (Van Wijk & Williams, 2005), because the 0.2 m resolution data were collected without a diffuser. More importantly, the coarse scale LAI-NDVI relationships were all stronger ($0.80 < r^2 > 0.94$) compared to the original study at 0.2 m ($r^2 = 0.73$) and outputs from the relationships differed by only a few percent. Further, maximum likelihood analyses (Van Wijk & Williams, 2005) undertaken on the data from this study indicated that the NDVI data alone were able to provide a satisfactory prediction of LAI at resolutions from 1.5 – 9 m, which was not the case for 0.2 m resolution data. This improvement in the capabilities of NDVI as a predictor of LAI is likely to be due to the averaging of LAI values occurring at coarser resolutions. NDVI performed poorly in estimating higher LAI values at 0.2 m resolution, but maximum LAI dropped sharply with scale aggregation (Figure 3.4) so this problem was negated.

The outcome of this hypothesis testing is that carefully calibrated LAI estimates developed at 0.2 m using destructive harvests have been used to develop a robust calibration of LAI-NDVI at a range of coarse resolutions which approach those typical of aircraft and satellite remote sensing. The error properties of the LAI-NDVI relationship are well characterised. As far as we know this study is the first to link direct measurements of canopy structure (i.e. LAI) at fine scales to remote sensing data with replication across scales spanning more than an order of magnitude.

3.6.3 Spatial distribution of LAI

We hypothesised (H3) that the range of LAI data estimated for a sample area would decline with a coarser sampling, and that the distribution of estimated LAI would

be increasingly skewed at finer measurement scales. We found clear shifts in probability density functions for LAI in the microscale study, with increasingly skewed distributions at finer scales (Figure 3.4). Spatial autocorrelation of LAI in the microscale study was greatest at <1 m separation (Figure 3.5), indicating that ~0.5 m was the approximate scale of vegetation patches. In accordance with this analysis, the greatest variation in NDVI and LAI was at the finest scale of sampling (0.2 m), while the range of both NDVI and LAI dropped rapidly at more aggregated scales. It is interesting that the LAI semi-variogram for the macroscale study has similar nugget values to the microscale semi-variogram, but sill values in the macroscale study are around half those in the microscale study. This comparison suggests that at coarser scales of measurement the variance of canopy characteristics declines as the values of extreme, small patches, are subsumed.

The quality of autocorrelation statistics depends on the quality of the datasets used to generate them, so their results must be interpreted cautiously. We used very simple geostatistical models, taking no account of topography, which is likely to be an important factor in controlling the distribution of vegetation.

3.6.4 Assessing LAI with satellite NDVI data

Our first objective was to test the quality of space-borne observations of NDVI against ground data. The comparison of ground estimated LAI versus Landsat NDVI was poor (though significant), with relatively large prediction errors (Figure 3.8). It is possible that georeferencing errors have degraded the correlation in our study, but such errors are inherent in most satellite remote sensing studies. The comparison of histograms of Skye and Landsat NDVI (Figure 3.6) show that there are clear differences between the landscape signals, that are unlikely to be explained by spatial errors of ~6 m

from the GPS. Other comparisons of Landsat NDVI versus LAI have shown similar, poor correlations for temperate and boreal ecosystems (Lee et al., 2004). A comparison of 1 km AVHRR NDVI versus LAI from tundra in the Alaskan arctic had a similar, weak correlation coefficient (Williams et al., 2001). Lee et al. (2004) concluded that satellite NDVI was generally not sensitive to LAI. Our ground based studies have shown that this is not the case, because Skye NDVI was highly sensitive to LAI. There was a poor correlation between Skye NDVI and Landsat NDVI data, and so it seems that errors in the satellite data cause the relationship observed at ground level to break down.

The poor Skye versus Landsat NDVI correlation and large offset of the satellite data reflects several uncertainties. Firstly, there were georeferencing errors in both the ground-based and satellite data. We explored these errors by introducing 7 m buffer zones into the ground data locations, corresponding to the GPS error. For the buffer zone around each Skye NDVI measurement, we determined the mean NDVI of all underlying Landsat pixels. The result was only a small improvement in the NDVI-NDVI correlation coefficient (data not shown) suggesting that small uncertainties in the handheld GPS and spatial uncertainty introduced by raising the sensor height were not the cause of the poor relationship. Secondly there were errors related to the temporal offset in NDVI collection. The Landsat data were from late August 2001, and the macroscale data were collected in late August 2004. Phenological differences between years are possible. Finally, there were errors introduced by differences between sensor optics, atmospheric attenuation of signals, and local illumination conditions (Alter-Gartenberg et al., 2002) to be considered. Atmospheric correction of the reflectance data could improve the estimate of NDVI, but the required atmospheric data were not available. Future studies should combine ground-based and airborne remote sensing

with the necessary atmospheric transmissivity information to reduce uncertainties in NDVI/LAI estimation at larger spatial scales.

3.6.5 Maps of LAI, and estimation errors

Our second objective was to generate maps of LAI across the macroscale site, using a variety of approaches with remote sensing data and geostatistics. We hypothesised (H4) that geostatistical interpolations of ground data combined with remotely sensed NDVI data, through Kriging, would produce better maps than either interpolation or satellite-based approaches alone, but our results showed this was not clear cut. All four approaches produced roughly the same level of mean estimation error (Figure 3.9). We found that ground-based NDVI data were excellent at generating local LAI estimates, with mean estimation errors of typically 0.08-0.17. However, spatial autocorrelation dropped rapidly with increasing separation, so that at <50 m separation LAI errors were typically ~0.3. The linear correlation model between Landsat NDVI and ground estimates of LAI had an RMSE of 0.28. The similarity in magnitude of the spatial error and the Landsat calibration error accounts for the similarity in prediction capability across the macroscale area. Of course, around the ground measurement locations the prediction error was smaller, and so methods like Kriging have the advantage of reducing prediction error wherever extra data are available (Figure 3.9), but the spatial variability of this arctic landscape is such that local measurements have a limited spatial influence.

3.6.6 Spatial data assimilation

The assimilation of multiple data sources requires a careful determination of data error, so that data can be suitably weighted to produce an analysis. Data assimilation (DA) approaches are now being used commonly in ecological research to

generate state estimates, by combining process information with multiple data series (Raupach et al., 2005; Williams et al., 2005). These techniques are now being used to assimilate remote sensing data sequentially into ecosystem models (Quaife et al., in press). For such time-series DA approaches to be applied across regions or globally, spatial assimilation approaches such as Kriging become important tools for generating estimates of initial conditions in state variables, and for generating spatial errors. There is an urgent need to develop a closely coupled spatio-temporal assimilation system. This system would combine the strengths of time-series analysis with geostatistical approaches, to simulate ecological processes, and more effectively link networks of field sites - with high resolution process data - with global, repeated reflectance data from Earth Observation systems.

3.7 Conclusions

With multiple nested reflectance measurements on an Arctic tundra, we showed that NDVI scaled linearly with increasing spatial grain, and that the LAI-NDVI relationship was scale invariant from 1.5 – 9.0 m resolution. Thus, a single exponential LAI-NDVI relationship was valid at all scales, with similar prediction errors. An analysis of semi-variograms showed that vegetation patches were of a scale of ~0.5 m, and at measurement scales coarser than this there was a sharp drop in LAI variance. Landsat NDVI data for the study catchment correlated significantly, but weakly, with ground based NDVI measurements. A variety of techniques were used to construct LAI maps across the catchment, including interpolation by inverse distance weighting, ordinary Kriging, and Kriging with an External Drift using Landsat data, and direct estimation from the Landsat NDVI-LAI calibration. All four methods produced similar estimates

of LAI and errors of similar magnitude. The Kriging approaches also generated maps of LAI estimation error based on semi-variograms. The spatial variability of this arctic landscape was such that local measurements assimilated by Kriging approaches had a limited spatial influence. Over scales >50 m interpolation error was of similar magnitude to the uncertainty in the Landsat NDVI calibration to LAI. The characterisation of LAI error in this study is a key step towards developing spatio-temporal data assimilation systems for assessing C cycling in Arctic ecosystems from combining models, field and remotely sensed data sources.

3.8 Acknowledgements

We acknowledge funding from the US National Science Foundation (Grant numbers OPP-0096523, OPP-0352897, DEB-0087046, and DEB-00895825), from the University of Edinburgh, and from the Natural Environment Research Council. We thank Sven Rasmussen for field assistance, and Terry Callaghan for the support and facilities of the Abisko Research Station, and Paul Stoy for his comments on the manuscript.

3.9 References

Alter-Gartenberg, R., Nolf, S.R., & Davis, R.E. (2002) A sensitivity assessment of terrestrial identification in remote sensing International journal of remote sensing, 23, 825-849.

Anderson, N.Å., Callaghan, T.V., & Karlsson, P.S. (1996) The Abisko Scientific Research Station in Plant Ecology in the Subarctic Swedish Lappland (eds. P.S. Karlsson and T.V.Callaghan). Ecological Bulletins, 45, 11-14.

Boelman, N.T., Stieglitz, M., Griffin, K.L., & Shaver, G.R. (2005) Inter-annual variability of NDVI in response to long-term warming and fertilization in wet sedge and tussock tundra. Oecologia, DOI 10.1007/s00442-005-0012-9.

Boelman, N.T., Stieglitz, M., Rueth, H.M., Sommerkorn, M., Griffin, K.L., Shaver, G.R., & Gamon, J.A. (2003) Response of NDVI, biomass, and ecosystem gas exchange to long-term warming and fertilization in wet sedge tundra. Oecologia, 135, 414-421.

Callaghan, T.V. & Karlsson, P.S. (1996) Plant ecology in the Swedish Lapland: summary and conclusions. Ecological Bulletins, 45, 220-227.

Chapin, F.S., III, Sturm, M., Serreze, M.C., McFadden, J.P., Key, J.R., Lloyd, A.H., McGuire, A.D., Rupp, T.S., Lynch, A.H., Schimel, J.P., Beringer, J., Chapman, W.L., Epstein, H.E., Euskirchen, E.S., Hinzman, L.D., Jia, G., Ping, C.-L., Tape, K.D., Thompson, C.D.C., Walker, D.A., & Welker, J.M. (2005) Role of land-surface changes in Arctic summer warming. Science, 657-660.

Cressie, N.A.C. (1993) Statistics for Spatial Data, Revised edn. Wiley, New York.

Deutsch, C.V. & Journel, A.G. (1998) GSLIB: Geostatistical Software Library and Users Guide (2nd Edition) Oxford University Press,, New York.

Essery, R., Best, M., & Cox, P. (2001). MOSES 2.2 Technical Documentation, Rep. No. HCTN 30. UK Met Office, Bracknell, UK.

Goovaerts, P. (1999) Geostatistics in soil science: State-of-the-art and perspectives. Geoderma 89, 1-45.

Harvey, L.D.D. (2000) Upscaling in global change research. Climatic change, 44, 225-263.

Isaaks, E.H. & Srivastava, R.M. (1990) Applied Geostatistics Oxford University Press.

Jia, G.S., Epstein, H.E., & Walker, D.A. (2006) Spatial heterogeneity of tundra vegetation response to recent temperature changes. Global Change Biology, 12, 42-55.

Lee, K.S., Cohen, W.B., Kennedy, R.E., & Maiersperger, T.K. (2004) Hyperspectral versus multispectral data for estimating leaf area index in four different biomes. Remote Sensing of Environment, 91, 508-520.

Lillesand, T.M., Kiefer, R.W., & Chipman, J.W. (2003) Remote Sensing and Image Interpretation, 5th edn. John Wiley and Sons.

Myneni, R.B., Keeling, C.D., Tucker, C.J., Asrar, G., & Nemani, R.R. (1997) Increased plant growth in the northern high latitudes from 1981-1991. Nature, 386, 698-702.

Owen, K.E., Tenhunen, J., Reichstein, M., Wang, Q., Falge, E., Geyer, R., Xiao, X.M., Stoy, P., Ammann, C., Arain, A., Aubinet, M., Aurela, M., Bernhofer, C., Chojnicki, B.H., Granier, A., Gruenwald, T., Hadley, J., Heinesch, B., Hollinger, D., Knohl, A., Kutsch, W., Lohila, A., Meyers, T., Moors, E., Moureaux, C., Pilegaard, K., Saigusa, N., Verma, S., Vesala, T., & Vogel, C. (2007) Linking flux network measurements to continental scale simulations: ecosystem carbon dioxide exchange capacity under non-water-stressed conditions. Global Change Biology, 13, 734-760.

Quaife, T., Lewis, P., De Kauwe, M., Williams, M., Law, B.E., M., D., & Bowyer, P. (in press) Assimilating Canopy Reflectance data into an Ecosystem Model with an Ensemble Kalman Filter. Remote Sensing of the Environment.

Raupach, M.R., Rayner, P.J., Barrett, D.J., DeFries, R.S., Heimann, M., Ojima, D.S., Quegan, S., & Schmullius, C.C. (2005) Model-data synthesis in terrestrial carbon observation: methods, data requirements and data uncertainty specifications. Global Change Biology, 11, 378-397.

Sitch, S., Smith, B., Prentice, I.C., Arneth, A., Bondeau, A., Cramer, W., Kaplan, J.O., Levis, S., Lucht, W., Sykes, M.T., Thonicke, K., & Venevsky, S. (2003) Evaluation of ecosystem dynamics, plant geography and terrestrial carbon cycling in the LPJ dynamic global vegetation model. Global Change Biology, 9, 161-185.

Street, L.E., Shaver, G.R., Williams, M., & Van Wijk, M.T. (2007) What is the relationship between changes in canopy leaf area and changes in photosynthetic CO2 flux in arctic ecosystems. Journal of Ecology, 95, 139-150.

Tian, Y.H., Woodcock, C.E., Wang, Y.J., Privette, J.L., Shabanov, N.V., Zhou, L.M., Zhang, Y., Buermann, W., Dong, J.R., Veikkanen, B., Hame, T., Andersson, K., Ozdogan, M., Knyazikhin, Y., & Myneni, R.B. (2002) Multiscale analysis and validation of the MODIS LAI product - I. Uncertainty assessment. Remote Sensing of Environment, 83, 414-430.

Tucker, C.J., Grant, D.M., & Dykstra, J.D. (2004) NASA's global orthorectified Landsat data set. Photogrammetric engineering and remote sensing, 70, 313-322.

Turner, D.P., Cohen, W.B., Kennedy, R.E., & Fassnacht, K.S. (1999) Relationships between leaf area index and Landsat TM spectral vegetation indices across three temperate zone sites. Remote Sensing of Environment,, 70, 52-68.

Van Wijk, M.T. & Williams, M. (2005) Optical instruments for measuring leaf area index in low vegetation: application in arctic ecosystems. Ecological Applications, 15, 1462-1470.

Williams, M. & Rastetter, E.B. (1999) Vegetation characteristics and primary productivity along an arctic transect: implications for scaling-up. Journal of Ecology, 87, 885-898.

Williams, M., Rastetter, E.B., Shaver, G.R., Hobbie, J.E., Carpino, E., & Kwiatkowski, B.L. (2001) Primary production in an arctic watershed: an uncertainty analysis. Ecological Applications, 11, 1800-1816.

Williams, M., Schwarz, P., Law, B.E., Irvine, J., & Kurpius, M.R. (2005) An improved analysis of forest carbon dynamics using data assimilation. Global Change Biology, 11, 89-105.

Woodcock, C.E. & Strahler, A.H. (1987) The factor of scale in remote sensing. Remote Sensing of Environment, 21, 311-322.

4. Topographic Controls on the Leaf Area Index of a Fennoscandian Tundra Ecosystem

Running title: Topographic controls on LAI in Arctic tundra

Luke Spadavecchia[1], Mathew Williams[1*], Robert Bell[1], Paul Stoy[1], Brian Huntley[2], Mark T. van Wijk[3]

[1] School of GeoSciences, Department of Atmospheric and Environmental Science, University of Edinburgh, Edinburgh

[2] Institute of Ecosystem Science, School of Biological and Biomedical Sciences, Durham University, Durham DH1 3LE, UK

[3] Plant Production Systems, Wageningen University, P.O. Box 430, 6700 AK Wageningen, the Netherlands

* Correspondence to Mathew Williams, mat.williams@ed.ac.uk.

KEY WORDS: Geostatistics, spatial autoregression, LAI, Arctic vegetation, multi-scale analysis, topography, terrain indices

* Corresponding author

4.1 Declaration

The following chapter was submitted to the *Journal of Ecology*. The data was collected by R. Bell, L. Street and Mark Van Wijk. M. Williams organised the field study and devised the experiments, whilst B. Huntley organised the aircraft flight which carried the LIDAR instrument used to produce the macroscale DEM: Ana Prieto-Blanco and Mathias Disney processed the raw LIDAR data, although subsequent analysis to produce the macroscale DEM was undertaken by me. P. Stoy provided the calculations for Compound Topographic Index (CTI), and conducted much of the georeferencing of the various data sets, although I took an active role in both of these tasks. I wrote the body text of the chapter, although M. Williams and P. Stoy provided comments and editorial changes. Otherwise, I undertook all of the reported analyses.

The discussion of this chapter interprets the macro-scale elevation gradient in LAI is likely being related to temperature: This is unlikely given the small range in sampled elevation; in the published version of this paper (Spadavecchia et al. 2008. 'Topographic controls on the leaf area index and plant functional type of a tundra ecosystem'. Journal of Ecology **96**(6): 1238-1251) we correct this statement, attributing the LAI elevation gradient to interactions with snow accumulation and freeze/thaw timing.

4.2 Abstract

Leaf area index (LAI) is an emergent property of vascular plants closely linked to primary production and surface energy balance, which can vary by an order of magnitude among Arctic tundra communities. We examined topographic controls on LAI distribution on the scales of tenths of metres ('microscale') and tens of metres ('macroscale') in an Arctic ecosystem in northern Sweden. Exposure was the most significant topographic control on LAI at the microscale, while on the macroscale the dominant explanatory variable was elevation, which explained ~12% of the total LAI variation. Across all scale lengths compound topographic index (related to surface drainage) failed to account for the observed spatial relationships in LAI. Similarly, potential insolation (determined from slope and aspect) failed to account for the observed patterns of LAI at the microscale, although a small spatial interaction effect was observed on the macroscale. The distribution of plant communities was strongly associated with topography, imposing a clear structure on LAI. Shrub communities, dominated by *Betula nana*, were associated with low elevation sites, while more exposed high elevation sites were dominated by cryptogam communities. Topographic parameters accounted for 32% of the variation in LAI at the macroscale, and 16% at the microscale. The large degree of autocorrelated latency in the data suggests that residual variation in LAI may be accounted for by edaphic constraints and/or facilitation amongst plant species. Our results suggest that topographic data can be combined with co-registered remotely sensed reflectance data to generate improved maps of spatial LAI.

4.3 Introduction

The recent rate of warming in the Arctic has been two to three times the global average rate (Kattsov et al. 2005, 2007), enhanced by the snow-albedo feedback (Camp and Tung 2007), and is likely to be exacerbated in the future by a vegetation-albedo feedback (Chapin et al. 2005). Warming is likely to result in significant changes in the distribution and structure of Arctic vegetation, with implications for the global carbon cycle and climate (ACIA 2005). Quantifying the present distribution of vegetation and its physical and biological determinants is thus a critical step towards improving understanding the controls on Arctic vegetation distribution in the present and for a more robust understanding of how it may change in the future.

Leaf area index (LAI) is an emergent property of vascular plants, strongly linked to primary production, evapotranspiration, surface energy balance and biogeochemical cycling (Williams et al. 2001, Shaver et al. 2007, Street et al. 2007). However, uncertainty in the temporal and spatial distribution of LAI (Williams and Rastetter 1999, van Wijk et al. 2005) limits efforts to predict Arctic photosynthesis and C cycling at multiple spatial scales (Williams et al. 2001). Asner et al (2003) found that spatial LAI variability in the Arctic was higher than in any of the other 15 biomes investigated. It is therefore necessary to improve understanding of the spatial distribution of Arctic LAI to estimate reliably the effects of climate change on tundra ecosystem processes.

Some aspects of the relationship between topography and vegetation distribution in Arctic ecosystems have been well established. Walker and Walker (1996) noted a consistent shift in vegetation community composition from riparian shrub to cryptogam with increasing distance to streams. Darmody et al. (2004) described variability in vegetation community type with respect to topographic position,

highlighting the role of elevation, exposure and hydrology in controlling plant community distribution in Arctic montane regions. Despite this research on the community level, fewer studies have considered Arctic LAI distribution and its controls on different spatial scales, for studies of ecosystem physiology and functioning (Williams & Rastetter 1999).

From these studies and others we can identify six broad controls on plant distribution and development that determine spatial patterns of LAI in Arctic ecosystems that can lead to testable hypotheses: (1) snow cover, through its impacts upon effective growing season length and winter soil temperature, as well as by redistributing energy and nutrients during snow melt; (2) climate, through the effects of temperature, insolation and exposure on plant development; (3) hydrology, through the effects of soil moisture; (4) biodiversity, determining the species pool; (5) soil/substrate variability, determining nutrient status and drainage characteristics; and (6) disturbance and site history, including the effects of ecosystem management.

The first three controls are broadly related to topography and form the focus of this study. Here we examine four related hypotheses to test the relative importance of topographical controls on LAI distribution in a tundra ecosystem; that the primary constraint on LAI distribution is through estimated landscape soil moisture (H1), topographic exposure (H2), potential insolation, (H3) or topographic parameters like elevation, slope and aspect (H4).

The relationships between topographic variables and LAI may vary with scale. For instance, insolation and exposure are likely to vary strongly with micro-topography (vertical scale on the order of tenths of metres), whereas air temperature is most likely to vary with macro-topographical changes in altitude on the order of tens to hundreds of metres. Hydrological variability may be important across a range of scales, from

hummocks to hill slopes. There are close links among the controls, which complicates attribution. For instance, soil conditions affect hydrology (Darmody et al 2004). Plants can also act to modify snow-cover, soils and micro-climate, and the role of facilitation, competition and adjacency may be another important spatial control (Callaway et al. 2002).

Spatial arrangement at any scale length is likely determined by a different set of controls. Thus, we tested the hypotheses at two different scales, defined by the horizontal resolution or "grain" of the LAI data. The first scale test was with 0.2 m horizontal resolution LAI data within a 40 x 40 m "microscale" area, and the second was with ~10 m resolution LAI data within a 500 x 500 m "macroscale" area. Detailed digital elevation maps were available at both scales with appropriate resolutions. Vegetation community information was collected at the macroscale allowing us to investigate the role of species assemblages on LAI distribution (Williams and Rastetter 1999).

This study is novel in that it uses a uniquely detailed dataset, on plant community distribution, vegetation structure (i.e. LAI) and topography, to investigate vegetation-environment interactions. The data were collected at two resolutions, allowing the influence of scale to be properly determined for the first time in Arctic tundra. We use contemporary statistical techniques that quantify spatial autocorrelation for appropriate fitting of geostatistical models, and demonstrate improvements in model selection by employing maximum likelihood (ML) techniques after first demonstrating the predictions from ordinary least squares (OLS). An additional goal of the paper is to demonstrate how topographic data can be used to improve landscape mapping of LAI, that is currently undertaken using remote sensing of land surface reflectance (Raynolds et al. 2006).

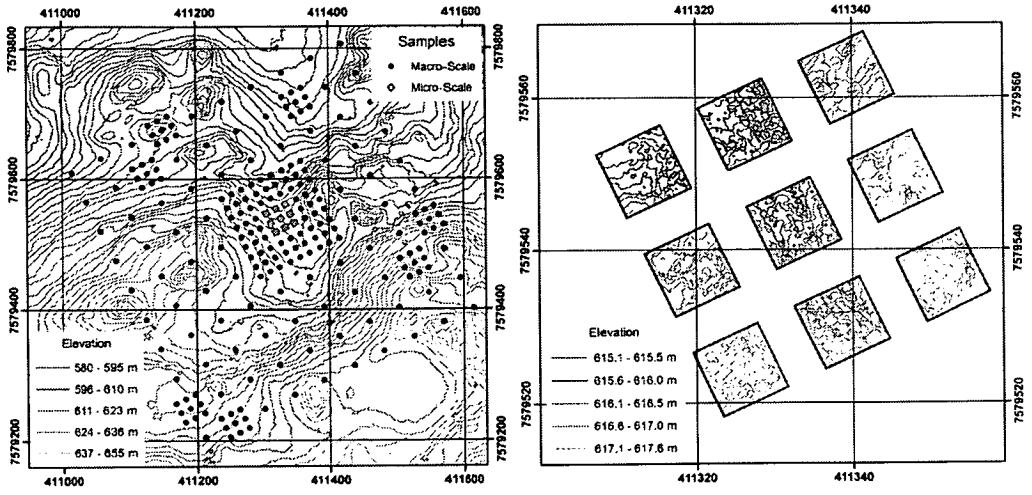

Figure 4.1 Digital elevation model of study site near Abisko, Sweden. The area in the left pane is the extent of the 'macroscale' data set The sample locations of the 'microscale' data set (van Wijk and Williams 2005) displayed in the right pane, are not shown, as their density (40 cm grid) would obscure the contours. The coordinates are in meters (UTM projection).

4.4 Methods

4.4.1 Study Site

The study site was located in the sub-Arctic zone of Fennoscandia, in Swedish Lapland, centred on 68°18'54" N, 18°50'58" E, a few kilometres south of the Abisko Research Station. The site, hereafter referred to as the Abisko 'intensive valley' site (IV, see Williams et al. in review), lies within a small (~1 ha) catchment in a transition zone that intersects the local tree line. The IV has a gentle (~5%) slope from south to north with an average elevation of 580m. A stream runs through the centre of the area. The Abisko weather station records an average rainfall of 300-400 mm per annum and an average temperature of –1°C (ASRS 2007). The hill slope surrounding the IV was characterised by mesoscale topographic features reflecting an extensive cover of glacial and fluvioglacial deposits, with hummocks and depressions at higher spatial frequencies on the order of several metres (Sonesson et al. 1975). The vegetation of the IV was

characterized by shrub tundra at lower elevations, above which Empetrum heath communities predominate (Karlsson and Callaghan 1996).

4.4.2 Vegetation Description

A number of distinct vegetation types were observed in the IV, referred to throughout the paper as willow, dwarf birch, heath, moss, graminoid and fell field communities. The willow assemblage was a shrubby riparian community dominated by grey-leaved *Salix* spp. with a *Betula nana* understorey. Dwarf birch was a community dominated by *Betula nana*, with *E. nigrum* and to a lesser extent *Vaccinium vitis-idea*. The heath community comprised the same species as observed in the dwarf birch community, but was lower-growing and dominated by *E. nigrum*. Moss refers to a community typified by *Sphagnum* spp. and characterised by the presence of *Rubus chamaemorus*, among other herb and graminoid species. The graminoid communities were assemblages of *Carex* or *Eriophorum* spp., and were associated with moist sites. The fell field community was associated with ridges and hummock tops, comprising of a patchy (typically < 25% ground cover) cryptogam community predominantly of lichens, and a few mosses, interspersed with *B. nana*, *E. nigrum*, stones and gravel.

4.4.3 LAI Measurements

Measurements of LAI were conducted on a nested sampling grid at two spatial scales in the IV (Figure 4.1) during the Arctic growing season. All location measurements were made in the Universal Transverse Mercator (UTM) projection; zone 34 North, WGS 1984 datum.

Microscale measurements were collected from 10th-31st July 2002 within a 40 m by 40 m area centred on the stream in the foot slopes of the IV. The microscale measurements were made in nine 10 m x 10 m plots laid out on a 3 x 3 grid, with 5 m

spacing between each plot (Figure 4.1). Within each of the nine microscale plots, indirect LAI measurements at a nominal resolution of 0.2 m were obtained using: (1) NDVI obtained with a Skye Instruments 2 Channel Sensor SKR1800 (Skye Instruments, Powys, UK, channel 1 = 0.56-0.68 μm, channel 2 = 0.725-1.1 μm) with the diffuser off, held 0.9 m above the ground (referred to hereafter as 'Skye NDVI'); and (2) a LI-COR LAI-2000 Canopy Analyzer (LI-COR, Lincoln, NE, USA), collecting one above- and one below-canopy measurement (referred to as 'LAI-2000 LAI'). The paired LAI-2000 and NDVI measurements were conducted on a regular grid at 0.4 m intervals for each plot, giving a total of 5625 measurements. Subsequently, nine destructive harvest measurements of vascular plant LAI were taken for each microscale plot, and were used to calibrate the indirect sensors (n = 81), see van Wijk and Williams (2005) for full details.

Macroscale measurements were collected on 14th-25th August 2004, in a 500 m x 500 m area encompassing the microscale area. The macroscale area was subdivided into one hundred 50 m x 50 m plots. Sixteen of these plots were further subdivided into nine intensive 10 m x 10 m plots, giving 228 measurement locations (Figure 4.1). The central intensive plot corresponded with and re-sampled the microscale area. At the centre of each of the macroscale sampling points, an NDVI measurement was made using the Skye sensor with its diffuser on, suspended at 3 m above ground level, resulting in a nominal resolution of ~9 m in diameter. Macroscale measurements of LAI were obtained using the calibration developed from the microscale data (van Wijk and Williams 2005), with a detailed recalibration to account for change of sensor resolution using multi-scale nested NDVI measurements (Williams et al. in review). The location of each plot was determined to an accuracy of ±6 m using a handheld GPS (Garmin e-trex). Some plots (n = 31) had a covering of birch trees over 2 m tall. It was not possible

to sample NDVI effectively with the suspended Skye sensor for these plots, so they were excluded from all subsequent analysis. We consider only the remaining 197 tundra vegetation plots in this study.

4.4.4 Digital Elevation Model

A digital elevation model was produced for the microscale site by manually surveying each of the 5625 sample locations with a level and a survey pole to record the level of the soil surface, as referenced to the lowest point in the plot, which was set to zero. These points were interpolated using inverse distance weighting (IDW) in ArcInfo (ESRI, Redlands, California) to produce a continuous surface.

The macroscale DEM was produced from airborne LIDAR data collected by a NERC aircraft flight in July 2005 using an Optech Airborne Laser Terrain Mapper 3033 (Optech Inc., Vaughan, Ontario, Canada). The generated point cloud was gridded at 4 m resolution, using minimum values of the last return pulse. Missing data values were interpolated using IDW, and standard pit removal procedures were undertaken in ArcInfo.

For both microscale and macroscale data, a series of topographic indices were generated related to slope, aspect, and surface curvature from the DEMs, by taking quadratic approximations to the first and second differentials of the surface (Evans 1980). The slope was simply the first differential of the elevation surface, whilst curvature was given by the Laplacian of the DEM. Aspect was derived from directional estimates of surface gradient (Zevenbergen and Thorne 1987).

4.4.5 Terrain Indices

The compound topographic index (CTI) was developed to summarize landscape level soil moisture (Beven 1977). CTI was calculated from surface drainage characteristics of the DEM, namely the upslope area (A_s) and local slope (β) (equation 4.1). A_s was estimated in ArcInfo by using slope and aspect to estimate how many upstream pixels drained into a candidate pixel (Burrough et al. 1998). Higher scores are associated with moist sites.

$$CTI = \ln(A_s / \tan(\beta)) \quad \textbf{(4.1)}$$

For exposure, Toposcale 1.2 AML (Zimmerman 1999) for ArcInfo was used to estimate the TOPEX (Pyatt 1969, Wilson 1987) index. TOPEX scores are developed from the difference between average elevation of a search window and the elevation at the central pixel of the window. The process was repeated at a number of increasing search radii, and the final TOPEX estimate is achieved by hierarchical integration over all scales (Zimmerman 1999). A high score indicates exposed positions, whilst negative scores indicate shelter. Although the scores are based on surface elevation, and therefore ignore the impact of vegetation, vegetation height in the region was typically only ~180 mm: Whilst trees may act as shelter belts, large specimens infrequent in the IV.

Potential incoming shortwave radiation was calculated over the growing season (mid-May to mid-September), using the Shortwave AML (Kumar et al. 1997) for ArcInfo. The model calculates the solar geometry for each time step (30 minutes), taking into account the instantaneous terrain effects (slope and aspect). Shadows are projected on the surface at each time step, so terrain adjacency issues are also accounted

for (Kumar et al. 1997). Edge effects were avoided by extending the DEM beyond the LAI data extent.

4.4.6 Data transformation and model testing

Prior to analysis we ensured that the pooled LAI data approximated a normal distribution using a Box-Cox transform (Box and Cox 1964). The Box-Cox transform (Y_t) of a variable Y is given by equation 4.2. The power parameter λ was estimated by maximum likelihood methods.

$$Y_t = (Y^{\lambda} - 1)/\lambda \qquad (4.2)$$

For much of the analysis ordinary least squares (OLS) regressions were fitted to the transformed data (LAI_t) to assess the significance of the derived terrain indices and models.

4.4.7 Ordination Methods

Due to the large data set used for the microscale analysis, some degree of data thinning was required for practical hypothesis testing. Topographic variables were selected on the basis of ordination, initially partitioning the parameter space using a regression tree (Breiman 1984). The regression tree method selects variables that are best able to classify the response (LAI) into distinct clusters in parameter space. The process proceeds by forward selection (binary recursive partitioning), splitting the data set using the predictor variable that explains the maximum amount of the remaining deviance in the response variable. The process results in a series of splitting rules, by which parameter space can be partitioned into ordered categories of LAI.

Trends in the parameter space were examined by principal components analysis (PCA) (Pearson 1901, Hotelling 1933). PCA re-projects the original parameter space onto an orthogonal coordinate system of principle axes, maximising the proportion of the variation in the parameter space represented by the first few dimensions. The new variables created by the rotation are referred to as principal components (PCs). By examining the first three PCs on Gabriel bi-plots (Gabriel 1971), we searched for clusters of parameters that were well associated with LAI_t.

4.4.8 Statistics to Measure Spatial Dependency

In order to assess the validity of OLS, we tested for autocorrelation in LAI_t using Moran's *I* statistic (Moran 1950). Moran's *I* tests for significant correlation in neighbouring points, controlled for the overall variance in the data set. Anselin (1995) extended the concept of Moran's *I* to a local indicator of spatial autocorrelation (LISA). We utilized LISA analysis to find clusters of high and low LAI_t values in the microscale data.

Semivariograms (Cressie 1991) were used to quantify the spatial autocorrelation structure of the data. We expressed the semivariogram in terms of a spatially continuous model to conveniently quantify spatial dependence in the data. A set of basic models which are known to be permissible were used (Christakos 1984, Mcbratney and Webster 1986), being the spherical and exponential functions. Spatial variation was characterised by the range (ϕ) over which autocorrelation was observed, and a 'nugget' (τ) noise parameter at zero separation.

4.4.9 Spatial Regression Models

In the presence of significant spatial autocorrelation, OLS regression was deemed unsuitable. We implemented spatial lattice models using maximum likelihood (ML) methods. Spatial lattice models are designed for data sampled on a grid, and include the effects of spatial autocorrelation by incorporating information on sample adjacency when fitting regressions. Adjacency was quantified using the sphere of influence (SOI) method (Jaromczyk and Toussaint 1992).

Three lattice-type models were applied to the macroscale data: lagged-response, lagged-error, and spatial Durbin models (Haining 2003). The lagged-response model was identical to a regular linear regression, except that the neighbouring values of LAI_t were also used in the prediction. Lagged-error models differ from OLS models by altering the error term to reflect the spatial dependence, by incorporating information about the magnitude of residuals in neighbouring points. The spatial Durbin model was the most complex model fitted, and incorporates a spatially lagged response, along with spatially lagged predictors, i.e. neighbourhood effects for all topographic variables tested, and an LAI_t autocorrelation term ρ. Details of these models can be found in the Appendix.

Lattice models were not feasible for the microscale data, due to computational restrictions on the 5625 data points. Instead we fitted spatial analysis of covariance (ANCOVA) models on a continuous spatial metric. A mixed effects type model was developed to test differences in selected topographic covariates between high and low LAI_t clusters, as identified from a LISA cluster analysis. The ANCOVA was fitted by ML methods, with two additional parameters (τ, ϕ) to describe the spatial error

structure, as defined by the semivariogram. All statistical analyses were carried out in R version 2.4.1 (R Foundation for Statistical Computing, Vienna, Austria).

4.5 Results

The microscale LAI data were heavily skewed, with most values between 0-1, but some values up to ~3 (Williams et al, in review). The macroscale data were more normally distributed, because of averaging occurring at a resolution of 9 m (Williams et al, in review). A Box-Cox transformation resulted in a normal distribution for all data, and a constant was added to the transformed LAI data to make them strictly positive. The maximum likelihood estimate of transformation parameter λ was 0.4. Unless otherwise stated, all analyses were undertaken using the transformed variable, LAI_t.

4.5.1 Microscale analysis

The median untransformed LAI of the microscale data was 0.9, ranging from 0.1 to 3.6. Elevation ranged from 615 – 618 m, with a mean of 616.6 m. Slopes were generally moderate, with 74% of all observations < 10°, although steep inclines were observed, with a maximum of 39°. Slopes were generally on a north-westerly aspect, with 31% of all slopes facing north, 23% facing east, 14% facing south, and 32% facing west. Surface curvature was generally convex, with a mean curvature of 6 and a mean TOPEX of 3. TOPEX was approximately normally distributed, with a standard deviation of 68, and a range of -297 – 274. CTI was generally above zero, with a mean of 2 and a maximum of 15. PI ranged from 10 – 25 MJ m^2 day^{-1}, with a median of 20 MJ m^2 day^{-1}. Histograms of the derived terrain indices are provided in Figure 4.2.

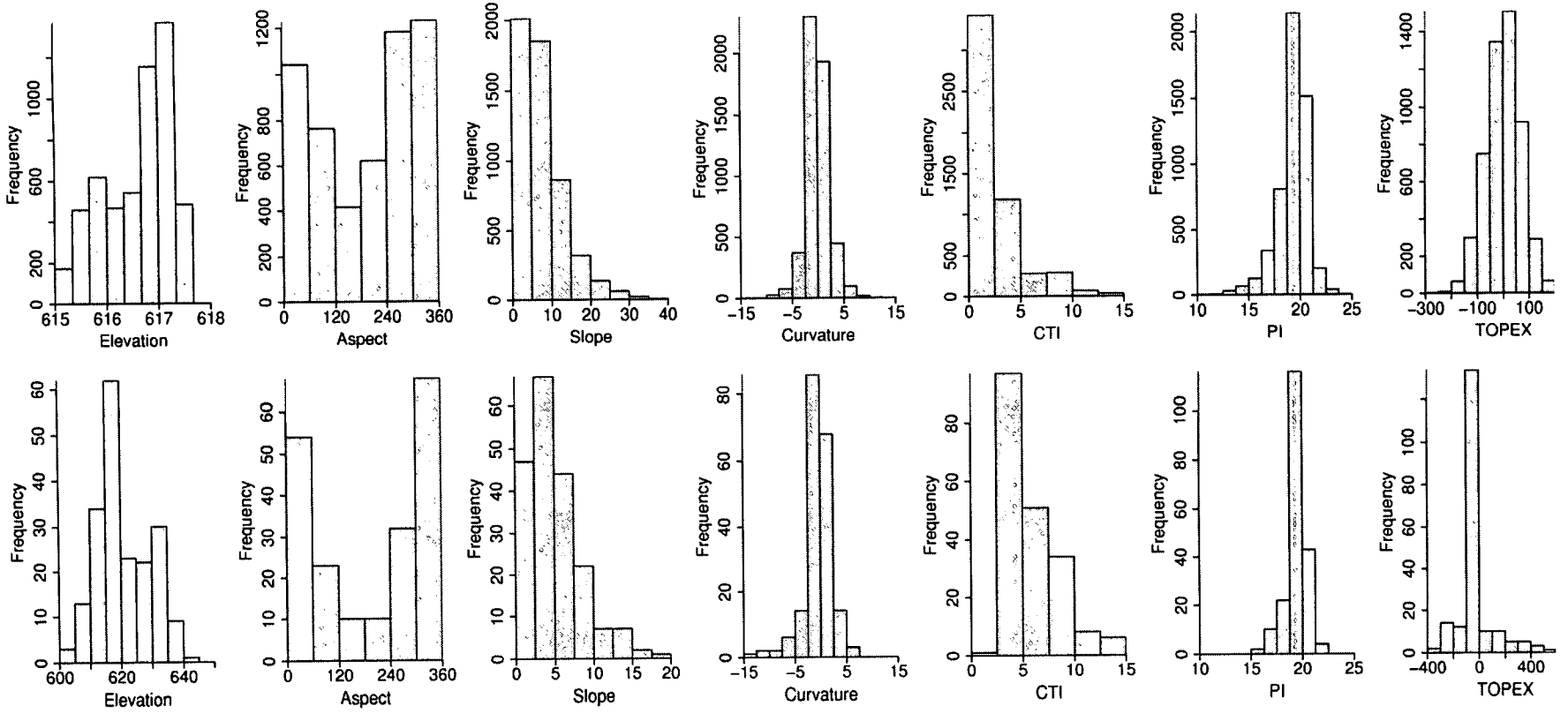

Figure 4.2 Histograms of DEM derived terrain indices. The top row summarizes the microscale data, whilst the bottom row contains microscale data. Elevations are in metres, slope and aspect are in degrees, Potential Insolation (PI) is measured in MJ/m2/day for the growing season, whilst Curvature, Compound Topographic Index (CTI) and Topographic Exposure (TOPEX) are unitless.

Table 4.1 Linear associations between transformed microscale (20 cm) LAI and terrain properties derived from a digital elevation model, at a study site near Abisko, Sweden..

	Microscale Data					
Parameter	Estimate	Std. Error	t Value	Pr (>|t|)	r^2	Kendall's □
Elevation (m)	-2.06×10^{-01}	1.29×10^{-02}	-16.00	<0.001	0.05	-0.15
*Aspect**	-2.89×10^{-02}	2.94×10^{-02}	-0.98	0.33	0.00	-0.01
Slope (°)	2.17×10^{-02}	1.48×10^{-03}	14.67	<0.001	0.04	0.13
Curvature	-3.02×10^{-04}	3.84×10^{-05}	-7.86	<0.001	0.01	-0.08
CTI§	1.61×10^{-02}	3.14×10^{-03}	5.12	<0.001	0.00	0.01
PI†	-4.30×10^{-02}	5.61×10^{-03}	-7.69	<0.001	0.01	-0.06
TOPEX‡	-1.63×10^{-03}	1.24×10^{-04}	-13.26	<0.001	0.03	-0.13

* Aspect converted to circular score ranging from 0:1 via sin(Aspect*π/360)
§ Compound topographic index
† Potential Insolation over the growing season (May-September) in Mj/m2/day
‡ Topographic exposure index

Exploratory analysis of the microscale data by univariate linear regression indicated that all topographic factors and physical models for LAI_t were highly significant ($P < 0.001$), with the exception of aspect ($P = 0.33$) (Table 4.1). Despite statistical significance, all factors had low r^2 values, with a maximum of 0.05 for elevation (Table 4.1).

Partitioning the parameter space via regression-tree analysis on the raw LAI values revealed that exposure, slope and elevation could best separate high and low LAI values (Figure 4.3). Higher LAI values (mean LAI = 0.82) were associated with sheltered sites with highly negative TOPEX (< -26). Lower LAI values (mean LAI = 0.48) were associated with exposed topographic positions on flat surfaces at higher elevations.

Re-projecting the parameter space via PCA similarly indicated that elevation, TOPEX and slope were strongly related to LAI_t. Principle component loadings positively associated with LAI had negative loadings of TOPEX and elevation, and

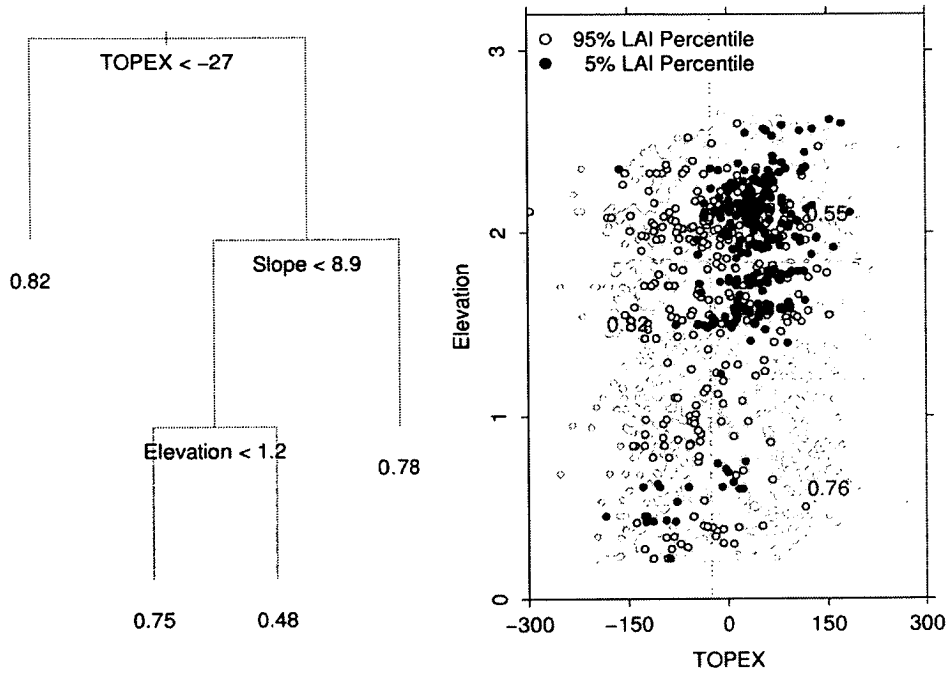

Figure 4.3 Regression tree for microscale LAI observations (left panel). Terminal points in the tree indicate clusters in parameter space associated with high or low LAI values (mean LAI of the cluster is displayed at the terminus). The right pane illustrates the ability of the regression tree to classify the 5% quantile LAI values, displayed as black circles. The broken grey lines indicate the breaks in the tree structure, with mean LAI values for each data subset indicated with dark grey labels.

positive loadings for slope (Table 4.2). In particular, principal component 3 (16% of variance) displayed a strong positive loading for LAI_b and strong negative loadings for elevation and TOPEX. Comparing the first 3 principal components on Gabriel bi-plots (Gabriel 1971), which were split into rotation and scores plots for clarity, the 0.05 and 0.95 percentiles were well separated by the coordinate rotation, particularly on the plane of PC1 and PC3, on which a clear manifold was visible in the parameter space linking LAI_t to elevation, TOPEX and slope (Figure 4.4).

Fitting a linear regression model to predict LAI_t from the parameters selected from ordination results indicated that all terms were highly significant ($P < 0.001$, $r^2 = 0.11$). However, significant autocorrelation in the data set (Moran's $I = 0.68$, $P < 0.0001$)

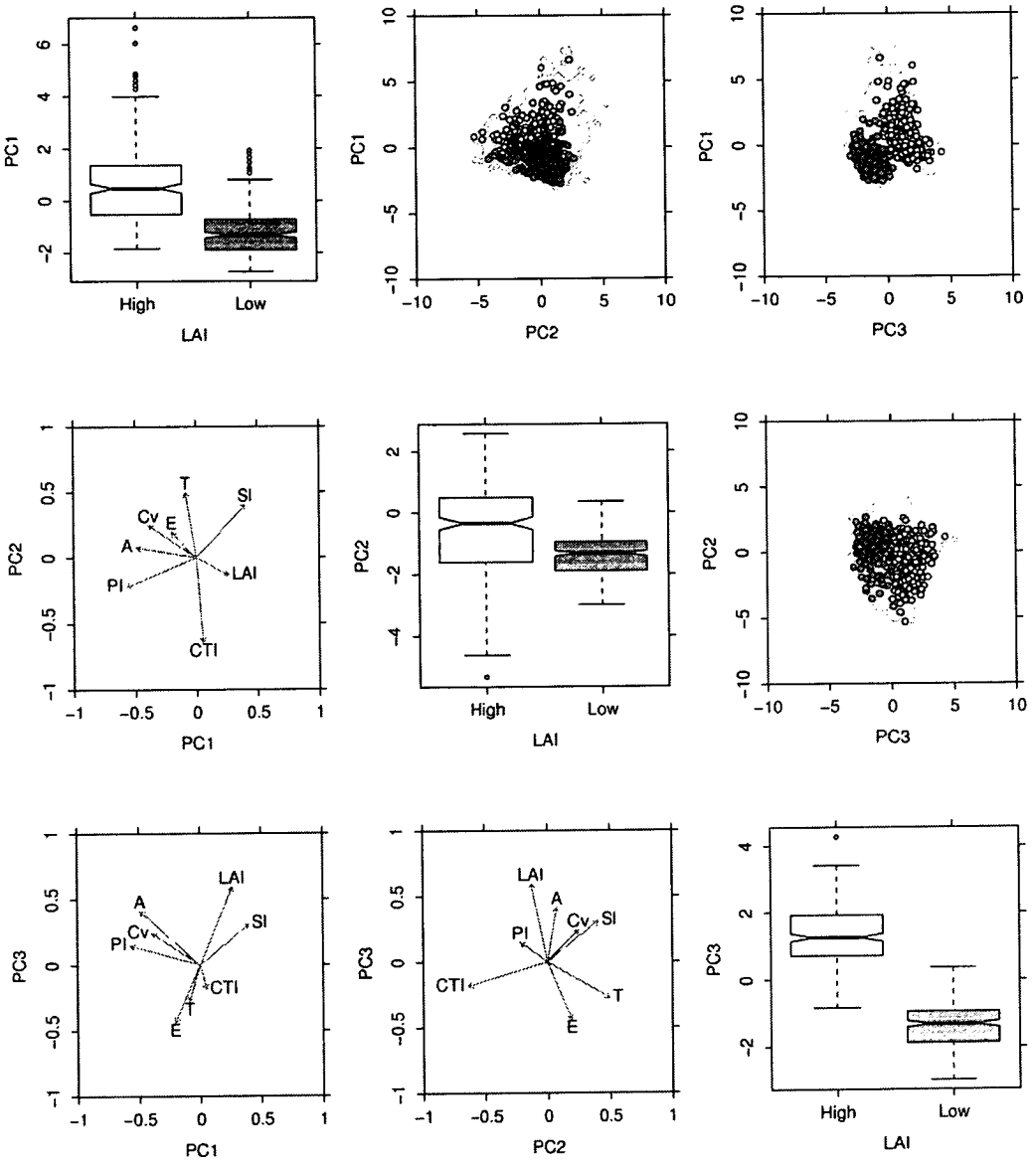

Figure 4.4 Ordination matrix from principal components (PC) analysis of the microscale data. The matrix illustrates the relationship between the first 3 principal components of the data set, which capture 62% of the total variation. For all plots, the 95% quantiles of LAI_t are indicated in white and the 5% quantiles in dark grey. The boxplots on the diagonal show the distribution of the PC scores for the 95% and 5% LAI_t quantiles, labelled High and Low respectively. Notches indicate the non-parameteric 95% confidence interval of the median. The scatter plots in the top right of the matrix show the pairwise relationship between components. The plots on the lower left of the matrix illustrate the rotation of the factors for each PC, and help to identify manifolds in parameter space. Abbreviated factor names are: LAI = transformed LAI, E = elevation, SI = slope, A = aspect, Cv = curvature, T = topographic exposure index, CTI = compound topographic index, PI = potential insolation over the growing season.

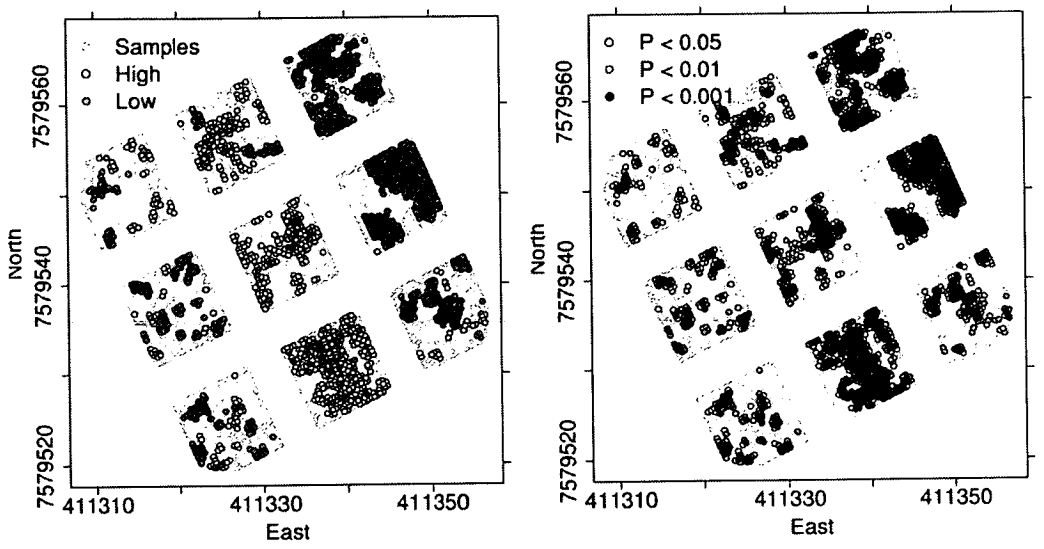

Figure 4.5 Moran's LISA cluster analysis for microscale data, indicating local anomalies (clusters) from the background LAI variation. In the left pane clusters of LAI values above the local mean are indicated as open circles, whilst clusters below the local mean are displayed as dark grey circles. The right pane indicates the significance of the spatial clusters. In both plots sample locations are indicated as open grey circles.

indicated that robust parameter inference was not possible by simple OLS methods. Examining the LAI_t data for spatial clustering via a LISA test indicated significant clusters ($P < 0.01$) of high LAI values around the stream, running centrally down the microscale site, while low LAI_t clusters ($P < 0.01$) are observed on the valley slopes (Figure 4.5).

The high and low clusters identified in the LISA analysis were examined for significant differences in relevant topographic indices, as identified above. A factorial ANCOVA for un-balanced sample sizes was fitted to the data (Table 4.3), and significant effects were identified for slope ($F = 33.4$, $P < 0.0001$) and TOPEX ($F = 37.8$, $P < 0.0001$). However, autocorrelation in the ANCOVA residuals was evident when semivariogram analysis was performed (Figure 4.6).

Table 4.2 PCA results for the microscale data set. Factor loadings for each component indicate the direction and magnitude of the rotation of each variable onto the component. Data capture is indicated by the cumulative variance.

	Loadings by Component							
Factor	PC1	PC2	PC3	PC4	PC5	PC6	PC7	PC8
LAI_t	0.26	-0.13	0.59	-0.21	0.42	-0.57	0.10	-0.04
Elevation (m)	-0.20	0.20	-0.44	-0.78	-0.05	-0.33	0.04	0.01
*Aspect**	-0.49	0.08	0.41	-0.27	0.16	0.33	-0.52	-0.33
Slope (°)	0.40	0.40	0.31	-0.29	-0.20	0.29	-0.17	0.59
Curvature	-0.39	0.25	0.24	0.29	-0.56	-0.54	-0.15	0.15
CTI§	0.05	-0.65	-0.19	-0.03	-0.01	-0.15	-0.61	0.39
PI†	-0.57	-0.22	0.15	-0.04	0.22	0.16	0.46	0.56
TOPEX‡	-0.09	0.50	-0.28	0.32	0.63	-0.16	-0.29	0.24
Standard Deviation	1.40	1.32	1.12	0.93	0.86	0.82	0.65	0.57
Variance	0.25	0.22	0.16	0.11	0.09	0.08	0.05	0.04
Cumulative Variance	0.25	0.47	0.62	0.73	0.82	0.91	0.96	1.00

* Aspect converted to circular score ranging from 0:1 via sin(Aspect*π/360)

§ Compound topographic index

† Potential Insolation over the growing season (May-September) in Mj/m2/day

‡ Topographic exposure index

In order explicitly to treat the autocorrelation present in the data, the ANCOVA, was repeated specifying exponentially structured spatial errors and spherically structured spatial errors (Figure 4.6). In both cases, the fitted semivariogram models indicated autocorrelation at separation distances below 2.5 m. The models with spatial error structures both outperformed the original model (Table 4.4), with the additional exponential spatial structure providing the best results (Likelihood ratio = 500.0, $P < 0.0001$). Inclusion of the exponential spatial error term altered the results significantly (Table 4.3); TOPEX remained highly significant ($F = 66.0$, $P < 0.0001$), but the slope effect became insignificant ($F = 2.2$, $P = 0.14$), and a significant effect of elevation was also revealed ($F = 8.1$, $P < 0.01$).

Table 4.3 Data summary of DEM derived topographic indices for the microscale spatial clusters LAI_t values from a tundra site near Abisko, Sweden. Significance is tested by analysis of covariance, using standard ANCOVA and an ANCOVA incorporating an exponential autocorrelation function for the errors.

	High Clusters		Low Clusters		ANCOVA		Spatial ANCOVA	
Parameter	Mean	SD	Mean	SD	F	Pr (>F)	F	Pr (>F)
*LAI**	1.51	0.42	0.20	0.22				
Elevation (m)	1.45	0.65	1.85	0.50	2.4	0.12	8.1	<0.01
Slope (%)	8.99	6.29	5.84	4.05	33.4	<0.0001	2.2	0.14
TOPEX‡	-7.21	76.82	22.65	54.66	37.8	<0.0001	66.0	<0.0001

* Back transformed LAI_t

‡ Topographic exposure index

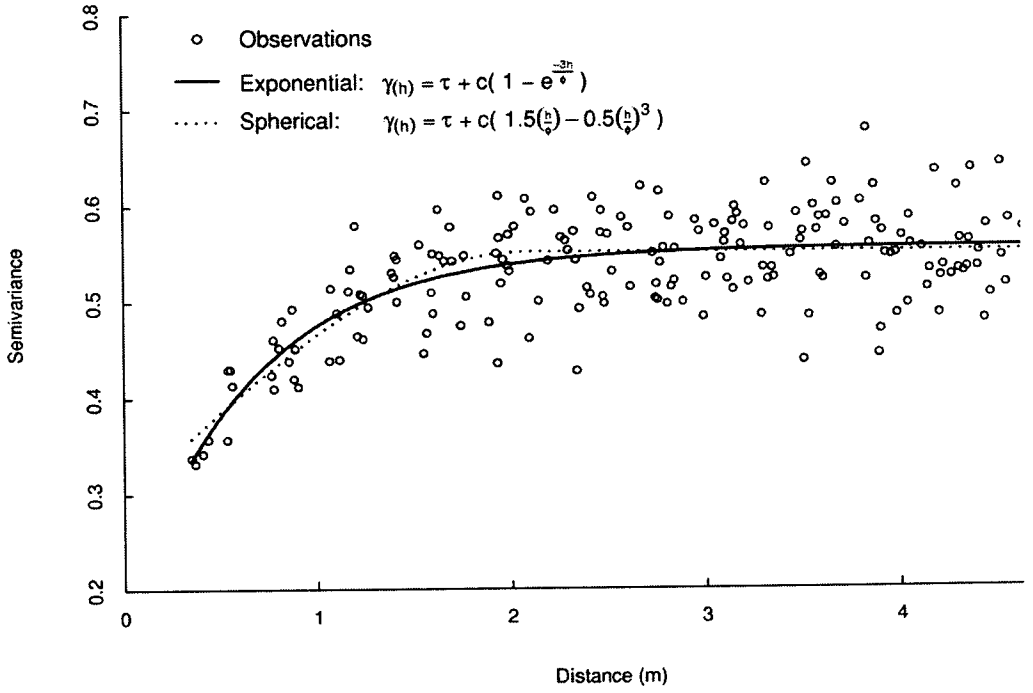

Figure 4.6 Semivariogram of the residuals of the microscale ANCOVA. Semivariance (γ) measures statistical difference between points separated by a distance vector (h). Two models were fitted to describe the spatial structure of the residuals. The solid line is an exponential model with intercept (τ) = 0.2, and range (φ) = 2.4 m. The broken line is a spherical model with τ = 0.3, φ = 2.3 m. In both cases, a contribution parameter (c) was used to scale the model. For separation distances greater than φ, the spherical model takes a value equal to the sill variance (τ+c).

Table 4.4 ANCOVA model selection criteria for microscale transformed leaf area index (LAI_t) data. The first model is a non-spatial analysis of covariance, fitted by maximum likelihood methods. The two spatial models add a spatially autocorrelated error function to the model, requiring an extra two degrees of freedom for the nugget (intercept τ) and (φ) range parameters.

Model	Log likelihood	AIC	BIC	Pseudo r^2	DF
ANCOVA	-776	1565	1597	18	6
Spatial ANCOVA 1[*]	-526	1069	1112	16	8
Spatial ANCOVA 2[§]	-528	1071	1115	16	8

* Autocorrelated errors with spherical functional form

§ Autocorrelated errors with exponential functional form

Table 4.5 Linear associations between transformed leaf area index (LAI_t) and individual macroscale terrain properties, derived from a digital elevation model, from a study site near Abisko, Sweden.

		Macroscale Data				
Parameter	Estimate	Std. Error	t Value	Pr (>|t|)	r^2	Kendall's τ
Elevation (m)	-1.71×10^{-02}	3.23×10^{-03}	-5.30	<0.001	0.12	-0.28
Aspect[*]	-3.70×10^{-01}	9.71×10^{-02}	-3.82	<0.001	0.06	-0.17
Slope (°)	8.20×10^{-03}	8.49×10^{-03}	0.97	0.35	0.00	0.07
Curvature	-1.30×10^{-02}	9.70×10^{-03}	-1.34	0.18	0.00	-0.05
CTI[§]	1.52×10^{-02}	1.18×10^{-02}	1.23	0.20	0.00	0.03
PI[†]	-8.32×10^{-02}	2.92×10^{-02}	-2.84	<0.01	0.03	-0.15
TOPEX[‡]	-8.00×10^{-04}	1.94×10^{-04}	-4.13	<0.001	0.08	-0.22

* Aspect converted to circular score ranging from 0:1 via sin(Aspect*π/360)

§ Compound topographic index

† Potential Insolation over the growing season (May-September) in Mj/m2/day

‡ Topographic exposure index

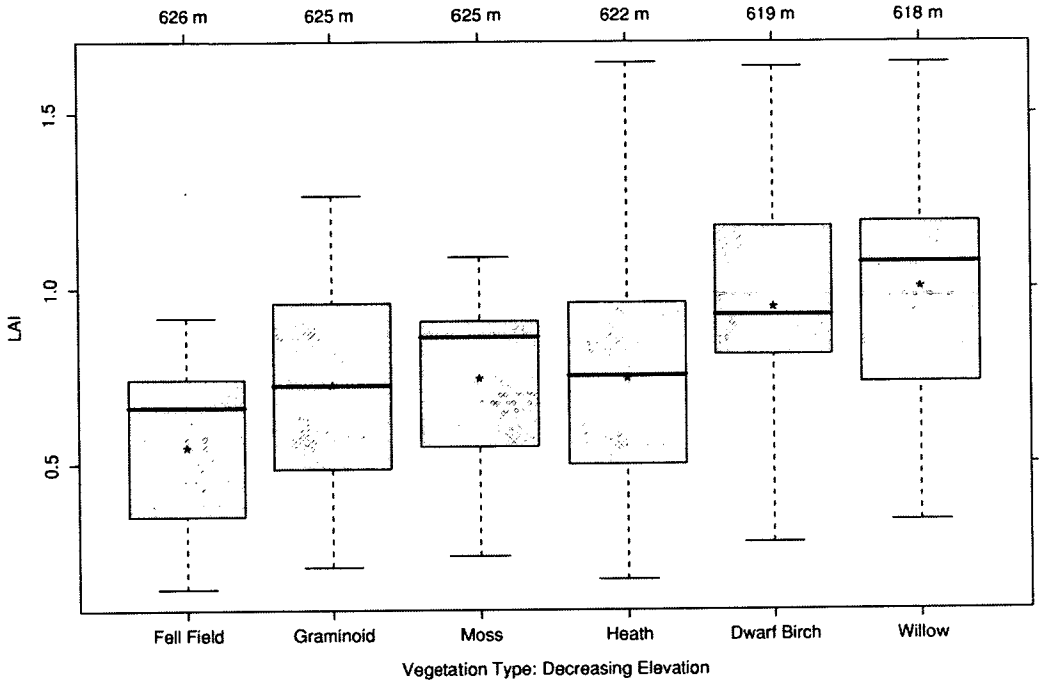

Figure 4.7 Box and whisker plots of macroscale LAI by plant community type, presented in decreasing order of mean elevation. The box extent indicates the interquartile range, whilst the bold central lines indicate the sample medians. The whiskers correspond to the sample maxima and minima. Mean LAI is indicated with an asterisk.

4.5.2 Macroscale analysis

The mean LAI at the macroscale was 0.8 with a standard deviation of 0.3 (Williams et al, in review). The elevation range sampled was 604 - 640 m, with a mean of 621. Slopes were moderate on the macroscale, with 91% of all observations < 10°, whilst the steepest slope recorded was 18°. The site was on a north-facing slope, with 51% of all observations on a northerly aspect. In general, the macroscale observations were collected on concave sites, with curvature and TOPEX scores below zero. The mean curvature was -0.3, whilst the mean TOPEX was -4. TOPEX scores were generally close to zero, indicating the macroscale DEM was significantly flatter then the microscale observations (Figure 4.2). CTI scores ranged from 2 to 14, with a median

Table 4.7 Summary of LAI and macroscale terrain properties by plant community type from a study site near Abisko, Sweden. Terrain properties were derived from a digital elevation model.

Vegetation	LAI	Elevation (m)	Slope (%)	Aspect*	Cv+	TOPEX‡	CTI§	PI†
Willow	0.99	616.52	11.57	0.27	-1.97	-39.71	4.83	18.70
Birch	1.01	618.71	6.60	0.61	0.64	90.92	5.75	19.93
Dwarf Birch	0.95	618.79	9.79	0.39	-0.16	-0.16	5.99	19.34
Heath	0.74	622.15	9.57	0.42	-0.28	-5.62	6.15	19.31
Moss	0.74	624.66	6.85	0.49	0.37	-54.68	6.33	19.81
Graminoid	0.72	624.98	4.03	0.47	-0.20	-42.00	8.13	19.86
Fell field	0.55	625.95	7.87	0.47	-0.08	18.36	5.91	19.61

* Aspect converted to circular score ranging from 0:1 via sin(Aspect*π/360)
\+ Surface curvature: Negative values are concave
§ Compound topographic index
† Potential Insolation over the growing season (May-September) in Mj/m2/day
‡ Topographic exposure index

Table 4.6 Linear model selection criteria for macroscale transformed leaf area index (LAI_t) data. The OLS model is a linear regression model fit by ordinary least squares methods. The other models are simultaneous spatial auto-regression models fit by maximum likelihood methods. The lagged response model adds a spatial interaction term for LAI_t, whilst the spatial error model adds a spatially interactive error term. The spatial Durbin model is the most complex, adding spatial interactions for all predictors, and LAI_t.

Model	Log likelihood	AIC	RMSE	Pseudo r^2	DF
OLS	-76.10	164.19	0.36	0.22	6
Lagged Response	-69.99	153.97	0.34	0.27	7
Lagged Error	-69.57	153.15	0.34	0.27	7
*Spatial Durbin**	-62.75	147.50	0.33	0.32	11

* Lagged response and lagged predictors

value of 6. PI ranged from 15 – 22 MJ m^2 day^{-1}, with a median of 20 MJ m^2 day^{-1}. A summary of the DEM derived topographic indices is presented in Figure 4.2.

Initial exploratory analysis of the macroscale data by univariate linear regression indicated that elevation ($P < 0.001$, $r^2 = 0.12$), aspect ($P < 0.001$, $r^2 = 0.06$), TOPEX ($P < 0.001$, $r^2 = 0.08$) and potential insolation ($P < 0.01$, $r^2 = 0.03$) were significantly related

Table 4.8 Spatial Durbin model of macroscale LAI_t against DEM derived terrain variables. The model incorporates local effects of topography at the prediction location, along with spatial interactions of these terms with neighbouring samples. A neighbourhood interaction in the response (ρ) is also included.

		Macroscale Data		
Parameter	Effect	Estimate	Likelihood Ratio	Pr (>|z|)
Intercept	Intercept	9.98		
Elevation	Local Effect	-8.07×10^{-02}	11.50	<0.001
*Aspect**	Local Effect	-2.44×10^{-01}	3.58	0.06
TOPEX‡	Local Effect	-2.32×10^{-04}	1.17	0.28
PI†	Local Effect	1.11×10^{-02}	0.08	0.77
Lagged Elevation	Spatial Interaction	7.18×10^{-02}	8.49	<0.001
*Lagged Aspect**	Spatial Interaction	4.43×10^{-01}	3.41	0.06
Lagged TOPEX‡	Spatial Interaction	-6.42×10^{-05}	0.03	0.87
Lagged PI†	Spatial Interaction	-1.69×10^{-01}	6.31	<0.05
ρ	Spatial autocorrelation	0.33	11.44	<0.001

* Aspect converted to circular score ranging from 0:1 via sin(Aspect*π/360)

† Potential Insolation over the growing season (May-September) in Mj/m2/day

‡ Topographic exposure index

to LAI_t (Table 4.5). However, a much greater percentage of the variation in LAI_t was accounted for by differences in community type ($P < 0.001$, $r^2 = 0.31$).

Summarizing topographic variables by vegetation type indicated a strong interaction between landscape level community structure and topographic position (Table 4.7). In particular, a toposequence of community types became apparent, with a corresponding downward shift in LAI with increasing elevation (Figure 4.7). We fitted a linear mixed effects model to the macroscale data to predict LAI_t from the full set of topographic indices and physical models, with fixed slopes for the topographic effects, and random intercepts by vegetation type. The optimal model was selected by linear stepwise regression, sequentially dropping terms that did not favourably affect the Akaike information criterion (Akaike 1974) of the model. The retained terms were

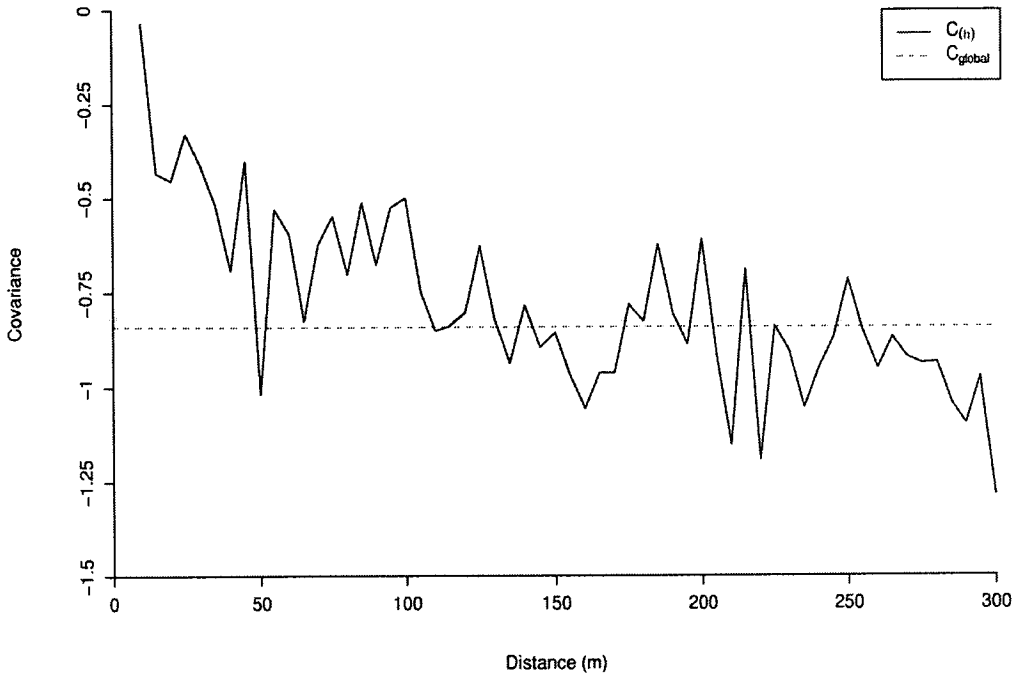

Figure 4.8 Spatial covariance of LAI and elevation in the macroscale data set. Spatially lagged covariance (c(h)) is displayed as a solid black line, whereas the global (non-spatial) covariance is indicated by the broken grey line.

vegetation type, elevation, TOPEX and potential insolation (PI), all of which were highly significant ($P < 0.001$), with an r^2 of 0.44. Analysis of the residuals of the fitted model showed that significant autocorrelation was present in the error term (Moran's I = 0.14, $P < 0.001$), indicating that OLS fitting methods were inappropriate. Residuals were found to be autocorrelated below a distance of 116 m, when an exponential autocorrelation structure was imposed upon the error term of the model.

To incorporate the spatial autocorrelation structure, a series of simultaneous autoregressive linear models were fitted to the data. Lagrange multiplier tests (Anselin 1988, Anselin and Rey 1991) indicated that fitting spatial autoregressive models were appropriate; diagnostics for lagged-response, lagged-errors and Durbin models were all highly significant ($P < 0.0001$).

Clear improvements to the model fit over OLS were observed for increasingly complex ML models (Table 4.6). The best choice of model, as indicated by AIC, was the spatial Durbin model (pseudo $r^2 = 0.32$). An examination of the terms of the Durbin model (Table 4.8) indicated that the only significant local topographic term was elevation ($P < 0.001$); however, significant adjacency effects were indicated for elevation ($P < 0.01$) and PI ($P < 0.05$). Significant residual variation was also indicated by the autocorrelation parameter ρ ($P < 0.001$). The residuals of the Durbin model were not autocorrelated (Moran's $I = -0.002$, $P = 0.47$), indicating robust estimation of model parameters.

To examine the adjacency effect of elevation, the covariance between LAI and elevation at increasing separation distances was plotted (Figure 4.8). The covariance between LAI and elevation was close to zero at short separation distances, but became increasingly negative as separation increased, indicating that the inverse relationship between LAI and elevation developed at larger spatial scales, with weaker local influence.

4.6 Discussion

The analyses at the macro- and microscales demonstrated that explicit treatments for the effects of spatial autocorrelation were required to make valid inferences regarding the distribution of LAI under our sampling strategy. Failure to treat for the autocorrelation in the data led to false inferences on the significance of effects, most clearly illustrated in the microscale analysis, in which slope appeared to be a highly significant parameter, until autocorrelation was accounted for. Similarly in the macroscale analysis, an erroneously high pseudo r^2 was arrived at before treating the

analysis for spatial effects. Problems arose because of the inflation of the probability for committing Type I errors in the presence of spatial autocorrelation, due to a bias towards artificially lowering the estimate of sample variance. This led to an overestimation of r^2 values, and hence incorrect hypothesis tests (Haining 2003, Kuhn 2007).

The macroscale analyses demonstrated that the major determinant of LAI was community type, which accounted for 31% of the variation in LAI_t. We disaggregated the community level effect from the topography, and still observed a highly significant effect ($P < 0.0001$), indicating that plant functional type was strongly associated with LAI.

There was a clear toposequence of vegetation types associated with the trough and hummock topography of the macroscale site. On high exposed sites, fell field communities dominated, with associated low vascular LAI values. Moving down the elevation profile, graminoid and moss-dominated sub-Arctic meadow communities were more common, associated with relatively flat but sheltered topographic positions. Below this were heath communities, with an increasing dominance of *Betula nana* as elevation decreased, and an associated increase in mean LAI. At the lowest elevations, the heath community was interspersed with an over-storey of small *Betula pubescens* individuals. On low elevation sites with steep slopes bordering the drainage channels, *Salix* communities dominated.

There was a clear, gradual decrease in LAI up the elevation gradient (Figure 4.7). Our findings are in general agreement with Walker and Walker (1996), who reported a similar toposequence and general trend between LAI and elevation on the North Slope of Alaska. Walker and Walker (1996) observed changes in vegetation physiognomy over

a scale of ~150-200 m, which agrees with the characteristic scale lengths over which macro scale LAI was autocorrelated in the present study (~120 m).

There was no significant relationship between CTI and LAI at either the microscale, or the macroscale, and hence we reject H1, that the primary constraint on LAI distribution was through landscape soil moisture. We observed that drainage at the site was complicated by the stony nature of the substrate, a result of the intense glacial activity in the late Pleistocene.

There was evidence at the microscale to support H2, that exposure was the dominant control on LAI, ($P < 0.0001$), where it was observed to be the most significant factor measured. However, there was no supporting evidence for exposure effects at the macroscale.

H3, that short wave radiation budget was the dominant control on LAI, can be rejected; no significant effect was observed at either scale. Interestingly, PI was observed to have a negative spatial interaction with LAI at the macroscale, indicating that an adjacent site with high solar intercept reduced the LAI at the prediction location. This may be an artefact of the dataset, or may be an outcome of the irregular hummocky topography of the site (e.g. an effect of projected shadows).

Elevation proved a significant determinant of LAI at both the macro- and microscales ($P < 0.001$, $P < 0.01$ respectively) and thus we accept H4. The macroscale effect of elevation most likely reflects an elevational temperature profile. Models of LAI distribution based solely on topographic parameters were able to account for ~30% and 20% of the LAI variation at the macro- and microscales respectively, which compares favourably with reflectance based approaches reported elsewhere, and outperforms reflectance-based efforts previously undertaken at the IV (17% at the macroscale site only, see Williams et al. in review).

The elevation response was most clearly observed at the macroscale, and decreased in influence and significance at the microscale. The decreasing importance of elevation as an explanatory variable as scale length decreased is clearly illustrated in Figure 4.8 where covariance with LAI tends to zero at small distances. Increased elevation is correlated with lower temperatures through adiabatic lapse rates (~0.6°C per 100 m). The elevation change in the IV was ~40 m, corresponding to ~0.2°C expected drop in mean temperature. The macroscale study suggests that this small drop in temperature has identifiable effects on LAI. While it would be intriguing to extrapolate the LAI-temperature response to determine an altitude for zero LAI, we expect that this relationship is likely to be non-linear.

At the microscale, higher order topographic effects, namely TOPEX, dominated LAI distribution, noting that TOPEX was derived in part from slope curvature. TOPEX is a better indicator of sheltering than instantaneous curvature because it integrates enclosure over a wide distance, rather than within the narrow confines of DEM pixel adjacency. Exposure influences LAI by increasing mechanical stress from wind-shear, and by modifying the local growth season through reduced snow accumulation, earlier snow melt and more variable soil temperatures (Wielgolaski et al. 1975).

There was a large degree of latency in the models presented, with significant autocorrelation in the error terms. This latency indicates that other variables, for which measurements were unavailable, exerted a substantial influence on the distribution of LAI. Analysis of the spatial structure of these errors, through the semivariogram, gave an indication of the characteristics of the residual process. For the microscale study the residuals displayed an exponential structure with a range of ~2.5 m, indicating an underlying phenomenon with rapid but ordered variation at small spatial scales.

The present study did not incorporate belowground processes and plant community interaction effects, and this may account for the residual variation in the spatial patterns of LAI. The soils of Abisko have low fertility (Hinneri et al. 1975, Ratcliffe 2005), but their spatial variability has not been well studied. Drainage patterns, the distribution of snowbeds, and the nature of the rocky substrate probably generate a heterogeneous distribution of soil nutrients that may explain the residual variation in LAI. It is also probable that significant variation in LAI is due to plant species interactions, site history and facilitation. Callaway et al (2002) reported positive interactions between plant communities in highly stressed environments, and it is possible that such facilitation processes may affect the LAI distributions observed here. Factors related to site history, reindeer management and disturbance may also play an important role in the distribution of LAI, but no historical data for the IV was available. Further research into below ground processes and community interactions are therefore likely to improve our understanding of the spatial patterning of Arctic LAI.

4.7 Conclusions

It is clear that vegetation type, topography and LAI are tightly coupled in tundra ecosystems. In this study we were able to characterize LAI variation through topographically derived indices more successfully than previous attempts utilizing satellite derived vegetation indices (Williams et al, in review). The improved results are most likely because the high spatial frequency LAI response to microtopography is not resolved by commonly used satellite borne vegetation mapping instruments (with resolutions ranging from ~20 m to 1 km), and the problems associated with atmospheric and illumination effects. We conclude that an understanding of the scale

dependent relationships between LAI and topographic position can improve landscape characterization of LAI. We have demonstrated a strong association between topography and LAI, especially at larger scales. In particular, elevation was a useful predictor of LAI at the small catchment scale, as reflected by its increasingly negative covariance with LAI as scale length increases. The relationship between LAI and elevation most likely reflects an altitudinal temperature profile, while local topographic position exerts an influence on the spatial patterning of LAI through local modification of the time of snow melt. We propose that combinations of satellite-derived surface reflectance with topographical information may result in improvements in estimating regional LAI distributions.

4.8 Acknowledgements

LS undertook all statistical modelling and wrote the text. MW devised the experiments, organised the field campaigns, assisted analysis and contributed to writing. RB undertook the macroscale field study, and assisted in its analysis. PS assisted the data analysis and contributed to writing. BH arranged the aircraft flight to provide DEM data and contributed to writing. MvW undertook the microscale field work and commented on the manuscript. We are very grateful to Ana Prieto-Blanco and Mathias Disney, UCL, for generating the DEM from the aircraft data, to Lorna Street and Sven Rasmussen for assistance collecting the microscale dataset, to Kerry Dinsmore for assistance with the macroscale data collection, to Gus Shaver for his support, and to the Abisko Research Station and Terry Callaghan for supporting the field work. The field work was funded by NSF grant DEB0087046 'LTER Cross-site 2000: Interactions

between climate and nutrient cycling in Arctic and sub-Arctic tundras" and by the University of Edinburgh.

4.9 References

ACIA. 2005. Arctic Climate Impact Assessment. Cambridge University Press, Cambridge; New York, N.Y.

Akaike, H. 1974. A new look at statistical-model identification. Ieee Transactions on Automatic Control Ac19:716-723.

Anselin, L. 1988. Spatial Econometrics: Methods and Models. Kluwer Academic Publishers, Dordrecht; Boston.

Anselin, L. 1995. Local indicators of spatial association - lisa. Geographical Analysis 27:93-115.

Anselin, L., and S. Rey. 1991. Properties of tests for spatial dependence in linear regression models. Geographical Analysis 23:112-131.

Asner, G. P., J. M. O. Scurlock, and J. A. Hicke. 2003. Global synthesis of leaf area index observations: implications for ecological and remote sensing studies. Global Ecology and Biogeography 12:191-205.

ASRS. 2007. Abisko scientific reasearch station weather data. Available online: http://www.ans.kiruna.se/ans.htm [Accessed 01-08-2007].

Beven, K. J. 1977. Distributed Hydrological Modelling: Applications of the TOPMODEL Concept. Wiley & Sons.

Box, G. E. P., and D. R. Cox. 1964. An analysis of transformations. Journal of the Royal Statistical Society Series B-Statistical Methodology 26:211-252.

Breiman, L. 1984. Classification and Regression Trees. Wadsworth International Group, Belmont, Calif.

Burrough, P. A., R. McDonnell, and P. A. Burrough. 1998. Principles of Geographical Information Systems. Oxford University Press, Oxford; New York.

Callaway, R. M., R. W. Brooker, P. Choler, Z. Kikvidze, C. J. Lortie, R. Michalet, L. Paolini, P. F.I., B. Newingham, E. G. Aschehoug, C. Armas, D. Kikodze, and B. J. Cook. 2002. Positive interactions among alpine plants increase with stress. Nature 417:844-848.

Camp, C. D., and K. K. Tung. 2007. Surface warming by the solar cycle as revealed by the composite mean difference projection. Geophysical Research Letters 34:L14703.

Chapin, F. S., M. Sturm, M. C. Serreze, J. P. McFadden, J. R. Key, A. H. Lloyd, A. D. McGuire, T. S. Rupp, A. H. Lynch, J. P. Schimel, J. Beringer, W. L. Chapman, H. E. Epstein, E. S. Euskirchen, L. D. Hinzman, G. Jia, C. L. Ping, K. D. Tape, C. D. C. Thompson, D. A. Walker, and J. M. Welker. 2005. Role of land-surface changes in Arctic summer warming. Science 310:657-660.

Christakos, G. 1984. On the problem of permissible covariance and variogram models. Water Resources Research 20:251-265.

Cressie, N. A. C. 1991. Statistics for Spatial Data. Wiley, New York; Chichester.

Evans, I. S. 1980. An integrated system of terrain analysis and slope mapping. Zeitschrift für Geomorphologie, N.F., Supplementband 36:274-295.

Gabriel, K. R. 1971. Biplot graphic display of matrices with application to principal component analysis. Biometrika 58:453-&.

Haining, R. P. 2003. Spatial Data Analysis: Theory and Practice. Cambridge University Press, Cambridge, UK; New York.

Hinneri, S., M. Sonesson, and A. K. Veum. 1975. Soils of Fennoscandian IBP tundra ecosystems. Pages 31-40 in F. E. Wielkolaski, editor. Fennoscandian Tundra Ecosystems. Part 1. Spinger Verlag, Berlin.

Hotelling, H. 1933. Analysis of a complex of statistical variables into principal components. Journal of Educational Psychology 24:417-441,498-520.

Jaromczyk, J. W., and G. T. Toussaint. 1992. Relative neighborhood graphs and their relatives. Proceedings of the Ieee 80:1502-1517.

Karlsson, P. S., and T. V. Callaghan. 1996. Plant Ecology in the Sub-Arctic Swedish Lapland. Blackwell Publishing, Boston.

Kattsov, V. M., E. Källén, H. Cattle, J. Christensen, H. Drange, I. Hanssen-Bauer, T. Jóhannesen, I. Karol, J. Räisänen, G. Svensson, S. Vavulin, D. Chen, I. Polyakov, and A. Rinke. 2005. Future climate change: Modelling and scenarios for the Arctic. Pages 100-150 in Arctic Climate Impact Assessment. Cambridge University Press, Cambridge; New York, N.Y.

Kuhn, I. 2007. Incorporating spatial autocorrelation may invert observed patterns. Diversity and Distributions 13:66-69.

Kumar, L., A. K. Skidmore, and E. Knowles. 1997. Modelling topographic variation in solar radiation in a GIS environment. International Journal of Geographical Information Science 11:475-497.

Mcbratney, A. B., and R. Webster. 1986. Choosing functions for semi-variograms of soil properties and fitting them to sampling estimates. Journal of Soil Science 37:617-639.

Moran, P. A. P. 1950. Notes on continuous stochastic phenomena. Biometrika 37:17-23.

Pearson, K. 1901. On lines and planes of closest fit to a system of points in space. The London Dublin and Edinburgh Magazine and Journal of Science, Sixth Series 2:557-572.

Pyatt. 1969. Guide to the site types of North and Mid-Wales. Forestry Commission, Forest Record No. 69.

Ratcliffe, D. 2005. Lapland: A natural history. Yale University Press, New York.

Raynolds, M. K., D. A. Walker, and H. A. Maier. 2006. NDVI patterns and phytomass distribution in the circumpolar Arctic. Remote Sensing of Environment 102:271-281.

Shaver, G. R., L. E. Street, E. B. Rastetter, M. T. Van Wijk, and M. Williams. 2007. Functional convergence in regulation of net CO2 flux in heterogeneous tundra landscapes in Alaska and Sweden. Journal of Ecology 95:802-817.

Sonesson, M., F. E. Wielgolaski, and P. Kallio. 1975. Description of Fennoscandian tundra ecosystems. Pages 3-28 in F. E. Wielkolaski, editor. Fennoscandian Tundra Ecosystems. Part 1. Spinger Verlag, Berlin.

Street, L. E., G. R. Shaver, M. Williams, and M. T. Van Wijk. 2007. What is the relationship between changes in canopy leaf area and changes in photosynthetic CO2 flux in arctic ecosystems? Journal of Ecology 95:139-150.

van Wijk, M. T., and M. Williams. 2005. Optical instruments for measuring leaf area index in low vegetation: Application in Arctic ecosystems. Ecological Applications 15:1462-1470.

van Wijk, M. T., M. Williams, and G. R. Shaver. 2005. Tight coupling between leaf area index and foliage N content in arctic plant communities. Oecologia 142:421-427.

Walker, D. A., and M. D. Walker. 1996. Terrain and vegetation of the Imnavait creek watershed. Pages 73-108 in Landscape Function and Disturbance in Arctic Tundra. Springer, Berlin; New York.

Wielgolaski, F. E., P. Kallio, and T. Rosswall. 1975. Fennoscandian Tundra Ecosystems: Part 1 Plants and Microorganisms. Springer-Verlag, Berlin.

Williams, M., R. Bell, L. Spadavecchia, L. E. Street, and M. T. van Wijk. in review. Upscaling leaf area index in an Artctic landscape using multi-scale reflectance observations.

Williams, M., and E. B. Rastetter. 1999. Vegetation characteristics and primary productivity along an arctic transect: implications for scaling-up. Journal of Ecology 87:885-898.

Williams, M., E. B. Rastetter, G. R. Shaver, J. E. Hobbie, E. Carpino, and B. L. Kwiatkowski. 2001. Primary production of an arctic watershed: An uncertainty analysis. Ecological Applications 11:1800-1816.

Wilson, J. D. 1987. Determining a TOPEX score. Scottish Forestry 38:251-256.

Zevenbergen, L. W., and C. R. Thorne. 1987. Quantitative analysis of land surface topography. Earth Surface Processes and Landforms 12:47-56.

Zimmerman, N. 1999. Toposcale AML. Available online: http://www.wsl.ch/staff/niklaus.zimmermann/programs/aml4_1.html [Accessed 01-08-2007].

4.10 Appendix

The spatial regression models employed all conceptualize the data set as a spatial lattice comprised of data values z posted at locations u, with first order Markov type interaction; that is, points deemed to be immediately adjacent on the lattice exert an influence on the prediction at location $z^*(u)$. We elect n spatial neighbours $\{z_i(u), i = 1,...,n\}$ via the sphere of influence (SOI) method.

SOI selection proceeds by finding the nearest neighbour distance d for every point on the lattice, and constructing circles around the points with radius equal to d. Points are said to be SOI adjacent if and only if their neighbourhood circles overlap (i.e. $|u^* - u_i| \leq d_i$). For each $z^*(u)$ we construct a set of weights $w(u)$, which code for adjacency. All SOI adjacent points exert equal influence on $z^*(u)$, so SOI neighbours

were ascribed equal weights of $1/n$, whilst points outside the SOI adjacency were ascribed a weight of zero.

Having established adjacency weights for each point, we can proceed with estimation by one of three methods; the spatial lag model (1), lagged error model (2), or the spatial Durbin model (3). These models allow horizontal interaction between the response, errors and response and predictors respectively.

The spatial lag model incorporates first order autocorrelations by including a term that incorporates neighbouring values of the variable of interest into the right hand side of the equation:

$$z^*(u) = \beta X(u) + \rho \sum_{i=1,n}^{n} w_i(u) z(u_i) \tag{4.3}$$

Where β is a vector of parameters, $X(u)$ is a vector of observed variables at the estimation location, and ρ is an autocorrelation parameter.

The lagged error model allows for spatial autocorrelation of the error term, relating the error at the estimation location with that of the n adjacent members of the lattice for $z^*(u)$:

$$z^*(u) = \beta X(u) + \lambda \sum_{i=1,n}^{n} w_i(u) \varepsilon(u_i) \tag{4.4}$$

Again, β is a vector of parameters, $X(u)$ is a vector of observed variables at the estimation location, and λ is an autocorrelation parameter on the errors.

The spatial Durbin model allows spatial interaction of all predictors and the response:

$$z^*(u) = \beta X(u) + \left[\Lambda \sum_{i=1,n}^{n} w_i(u) X(u_i)\right] + \left[\rho \sum_{i=1,n}^{n} w_i(u) z(u_i)\right] \quad \textbf{(4.5)}$$

Again, β is a vector of parameters, X is the matrix of observed explanatory variables, Λ is a vector of parameters for the lagged predictors, and ρ is an autocorrelation parameter for the response.

5. Can Spatio-Temporal Geostatistical Methods Improve High Resolution Regionalisation of Meteorological Variables?

Running title: Geostatistical Estimation of model drivers

L. Spadavecchia[1] and M. Williams[1*]

[1] School of GeoSciences, Institute of Atmospheric and Environmental Science, University of Edinburgh, Edinburgh EH9 3JN, UK.

* Correspondence to Mathew Williams, mat.williams@ed.ac.uk.

KEY WORDS: Spatio-temporal geostatistics, product-sum covariance model, meteorological upscaling

* Corresponding author

5.1 Declaration

The following chapter was submitted to *Agricultural Forest Meteorology*. I undertook all analyses and wrote all the software required for the analysis. I also wrote all of the body text for the paper, although M. Willimas provided comments and made editorial changes. M. Williams also made suggestions for the scientific questions and hypotheses addressed in the chapter.

5.2 Abstract

Models are often used to make estimates of ecological and hydrological phenomena (e.g. land surface exchanges of carbon and water) over large spatial domains. Generally such models require the input of meteorological information for the region for each time step of the state vector. We investigate the potential improvements to space-time regionalisations of sparse meteorological data sets when including information on temporal correlations between successive measurements of minimum temperature (T_{min}), maximum temperature (T_{max}) and precipitation (P) from 112 stations across Central Oregon. We compare a number of increasingly complex geostatistical models based on Kriging with a baseline inverse distance weighting algorithm. We varied the number of interpolation data used in both space and time and assessed the impact on interpolation skill. Furthermore, we assessed the error and bias reduction resulting from aggregating estimates over increasingly large temporal supports. We hypothesised that incorporating temporal information would decrease errors, and that error and bias would be reduced when considering estimates aggregated over longer time periods. We found that incorporation of information on temporal autocorrelation decreased interpolation skill by ~10%, contrary to our expectations. However, increasing the temporal aggregation of estimates was shown to decrease error by up to 50% and bias by up to 30% (daily *vs.* annual support). These results indicate that instantaneous error may be diluted for phase lagged or integrating elements of the state vector, such as soil moisture, when implementing such surfaces in modelling applications. Results were more successful for temperature than precipitation (T_{min} = 52, T_{max} = 13, P = 128 % error), reflecting the stochastic nature of precipitation, and problems with non-linearity for the Kriging algorithm.

5.3 Introduction

Models are often used to make estimates of ecological and hydrological phenomena (e.g. land surface exchanges of carbon and water) over large spatial domains. The model, parameterized at the plot level with detailed measurements, upscales information to the region of interest (e.g. Law et al., 2004; Law and Waring, 1994; Running, 1994; Van Tuyl et al., 2005; Williams et al., 2001b). Generally such models require the input of meteorological information for the region for each time step of the state vector. For example, air temperature, solar radiation and precipitation are all important controls on surface energy balance and ecosystem processes. A critical choice in the modelling process is the spatial resolution of the simulations. Given the high degree of heterogeneity in the land-surface, higher resolutions are advantageous. However, generating meteorological drivers to allow models to run at high resolutions is a difficult process.

Meso-scale climate models and reanalysis products can provide detailed global meteorology at resolutions down to ~50 km, (e.g. PRECIS Jones et al., 2004). These spatially averaged data do not resolve climatic variability - altitudinal, latitudinal or continental - that exists at the sub-grid scale (e.g. <= 1 km) and may be important ecologically. Earth observation data from space-borne instruments have been used in the past to successfully quantify surface temperature and humidity from thermal infra-red retrievals (Goward et al., 1994; Prihodko and Goward, 1997). However these products are limited by temporal revisit time versus spatial resolution, and their complex retrieval schemes are sensitive to atmospheric conditions, so uncertainties are large.

An alternative to downscaled climate models is to upscale data from station observation networks. However, data from these networks may exhibit temporal 'drop out', due to sensor failure, and spatial gaps. The sparse and temporally incomplete data

must be converted into a continuous surface to drive models. Various solutions to the problem of upscaling meteorological point data have been proposed. Conceptually simple methods based on the concept of nearest neighbour polygons (Thiessen, 1911) are easily implemented, but are fairly crude, and ignore fine-scale spatial variation.

A variety of linear regression approaches have been proposed for upscaling, with the simplest of these linking meteorological observations to auxiliary data on topography (e.g. PRISM, Daly et al., 1994). Weighted regression schemes such as Inverse Distance Weighting (IDW, Williams et al., 2001b), or Gaussian convolution (MTCLIM, Hungerford et al., 1989; Thornton et al., 1997) provide good results (Glassy and Running, 1994), but are subjective and lack optimality in terms of least squares (LS) error. Solutions which are LS optimal under mild assumptions include the thin plate spline (Hutchinson, 1995) and geostatistical 'Kriging' algorithms (Goovaerts, 1999). These approaches are data driven, and are more objective, although subjective decisions to make certain assumptions are implicit.

Kriging is a powerful interpolation algorithm as it is data driven, able to include linear relationships with topography (Goovaerts, 2000; Hudson and Wackernagel, 1994), and easily extended to the space-time domain (De Iaco et al., 2001; Kyriakidis and Journel, 1999). Also Kriging provides an estimation variance for all locations considered. Estimation variance is highly desirable in the light of model error analysis (Van Meirvenne and Goovaerts, 2001), and the move towards model-data fusion approaches to state estimation (Bertino et al., 2002; Williams et al., 2005).

In general, estimation of the temporal trajectory of meteorological variables over some spatio-temporal domain has previously been accomplished using models with no temporal covariance (e.g. Williams et al., 2001b) by creating regionalisations independently for each day. Developments in the field of geostatistics in the last ten

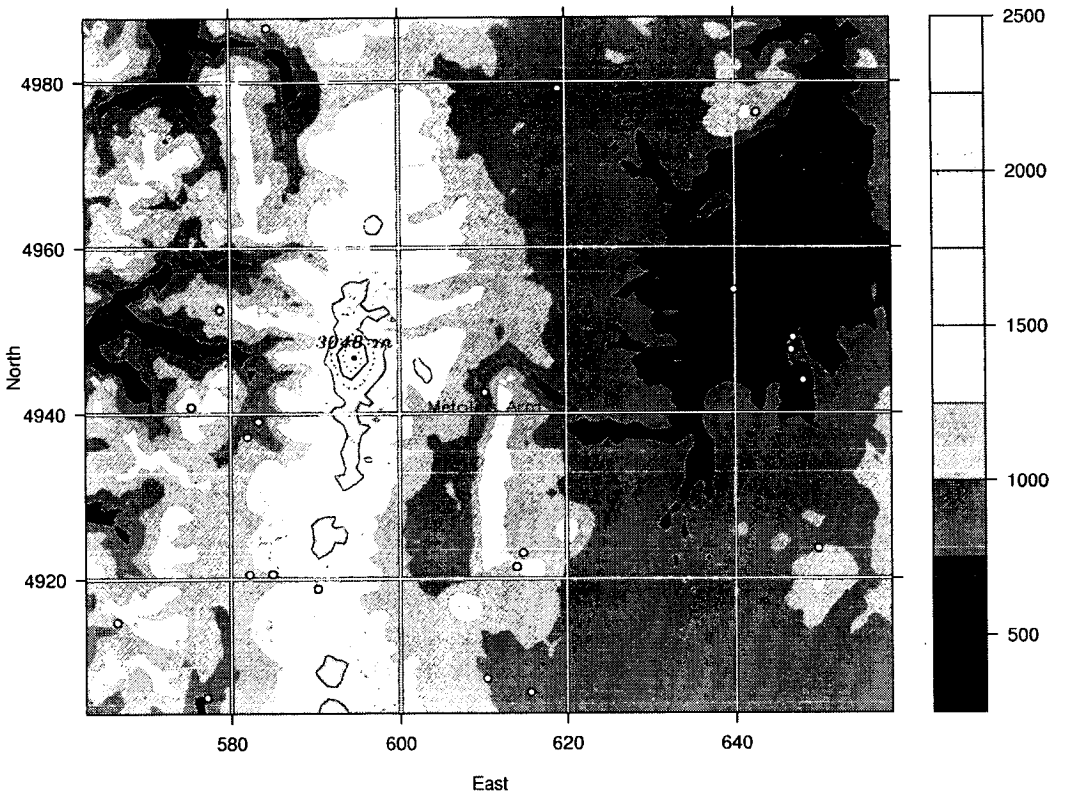

Figure 5.1 Digital elevation model of the central Cascades region, obtained from the NASA Space Shuttle Radar Tomography (SRTM) mission. Elevations are mapped at a horizontal resolution of 1 km, with vertical units expressed in metres (see scale to right). Solid contours correspond to 500 m of rise, whilst broken contours indicate 250 m of rise. The maximum DEM elevation of Mount Jefferson is indicated by a solid black point. Open points indicate the locations of meteorological stations within the study area. The point closest to the centre of the region is station 82 (Metolius Arm).

years allow the use of the spatio-temporal correlation between observations via the product-sum covariance model (De Cesare et al., 2001a), in a manner which fully represents space-time data interactions.

In this paper we demonstrate the first application of the spatio-temporal Kriging paradigm to regional meteorological data. This application addresses a key question: Does the inclusion of temporal correlation structures in interpolation schemes reduce errors of surface estimates? We hypothesised that incorporating temporal information would decrease errors (H1), by 'borrowing strength' from neighbouring data points in

time in the event of missing data, and by stabilizing the lapse relationship between topography and meteorology through reducing noise in the trend model. We also hypothesised that errors and biases would be reduced when aggregating the estimates over larger time periods (H2), as stochastic noise was filtered as errors cancelled out, with possible implications for end users of the meteorological surfaces produced.

We investigated the potential improvements to space-time regionalisations of sparse meteorological data sets when including information on temporal correlations between successive measurements of minimum temperature (T_{min}), maximum temperature (T_{max}) and precipitation (P) from 112 stations across Central Oregon. We selected these three variables as they were common to all 112 station inventories. Although other variables such as solar radiation and vapour pressure deficit (VPD) are important for ecosystem modelling, we chose not to interpolate them because of data scarcity, and because of the existence of well-tested relationships to derive these variables from temperature and precipitation datasets (Bristow and Campbell, 1984; Murray, 1967; Thornton and Running, 1999). We compared a variety of interpolation methods of increasing complexity, to assess the relative merit of incorporating temporal information at the cost of increasing model complexity.

5.4 Methods

5.4.1 Study Area

This study is focused on an area of 100 x 100 km in Central Cascades region of Oregon, USA (Figure 5.1). It is an area of considerable altitudinal variation, with Mount Jefferson rising to ~3200 m towards the centre of the site from a lowest point of ~300 m in the 'high desert' plains to the northeast of the region. Increasing hygric

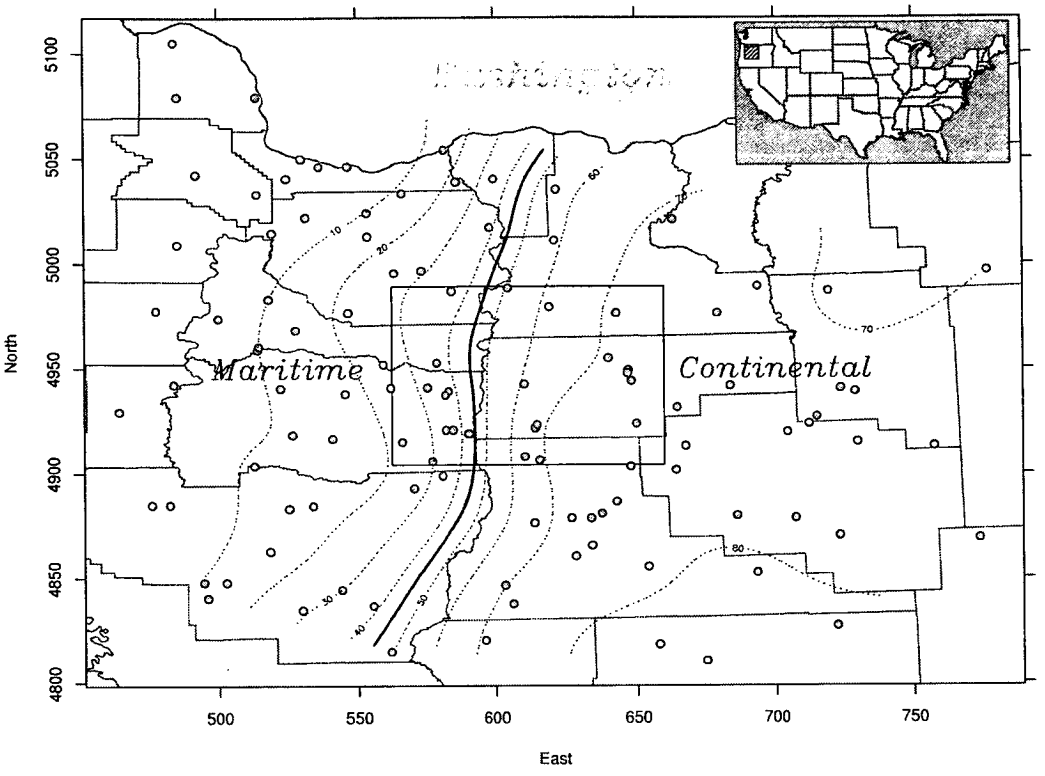

Figure 5.2 Increasing hygric continentality (HC) *cotan(elevation / mean annual precipitation)* across the longitudinal gradient. HC < 45° indicates a maritime climate, whilst HC > 45° indicates a dryer, more continental climate. The bold black line indicates the divide between hygric maritime and hygric continental climates, whilst the broken contours indicate 10° increments in HC. The rectangular outline indicates the 100 x 100 km region of interest. Points indicate the positions of meteorological stations used to derive the HC scores. All data are publicly available from the Agrimet, Ameriflux, Coop, Raws, and Snotel networks. Only stations in North/Central Oregon, with data available between January 2000 and December 2004 were considered for analysis, resulting in 112 temporal vectors, comprising some 184660 data points.

continentality (cotan[elevation / mean annual precipitation], Karrasch, 1973) (Figure 5.2) imposes longitudinal gradients on the climatology, as does topographic modification of wind patterns, temperature and rainfall (Taylor and Hannan, 1999). We selected this site because of the readily available meteorological data and interesting climatology as a result of topography and continentality. The area also includes a long term ecological study site at the Metolius Natural Research Area (MNRA 44°,25' N 121°,40' E), maintained by Oregon State University (Waring and Peterson, 1994), at

which a large body of ecological modelling and upscaling work has already been carried out (Law et al., 2001; Running, 1994; Williams et al., 2001a; Williams et al., 2005).

5.4.2 Meteorological Data

The data set comprised of 112 meteorological stations across northern Oregon, using publicly available data from the AgriMet (U.S. Department of the Interior, Bureau of Reclamation, Washington, District of Columbia; 3 stations), COOP (National Weather Service, Silver Spring, Maryland; 57 stations), RAWS (National Weather Service; 43 stations) and SNOTEL (Natural Resources Conservation Service, Washington, District of Columbia; 7 stations) networks for the five year period 2000 - 2004. These data were augmented with observations from two stations located at the Metolius eddy covariance towers, part of the Ameriflux network (Law et al., 2003). The stations were selected to surround the study region to prevent edge effects, and sample a wide range of topographic (Figure 5.1) and longitudinal variability (Figure 5.2).

All data were converted to SI units, collated and quality controlled prior to analysis. Quality control procedures rejected data that exceeded the Oregon state climate records (NOAA, 2007). Only variables common to all data sets were interpolated via the spatial algorithms described in this paper. The common variable set included daily minimum temperature ($T_{min,}$ °C), maximum temperature ($T_{max,}$ °C) and total precipitation (P, mm/day). Snow events were included as snow water equivalent. In order to produce climate summaries, T_{min} and T_{max} were converted to average daily temperature (T_a) using equation 5.1 provided in Running et al. (1987) and validated for our study region in Thornton and Running (1999):

$$T_a = 0.606 * T_{max} + 0.394 * T_{min} \quad \textbf{(5.1)}$$

The resulting data table contained 184660 entries, although not all entries had complete records for all three parameters. The table contained 180850 T_{min} records, 181667 T_{max} records, and 134432 P records.

We sourced location data for each station from online metadata, and converted the location information from geographic coordinates (Degrees, minutes and seconds) to meters, using the Universal Transverse Mercator (UTM) projection (zone 10 north, WGS84 datum) (Figure 5.2). The UTM projection allowed distances between stations to be determined in SI units, and provided consistency with elevation products.

5.4.3 Digital Elevation Model

A digital elevation model (DEM) for northern Oregon was generated from the NASA Space Shuttle Radar Tomography (SRTM) mission (Rabus et al., 2003) (Figure 5.1). The SRTM DEM provides terrain information at 10 m resolution, with an absolute vertical error of ± 10 m (Rabus et al., 2003). From this data set, elevation data were extracted for each of the 112 meteorological stations considered in a GIS (ArcInfo, ESRI, Redlands, California).

5.4.4 Trend Models

To examine the effect of elevation on the common set of meteorological variables, simple linear regression models of the variables were fitted against elevation and easting. We also investigated the possibility that the topographic and longitudinal trends were not consistent throughout the year, by fitting mixed effects models (Pinheiro and Bates, 2000) to the data, and then checked for significant improvements over the common slope and intercept models when incorporating monthly effects.

Quantification and removal of large scale effects were necessary prior to investigating the autocorrelation structure of the data, because the model of spatial

variability assumes constant mean and variance (stationarity) throughout the domain (Goovaerts, 1997). Decomposition of the data into high frequency, autocorrelated departures from the local mean (signal) and a large-scale trend (m) allows this assumption of stationarity to be satisfied. For the purposes of detrending, continuous space-time trend models were constructed using a first order Fourier series with a period of 365 days, and a fixed linear relationship with a secondary variable:

$$m = \alpha + \beta_1 \sin(t\omega) + \beta_2 \cos(t\omega) + \beta_3 s$$
$$\omega = \frac{2\pi}{365} \qquad (5.2)$$

Where $\beta_{1\text{-}3}$ are parameters, t is time in days, and s is a secondary variable; an altitudinal lapse rate for T_{min} and T_{max}, or a fixed longitudinal response for P, reflecting the strong rain shadow effect imposed by the Cascade mountains.

5.4.5 Semivariograms

Having removed the large-scale deterministic trend component m, the residual autocorrelated component of variation in the meteorological data can be summarised. A collection of n data points $Z(u,t)$ with spatial coordinates u and temporal coordinates t can be completely summarized by their mean, variance, and some measure of their autocorrelation structure, such as a semivariogram (Deutsch and Journel, 1998). The semivariogram describes the way in which similar observation values are clustered in space-time, in accordance with Tobler's first law of geography (Tobler, 1970). The semivariogram is therefore a measure of the *dissimilarity* of data pairs as the space-time separation between them increases (Deutsch and Journel, 1998). The semivariance ($\hat{\gamma}$) is calculated for lagged sets of separation vectors h_u and h_t as half the mean squared pairwise difference between the n observed values within the space-time lag ($n(h_u,h_t)$):

$$\hat{\gamma}_{u,t}(h_u,h_t) = \frac{1}{2n(h_u,h_t)} \sum_{i=1}^{n(h_u,h_t)} \left[z(u_i,t_i) - z(u_i + h_u, t_i + h_t) \right]^2 \qquad \textbf{(5.3)}$$

In order to summarize the autocorrelation in space and time, a product-sum covariance model was fitted to the semivariogram, as described by De Iaco et al (2001). First, only the simple spatial and temporal semivariograms ($\hat{\gamma}_{s,t}(h_s,0)$ and $\hat{\gamma}_{s,t}(0,h_t)$ respectively) were considered. Valid semivariogram models (see Deutsch and Journel, 1998, pp. 24-26) were fitted to them, estimating the spatial and temporal 'partial' ranges (ϕ_s, ϕ_t) and sills ($sill_s$, $sill_t$), and adding a 'nugget' discontinuity (τ_w) at the origin to reflect spatial uncertainty if required.

Semivariogram models must be selected from a set of allowable functions that are conditionally negative definite (Mcbratney and Webster, 1986), such as the spherical, exponential or Gaussian models (Deutsch and Journel, 1998). It is possible to model a semivariogram as a 'nested' model, using any additive linear combination of these models. There is some argument over the correct way to proceed in semivariogram model fitting (see Diggle et al., 2002; Goovaerts, 1997 p. 98, for contrasting views); here we favour initial fitting by OLS methods, followed by adjustment by eye, to reduce the effect of outliers.

Having described the spatial and temporal behaviour separately, we examined the values of the semivariogram beyond the spatial and temporal ranges ($\hat{\gamma}_{s,t}(h_s > \phi_s, h_t > \phi_t)$) to find the global sill ($sill_g$). We then checked the validity of the fitted model, using the values of $sill_s$, $sill_t$ and $sill_g$ via the diagnostics detailed in De Cesare et al (2001), to ensure the resulting space-time semivariance function was negative definite.

5.4.6 Interpolation methods

All of the interpolation methods considered in this paper produce estimates through weighted linear combination of a subset of the data $\{z_i(u,t), i = 1,...,n\}$. Data were selected on the basis of spatial and temporal distance from the estimation datum. The spatial effects were decomposed into a global trend m, and a high frequency autocorrelated residual component, formed from a weighted combination of the residuals $\{z(u,t) - m(u,t)\}$ (equation 5.4). Therefore the only difference in the prediction algorithms was the method by which the weights (λ) were derived:

$$z^*(u,t) = m(u,t) + \sum_{i=1}^{n} \lambda_i(u,t)[z_i(u,t) - m(u,t)] \qquad \textbf{(5.4)}$$

The 'baseline' algorithm, by which the other methods were judged, was inverse distance weighting (IDW), with no temporal information content. Estimation proceeded by removing the trend component m from the data, and weighting the residuals using the inverse of the squared distance to the estimation location $z^*(u,t)$ raised to the power of 2. The inverse square law produced a map similar to that of a practitioner contouring 'by eye' (O'Sullivan and Unwin, 2003, Pp. 230-231). The weights were standardized such that they summed to one.

Also implemented were three variants of the Kriging algorithm; simple Kriging (SK), ordinary Kriging (OK) and Kriging with an external drift (KED). Kriging refers to a set of multiple linear regression procedures by which the best linear unbiased estimate (BLUE) of an unobserved datum value is arrived at by the weighted linear combination of surrounding observations (see Cressie, 1990 for a historical perspective), such that the prediction error is minimized (Cressie, 1991; Isaaks and Srivastava, 1989). The conditioning data were weighted by taking into consideration the clustering of the data

locations (with points from over-sampled locations being down-weighted), and the proximity of each observation to the prediction location. These spatial effects are included through reference to the autocorrelation structure of the data set, as summarized by the semivariogram.

In the case of SK, a known trend function m is removed from the data, and the residual variation is interpolated. The resulting estimate is therefore a combination of a deterministic trend function m and autocorrelated stochastic departures from this trend. In the case of OK, m is treated as unknown, and is derived from the conditioning data as part of the interpolation process. OK derives a simple mean function for m, equivalent to an intercept-only model. KED extends m to include covariates such as elevation, by fitting a local trend function from the conditioning data as part of the interpolation process (Hudson and Wackernagel, 1994). The parameters of the trend function are readily recoverable (Wackernagel, 1998). All Kriging algorithms implemented have the considerable advantage of returning estimation variances along with the BLUE. Kriging variances provide an assessment of the uncertainty of the estimate at $z^*(u,t)$, providing the semivariogram is correctly specified (Goovaerts, 1999).

Because all of the interpolation methods implemented are able to result in negative daily precipitation estimates, we truncated the results for P at zero, and treated all negative estimates as zero rainfall events. All interpolations were carried out on a 1 km^2 resolution grid, on a daily time-step using the Edinburgh Space-Time geostatistics software (Luke Spadavecchia, University of Edinburgh, UK), and statistical post-processing was carried out in R version 2.4.1 (R foundation for statistical computing, Vienna, Austria).

5.4.7 Error Assessment

Interpolation skill of the methods was assessed by 'cross validation' resampling. Each station, in turn, was temporarily excluded from the network, and the data from the remaining stations were interpolated to the space-time coordinates of the excluded observations (Deutsch and Journel, 1998). The differences between each of the observed and predicted meteorological variables were then assessed to determine the interpolation skill.

In order to test the effects of incorporating larger numbers of conditioning data on interpolation skill, we ran a number of experiments varying the number of spatial neighbours used, and the size of the temporal window from which data were selected. The n data considered were selected from the n_s spatial neighbours from the estimation day, with n_s data harvested from the $\pm n_t$ days. Thus the total number of observations on which an estimate was conditioned was $n = n_s + n_t n_s$.

We also considered the effect of estimating meteorology on increasingly large time steps, by comparing the cross validation results on different temporal aggregation schemes. This comparison was achieved by taking the weekly, monthly and annual averages of the daily cross validation estimates and comparing them with the observed

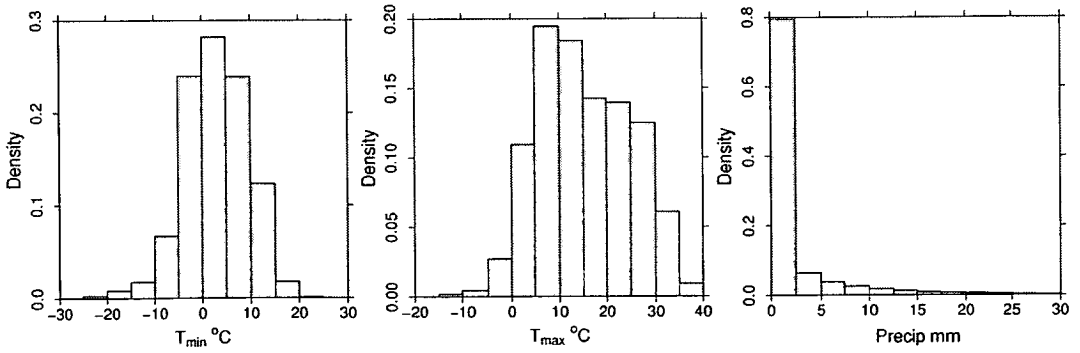

Figure 5.3 Histograms of the three daily meteorological variables T_{min}, T_{max} and precipitation, gathered from 112 stations in North/Central Oregon, between January 2000 and December 2004.

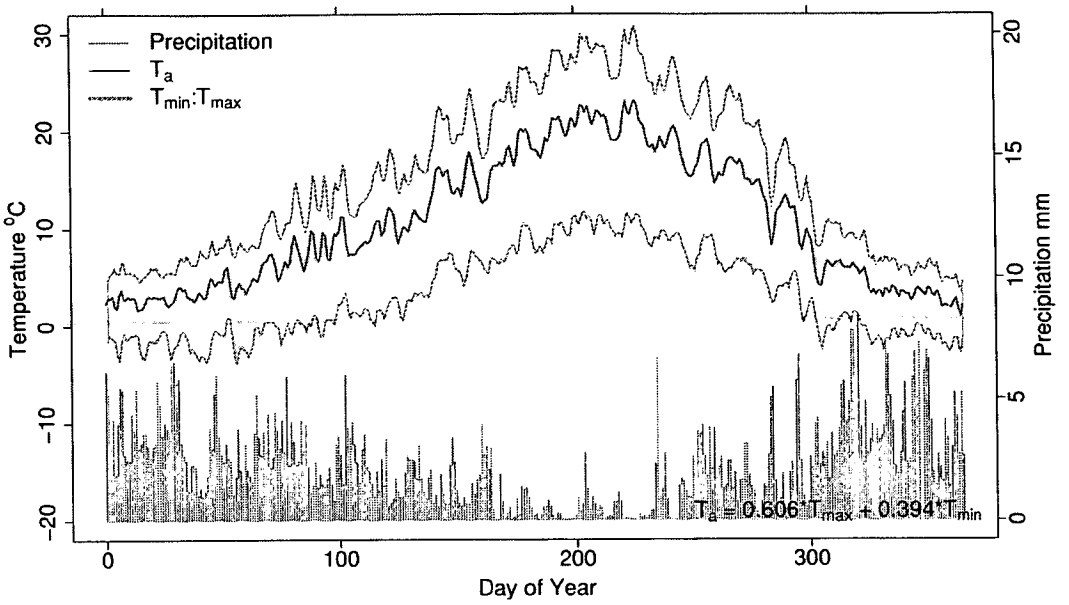

Figure 5.4 Average meteorological variables by day of year (day 1 = January 1st) for 112 meteorological stations across North/Central Oregon over the period 2000-2004. Average temperature (T_a) is indicated as a solid black line, and was calculated from Average minimum temperature (T_{min}) and average maximum temperature (T_{max}), displayed as broken black lines, with the range indicated as a light gray envelope. Vertical gray lines indicate average daily precipitation (right-hand scale).

aggregates for the same time period.

5.5 Results

5.5.1 Exploratory Analysis

The temperature variables appeared to be approximately normally distributed (Figure 5.3), whilst the distribution of P was strongly positively skewed (Figure 5.3) (skew = 5.52), reflecting the stochastic nature of precipitation (66% of P observations = 0). Initial exploratory analysis of the data over five years indicated a mean annual precipitation of 929 mm, and mean annual T_a of ~10 °C. Temperature extremes ranged from a T_{min} of -36 °C (Sunriver station, 30th October 2002, 1317 m a.s.l.), to a T_{max} of 44°C (29th July 2003, Fossil station, 809 m a.s.l.) in the high desert plains of the northeast

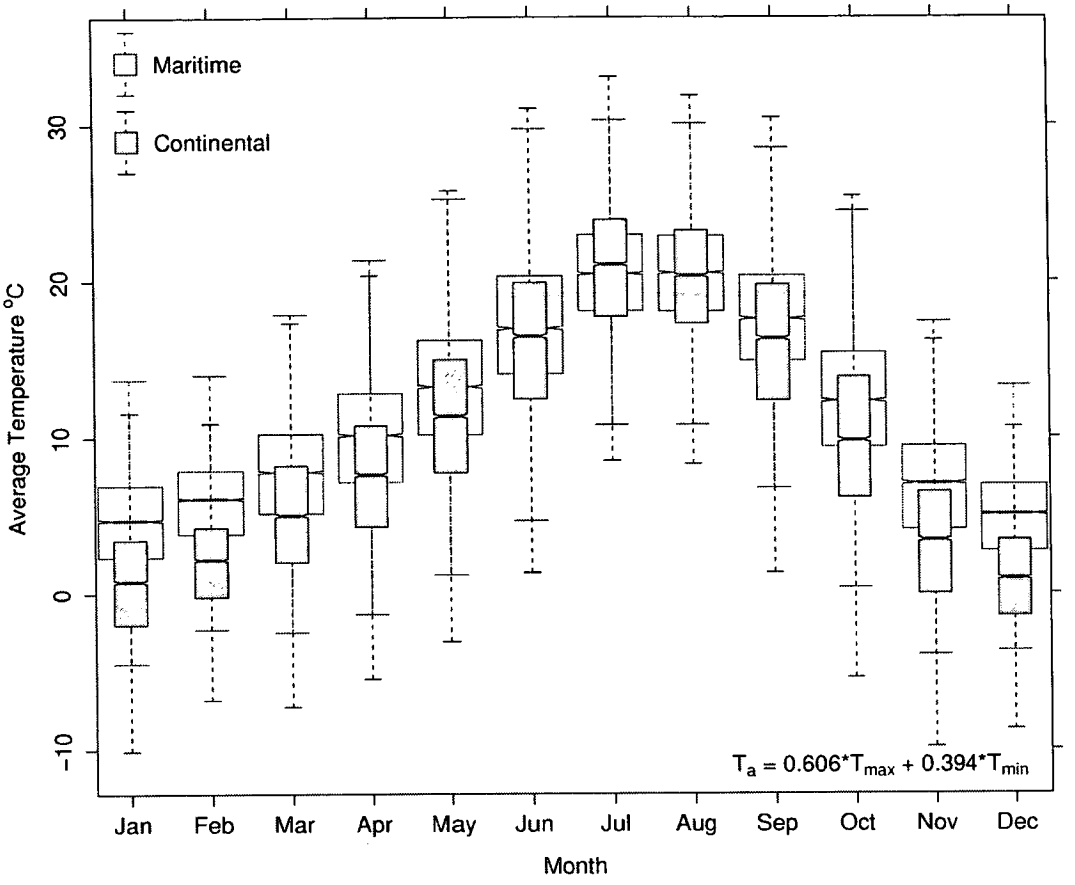

Figure 5.5 Differing thermal climate regimes by hygric continentality for the central Cascades study area. The study area is divided in two by a longitudinal gradient; the western seaboard side of the Cascades is hygric maritime, having significantly higher thermal stability over the year than the eastern region. Climate to the east of the Cascades is hygric continental, with greater seasonal extremes and higher within-month variability. Box extent indicates the interquartile range, whilst notches indicate the 95% non-parametric confidence interval of the median. Whiskers indicate the extremes of the distribution.

of the region. The daily average temperatures for these sites were -24 and 32 °C respectively. Annual climatology indicates that the daily range of temperatures increases in the summer months, and is associated with extreme aridity (Figure 5.4).

There was a highly significant longitudinal gradient of hygric continentality (HC) across the region ($P < 0.001$ $r^2 = 0.75$). An HC of < 45° is associated with a maritime climate, whilst an HC > 45° is indicative of a continental climate. The 45° HC iso-contour runs along the latitudinal path of the Cascade mountain range, dividing the state

into two climatic regimes (Figure 5.2). To the west of the Cascades, HC < 45° and the climate was wetter (mean annual precipitation 1452 mm, with a daily σ of 9 mm), milder and more thermally stable (mean annual temperature 12 ± 7 °C). To the east of the Cascades HC > 45° and the climate was dryer (mean annual precipitation 370 mm, with a daily σ of 4 mm), cooler, and more thermally variable (mean annual temperature 9 ± 9 °C). The west-east temperature regimes were significantly different ($t = 64.1$, $P < 0.0001$, Figure 5.5); the continental region had greater within-month variability, with higher seasonal extremes. Differences in precipitation between HC regions were clear, with 43% of observations in the maritime region corresponding to a precipitation event, while only 26% of observations in the continental region corresponded to precipitation events.

5.5.2 Trend Modelling

Elevation best explained the large-scale spatial patterning of temperature variables, while easting best described the large-scale variation in precipitation. T_{min} and T_{max} had significant relationships with elevation, with an overall lapse response of -0.004 °C per metre for T_{min} ($P < 0.001$, $r^2 = 0.12$), -0.003 °C per metre for T_{max} ($P < 0.001$, $r^2 = 0.02$). The longitudinal gradient in hygric continentality (Figure 5.2) was reflected in an overall longitudinal trend of -0.014 mm of precipitation per km east ($P < 0.001$ $r^2 = 0.02$).

Table 5.1 Temporal trends in meteorological variables with elevation, showing the intercept and elevation coefficients from a mixed effects regression model for unbalanced data. All data drawn from the central Oregon meteorological network over 2000-2004.

	Min Temperature °C		Max Temperature °C		Precipitation mm	
Month	Intercept	Elevation	Intercept	Elevation	Intercept	East
Jan	2.3	-0.005	8.8	-0.004	14.9	-0.018
Feb	2.4	-0.005	11.4	-0.005	15.2	-0.020
Mar	3.6	-0.005	13.8	-0.004	12.3	-0.015
Apr	5.0	-0.005	17.0	-0.004	13.5	-0.017
May	7.6	-0.004	20.2	-0.003	3.8	-0.003
Jun	10.3	-0.004	24.4	-0.002	6.1	-0.007
Jul	12.0	-0.003	28.1	-0.001	1.1	-0.001
Aug	11.9	-0.003	28.0	-0.001	2.5	-0.002
Sep	10.1	-0.004	24.8	-0.002	11.5	-0.015
Oct	7.0	-0.005	18.3	-0.003	10.9	-0.014
Nov	3.4	-0.005	11.6	-0.004	23.5	-0.031
Dec	2.8	-0.005	8.9	-0.004	25.9	-0.034

In all cases a variable-intercept, variable-slope model (Table 5.1) outperformed the fixed slope model ($P < 0.001$). The trend models were all found to be highly significant ($P < 0.001$), and adequately described the large-scale spatio-temporal behaviour of the meteorology (T_{min} $r^2 = 0.70$, T_{max} $r^2 = 0.92$, P $r^2 = 0.18$). The seasonal cycle of the meteorology was clearly reflected in the intercepts of the model, while interesting temporal interactions with the spatial patterns were evident (Table 5.1). For the temperature variables, the strength of the altitudinal lapse response weakened in the summer months, and the distribution of temperature became more uniform. Similarly, the longitudinal gradient in precipitation became less pronounced in the summer months.

5.5.3 Semivariograms

To quantify the spatial semivariance structure of the small scale component of the spatio-temporal variation, continuous time trend functions were removed from the data, with fixed elevation (T_{min}, T_{max}) or longitudinal (P) effects. Although there were significant changes in the lapse gradients over time (Table 5.1), the improvements to the r^2 over a fixed slope model were typically only ~1% over the fixed slopes models.

Having removed the large-scale trend from the data, residual semivariograms were calculated (Figure 5.6). We modelled the spatial variation of T_{min} and T_{max} with a nested spherical ($\varphi_{u.sph}\, T_{min}$ = 23.8 km, $\varphi_{u.sph}\, T_{max}$ = 9.67 km), exponential model ($\varphi_{u.exp}\, T_{min}$ = 154.2 km, $\varphi_{u.exp}\, T_{max}$ = 196.6 km). For P, a Gaussian model ($\varphi_{u.gaus}$ = 34.7 km) with a small nugget effect (τ = 0.2 mm) best captured the patterns of small-scale spatial variation. All three variables displayed exponential semivariance structures in time, with ranges of ~1 week for T_{min} and T_{max}, and a shorter temporal range of 2 days for precipitation, indicating lower temporal continuity in the time series. The sill parameters fitted for each variable were $sill_u$ = 6.4, $sill_t$ = 11.69 and $sill_g$ = 12.8 for T_{min}; $sill_u$ = 10, $sill_t$ = 23.1 and $sill_g$ = 32.46 for T_{max} ; and $sill_u$ = 20.0, $sill_t$ = 38.44 and $sill_g$ = 49.3 for precipitation.

The large scale temporal trends evident in Figure 5.6 operated on temporal separations > one month. As long as the implemented search strategy conditioned the estimate on a data subset taken from a window of <one month, the effect of seasonality on the estimate should be nil. Thus, for the methods that dynamically estimate m from the conditioning data the only remaining trend is the altitudinal lapse response for T_{min} and T_{max}, or the longitudinal effect for P.

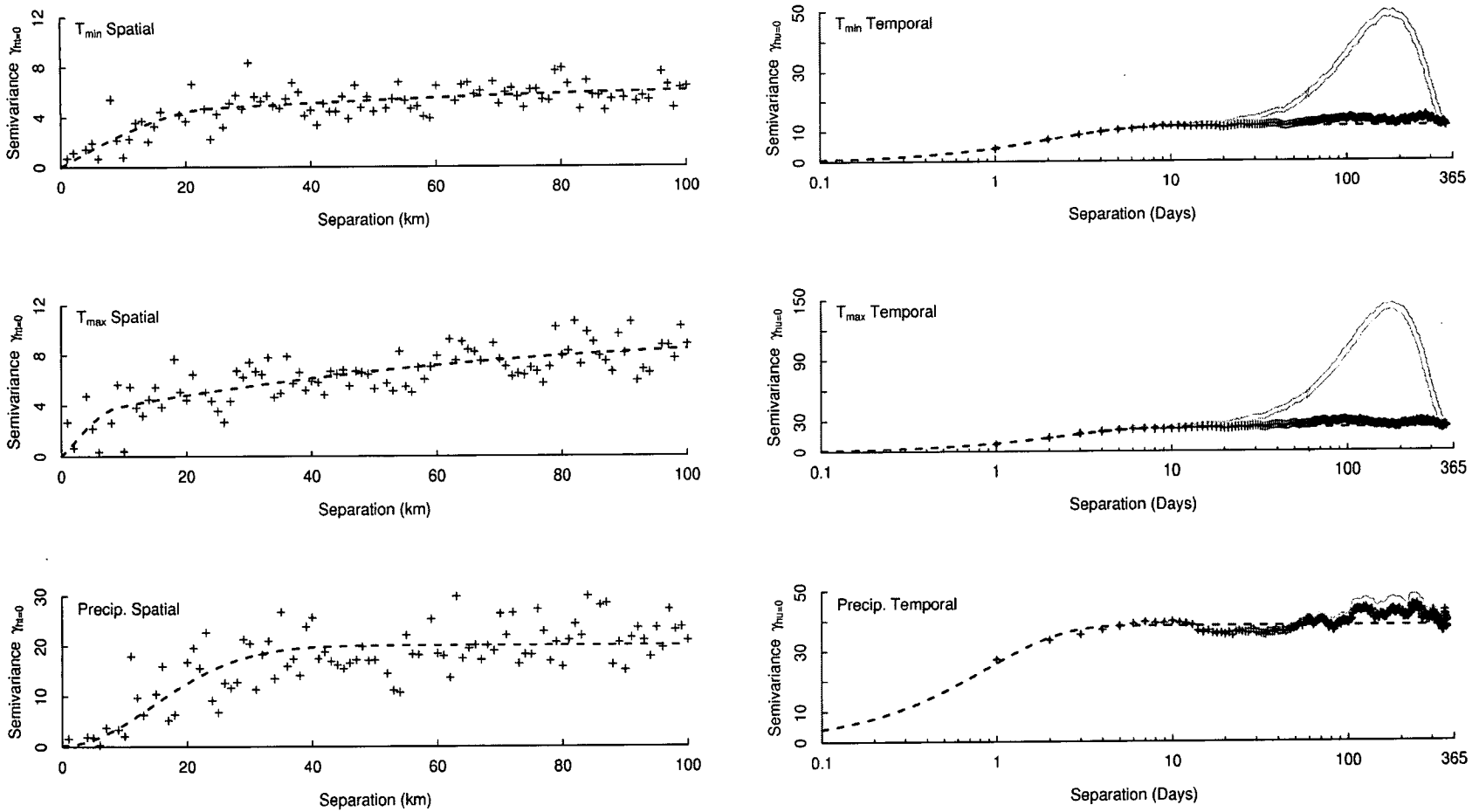

Figure 5.6 Semivariograms of meteorological data from the Central Cascades study area. Data were de-trended prior to analysis. Spatial semivariograms ($\gamma_{hs=0}$) were constructed by considering pairs of observations from the same day at increasing spatial separations. Temporal semivariograms ($\gamma_{hu=0}$) were constructed from pairs of observations from the same station at increasing temporal separation, and plotted on a log axis for clarity. For all plots, detrended observations are shown as black crosses and semivariogram models are indicated as broken black lines. Grey points on the temporal plots are raw data prior to detrending.

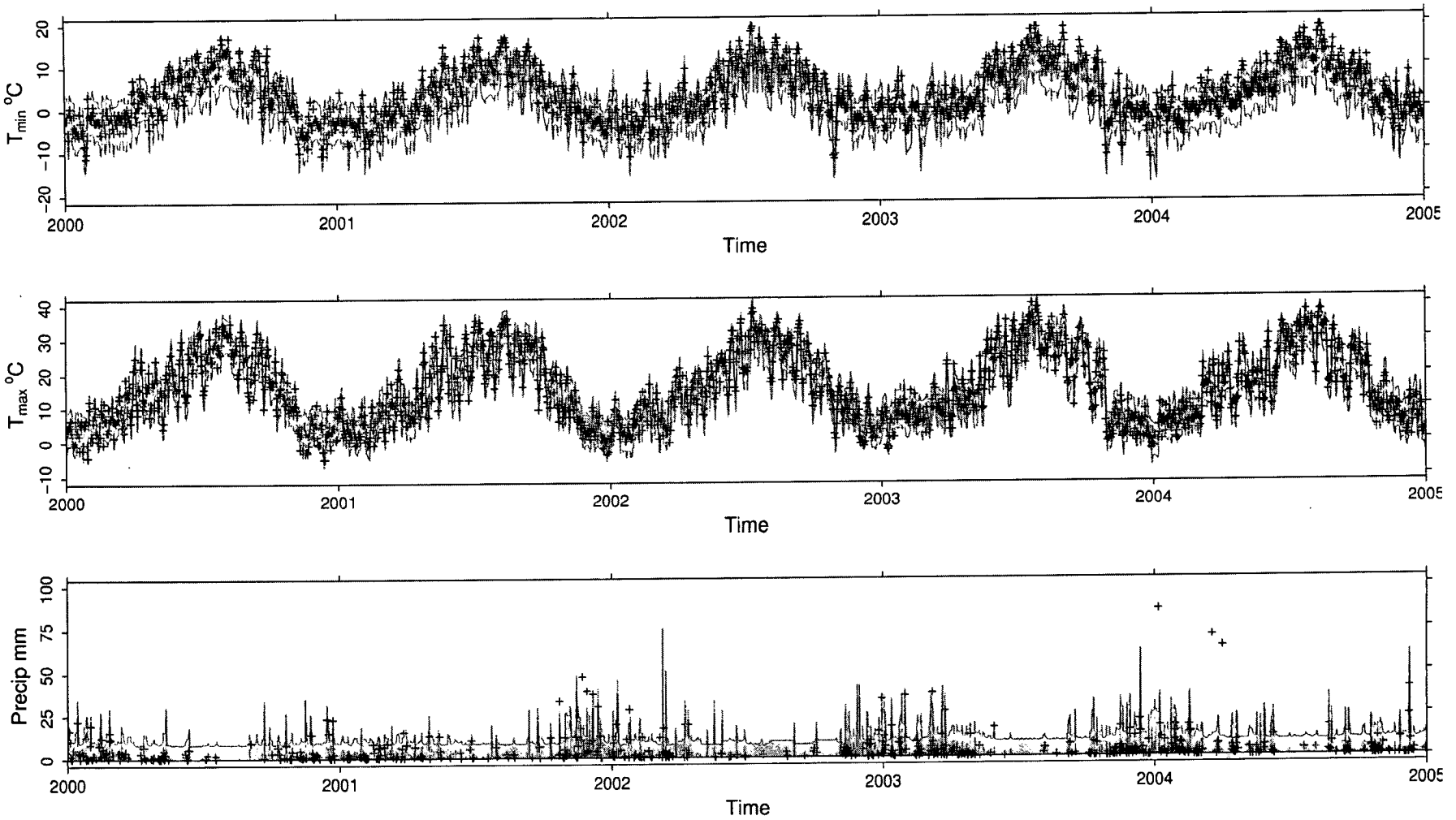

Figure 5.7 Cross validation of daily meteorological data estimated at station 84 (Metolius Arm) by external drift Kriging (KED) with observations from the same station, for the period 2000-2005. The observations were excluded from the interpolation. The Tmin and Tmax KED estimates were conditioned on 32 nearest neighbours in space, Whilst the P estimates used 4 spatial neighbours. No temporal neighbours were used. The light gray envelope indicates the 95% confidence interval of the estimate, the dark gray line indicates the KED estimate, and the crosses indicate non-zero observations. The station was selected because of its central position in the study region.

Table 5.2 Cross validation comparison of interpolation methods for the three meteorological variables considered. Methods used were IDW = Inverse Distance squared Weighting, SK = Simple Kriging, OK = Ordinary Kriging, and KED = Kriging with an External Drift. The algorithms were conditioned on 32 spatial neighbours, plus 32 observations from each day in the temporal window (total = spatial + spatial*days); a temporal window greater than zero incorporates both spatial and temporal autocorrelation into the estimate. Error statistics were calculated for each experiment: MAE = Mean Absolute Error, RMSE = Root Mean Squared Error. Also shows are r^2, % observations within ± 1 standard deviation of the estimate, and the % observations within the 95% confidence interval of the estimate; although calculation of these statistics was limited to the Kriging methods.

	Neighbours			Minimum Temperature °C				
Method	Spatial	± Days	Total	MAE	RMSE	r^2	% in SD	% in CI
IDW	32	0	32	1.96	2.69	0.81	NA	NA
SK	32	0	32	1.95	2.61	0.82	61.7	87.2
OK	32	0	32	1.95	2.61	0.82	61.7	87.2
KED	32	0	32	1.82	2.48	0.84	65.9	88.5
SK	32	7	256	1.95	2.61	0.82	61.6	87.2
OK	32	7	256	1.95	2.61	0.82	61.5	87.2
KED	32	7	256	1.88	2.55	0.83	64.2	87.7
	Neighbours			Maximum Temperature °C				
Method	Spatial	± Days	Total	MAE	RMSE	r^2	% in SD	% in CI
IDW	32	0	32	2.19	2.93	0.90	NA	NA
SK	32	0	32	2.31	3.05	0.90	59.3	86.1
OK	32	0	32	2.31	3.05	0.90	59.3	86.1
KED	32	0	32	2.01	2.70	0.92	66.9	89.7
SK	32	7	256	2.32	3.06	0.89	59.1	86
OK	32	7	256	2.32	3.06	0.89	59.1	86
KED	32	7	256	2.06	2.75	0.91	65.5	89.2
	Neighbours			Precipitation mm				
Method	Spatial	± Days	Total	MAE	RMSE	r^2	% in SD	% in CI
IDW	32	0	32	2.51	5.80	0.32	NA	NA
SK	32	0	32	3.53	16.91	0.03	20.5	34.1
OK	32	0	32	3.53	10.97	0.09	73.9	82.8
KED	32	0	32	3.51	11.00	0.10	74.2	82.9
SK	32	7	256	3.92	48.58	0.00	11.8	16.6
OK	32	7	256	3.91	11.91	0.08	71.7	81.1
KED	32	7	256	3.92	11.93	0.08	71.9	81.1

Table 5.3 Comparison of mean absolute errors resulting from cross validation of search strategies implemented in the KED interpolation algorithm for all three meteorological variables. S is the number of spatial neighbours, t is the temporal window size in ± days (i.e. no window, 1 week, 2 weeks, 1 month). It was not possible to produce estimates for precipitation with more than 32 spatial neighbors, because not all days had an adequate number of stations for conditioning the estimates.

	Minimum Temperature °C			
	t0	*t3*	*t7*	*t15*
s4	3.86	3.74	3.75	3.77
s8	2.71	2.71	2.72	2.73
s16	2.53	2.56	2.58	2.60
s32	2.48	2.53	2.55	2.57
s64	2.49	2.53	2.54	NA
	Maximum Temperature °C			
	t0	*t3*	*t7*	*t15*
s4	4.31	4.27	4.23	4.21
s8	2.97	3.00	2.98	2.98
s16	2.73	2.77	2.77	2.77
s32	2.70	2.75	2.75	2.76
s64	2.71	2.75	2.76	NA
	Precipitation mm			
	t0	*t3*	*t7*	*t15*
s4	9.83	9.44	9.24	9.14
s8	10.24	10.70	10.80	11.07
s16	10.77	11.36	11.48	11.75
s32	11.00	11.78	11.93	12.25

5.5.4 Comparison of Interpolation Algorithms

In all cases KED with no temporal neighbours performed best out of all the geostatistical algorithms considered, although the relative improvement in skill was in some cases marginal (Table 5.2). KED with no temporal neighbours improved interpolation skill over IDW by 7% for T_{min}, and 8% for T_{max}. The baseline interpolation of P by IDW outperformed all other methods (Table 5.2), but KED provided a 2% improvement in skill over SK and OK for P. For T_{min} and T_{max}, the lowest interpolation errors were observed when using moderately large numbers of spatial neighbours (n, 16 – 32), with no temporal neighbours. Temporal neighbours only improved interpolation

Table 5.4 Effects of increasing temporal aggregation on estimation error (RMS) derived by cross validation resampling of the station network for all three meteorological variables considered. Interpolation results are from external drift Kriging (KED) with 32 spatial neighbours, and no temporal interaction in the case of Tmin and Tmax, and KED with 4 spatial neighbours and no temporal interaction for precipitation.

				Mean T_{min}, °C			
	RMSE	MAE	% Error	Bias	Gain	% Bias	r^2
Daily	2.5	1.8	52	0.2	0.9	6	0.84
Weekly	1.9	1.4	40	0.1	0.9	2	0.88
Monthly	1.7	1.2	36	0.0	0.9	1	0.89
Annual	1.5	1.1	32	0.4	0.8	13	0.71
				Mean T_{max}, °C			
	RMSE	MAE	% Error	Bias	Gain	% Bias	r^2
Daily	2.7	2	13	0.9	0.9	6	0.92
Weekly	1.7	1.3	8	0.2	1.0	2	0.96
Monthly	1.5	1.1	7	0.2	1.0	1	0.97
Annual	1.3	0.9	6	3.2	0.8	20	0.72
				Total precipitation mm			
	RMSE	MAE	% Error	Bias	Gain	% Bias	r^2
Daily	9.8	3.2	128	1.9	0.5	51	0.12
Weekly	34.2	14.6	91	9.5	0.7	39	0.24
Monthly	104.7	49.7	69	32.7	0.8	31	0.34
Annual	548.2	311.0	50	176.3	1.0	26	0.51

skill when very few spatial neighbours were implemented. For *P*, the most successful Kriging results resulted from KED with 4 spatial neighbours. In all cases, the use of large numbers of spatial neighbours produced increased estimation error (Table 5.3).

We were able to reproduce regional climatology for a time period of five years using KED with expected patterns of temporal variation reproduced for all variables (Figure 5.7). Estimation skill for T_{min} and T_{max} was reasonable (RMSE T_{min} = 2.5, T_{max} = 2.7), large errors were rare, and were associated with extreme events which are poorly reproduced using least squares techniques such as Kriging, which tend to smooth the estimate of $z^*(u,t)$. There was a strong linear relationship (r^2 T_{min} = 0.84, T_{max} = 0.92) between the observed and predicted temperature variables, indicating good overall interpolation performance.

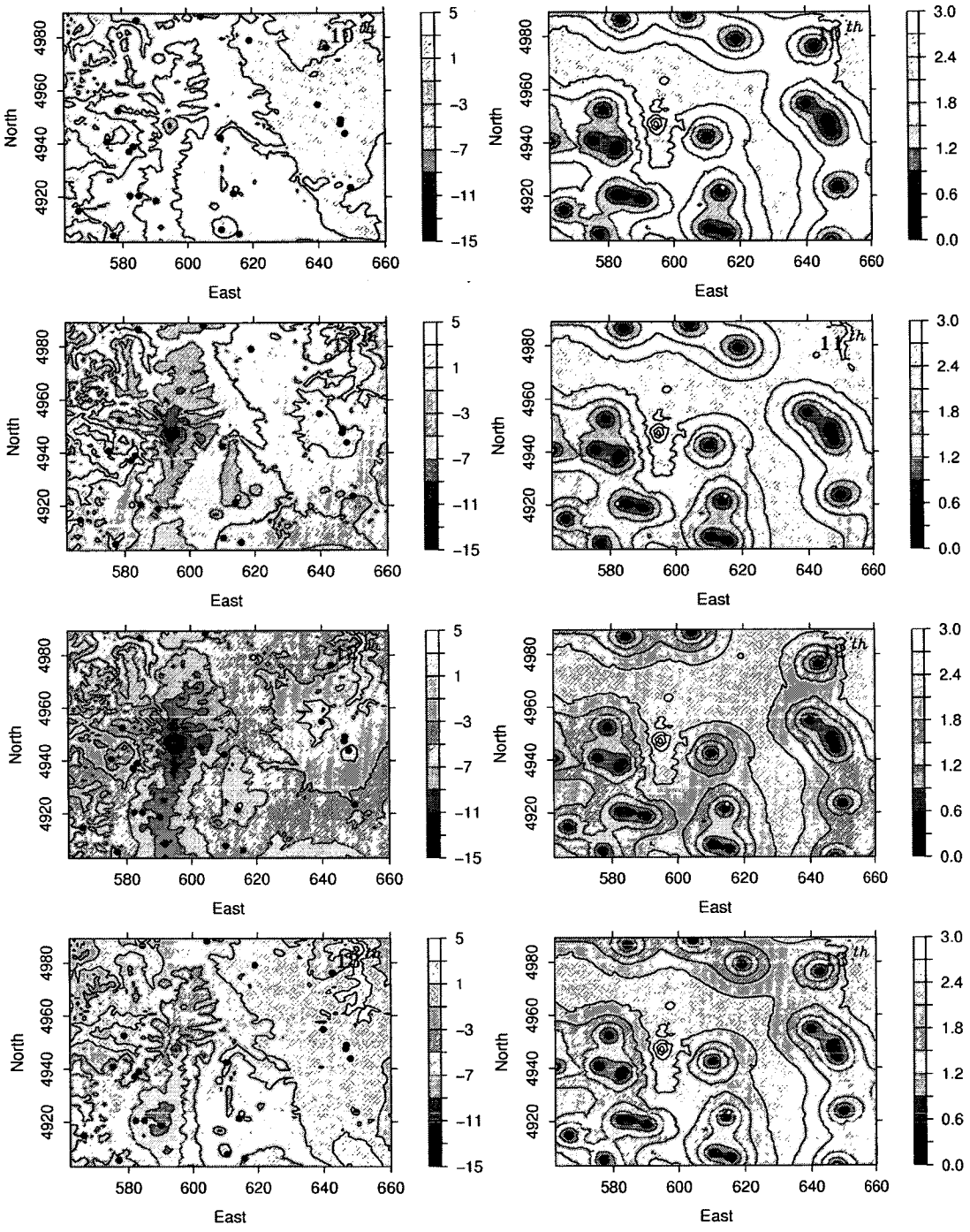

Figure 5.8 Spatial plots of minimum daily temperature (T_{min}) taken on 4 consecutive days (10 – 13th January 2000). Plots on the left of the figure indicate the external drift Kriging estimates, whilst plots on the right indicate the variance of the estimate. T_{min} contours are at 2 °C intervals, ranging from -15 to 5 °C. Standard deviation contours are plotted at 0.3 °C intervals, ranging from 0 to 3 °C. Low values are plotted in darker colours. Active stations are indicated as black points, whilst stations with missing data are indicated as open points.

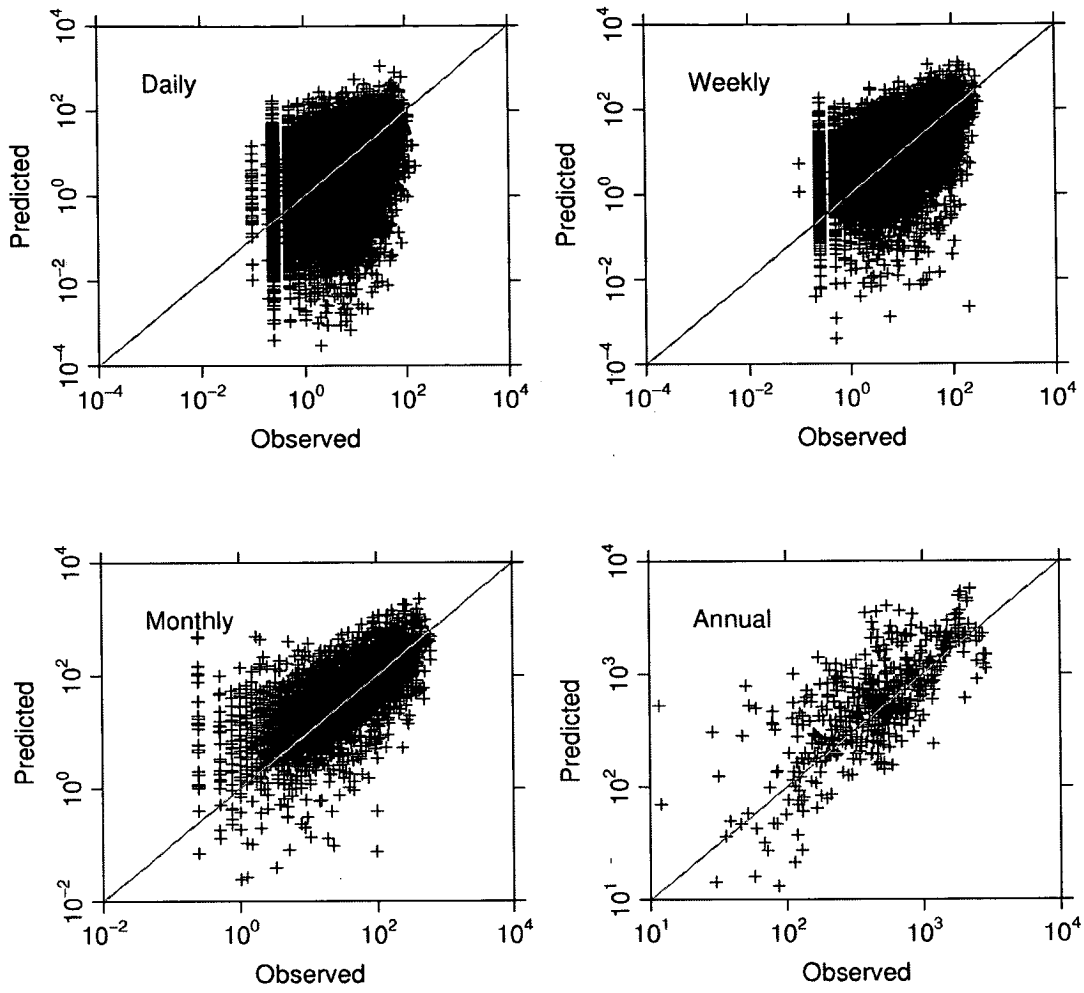

Figure 5.9 Error scaling with increasing temporal aggregation for predicted precipitation fields.

Results for P were poorer, with RMSE P = 9.8 mm, corresponding to 128% of the daily average observation for the study site (Table 5.4). Although the magnitude of precipitation events was poorly reproduced by KED, with a general overestimation by 1.9 mm (Table 5.4), the temporal patterns of drought and storm events appear to be well represented in Figure 5.7. However, in binary terms, rainfall was successfully predicted in 27% of all cases, whilst dry events were successfully predicted in 44% of all cases. False positives ($P > 0$) occurred in 22% of all dry events, whilst only 7% of all

rainfall events were predicted as dry. The spatial patterns of variation were well reproduced, with the longitudinal gradient in climatology in evidence for all variables ($P < 0.001$) (Figure 5.8). The spatial patterns due to elevation were recreated in the interpolations, with good agreement between the overall predicted lapse response and that of the data (T_{min} $z = -0.8$, $P = 0.42$; T_{max} $z = 0.5$, $P = 0.65$; P $z = -0.2$, $P = 0.85$).

Estimation uncertainty as reflected by the Kriging variance was typically low for most of the study site ($< \pm 2$ °C for T_{min} and T_{max}, $< \pm 2$ mm for P), and scaled with the distance to the nearest observation (Figure 5.8). We note the increase in the Kriging variance of temperature estimates when the KED algorithm extrapolated the trend model to elevations outside the data range (Figure 5.8).

For all variables considered, recreation of spatio-temporal behaviour improved with increasing temporal aggregation (Table 5.4). The r^2 of predicted *versus* observed on the monthly timescale was 89% for T_{min}, 97% for T_{max} and 34% for P. Temporal aggregation of the estimate improved interpolation skill particularly strongly for total precipitation (Figure 5.9); as aggregation increased, the comparison between observed and estimated data became increasingly linear, and r^2 generally increased. For T_{min} and T_{max}, annual climatology was not as well reproduced as monthly aggregates (Table 5.4). For all variables considered, positive bias in the results indicated a general overestimation, although this was relatively mild for the temperature variables (typically < 3% of the observed mean). Bias was higher for annual aggregations (T_{min} 12%; T_{max} 20%); positive bias for the P estimations were much more serious, typically ~37% of the observed mean (Table 5.4).

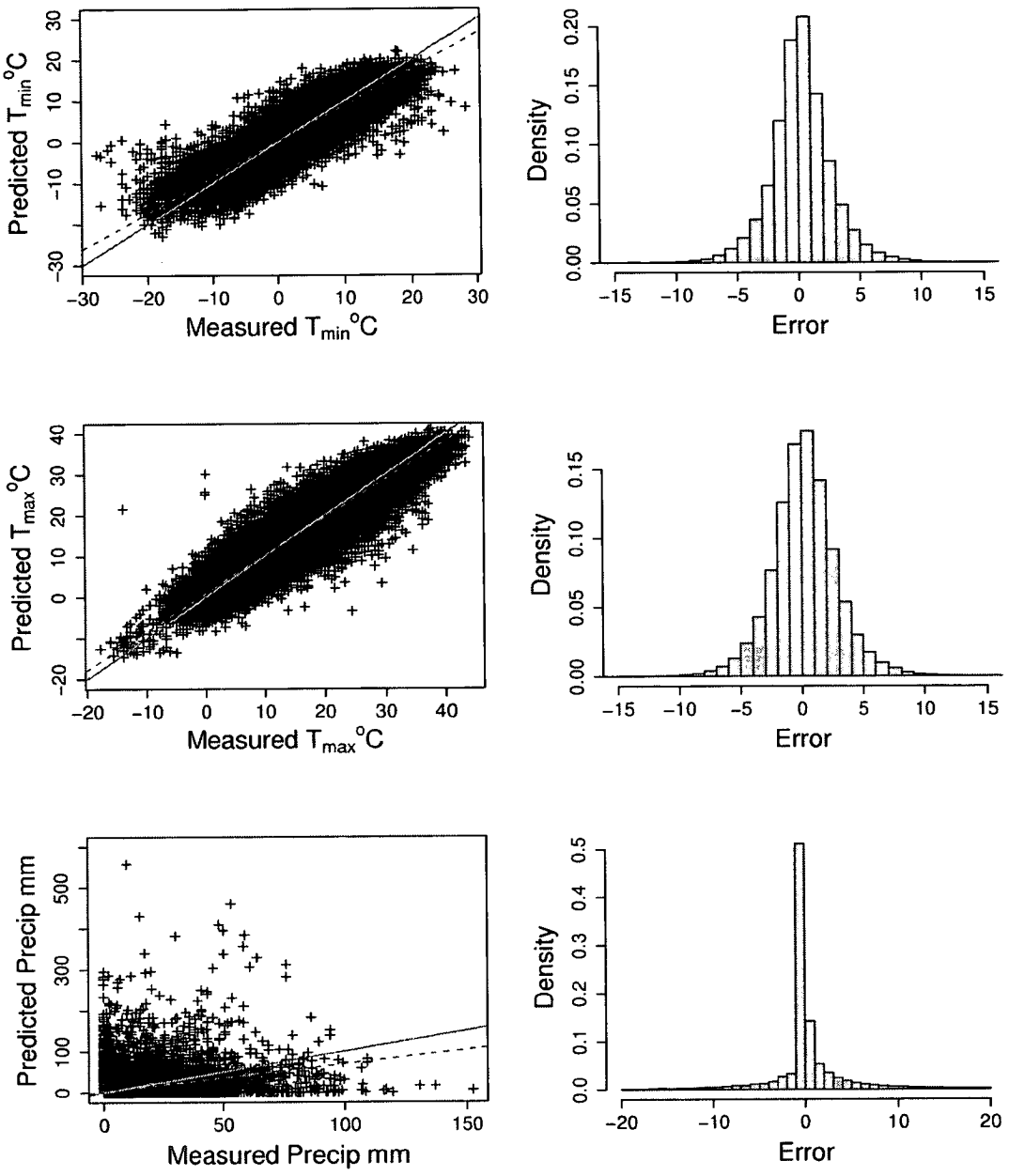

Figure 5.10 Predictive skill of the external drift Kriging estimate for all meteorological data for the central Cascades study area, 2000-2004. The left-hand panels shows the estimates *vs.* the observations for each variable, with the 1:1 line in solid gray, and a linear fit between observed and estimated meteorology as a broken dark gray line. The right-hand panels show the distributions of the residuals (seeTable 5.3).

Errors appeared to be normally distributed (Figure 5.10), but were spatially coloured with respect to hygric continentality. Mean absolute error (MAE) for the hygric maritime region was 1.6 °C for T_{min}, 2.0 °C for T_{max}, and 4.7 mm for P, whilst

MAE for the hygric continental region was 2.8 °C for T_{min}, 2.6 °C for T_{max} and 1.7 mm for *P*. These differences for all three variables were highly significant ($P < 0.001$) under t tests, despite the lower overall bias for T_{max}.

5.6 Discussion

We were able to produce temperature surfaces with good accuracy using Kriging with an external drift, achieving good correspondence with temperature observations (T_{min} r^2 = 82%, T_{max} r^2 = 94%). The errors for daily temperature variables were typically ~2 °C, and compared very favourably with the mean daily temperature range over the study area (~12 °C, σ = 3.8 °C). However, results for precipitation were generally poor under the Kriging algorithms (r^2 ~ 10%).

Of the Kriging algorithms implemented, the best results were always achieved through Kriging with an external drift. Increasing model complexity reduced errors. However, the added complexity of incorporating temporal covariance did not improve interpolation performance for any of the three variables (Table 5.2), and thus we reject H1.

Performance was linked to the number of available data points, with T_{max} (the variable with the most observations overall) performing best (Table 5.3). The poor performance of the geostatistical technique for regionalization of precipitation was most likely due to the highly left-skewed distribution of the data, which violated the underlying Gaussian assumption of the method (Deutsch and Journel, 1998). The improved linear fit of the temporally aggregated precipitation data (Figure 5.9) was a result of central limit theorem, with increasing normality of observations, and filtering

of temporal stochastic noise, for the less temporally continuous precipitation data, as reflected by the temporal range (φ_t = 2 days).

Geostatistical methods exist for interpolation of non-normally distributed data (Armstrong and Matheron, 1986a; Armstrong and Matheron, 1986b), based on analysis of the distribution by some anamorphosis function; e.g. decomposition by Hermite polynomials (Wackernagel, 1998). Distribution-free methods based on indicator Kriging of binary data codings at various thresholds have also been used (Cressie, 1991 pp. 281-283), but these have been criticized due to the 'destucturation' effect at higher threshold cutoffs (Armstrong and Matheron, 1986a), whereby spatial structure is artificially diluted by data scarcity at the extremes of the distribution. Further exploration of these techniques may prove fruitful for improving interpolation skill of precipitation.

It is clear from the results that to make informed estimates of meteorology for any reasonably sized space-time region, some knowledge of the effects of topography on climate is required. This is well illustrated by the consistent improvement in performance of KED over OK, which utilizes no topographic information (Table 5.2). The variability in the strength of these topographic relationships over time is noteworthy (Table 5.1), and it seems that any model attempting to reproduce the observed large-scale spatio-temporal trends requires some dynamic temporal trend component. The fixed slope trend model that was removed from the data prior to interpolation by SK was less able to reproduce the observed meteorology than a model fit on a day-by-day basis by the KED algorithm (Table 5.2). As such the best results were generally obtained from KED (although we note the poor performance of all Kriging algorithms for precipitation), which locally fitted the trend model as part of the interpolation scheme (Table 5.2). The superiority of KED was particularly true for T_{max}, with less sophisticated Kriging algorithms outperformed by the baseline IDW

interpolation. The temporal cycle in the thermal lapse gradient was likely due to adiabatic rise in the summer months 'diluting' the lapse response. Temporal cycling in the longitudinal precipitation gradient was likely due to the low precipitation rates uniformly observed across the region during the summer months.

Somewhat surprisingly, incorporation of temporal information did not improve interpolation skill for any of the Kriging algorithms implemented (Table 5.3). We believe this to be due to excessive smoothing of the estimate of the local mean. Increasing the size of the temporal window tends to filter off extreme events, which are poorly reproduced by least squares methods such as Kriging. Similarly, the use of very large numbers of spatial neighbours ($n > 32$) had a detrimental effect on interpolation skill, which we attribute to over-smoothing of the estimates. Too few neighbours produced poor interpolation results, and it seems that for all parameters, a search strategy comprising 16 – 32 spatial neighbours and no temporal window produced the best results. The optimal size of search strategy is a function of the data distribution, as the secondary information required to fit the external drift parameters must have an adequate range; Kriging variances increased for high elevations when conditioning data was from stations at lower elevations (Figure 5.8). Thus enough data are required to give a good range of secondary data values, but a small enough data range to prevent over smoothing of the trend function.

Bias in the estimates was found to be spatially coloured, and largely corresponded to the climatic regimes imposed by the topography. On the maritime side of the study region, lower temperature errors were found, whilst precipitation errors were higher than those observed at stations on the continental side of the Cascades. These contrasts can be explained by the general climatic differences between the two halves of the region. On the maritime side, the thermal inertia of the Pacific Ocean

provided thermal stability, reducing the variability of the temperature signals, and making them more ameliorable to interpolation. The higher degree of stochasticity in the thermal climate of the continental region made interpolation more challenging. With respect to precipitation, it is likely that the reduced frequency of rainfall events on the eastern side of the Cascades reduced error, because precipitation estimates were truncated at zero. Temporal bias for the temperature variables was weakly positive, equal to 6% of the mean of the daily observations for both T_{min} and T_{max}. The temporal bias in the precipitation fields is of much greater concern, with daily biases equal to 51% of the mean daily observations (Table 5.4).

Increasing temporal aggregation of the interpolation results generally led to decreased error and percent bias (Table 5.4, Figure 5.9), and thus we cannot reject H2. This is in accordance with the findings of an earlier study (Ashraf et al., 1997), showing that interpolation of monthly or annual averages was more successful than interpolation of daily data. This improvement is likely due to smoothing of extremes (which are poorly reproduces by LS estimators), and the reduction in stochastic errors over larger temporal units as errors 'cancel out'. Whereas Ashraf et al. (1997) examined error reduction when interpolating temporally aggregated data, our approach was to examine error reduction when aggregating daily estimates over various temporal supports (i.e. *post hoc* processing), in a way which more closely reflects error reduction over longer time scales for state variable models. These results indicate that instantaneous error may be diluted for phase lagged or integrating elements of the state vector (e.g. soil moisture) when implementing such surfaces in modelling applications.

While previous studies have found Kriging to be marginally better in terms of predictive skill (Thornton et al., 1997), simpler methods such as IDW are much easier and computationally cheaper to implement. Here we find a similar result for

temperature variables, but an increase in interpolation skill for precipitation when using simpler IDW methods.

The critical advantage of geostatistical methods is in providing spatial uncertainty estimates on the meteorological variables. The meteorological driver uncertainty can be propagated through the ecological or hydrological models (Williams et al 2001b) to determine the effects on model prediction uncertainty. Policy makers, land use managers and environmental stakeholders are increasingly reliant on landscape models for decision support. A detailed quantification of model uncertainty is vital in this regard. The geostatistical methods described here provide a means to locate areas of higher predictive uncertainty, and allow end users to take account of this information.

5.7 Conclusions

We reject hypothesis H1 that incorporating temporal information improves the regionalization of meteorological data, as we were unable to produce a statistically significant increase in interpolation skill when incorporating data from any temporal window larger than zero. We could not disprove hypothesis H2, that increasing temporal aggregation of meteorological variables reduces stochastic errors, and we observed a general improvement in interpolation skill with increasing temporal aggregation, with a corresponding reduction in bias.

Despite the poor performance of geostatistical techniques for describing the spatio-temporal variation of precipitation, temperature fields were well represented. We maintain that the techniques are useful, particularly in the provision of spatio-temporal uncertainty estimates. Issues of positive bias for the precipitation fields are serious, and limit the usefulness of the outputs. Further investigation into more suitable interpolation

schemes is necessary before usable high-resolution precipitation products can be provided.

The decrease in error associated with temporal aggregation indicates that errors in the daily meteorological surfaces may be unimportant for some ecological or hydrological processes with larger time constants, such as soil moisture, and this finding warrants further study.

5.8 Acknowledgements

We are grateful to Bev Law for access to meteorological data from the Metolius flux towers. The Oregon Climate Service provided useful information and data sources (available online: http://www.ocs.oregonstate.edu/index.html), especially Wayne Gibson and Chris Daly. Kind thanks also go to Isobel Clark, Pierre Goovaerts and Hans Wackernagel for advice during the development of the Edinburgh Space-Time Geostatistics software.

5.9 References

Armstrong, M. and Matheron, G., 1986a. Disjunctive kriging revisited 1. Mathematical Geology, 18(8): 711-728.

Armstrong, M. and Matheron, G., 1986b. Disjunctive kriging revisited 2. Mathematical Geology, 18(8): 729-742.

Ashraf, M., Loftis, J.C. and Hubbard, K.G., 1997. Application of geostatistics to evaluate partial weather station networks. Agricultural and Forest Meteorology, 84(3-4): 255-271.

Bertino, L., Evensen, G. and Wackernagel, H., 2002. Combining geostatistics and Kalman filtering for data assimilation in an estuarine system. Inverse Problems, 18(1): 1-23.

Bristow, K.L. and Campbell, G.S., 1984. On the relationship between incoming solar-radiation and daily maximum and minimum temperature. Agricultural and Forest Meteorology, 31(2): 159-166.

Cressie, N., 1990. The origins of kriging. Mathematical Geology, 22(3): 239-252.

Cressie, N.A.C., 1991. Statistics for Spatial Data. Wiley series in probability and mathematical statistics. Applied probability and statistics. Wiley, New York; Chichester, xx, 900 p pp.

Daly, C., Neilson, R.P. and Phillips, D.L., 1994. A statistical topographic model for mapping climatological precipitation over mountainous terrain. Journal of Applied Meteorology, 33(2): 140-158.

De Cesare, L., Myers, D.E. and Posa, D., 2001a. Estimating and modeling space-time correlation structures. Statistics & Probability Letters, 51(1): 9-14.

De Cesare, L., Myers, D.E. and Posa, D., 2001b. Product-sum covariance for space-time modeling: an environmental application. Environmetrics, 12(1): 11-23.

De Iaco, S., Myers, D.E. and Posa, D., 2001. Space-time analysis using a general product-sum model. Statistics & Probability Letters, 52(1): 21-28.

De Iaco, S., Myers, D.E. and Posa, D., 2003. The linear coregionalization model and the product-sum space-time variogram. Mathematical Geology, 35(1): 25-38.

Deutsch, C.V. and Journel, A.G., 1998. Gslib: Geostatistical software library and user's guide. Oxford University Press, New York.

Diggle, P.J., Ribero, P.J. and Cristensen, O.F., 2002. An introduction to model based geostatistics. In: J. Møller (Editor), Spatial Statistics and Computational Methods. Lecture Notes in Statistics. Springer-Verlag, New York.

Dimitrakopoulos, R.E., 1994. Geostatistics For the Next Century: International Forum: Selected Papers. Kluwer Academic.

Glassy, J.M. and Running, S.W., 1994. Validating diurnal climatology logic of the mt-clim model across a climatic gradient in Oregon. Ecological Applications, 4(2): 248-257.

Gneiting, T., 2002. Nonseparable, stationary covariance functions for space-time data. Journal of the American Statistical Association, 97(458): 590-600.

Gneiting, T. and Schlather, M., 2004. Stochastic models that separate fractal dimension and the Hurst effect. Siam Review, 46(2): 269-282.

Goovaerts, P., 1997. Geostatistics for Natural Resources Evaluation. Applied geostatistics series. Oxford University Press, New York; Oxford, xiv,483p pp.

Goovaerts, P., 1999. Geostatistics in soil science: state-of-the-art and perspectives. Geoderma, 89(1-2): 1-45.

Goovaerts, P., 2000. Geostatistical approaches for incorporating elevation into the spatial interpolation of rainfall. Journal of Hydrology, 228(1-2): 113-129.

Goward, S.N., Waring, R.H., Dye, D.G. and Yang, J.L., 1994. Ecological remote-sensing at otter - satellite macroscale observations. Ecological Applications, 4(2): 322-343.

Heuvelink, G.B.M. and Webster, R., 2001. Modelling soil variation: past, present, and future. Geoderma, 100(3-4): 269-301.

Hudson, G. and Wackernagel, H., 1994. Mapping temperature using kriging with external drift - theory and an example from Scotland. International Journal of Climatology, 14(1): 77-91.

Hungerford, R.D., Nemani, R.R., Running, S.W. and Coughlan, J.C., 1989. MTCLIM: a mountain microclimate simulation model. US For. Serv. Res. Pap. INT-414.

Hutchinson, M.F., 1995. Interpolating mean rainfall using thin-plate smoothing splines. International Journal of Geographical Information Systems, 9(4): 385-403.

Isaaks, E.H. and Srivastava, R.M., 1989. Applied Geostatistics. Oxford University Press, New York; Oxford, xix, 561 p pp.

Jones, R.G. et al., 2004. Generating High Resolution Climate Change Scenarios Using PRECIS. Met Office Hadley Centre, Exceter, UK, 40 pp.

Jost, G., Heuvelink, G.B.M. and Papritz, A., 2005. Analysing the space-time distribution of soil water storage of a forest ecosystem using spatio-temporal kriging. Geoderma, 128(3-4): 258-273.

Karrasch, H., 1973. Microclimatic studies in the Alps. Arctic and Alpine Research, 5(3): A55-A63.

Kyriakidis, P.C. and Journel, A.G., 1999. Geostatistical space-time models: A review. Mathematical Geology, 31(6): 651-684.

Kyriakidis, P.C. and Journel, A.G., 2001a. Stochastic modeling of atmospheric pollution: a spatial time-series framework. Part I: methodology. Atmospheric Environment, 35(13): 2331-2337.

Kyriakidis, P.C. and Journel, A.G., 2001b. Stochastic modeling of atmospheric pollution: a spatial time-series framework. Part II: application to monitoring monthly sulfate deposition over Europe. Atmospheric Environment, 35(13): 2339-2348.

Law, B.E., Sun, O.J., Campbell, J., Van Tuyl, S. and Thornton, P.E., 2003. Changes in carbon storage and fluxes in a chronosequence of ponderosa pine. Global Change Biology, 9(4): 510-524.

Law, B.E., Thornton, P.E., Irvine, J., Anthoni, P.M. and Van Tuyl, S., 2001. Carbon storage and fluxes in ponderosa pine forests at different developmental stages. Global Change Biology, 7(7): 755-777.

Law, B.E. et al., 2004. Disturbance and climate effects on carbon stocks and fluxes across Western Oregon USA. Global Change Biology, 10(9): 1429-1444.

Law, B.E. and Waring, R.H., 1994. Combining remote-sensing and climatic data to estimate net primary production across Oregon. Ecological Applications, 4(4): 717-728.

Mcbratney, A.B. and Webster, R., 1986. Choosing functions for semi-variograms of soil properties and fitting them to sampling estimates. Journal of Soil Science, 37(4): 617-639.

Murray, F.W., 1967. On the computation of saturation vapor pressure. Journal of Applied Meteorology, 6: 203-204.

O'Sullivan, D. and Unwin, D., 2003. Geographic Information Analysis. John Wiley and Sons, Inc., Hoboken, New Jersey.

Pinheiro, J.C. and Bates, D.M., 2000. Mixed-Effects Models in S and S-PLUS. Statistics and computing. Springer, New York, xvi, 528 p. pp.

Prihodko, L. and Goward, S.N., 1997. Estimation of air temperature from remotely sensed surface observations. Remote Sensing of Environment, 60(3): 335-346.

Rabus, B., Eineder, M., Roth, A. and Bamler, R., 2003. The shuttle radar topography mission - a new class of digital elevation models acquired by spaceborne radar. Isprs Journal of Photogrammetry and Remote Sensing, 57(4): 241-262.

Running, S.W., 1994. Testing forest-bgc ecosystem process simulations across a climatic gradient in Oregon. Ecological Applications, 4(2): 238-247.

Running, S.W., Nemani, R.R. and Hungerford, R.D., 1987. Extrapolation of synoptic meteorological data in mountainous terrain and Its use for simulating forest evapotranspiration and photosynthesis. Canadian Journal of Forest Research-Revue Canadienne De Recherche Forestiere, 17(6): 472-483.

Taylor, G.H. and Hannan, C., 1999. The Climate of Oregon: From Rainforest to Desert. Oregon State University Press, Corvallis.

Thiessen, A.H., 1911. Precipitation averages for large areas. Monthly Weather Review, 39(7): 1082-1089.

Thornton, P.E. and Running, S.W., 1999. An improved algorithm for estimating incident daily solar radiation from measurements of temperature, humidity, and precipitation. Agricultural and Forest Meteorology, 93(4): 211-228.

Thornton, P.E., Running, S.W. and White, M.A., 1997. Generating surfaces of daily meteorological variables over large regions of complex terrain. Journal of Hydrology, 190(3-4): 214-251.

Tobler, W.R., 1970. A computer movie simulating urban growth in the Detroit region. Economic Geography, 46: 234-240.

Van Meirvenne, M. and Goovaerts, P., 2001. Evaluating the probability of exceeding a site-specific soil cadmium contamination threshold. Geoderma, 102(1-2): 75-100.

Van Tuyl, S., Law, B.E., Turner, D.P. and Gitelman, A.I., 2005. Variability in net primary production and carbon storage in biomass across Oregon forests - an assessment integrating data from forest inventories, intensive sites, and remote sensing. Forest Ecology and Management, 209(3): 273-291.

Wackernagel, H., 1998. Multivariate Geostatistics: An Introduction With Applications. Springer, Berlin; London, xiv,291p pp.

Waring, R.H. and Peterson, D.L., 1994. Oregon transect ecosystem research (otter) project. Ecological Applications, 4(2): 210-210.

Williams, M., Law, B.E., Anthoni, P.M. and Unsworth, M.H., 2001a. Use of a simulation model and ecosystem flux data to examine carbon-water interactions in ponderosa pine. Tree Physiology, 21(5): 287-298.

Williams, M. et al., 2001b. Primary production of an arctic watershed: An uncertainty analysis. Ecological Applications, 11(6): 1800-1816.

Williams, M., Schwarz, P.A., Law, B.E., Irvine, J. and Kurpius, M.R., 2005. An improved analysis of forest carbon dynamics using data assimilation. Global Change Biology, 11(1): 89-105.

6. Uncertainty in predictions of forest carbon dynamics – separating driver error from model error

Running Title: Partitioning Sources of Model Error

L. Spadavecchia[1], M Williams[1*], B Law[2]

[1] School of GeoSciences, Institute of Atmospheric and Environmental Science, University of Edinburgh, Edinburgh EH9 3JN, UK.

[2] Oregon State University,

* Correspondence to Mathew Williams, mat.williams@ed.ac.uk.

KEY WORDS: Spatio-temporal geostatistics, geostatistical simulation, data assimilation, product-sum covariance model, process based modelling, carbon dynamics

* Corresponding Author

6.1 Declaration

The following chapter is intended for submission to *Global Change Biology*. I conducted all the analyses reported, except for the production of the parameter ensemble, which was undertaken by M. Williams using his Ensemble Kalman Filter code. All of the model runs reported were produced using a version of the DALEC model coded by me with reference to M. Williams' original code. I wrote all the body text, except for the sections *Modelling daily exchanges of C and water* (6.4.2) and *DALEC parameterisation* (6.5.1), which were provided by M. Williams. M. Williams also provided comments and made editorial changes to the text.

6.2 Abstract

We present an analysis of the relative magnitude and contribution of parameter and driver uncertainty to the uncertainty of estimates of net carbon fluxes. Model parameters may be difficult or impractical to measure, whilst driver fields are rarely complete, with data gaps due to sensor failure. Parameters are generally derived through some optimisation method, whilst driver fields may be interpolated from available data sources. For this study, we used data from a young Ponderosa pine stand at Metolius, Central Oregon, and a simple model of coupled carbon and water fluxes (DALEC). We retrieved a set of 375 acceptable parameterisations *via* an Ensemble Kalman filter, which used observations of net C exchange to retrieve model parameters. We generated an ensemble of meteorological driving variables for the site, consistent with the spatio-temporal autocorrelations inherent in the observational data *via* geostatistical simulation. The simulated meteorological dataset was propagated through the model to derive the uncertainty on the CO_2 flux resultant from driver uncertainty typical of spatially extensive modelling studies. Furthermore, we partitioned the model uncertainty between temperature and precipitation, to examine which driver contributes the most to the net flux uncertainty. Our results indicated that driver uncertainty was relatively small (~10 % of the total net flux), whilst parameterisation uncertainty was larger, ~50 % of the total net flux. The largest source of driver uncertainty was due to temperature (8% of the total flux). The combined effect of parameter and driver uncertainty was ~53 % of the total net flux. We discuss issues of bias in contributing to flux errors, and identified bias problems with both temperature and precipitation data. We recommend better constraint of temperature fields when attempting regional to catchment scale modelling,

but suggest that parameterisation issues are of greater importance to constrain the CO_2 flux, presenting novel challenges for regionalised modelling of C dynamics.

6.3 Introduction

Modern catchment scale studies of environmental phenomena commonly employ some sort of modelling approach for extrapolation and prediction (Law et al., 2001a; Running, 1994; Runyon et al., 1994; Williams et al., 2001b; Williams et al., 2005b). In general, the practitioner is faced with the problem of upscaling detailed observations made at a small number of sites to a wider area, due to the expense and technical difficulties associated with direct observation (Thornton et al., 1997; Williams et al., 2005b). Process based models formalise knowledge of ecological processes, and allow integration of observations at various scales to be incorporated into regional analyses (Canham et al., 2003; Heuvelink and Webster, 2001; Williams et al., 2005b). Such models typically require initial estimates of rate parameters and surface characteristics, along with a set of meteorological driving variables, from which estimates of the state vector are derived.

The situation is complicated by the difficulty in measuring and setting parameters, and finding adequate data to drive the model. On one hand, parameters may be difficult or impossible to measure in practice, particularly if the rates of the processes they represent are slow, with time constants greater than a few months. On the other hand, sourcing adequate data to drive the model over the required spatio-temporal extent may be difficult due to sparse sensor networks and missing observations resultant from sensor failure etc. (Thornton et al., 1997).

In general we rely on some optimisation procedure to infer appropriate parameter sets (e.g. Klemedtsson et al., 2007; Williams et al., 2005b), and utilise interpolation schemes to gap-fill meteorological drivers (e.g. Daly et al., 1994; Goovaerts, 2000; Hudson and Wackernagel, 1994; Hungerford et al., 1989; Running et al., 1987; Thiessen, 1911; Thornton et al., 1997). The errors resultant from these activities are difficult to quantify, and in the case of driver interpolation rarely explored (Fuentes et al., 2006).

Parameter errors can be explored through a variety of techniques, usually based on Monte Carlo analyses: Parameters may be perturbed by a series of fixed percentages to probe the effect on the state vector (e.g. Oijen et al., 2005; Williams et al., 2005b). More formally, we may chose to parameterise the model using a Bayesian framework, and directly sample parameter error from the posterior distribution of the parameter set computationally (Kennedy et al., 2008; Klemedtsson et al., 2007; Verbeeck et al., 2006). Here we explore an alternative Bayesian technique, whereby an *a priori* parameter set is updated by comparing the model trajectory with observations via data assimilation. This technique has been popular amongst meteorologists and oceanographers (Eknes and Evensen, 2002; Evensen, 1994), and confers the advantage of balancing the observation and model error in an optimal sense (Maybeck, 1979).

Quantification of error resultant from meteorological driver uncertainty may be assessed through geostatistical simulation techniques (Fuentes et al., 2006; Goovaerts, 2001). We generate a moderately large ($n \sim 1000$) ensemble of equi-probable meteorological fields from the available observations, honouring the spatio-temporal autocorrelation structure of the data. The error magnitude of the state vector is quantified after propagating the ensemble through the model *via* Monte Carlo analysis of the n model estimates (e.g. Fuentes et al., 2006).

In a previous paper we illustrated the issue of driver error inflation with data scarcity when utilizing geostatistical upscaling of meteorological drivers over a moderately large spatio-temporal extent (Spadavecchia and Williams, In review). However, it is not clear how errors in the meteorological fields affect the state vector, especially in the light of error reduction over increasing temporal support (Spadavecchia and Williams, In review): Processes which respond instantaneously to the driver fields are likely to have larger error magnitudes than those which integrate driving variables over time. As a result, driver errors, which in some cases are appreciable (Spadavecchia and Williams, In review), may in fact cancel out over the model run.

We present an analysis of the sources and magnitude of model errors using DALEC; a simple process-based ecosystem model of coupled carbon and water dynamics. The model is multi-output, supplying estimates of C stocks, soil moisture and fluxes of carbon and water on a daily time-step. We parameterise the model for a well-sampled Ponderosa pine forest at Metolius, Central Oregon *via* the Ensemble Kalman filter (EnKF) (Evensen, 2003), and sample the uncertainty in the net ecosystem carbon exchange (NEE) associated with parameter uncertainty. We then replace the observed meteorology with an ensemble of geostatistical simulations conditioned on observations surrounding the study site, and run the parameterised model to sample the resultant uncertainty in NEE due to driver uncertainty. Finally, we undertake a full uncertainty analysis *via* Monte Carlo sampling of both parameter and driver sets to examine the cumulative uncertainty of the NEE.

The objectives of this paper are to examine and compare the magnitude of model error resultant from parameter uncertainty and driver uncertainty on a fine temporal support of one day. Furthermore, we intend to characterise the error magnitude resultant from uncertainty in a variety of daily driver fields, to diagnose

which fields are critical to constrain model predictions. In doing so we aim to address the following hypotheses:

- **H1:** Driver error will be larger than the parameter error, since the likely range of parameters are well constrained locally, whilst meteorological simulations are conditioned on patchy, spatially dispersed data.
- **H2a:** Precipitation will contribute most to model uncertainty: Precipitation has the largest interpolation error, and ecosystem production is drought-limited in the study region (Law et al., 2001a; Van Tuyl et al., 2005).
- **H2b:** Temperature will contribute most to model uncertainty: Errors associated with precipitation will average out over time, as plant response to precipitation is resultant from drought. Drought integrates precipitation uncertainty over time through soil moisture content, so instantaneous temperature effects on heterotrophic processes will dominate the NEE error signal.

6.4 Methods

6.4.1 Study Site

The Metolius young Ponderosa Pine site is located on a private forestry concession near the Metolius Natural Research area (44°26'N, 121°34'W, elevation ~ 1165m) (Figure 6.1). The site was clear-cut in the late 1980s, and since then has been allowed to naturally regenerate, with some thinning in 2002. The canopy layer is exclusively comprised of *Pinus ponderosa*, with an understory of *Purshia tridentata* and *Pteridium aquilinum*, and a herb layer of *Fragaria vesca*. From 2000-2002 the site had a continuously functioning eddy covariance system, forming part of the Ameriflux observational network. Fluxes were measured at ~9m above the canopy. The site is

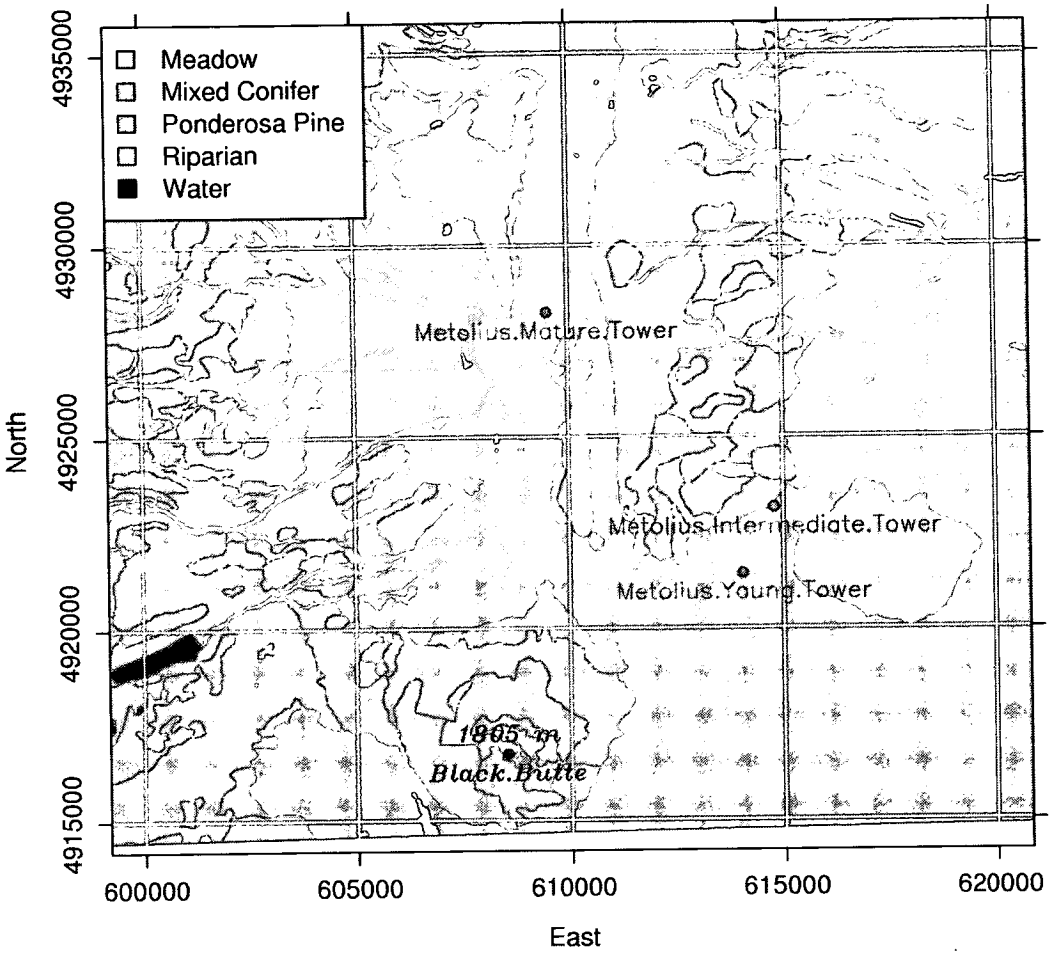

Figure 6.1 Metolius Young Ponderosa pine site and surrounding area, Deschutes County, Oregon. Two other Ameriflux towers are situated to the north. The area is extensively forested with Ponderosa pine and mixed coniferous vegetation (vegetation data courtesy of USDA forest service: Sisters Ranger Station, Sisters, Oregon).

characterised by warm dry summers and wet cool winters. Diurnal temperature variation can be high (1.5 – 18.6 °C), and the site is prone to drought (mean annual precipitation = 402 mm, mean number of dry days = 224). Two other flux towers are positioned to the north of the site, one of which (Metolius intermediate Ponderosa Pine site) has been in continuous operation since 2002. No flux data from these towers is employed in this study, although Meteorological observations from the intermediate tower are used: The locations are indicated primarily to provide context with earlier studies.

6.4.2 Modelling daily exchanges of C and water

6.4.2.i Canopy processes

The model consists of a 'big leaf' photosynthesis (GPP) and evapotranspiration (ET) model (Aggregated Canopy Model, ACM: Williams et al., 1997) coupled to a module that tracks the allocation and mineralisation of carbon, and a module that tracks the dynamics of soil moisture. This coupled model is henceforth referred to as the data assimilation linked ecosystem carbon model, or DALEC model (Figure 6.2).

The ACM calculates GPP and ET as a function of vegetation properties (leaf area index, and foliar N for GPP), meteorology (maximum daily temperature, daily temperature range, maximum daily vapour pressure deficit, total daily irradiance) and soil properties (soil hydraulic resistance and soil water potential). The ACM model was parameterised from locally calibrated SPA predictions of GPP and ET (Schwarz et al 2004), using the approach laid out in Williams et al. (1997).

6.4.2.ii C cycling

The carbon module apportions the predicted gross primary production (GPP) into autotrophic respiration and the growth of plant C pools (DALEC: Williams et al., 2005b) and then tracks additions to and mineralisation of litter and soil organic matter (SOM). DALEC requires the specification of ten carbon parameters to control the fate of C in the ecosystem. These parameters relate to the rate of decomposition, fraction of GPP respired, fraction of NPP allocated to foliage, fraction of remaining NPP allocated

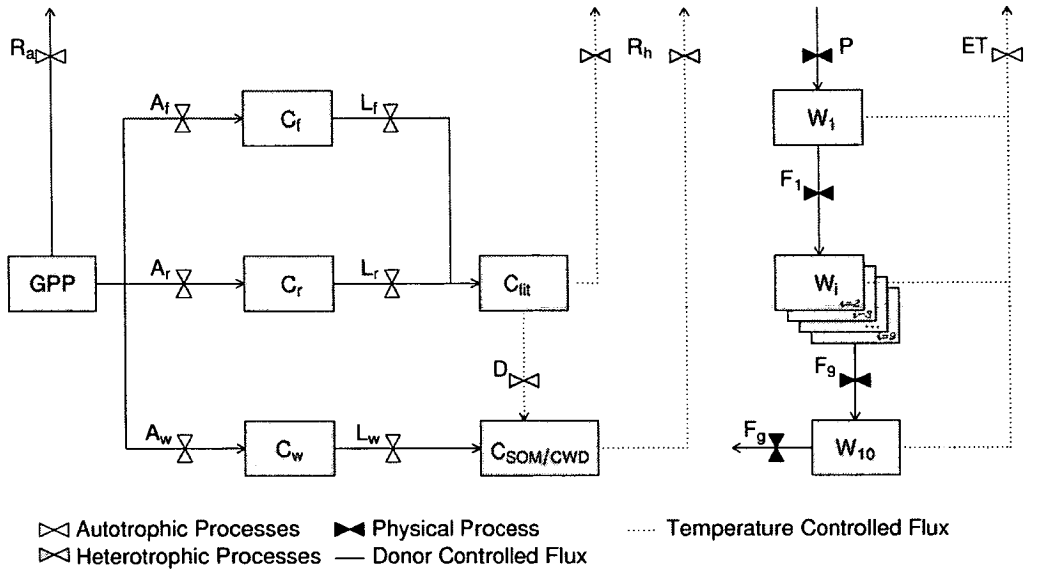

Figure 6.2 DALEC C and Water dynamics model. Pools are shown as grey boxes, whilst fluxes are represented as arrows. The left hand plot illustrates the C module: GPP (gross primary production) is allocated to foliage (f), roots (r) or woody (w) material. Allocation fluxes are marked A, whilst losses are marked L. C loss is through respiration fluxes (R), split between autotrophic (a) and heterotrophic (h) sources. The right panel details the flow of water through the model: Precipitation (P) is allocated between 10 soil water layers ($W_{1...10}$). Vertical drainage flows ($F_{1...9}$) occur when soil layers are saturated. Water may be lost through gravitational drainage (F_9) to groundwater or evapotranspiration (ET).

to fine roots, turnover rates of foliage, wood ,fine roots, litter and SOM, and the temperature sensitivity of litter and SOM mineralisation. DALEC also requires an initial estimate of the C stock present in five pools; foliage, fine roots, woody stems, litter and SOM (see Williams et al., 2005b).

The model takes daily inputs of minimum temperature (T_{min}), maximum temperature (T_{max}), and precipitation (P). Temperature observations are converted to daily average temperature (T_a), maximum daily vapour pressure deficit (VPD), and solar radiation (RAD) using well-tested relationships (Running et al., 1987; Thornton et al., 1997). VPD is estimated using Murray's formula (Murray, 1967), whilst RAD is predicted using the Allen model (Allen, 1997). Details of these models are provided in the appendix.

6.4.2.iii Modelling soil water dynamics and drought stress

Based on intensive hourly modelling studies at the site (Williams et al. 2001, Schwarz et al 2004), we generated a simple daily model of soil water dynamics. The model tracks water inputs and outputs in a 10 layer 'bucket' model extending to 3 m in depth. Moisture is drained from soil layers when water content exceeds field capacity. We used relationships from Saxton et al (1986) and local measurements of soil texture to determine porosity and field capacity. Soil hydraulic resistance was determined based on soil texture, root biomass and water fraction in each soil layer (Williams et al 2001). Soil water potential (Ψ_s) was generated from a locally determined empirical relationship (Ψ_s=-1.74+3.997θ) on soil water fraction (θ). Rooting depth was determined as a function of root biomass using data from nearby ponderosa pine stands (Schwarz et al 2004). More details of this approach are provided in Fisher et al. (In press).

6.4.3 Data

6.4.3.i Flux Observations

We used three years of data from the Metolius young Ponderosa pine plot (Law et al., 2001a; Law et al., 2001b) to parameterise DALEC. The data consist of records of net ecosystem exchange (NEE), total ecosystem respiration (Re), evapotranspiration (ET) and a set of meteorological observations, sampled at the daily time-step. Direct observation of T_{min}, T_{max}, T_a, P, VPD and RAD were made simultaneously with the flux data.

There were 684 daily NEE observations over the 1096 days from 2000-2. Gaps in the data resulted from sensor failure and filtering to remove observations with low friction velocity (u^*), or physically implausible magnitudes ($|F_c| > 25$ μmol m^{-2} sec^{-1}).

6.4.3.ii Canopy Density Observations

In order to constrain the parameterisation of DALEC, we utilised observations of the leaf area index (LAI) of the forest canopy. Observations were made at four times during the three-year period, using an LAI-2000 plant canopy analyser (LI-COR, Lincoln, NE, USA). Observations were collected on a 10 m square grid, and were corrected for clumping at the needle, shoot and stand levels (Law et al., 2001c; Law et al., 2001d). These observations were related to the model foliar carbon estimate *via* direct measurements of the specific leaf mass from foliage samples, see Williams (2005) for further details.

We augmented this set of observations with retrievals of LAI from the MODIS satellite (Knyazikhin et al., 1998; Myneni et al., 2002), with a sampling frequency of eight days. We filtered the MODIS LAI observations using the provided QC flags, to reject data from cloudy days or aberrant spectral signatures (Knyazikhin et al., 1998).

6.4.3.iii Meteorological Observations

In order to generate meteorological simulations at the study site, we sourced the 13 closest meteorological monitoring stations with data available for the period 2000-2002 (Table 6.1, Figure 6.3). These stations were selected so that there would be a minimum of 8 T_{min}, T_{max}, and P observations per day on which to condition meteorological simulations. Observations were filtered such that the values would not exceed the state extremes for Oregon (National Oceanic and Atmospheric Administration (NOAA), Silver Spring, Maryland, USA). Meteorological records for stations further than 25km away were also sourced to examine the effect of data scarcity on NEE uncertainty Figure 6.3.

Table 6.1 Locations and data summary for surrounding meteorological stations

Name	East*	North*	Elevation*	Network	Records Began	Distance to Site†	T_{min} °C		T_{max} °C		Precip. mm‡	
Belnap Springs	577110	4905648	677	COOP	1960	40	2.8	(4.8)	16.3	(10.5)	6.7	(15.2)
Marion Forks Hatchery	583329	4939053	804	COOP	1948	35	2.0	(4.6)	15.1	(9.8)	4.3	(8.8)
Redmond FAA Airport	647656	4903155	935	COOP	1948	38	0.3	(6.2)	17.5	(9.7)	0.7	(2.2)
Santiam Junction	582241	4920523	1121	COOP	1986	32	-1.0	(5.1)	13.0	(10.1)	5.3	(11.5)
Sisters	615665	4906216	966	COOP	1958	15	-0.3	(5.9)	16.1	(10.5)	0.8	(3.0)
Colgate	610384	4907884	1010	RAWS	1985	14	0.1	(5.6)	17.8	(10.2)	0.9	(3.5)
Haystack	649826	4923610	985	RAWS	1985	36	3.9	(6.5)	16.0	(9.9)	0.4	(2.2)
Metolius Arm	610194	4942510	1029	RAWS	1991	21	3.4	(6.2)	15.5	(10.3)	1.4	(5.0)
Pebble	580919	4898658	1076	RAWS	1991	40	2.9	(5.3)	15.4	(9.1)	3.4	(7.9)
Marion Forks	582030	4937184	1111	SNOTEL	1981	36	2.4	(4.6)	14.0	(10.5)	4.4	(9.7)
Santiam Junction	584894	4920557	1165	SNOTEL	1979	29	0.0	(5.1)	13.6	(9.4)	4.4	(9.2)
Hogg Pass	590225	4918777	1439	SNOTEL	1980	24	0.5	(5.8)	11.5	(9.6)	5.1	(9.8)
Otter Intermediate Tower	614792	4923138	1253	AMERIFLUX	2001	2	4.1	(7.1)	12.4	(8.9)	0.5	(1.9)

Mean meteorological observations. Standard deviations indicated in parentheses.
* Coordinates in meters UTM zone 10, WGS84 datum.
† Distance to Metolius Young Ponderosa pine site (km).
‡ Daily mean precipitation (mm); insufficient data at some sites for reliable annual averages.

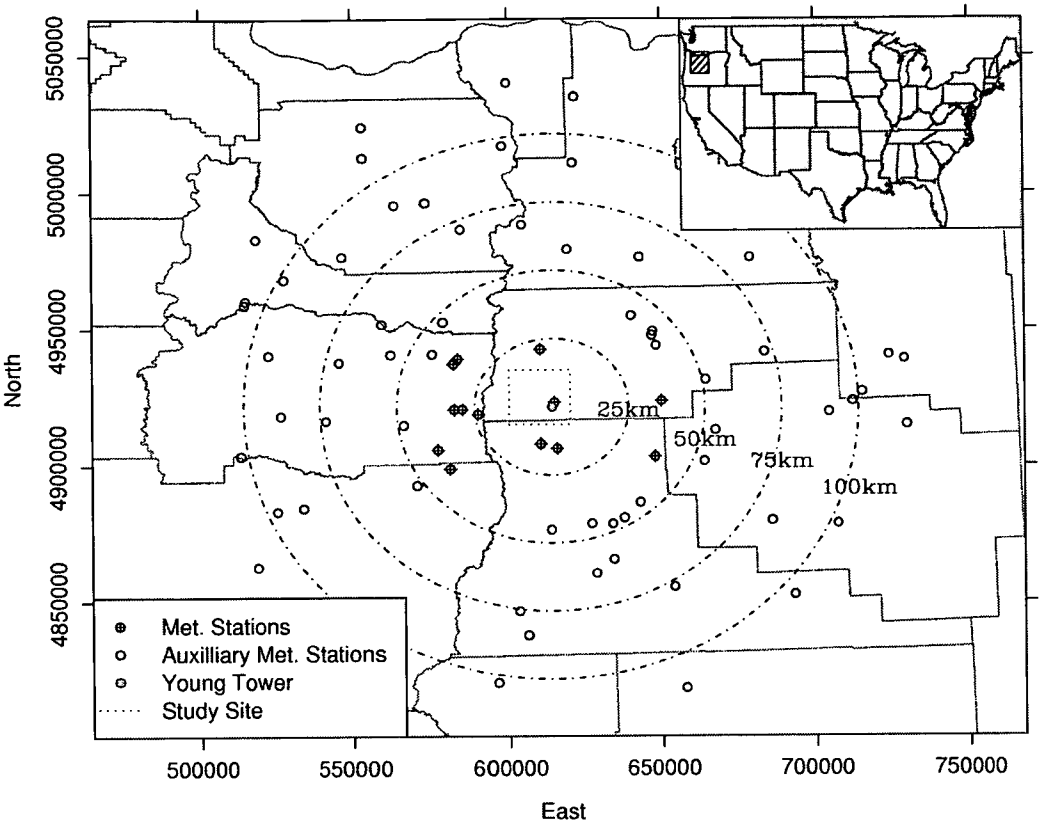

Figure 6.3 Meteorological monitoring stations surrounding the Metolius Young Ponderosa pine site, indicated as a gray point. Crosshairs represent the 13 core stations used for the simulations, whilst auxiliary stations at increasing distance from the study site are indicated as open circles. Light grey lines indicate county boundaries. The extent of figure 6.1 is indicated as a broken black rectangle, which lies in Deschutes County.

6.4.4 DALEC Parameterisation

Many of the parameters associated with the processes of photosynthesis, evapotranspiration and soil water physics have been derived from the literature or from previous research at the study site (Schwarz et al., 2004; Williams et al., 2001a; Williams et al., 2005a). The most uncertain parameters are the 10 associated with respiration, turnover and allocation of C among plant and soil pools. We add an eleventh parameter

to these, the parameter from the ACM GPP model that relates foliar N content to photosynthetic capability, to include an estimate of uncertainty in the GPP calculations.

We used an Ensemble Kalman filter (EnKF, Williams et al 2005) to estimate the likely distributions for these uncertain parameters. The EnKF combines a model of a system (i.e. DALEC) with observations of that system over time (i.e. NEE and LAI observations). The model generates predictions of the state vector (C pools and fluxes, soil moisture and water fluxes) for each time step. NEE and LAI predictions are then compared with independent observations. Based on an assessment of model forecast and observational uncertainty, the predicted NEE and LAI are adjusted. The model error covariance matrix, as determined in the EnKF, is then used to adjust the full state vector accordingly.

We adjusted the EnKF approach used in Williams et al. (2005) from a state estimation problem to a parameter estimation problem. We added the 11 model parameters to the state vector supplied to the EnKF. We set the model error on the fluxes and pools of C and water to relatively low values (0.01%) compared to the uncertainty on the 11 parameters (0.2%). The error on the NEE observations was estimated at 0.7 gC m^{-2} d^{-1} and on LAI estimates at 10%. The number of ensembles used was set at 400.

The initial EnKF analysis used parameter estimates from an earlier study (Williams et al. 2005). After the initial analysis, we used the final parameter estimates to reinitialise the parameters, and ran the EnkF again. We repeated this process again, at which point the parameter ensembles stabilised.

We then ran the model with each element of the acceptable parameter ensemble in turn to evaluate the effect of parameter uncertainty on the NEE estimate (experiment 1).

6.4.5 Meteorological Simulation

In order to quantify the uncertainty of interpolated driving variables at the Metolius site, we employed the sequential Gaussian simulation (SGS) (Goovaerts, 1997), which may be regarded as an extension of the commonly used Kriging technique (e.g. Ashraf et al., 1997; Goovaerts, 2000; Hudson and Wackernagel, 1994; Spadavecchia and Williams, In review).

Kriging estimates represent the most likely value of the estimate given the surrounding observations, based on a probabilistic model. Kriging variances produce a valid estimate of uncertainty for the estimate when taken in isolation, but they are less useful for assessing the uncertainty of the regionalisation as a whole (Goovaerts, 1997). SGS expands on Kriging by drawing equally possible realisations of the whole field from the probabilistic model, preserving the surface roughness of the estimated field and avoiding the characteristic smoothing effect of Kriging (Deutsch and Journel, 1998; Goovaerts, 1997; Goovaerts, 1999; Goovaerts, 2001). The outcome is a set of equally likely estimates of the meterology at the study side given our limited knowledge.

We modelled the autocorrelation structure of the T_{min}, T_{max} and P observations at the meteorological stations by calculating their empirical semivariograms. The semivariogram γ quantifies the dissimilarity between pairs of observations separated by increasing spatiotemporal lag distances:

$$\gamma(h_u,h_t)=\frac{1}{2N(h_u,h_t)}\sum_{i=1}^{N(h_u,h_t)}\left[z(u_i,t_i)-z(u_i+h_u,t_i+h_t)\right]^2 \qquad \textbf{(6.1)}$$

Where h_u and h_t are the separation lags in space and time respectively, $z(u,t)$ is the observed variable at a given spatio-temporal coordinate, $N(h_u,h_t)$ is the number of pairs in the lag.

We selected and fit permissible semivariance models (Christakos, 1984; Gringarten and Deutsch, 2001; Mcbratney and Webster, 1986) to summarise the empirical semivariograms. The spatial and temporal semivariogram models were then combined using the product-sum covariance model of De Cesare et al. (De Cesare et al., 2001; De Iaco et al., 2001).

Simulation proceeded as follows:

1. Initialise a random visiting schedule for the grid of G locations, with a data heap of n observations.
2. Visit the i^{th} node of the grid and estimate the mean and variance *via* Kriging conditioned on the values in the data heap.
3. Draw a random value from the Gaussian distribution of the node, defined by the Kriging estimate (mean) and Kriging variance. The resultant value was the SGS estimate z_i^*.
4. The realization z_i^* was then treated as an observation for subsequent estimates, and added to the data heap ($n+i$ conditioning data).
5. Iterate from 2 until all grid locations were visited ($i=G$).

As in all geostatistical techniques, it is possible to incorporate covariates into the simulations: We specified a linear lapse relationship between elevation and temperature, and a longitudinal gradient in precipitation, the parameters of which were estimated as part of the simulation process, via the external drift method (Hudson and Wackernagel, 1994; Wackernagel, 1998).

6.4.6 Partitioning Driver Uncertainty

We generated 1000 simulations of T_{min}, T_{max} and P at the Metolius site for the full three years of the study conditioned on data from the 8 closest spatial neighbours over a temporal window of ± 10 days (88 observations) *via* SGS. Meteorological observations at the site were excluded so as to explore the uncertainty resultant from modelling C dynamics over sparsely sampled regions. We then ran the parameterised model with each of the 1000 simulations in turn, to inspect the variability in the predicted NEE ensemble. We then ran three experiments; (2.i) locally observed temperatures, *VPD* and *RAD* with simulated precipitation, (2.ii) locally observed precipitation with simulated temperatures, *VPD* and *RAD* (2.iii) locally observed precipitation, *VPD* and *RAD* with simulated temperatures. Experiment 2.iii was devised to decouple the NEE uncertainty resultant from deriving *VPD* and *RAD* from temperature within the model. Finally, having generated a parameter ensemble and 1000 equi-probable meteorologies, we generated a sample of 1000 parameter and meteorology permutations to test the combined effect of parameter and driver uncertainty on the model (experiment 3).

In order to test H2 we compared the precipitation regime of the data with the simulated rainfall trajectories. We calculated the number of days since a precipitation event ($n_{P=0}$) for the 1000 simulations generated in experiment 2.i. We subtracted the number of days since a precipitation event in the local observations from $n_{P=0}$ to generate a metric of drought (Δ_P). We considered data where Δ_P was positive (i.e. simulations with longer dry spells than observed in the data) to examine the effect of drought on the uncertainty of the NEE trajectory.

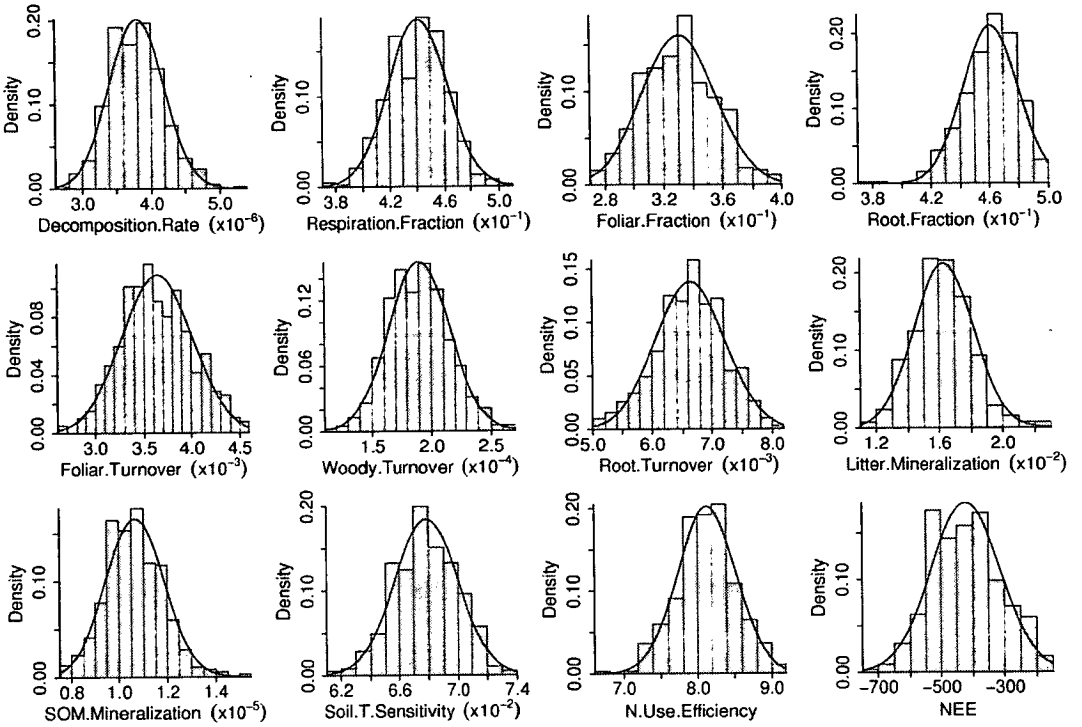

Figure 6.4 Marginal parameter distributions retrieved from an ensemble of 375 elements derived from the Ensemble Kalman filter and passing a goodness-of-fit test against the observed NEE time series 2000-2002. The resultant total net ecosystem exchange (NEE gC m^{-2}) over three years is also indicated.

6.4.7 Sparsity of Meteorological Conditioning Data

Given that interpolation uncertainty is related to the distance to the nearest neighbours (Spadavecchia and Williams, In review), we investigated the effect of increasing data sparsity by conditioning simulations on data from increasing search radii (Figure 6.3), ignoring weather stations closer than the threshold distances of 25, 50, 75 and 100 km. In each case, the closest 4 stations beyond the threshold distance were used to condition the simulations. We ran the model with each of these meteorological ensembles to test the robustness of the comparison of meteorological and parameterisation uncertainties on the uncertainty of the final NEE analysis (experiment 4).

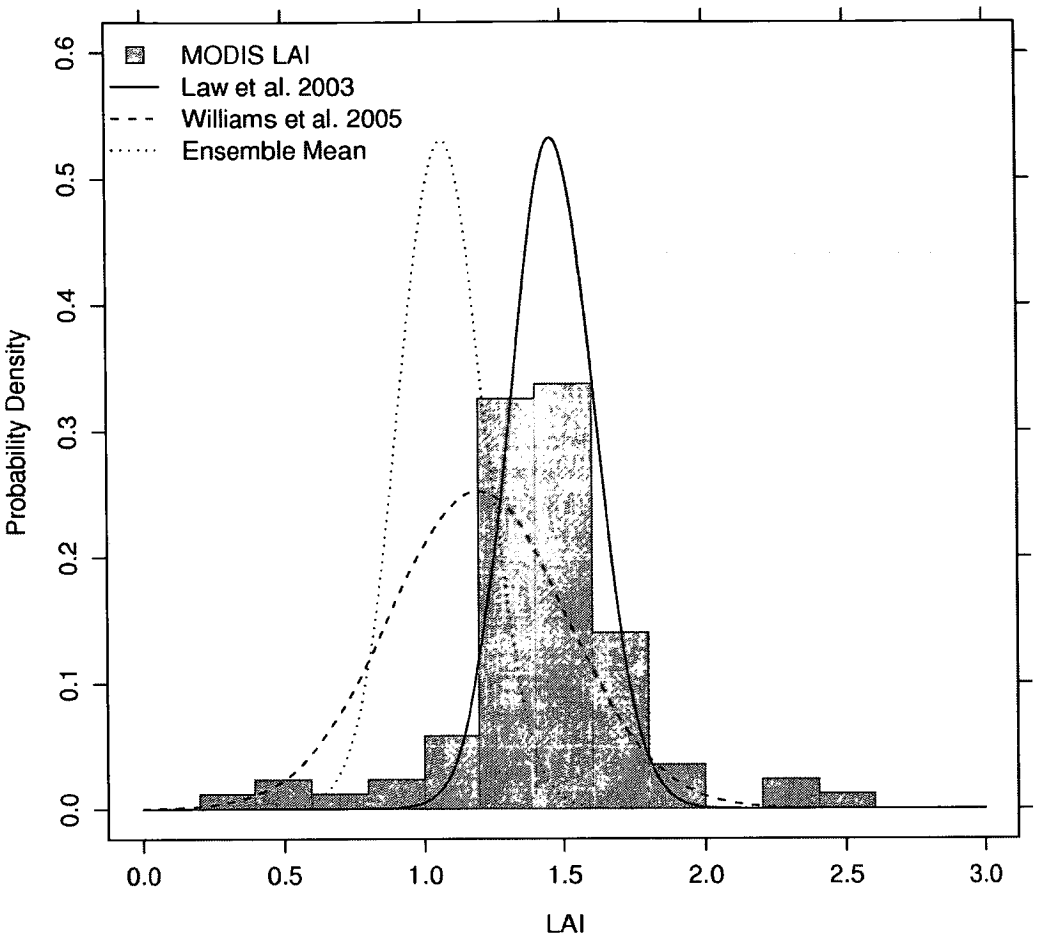

Figure 6.5 MODIS leaf area index (LAI) distribution for the Metolius Young Ponderosa pine site for a three-year period (2000-2002). Reported distributions from the literature are also indicated as solid and broken black lines. The finely broken black line indicates the 375-element ensemble mean retrieved from the Ensemble Kalman Filter.

6.5 Results

6.5.1 DALEC Parameterisation

The EnKF propagated observations of NEE and LAI into an ensemble of 400 state vector predictions, thereby generating estimates of the 11 parameters included in the state vector. These ensembles were subject to a Chi-Squared goodness of fit test of the NEE observations as a check on the parameterisations. The DALEC model was

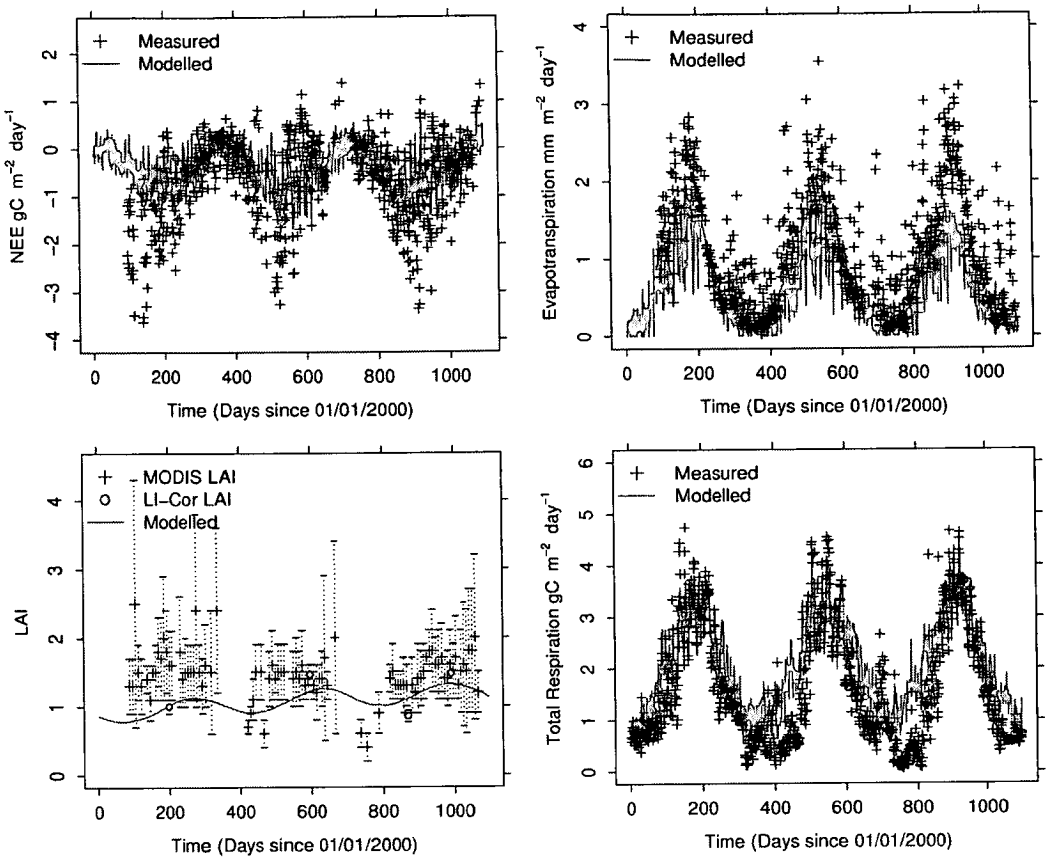

Figure 6.6 Model data comparison for four fluxes. In all cases the dark grey line indicates the mean trajectory of the 375-element ensemble trajectory retrieved from the Ensemble Kalman filter. Observations are indicated as black crosses. The modelled LAI is compared with ground based Li-Cor LAI2000 observations and MODIS satellite retrievals. LAI error bars are included to show the high variability of the satellite retrievals.

run in normal forward mode (i.e. without the EnKF) using each of the 400 sets of parameter estimates, and the chi-squared test was applied on the predictions and observations of daily NEE to test their similarity. Of the 400 parameter sets, 375 passed this test (c^2 = 717, DF = 656, P > 0.95) and were used in further analyses. The distribution of the parameter ensembles is illustrated in Figure 6.4, along with the resultant total NEE distribution.

The model ensemble appeared to represent the LAI reasonably well, and seemed to be in good agreement with the various available data sources for the site (Figure 6.5). A t-test indicated no significant difference between the means of the LAI2000 and

Table 6.2 Summary of model fits for various model outputs

Data Source	r^2	RMSE	Pearsons r	kendalls τ
*NEE**	0.39	8.70	0.62	0.44
ET†	0.55	9.90	0.74	0.55
Li-Cor LAI2000‡	0.70	0.12	0.84	0.67
MODIS LAI‡	0.03	1.34	0.17	0.15
R_e§	0.78	13.00	0.88	0.67

* Net ecosystem exchange, gC m^{-2} day^{-1}
† Evapotranspiration, mm m^{-2} day^{-1}
‡ Leaf Area Index, unitless
§ Total ecosystem respiration, gC m^{-2} day^{-1}

MODIS distributions (t = -1.7, P = 0.09), although this is may have been due to the large uncertainties attached to the MODIS retrievals. Despite the good match between MODIS LAI and the ground observations, the model LAI was found to be significantly different (t = -142.9, P<0.001); the mean MODIS LAI was 1.5, significantly higher than the mean model LAI of 1.1.

Visually examining the mean ensemble trajectory for four major components of the flux indicated that NEE and LAI were well reproduced, while the trajectories of total ecosystem respiration (R_e) and evapotranspiration (ET), data not used in the assimilation, were reasonably replicated (Figure 6.6). Quantitative tests revealed the model to be performing well with respect to all data streams, except the MODIS LAI, which appeared to be an overestimate with respect to the model trajectory (Table 6.2).

The optimised model estimated a total carbon uptake of 423 gC m^{-2} over three years, with a 95% confidence interval of ± 213.64 gC. The NEE uncertainty resultant from parameterisation was therefore substantial, representing 51% of the total net flux. A detailed analysis of the NEE error indicated relatively unbiased estimates; a simple linear regression between the estimates and observations indicated an intercept of -0.299 and a slope of 0.302 (Figure 6.7), suggesting that the model tended to smooth the NEE

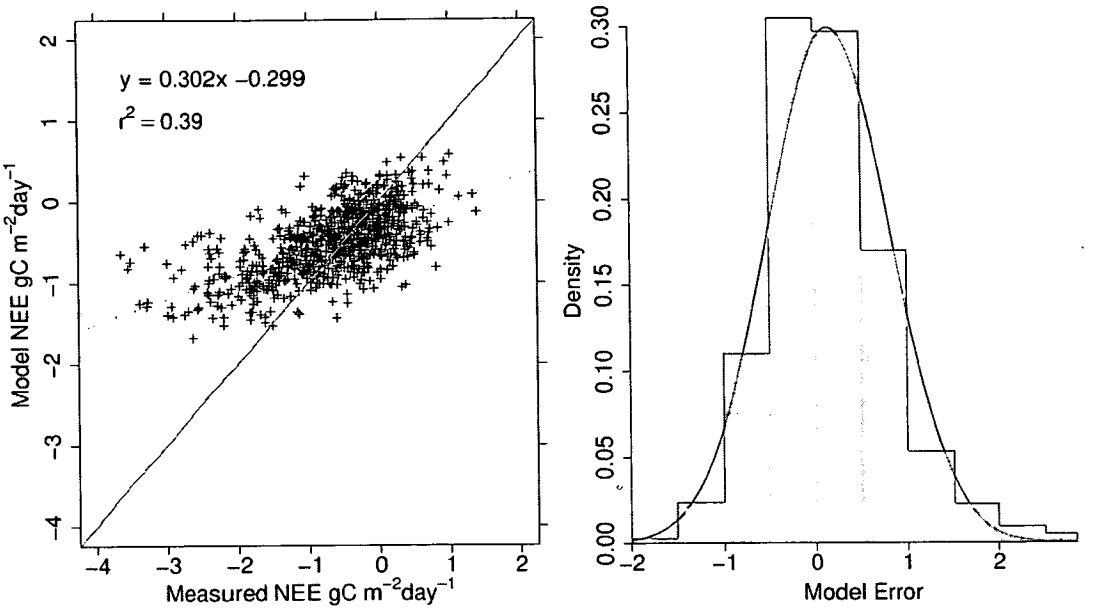

Figure 6.7 Net ecosystem exchange (NEE) model data comparison. Model values are the 375-element ensemble means retrieved from the Ensemble Kalman filter. The model error distribution is indicated in the right panel. The heavy right hand tail indicates an underestimate of the summer C uptake.

trajectory, underestimating the distribution at the extremes, with a small bias towards underestimation of the daily C uptake.

6.5.2 Meteorological Simulation

In order to simulate an ensemble of meteorological regimes we first calculated semivariograms for T_{min}, T_{max} and P. We modelled the spatial variation of $T_{\min}$ and $T_{\max}$ with a nested spherical ($\varphi_{u.sph}\, T_{min}$ = 23.8 km, $\varphi_{u.sph}\, T_{max}$ = 9.67 km), exponential model ($\varphi_{u.exp}\, T_{min}$ = 154.2 km, $\varphi_{u.exp}\, T_{\max}$ = 196.6 km). For P, a Gaussian model ($\varphi_{u.gaus}$ = 34.7 km) with a small nugget effect (τ = 0.2 mm) best captured the patterns of spatial variation. All three variables displayed exponential semivariance structures in time, with ranges of ~1 week for $T_{\min}$ and $T_{\max}$, and a shorter temporal range of 2 days for precipitation, indicating lower temporal continuity in the time series. The sill parameters fitted for each variable were $sill_u$ = 6.4, $sill_t$ = 11.69 and $sill_g$ = 12.8 for $T_{\min}$; $sill_u$ = 10, $sill_t$ = 23.1

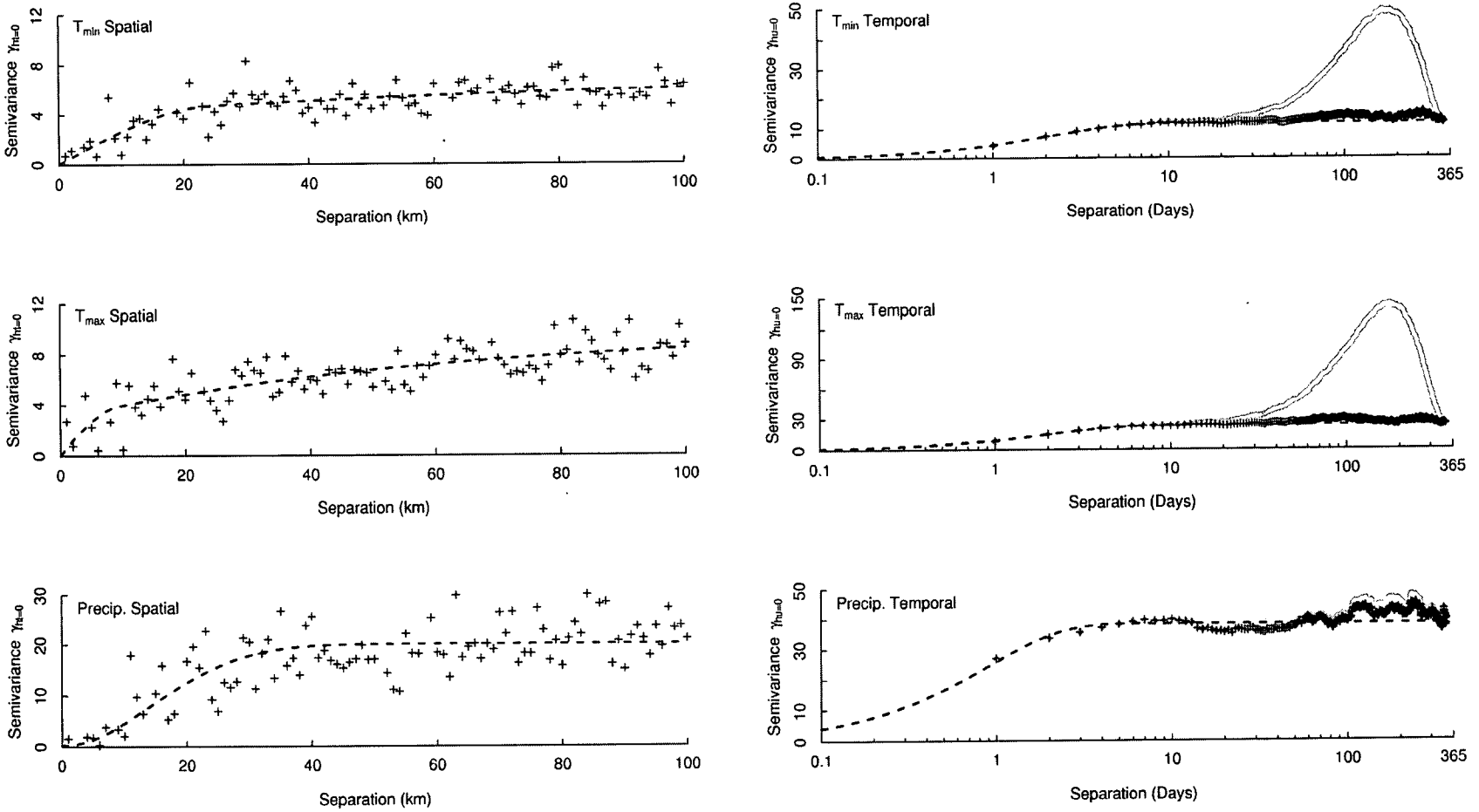

Figure 6.8 Semivariograms of meteorological data from the Central Cascades study area. Data were de-trended prior to analysis. Spatial semivariograms ($\gamma_{ht=0}$) were constructed by considering pairs of observations from the same day at increasing spatial separations. Temporal semivariograms ($\gamma_{hu=0}$) were constructed from pairs of observations from the same station at increasing temporal separation, and plotted on a log axis for clarity. For all plots, detrended observations are shown as black crosses and semivariogram models are indicated as broken black lines. Grey points on the temporal plots are raw data prior to detrending.

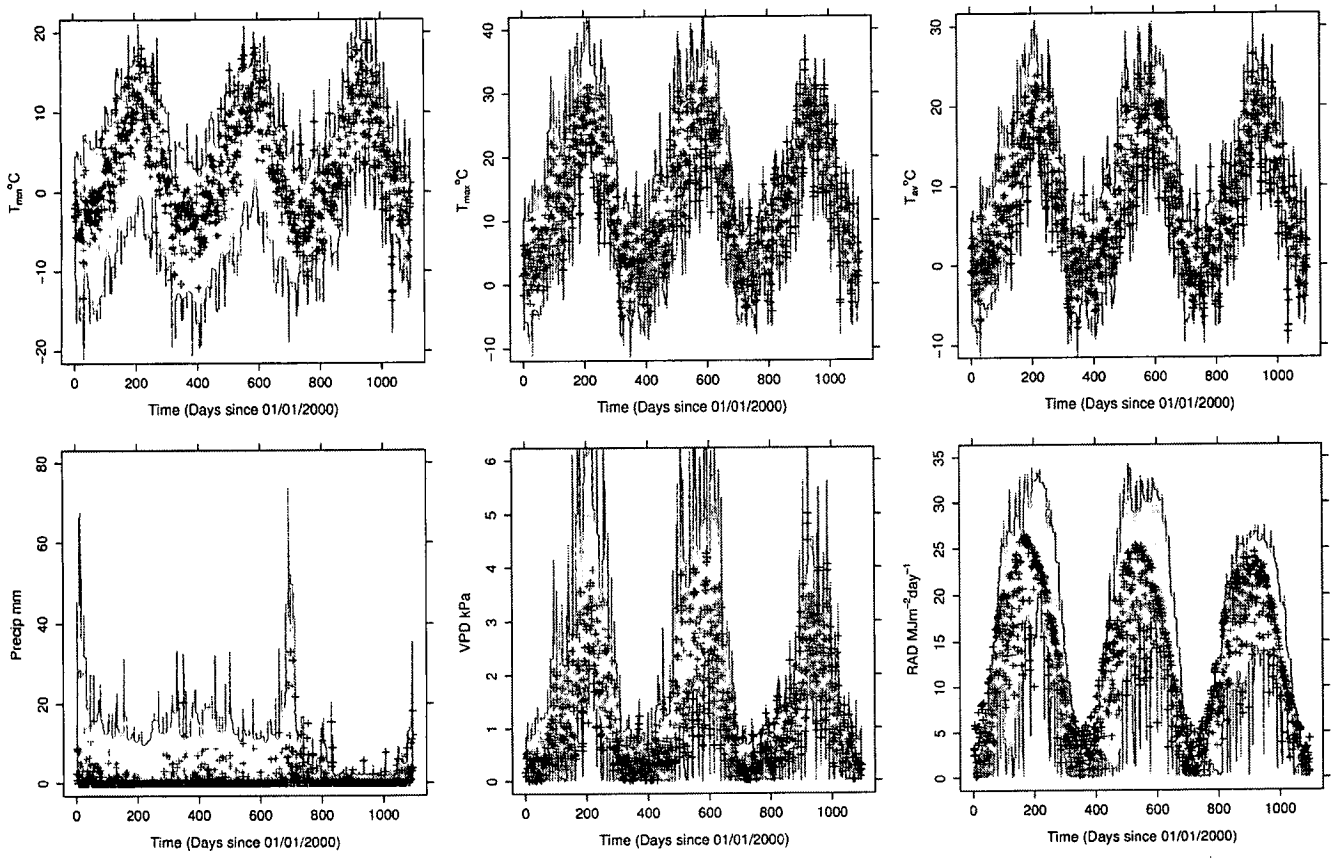

Figure 6.9 1000 meteorological time series derived from geostatistical simulation. Each element of the meteorological ensemble is indicated as a grey line, whilst observations are indicated as black crosses.

Table 6.3 Simulation versus data comparison for the Metolius Young Ponderosa pine site

Driver	Simulated		Observed		Bias	Gain	r^2
T_{min} °C	2.8	(6.6)	1.3	(5.6)	0.95	0.79	0.88
T_{max} °C	12.8	(9.2)	13.6	(9.8)	-0.34	1.04	0.96
T_a °C	7.78	(7.7)	8.7	(7.9)	-0.88	1.01	0.97
*Precip mm**	657.8	(273.6)	402.4	(60.9)	0.69	1.01	0.56
RAD MJ m^{-2} day^{-1}	12.4	(7.5)	13.6	(8.5)	-0.78	1.03	0.82
VPD kPa	1.2	(1.0)	1.3	(1.2)	-0.04	1.13	0.91

Mean daily meteorology. Standard deviations indicated in parentheses.
*Mean annual precipitation (mm)

Table 6.4 Summary of 375 element parameter ensemble retrieved from ENKF fitting

Name	Parameter	Mean	SD	Scale
t_1	*Decomposition Rate*	3.80	(0.40)	$x10^{-6}$
t_2	*Respiration Fraction*	4.41	(0.22)	$x10^{-1}$
t_3	*Foliar Fraction*	3.30	(0.25)	$x10^{-1}$
t_4	*Root Fraction*	4.61	(0.19)	$x10^{-1}$
t_5	*Foliar Turnover*	3.64	(0.37)	$x10^{-3}$
t_6	*Woody Turnover*	1.90	(0.26)	$x10^{-4}$
t_7	*Root Turnover*	6.64	(0.58)	$x10^{-3}$
t_8	*Litter Mineralization*	1.63	(0.19)	$x10^{-2}$
t_9	*SOM Mineralization*	1.07	(0.12)	$x10^{-5}$
t_{10}	*Soil T Sensitivity*	6.79	(0.22)	$x10^{-2}$
t_{11}	*Photosynthetic scalar*	8.13	(0.39)	

and $sill_g$ = 32.46 for T_{max} ; and $sill_u$ = 20.0, $sill_t$ = 38.44 and $sill_g$ = 49.3 for precipitation (Figure 6.8). The large-scale temporal trends (Figure 6.8) operated on temporal separations greater than one month. This temporal separation was smaller than the implemented search strategy of ± 10 days, and was therefore irrelevant for the generation of simulations.

1000 simulations were drawn from the data using the specified covariance models. We generated estimates of *VPD* and *RAD* from T_{min} and T_{max} via Murray's formula (A = 0.978, B = 22.23, C = 243.95) and the Allen model (K_{ra} = 0.17), which were calibrated locally. We were able to reproduce the observed meteorology

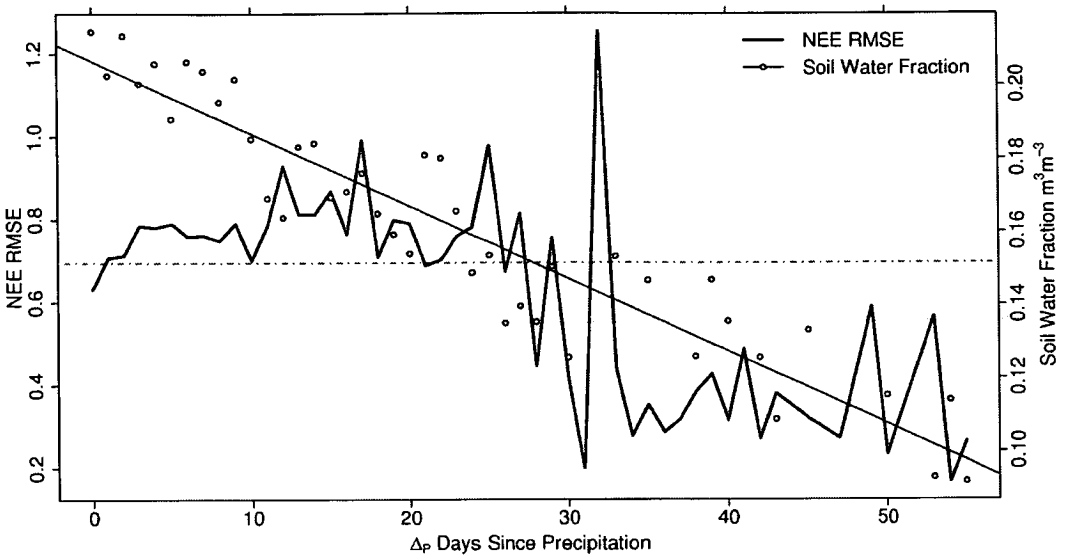

Figure 6.10 Effect of drought on NEE error. Δ_P is the number of days simulated as dry on which precipitation events were measured: Δ_P records the number of days that $P_{simulated} = 0$ whilst $P_{observed} > 0$. As Δ_P increases the model goes into mis-specified drought, as indicated by the modelled soil water fraction (right axis). The deviation in modelled and observed NEE trajectories attributable to mis-specified drought is plotted on the left axis as the root mean squared error (RMSE). The background RMSE of the model resultant from precipitation uncertainty is 0.7, indicated as a broken grey line.

successfully for all variables (Figure 6.9), with r^2 values exceeding 0.8 for all variables except *P*, which had an r^2 of 0.56 and a considerable positive bias (Table 6.3).

We propagated the 1000 meteorological realisations through DALEC to sample the NEE uncertainty resultant from driver uncertainty. All experiments were run using the mean parameter set retrieved from the EnKF (Table 6.4). With all meteorological observations replaced with simulated values, the model predicted a total NEE of -425 gC m^{-2} with a 95% confidence interval of ± 37.24 gC. The mean daily ensemble variance for the parameter and meteorological trajectories were 0.24 and 0.12 gC m^{-2} day^{-1} respectively, indicating significantly greater sensitivity of the model to parameterisation uncertainty (t = 24.03, P<0.0001). Replacing only *P* with simulated values (experiment 2.i) resulted in a total flux of -513 ± 16.9 gC m^{-2}. Replacing all temperature (T_{min}, T_{max}, T_d) and temperature derived variables (*VPD, RAD*) with simulated values (experiment 2.ii)

resulted in a total NEE of -338 ± 23.66 gC m^{-2}. When we replaced only the temperature observations with simulated values (experiment 2.iii), a total NEE of -337 ± 23.66 gC m^{-2} was observed (Table 6.5). Although NEE uncertainty attributable to the drivers was relatively small (typically < 4%), larger differences in the total flux were observed. The directions of bias for *P* and temperature were opposite, but of similar magnitude (~85 gC m^{-2}), and seemed to cancel each other out when the full meteorological uncertainty was propagated through the model (Table 6.5), and the total NEE estimated in experiments 1 and 2 were well within one standard deviation of each other, and were not significantly different (t = 0.37, P = 0.71).

We examined the temporal period over which drought stress occurred, by comparing the number of days since the last predicted rainfall event for each simulation with the observed rainfall regime (Δ_P). Positive values of Δ_P indicated that the model was going into drought while the observed *P* was greater than zero (mis-specification). The maximum value of Δ_P was 55 days, whilst the mean Δ_P was -3, indicating an overall positive bias in the number of simulated rainy days. Mis-specified droughts had a mean length of 3.5 days with a standard deviation of 3.9 days. The mean number of days between rainfall events for the observations was 4.1, with a standard deviation of 6.9.

Increasing Δ_P was linearly related to a decrease in modelled soil water content (r^2 = 0.58, P < 0.0001), and a corresponding decrease in ET (r^2 = 0.29, P < 0.001). The RMS error of modelled *versus* observed NEE decreased with increasing drought stress (r^2 = 0.46, P < 0.0001). Drought was initiated after approximately 30 dry days, as indicated by the step change in Figure 6.10. The background RMSE attributable to precipitation uncertainty was 0.7. When Δ_P < 30 the RMSE was approximately equal to background levels (0.71). However, as Δ_P > 30 the RMSE dropped to 0.39.

Table 6.5 Total NEE estimates from various uncertainty sources.

		NEE gC m^{-2}							
Experiment	Source of Variation	2000		2001		2002		Total	
1	*Parameters*	-120	(28)	-148	(44)	-155	(41)	-423	(109)
2	*Meteorology*	-115	(10)	-152	(12)	-159	(7)	-425	(19)
2.i	*Precipitation*	-143	(5)	-186	(7)	-183	(4)	-513	(10)
2.ii	*Temperature VPD and RAD*	-84	(6)	-114	(8)	-140	(6)	-338	(14)
2.iii	*Temperature*	-82	(7)	-101	(8)	-155	(6)	-337	(14)
3	*Total*	-114	(30)	-148	(44)	-147	(45)	-409	(111)

Values are in gC m^{-2} per time period. Standard deviations are indicated in parentheses.

Table 6.6 Effect of increasing data scarcity on NEE uncertainty. Simulations were run using the mean parameter values from Table 6.4. Meteorological data scarcity was increased via a reduction in the proximity of conditioning data through exclusion of data below the search threshold. Simulations were conditioned on the four closest stations for each search threshold.

Search Threshold	2000		2001		2002		Total		
(Closest Station)	Mean	SD	Mean	SD	Mean	SD	Mean	SD	95% CI*
< 25 km	-113	(11)	-152	(12)	-158	(7)	-424	(20)	9
> 25 km	-103	(11)	-139	(14)	-165	(14)	-408	(27)	13
> 50 km	-123	(11)	-169	(13)	-185	(17)	-477	(28)	11
> 75 km	-120	(12)	-165	(14)	-188	(19)	-473	(33)	14
> 100 km	-111	(14)	-169	(19)	-191	(21)	-471	(47)	19

Mean NEE m^{-2} per time period. Standard deviations indicated in parentheses.
*95% Confidence interval of NEE expressed as a percentage of the total flux.

6.5.3 Monte Carlo Sampling of NEE Uncertainty

We generated 1000 permutations of parameter and driver combinations at random from the pool of 375 parameter sets and 1000 driver sets (sampling with replacement) and ran the model with each in turn. These runs resulted in a total predicted NEE for 2000-2 of -409 ± 217.56 gC m^{-2} (Table 6.5). A comparison of the daily flux estimates for the main experiments (1, 2 and 3) revealed broadly similar ensemble trajectories (Figure 6.11). However, the range of experiment 2 was asymmetrical about the mean, with a greater deviation in the positive (weaker uptake) direction. As such, the summer extremes in uptake appear to be less well replicated in experiment 2 than experiment 1. Furthermore, winter uptake appeared weaker in experiment 2 in comparison with experiment 1.

Whilst the NEE variability of experiment 1 exceeded that of experiment 2, we examined the robustness of this result by increasing the variability of the meteorological ensemble in experiment 4: We decreased the amount of conditioning data to four neighbours whilst sequentially increasing the minimum distance to an observation (Table 6.6). In all cases, the NEE uncertainty attributable to meteorological uncertainty was less than the uncertainty attributable to parameter uncertainty (9 - 19% and 51% respectively). The results of experiment 4 indicate a general increase in NEE uncertainty with increasing distance to conditioning data, although results from the 25 km threshold distance were more uncertain than the results from the >50 km threshold (Table 6.6).

A comparison of the cumulative NEE allowed an examination of the growth in uncertainty over time for the three main experiments (Table 6.5, Figure 6.12). Again, the mean ensemble trajectories appear broadly similar, with little difference in total uptake

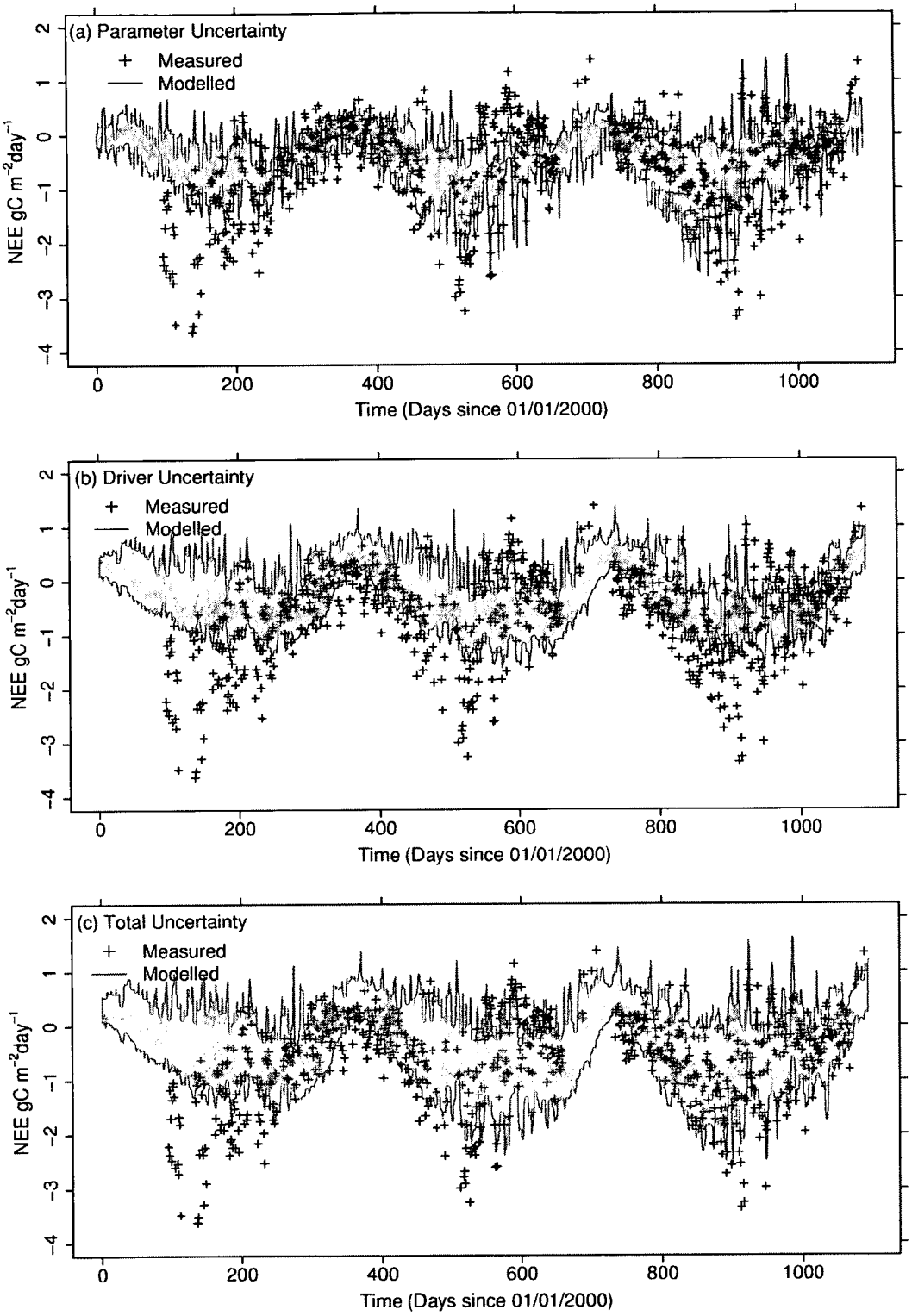

Figure 6.11 NEE trajectories for three years (2000-2002) under different uncertainty sources Ensemble ranges are indicated in light grey, whilst the ensemble mean is indicated in dark grey. Observations are represented as black crosses. Ensemble uncertainty is resultant from (a) 375 parameter sets, (b) 1000 geostatistical simulations of meteorology, (c) 1000 combinations of a and b.

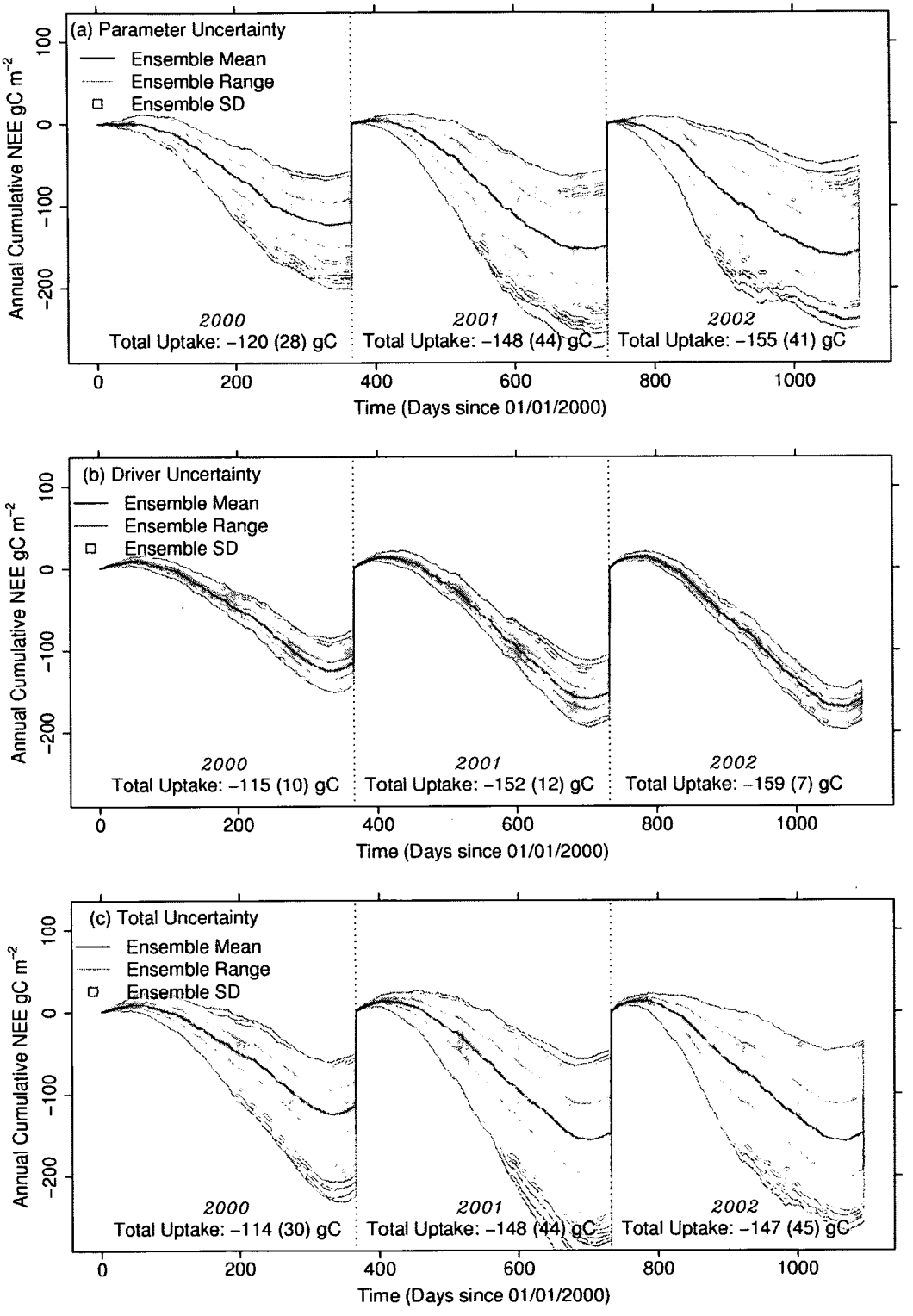

Figure 6.12 Cumulative NEE estimates over three years (2000-2002) under different sources of uncertainty. The ensemble mean is indicated in black, whilst its uncertainty is represented as a dark grey polygon. The individual ensemble members are indicated as light grey lines. Ensemble uncertainty is resultant from (a) 375 parameter sets, (b) 1000 geostatistical simulations of meteorology, (c) 1000 combinations of a and b. Mean total uptake for each year is indicated at the bottom of the plots in gC year^{-1}, with standard deviations indicated in parenthesis.

for inter-annual comparisons, which were approximately within one standard deviation of each other. However, it was clear that the greater variability in NEE imposed by parameter uncertainty compounds to a much larger annual uncertainty than for driver uncertainty. The total cumulative uncertainty (experiment 3, Figure 6.12c) was not very different to experiment 1, save for exaggerated extremes and a more pronounced end of season die-back, also exhibited in experiment 2 (Figure 6.12b).

6.6 Discussion

We were able to retrieve an unbiased flux estimate when parameterising DALEC using the EnKF, resulting in a total net C flux estimate consistent with the data and previous literature for the site (Law et al., 2003; Williams et al., 2005b). We found a large range of permissible parameter sets, resulting in cumulative NEE uncertainties over the three years of the study corresponding to ~50% of the total net flux (95% confidence interval of NEE expressed as a percentage of the total flux). The cumulative NEE over three years using EnKF for parameter estimation was 423 ±90 gC m^{-2} (mean ± SD of ensemble). This mean analysis was very close to that reported by Williams et al. in an earlier study using the EnKF at the same site for state (rather than parameter) estimation, 419±29 gC m^2 (Williams et al. 2005). The larger uncertainty associated with the parameter estimation approach was due to the constraint of setting constant parameter values for the entire 3 year run. In the state estimation approach, adjustments to the analysed C fluxes and pools were made throughout the three year period according to the observations, resulting in a closer fit to the data.

MODIS LAI retrievals compare well with ground observations (Law et al., 2003; Williams et al., 2005b) and model retrievals via data assimilation (Williams et al., 2005b).

However, MODIS retrievals of LAI were significantly different from the modelled LAI, and in general seem higher than we expect for the site. The fundamental issue of scale when validating 1 km^2 pixels against ground surveys undertaken at a scales orders of magnitude smaller makes direct comparison difficult (Tan et al., 2006; Yang et al., 2006), although published comparisons for the site report an r^2 of 76% with minimal bias (Cohen et al., 2006). Despite the large uncertainties associated with the MODIS LAI data stream, it still provides useful information due to its dense temporal coverage (8 day return period). Recent studies have indicated the use of satellite measured radiances may be preferable to LAI products in the case of assimilation, and novel ways to utilise such data streams may improve parameter constraint in the future (Quaife et al., 2008).

Meteorological simulations for the three-year period display a high degree of variability, which decreases in the final year (Figure 6.9). This decrease in uncertainty is due to observations at the nearby Metolius 'Intermediate' tower starting on project day 732 (1 January 2002). Geostatistical simulation techniques are able to reproduce the roughness of the driver fields, preserving data extremes, which may be particularly important for regionalisation of precipitation: The precipitation signal comprises of a background fluctuation ~0mm, with rare but sizable events which may be on the order of 100 mm day^{-1}. Thus, reproduction of extreme events over the average behaviour may be critical, and it is in this respect that SGS confers an advantage over Kriging techniques. In general we were able to satisfactorily replicate the meteorology for the site, but issues of bias arose, particularly for precipitation.

Positive bias in precipitation simulations resulted in a positive bias in NEE estimates when all other meteorological drivers were held at their observed values. Whilst precipitation variability was comparatively large, its effects did appear to be temporally buffered by the effect of soil capacitance (Figure 6.10). A reduction in RMSE

error was observed with increasing drought stress that reflected a decrease in the positive bias imposed by the simulated precipitation. Drought stress manifested itself after ~30 days without rain. The mean length of mis-specified drought events was 3.5 days, whilst on average the simulations had an increased frequency of precipitation events with respect to the observations: On average, simulated dry spells were 3 days shorter than those measured at the site. This indicates that the time scales on which precipitation errors occur in the simulations are much shorter than the temporal scales over which drought operates in the model. Thus precipitation errors are reduced by the model, since temporal aggregation has previously been shown to reduce driver uncertainty (Spadavecchia and Williams, In review).

Despite considerable uncertainty in the simulated driver sets, the resultant NEE uncertainty was 9% of the total flux, contributing only ~3% to the total combined NEE uncertainty, and well within the uncertainty attributable to parameterisation. This result was robust under significant degradation of the meteorological data set, with a maximum driver uncertainty of ~20% when conditioning simulations on four neighbours separated by distances greater than 100 km from the study site. We therefore reject H1; that the dominant source of NEE uncertainty is due to driver uncertainty.

Experiments on the effect of data scarcity indicated a general increase in NEE uncertainty with increasing distance to conditioning data. This result is expected, given Tobler's first law of geography (Tobler, 1970), specifying that similarity of observations is directly related to separation distance. The slight increase in uncertainty of the run conditioned on data >25 km from the site over the run conditioned on data >50 km away is most likely due to the large elevation difference between the conditioning data and study site at 25 km, as this roughly corresponds to the distance between the study site and the peaks of the Cascade mountain range to the West.

Examining the error contribution of each driver to the NEE trajectory revealed interesting bias effects: The positive bias in simulations of precipitation elevated the estimated C uptake by ~30 gC m^{-2} $year^{-1}$, whilst smoothing of the temperature signal (overestimation of mean T_{max} underestimate of mean T_{max}) resulted in underestimation of C uptake by ~30 gC m^{-2} $year^{-1}$. These opposing signals act to cancel out when considering the total meteorological uncertainty, resulting in an unbiased estimate of total NEE, with a small uncertainty (Table 6.5).

Bias issues in the meteorological simulations are a concern, and whilst in this study the precipitation and temperature biases cancel out, it is not clear whether this was by chance alone. It is likely that the bias cancellation was fortuitous for our study site, and there may be significant bias problems for other locations and ecosystems. A broader study of these bias issues for regional meteorological drivers is thus vital.

Of the meteorological drivers considered, temperature appeared to have the largest impact on NEE uncertainty, with approximately twice the influence of precipitation on the signal. As such we reject H2a, and accept the alternative proposition that instantaneous temperature variability dominates the flux uncertainty. This is likely due to the sensitivity of both GPP and heterotrophic respiration (*via* a Q_{10} relationship) to daily air temperature in DALEC. Decoupling the effect of deriving VPD and daily insolation from temperature drivers in DALEC indicates that indirect estimation of these drivers have a minimal impact on the total NEE.

6.7 Conclusions

We were able to retrieve statistically permissible parameter sets at a data rich location, but still faced appreciable uncertainties in flux estimates resultant from

parameter uncertainty. As such, spatially explicit modelling exercises may struggle to characterise the regional flux without considerable fieldwork, or investment in remote sensing methodologies to retrieve well-constrained parameter sets for the region of interest. Modelling the young ponderosa pine site at Metolius is challenging, because the system is aggrading rapidly. Observed annual increases in LAI result in increasing rates of C cycling. So the model parameterisation must be able to allocate C to grow the plant tissues realistically.

Minimisation of uncertainty in regionalisations of meteorological drivers may not be critical in terms of quantification of the regional carbon budget. We found considerable variability in simulated driver trajectories resulted in a small contribution to the net uncertainty. Issues of bias in meteorological upscaling are of much greater concern, but seemed to cancel out over time when propagated through the model. It is likely that the cancellation of bias due to temperature and precipitation is by chance alone, and further research into issues of bias in driver fields is warranted.

We have presented a robust analysis of the relative magnitude of parameterisation and driver errors using novel techniques. Quantification of the uncertainty associated with regionalised meteorological fields at relevant resolutions for catchment scale studies has been presented for the first time, with significant utility for policy making, and represents a key step in the application of data assimilation approaches on the catchment scale. It appears that improved model parameterizations and calculations of bias in meteorological fields are a research priority for spatially explicit regional modeling exercises, especially where data may be sparse.

6.8 Acknowledgements

Special thanks to Bev Law, James Irvine and Meredith Kurpius for supplying flux and respiration data, and all at the Oregon Climate Service for useful advice on meteorological data sources. Thanks also to Martin De Kauwe, who supplied MODIS LAI data and provided useful remarks on the manuscript. JP Gosling also provided many useful remarks on the methodology. We would also like to thank all at the Sisters Forest Rangers Station, especially Pam Fahey who provided the vegetation classification data.

6.9 References

Allen, R., 1997. Self-calibrating method for estimating solar radiation from air temperature. Journal of Hydrological Engineering, 2: 56–67.

Ashraf, M., Loftis, J.C. and Hubbard, K.G., 1997. Application of geostatistics to evaluate partial weather station networks. Agricultural and Forest Meteorology, 84(3-4): 255-271.

Canham, C.D.W., Cole, J. and Lauenroth, W.K., 2003. Models in ecosystem science. Princeton University Press, Princeton, N.J. ; Oxford, xv, 476 p. pp.

Christakos, G., 1984. On the problem of permissible covariance and variogram models. Water Resources Research, 20(2): 251-265.

Cohen, W.B. et al., 2006. MODIS land cover and LAI collection 4 product quality across nine sites in the western hemisphere. IEEE Transactions on Geoscience and Remote Sensing, 44(7): 1843-1857.

Daly, C., Neilson, R.P. and Phillips, D.L., 1994. A statistical topographic model for mapping climatological precipitation over mountainous terrain. Journal of Applied Meteorology, 33(2): 140-158.

De Cesare, L., Myers, D.E. and Posa, D., 2001. Estimating and modeling space-time correlation structures. Statistics & Probability Letters, 51(1): 9-14.

De Iaco, S., Myers, D.E. and Posa, D., 2001. Space-time analysis using a general product-sum model. Statistics & Probability Letters, 52(1): 21-28.

Deutsch, C.V. and Journel, A.G., 1998. Gslib: Geostatistical software library and user's guide. Oxford University Press, New York.

Eknes, M. and Evensen, G., 2002. An ensemble Kalman filter with a 1-D marine ecosystem model. Journal of Marine Sience, 36: 75-100.

Evensen, G., 1994. Sequential data assimilation with a non-linear quasi-geostrophic model using Monte Carlo methods to forcast error statistics. Journal of Geophysical Research, 99: 10143-10162.

Evensen, G., 2003. The ensemble Kalman filter: theoretical formulation and practical implementation. Ocean Dynamics, 53: 343-367.

Fisher, R., Williams, M., Ruivo, M.d.L., costa, A.L.d. and Meir, P., In press. Evaluating climatic and edaphic controls on dry season gas exchange at two Amazonian rain forest sites. Agricultural and Forest Meteorology.

Fuentes, M., Kittel, T.G.F. and Nychka, D., 2006. Sensitivity of ecological models to their climate drivers: Statistical ensembles for forcing. Ecological Applications, 16(1): 99-116.

Goovaerts, P., 1997. Geostatistics for Natural Resources Evaluation. Applied geostatistics series. Oxford University Press, New York; Oxford, xiv,483p pp.

Goovaerts, P., 1999. Impact of the simulation algorithm, magnitude of ergodic fluctuations and number of realizations on the spaces of uncertainty of flow properties. Stochastic Environmental Research and Risk Assessment, 13(3): 161-182.

Goovaerts, P., 2000. Geostatistical approaches for incorporating elevation into the spatial interpolation of rainfall. Journal of Hydrology, 228(1-2): 113-129.

Goovaerts, P., 2001. Geostatistical modelling of uncertainty in soil science. Geoderma, 103(1-2): 3-26.

Gringarten, E. and Deutsch, C.V., 2001. Variogram interpretation and modeling. Mathematical Geology, 33(4): 507-534.

Heuvelink, G.B.M. and Webster, R., 2001. Modelling soil variation: past, present, and future. Geoderma, 100(3-4): 269-301.

Hudson, G. and Wackernagel, H., 1994. Mapping temperature using kriging with external drift - theory and an example from Scotland. International Journal of Climatology, 14(1): 77-91.

Hungerford, R.D., Nemani, R.R., Running, S.W. and Coughlan, J.C., 1989. MTCLIM: a mountain microclimate simulation model. US For. Serv. Res. Pap. INT-414.

Kennedy, M. et al., 2008. Quantifying uncertainty in the biospheric carbon flux for England and Wales. Journal of the Royal Statistical Society Series a-Statistics in Society, 171: 109-135.

Klemedtsson, L. et al., 2007. Bayesian calibration method used to elucidate carbon turnover in forest on drained organic soil. Biogeochemistry, (in press). DOI 10.1007/s10533-007-9169-0.

Knyazikhin, Y., Martonchik, J.V., Mynen, R.B., Diner, D.J. and Running, S.W., 1998. Synergistic algorithm for estimating vegetation canopy leaf area index and fraction of absorbed photosynthetically active radiation from MODIS and MISR data. Journal of Geophysical Research, 103(24): 32257-32276.

Law, B.E. et al., 2001a. Carbon dioxide and water vapor exchange by young and old ponderosa pine ecosystems during a dry summer. Tree Physiology, 21(5): 299-308.

Law, B.E. et al., 2001b. Spatial and temporal variation in respiration in a young ponderosa pine forests during a summer drought. Agricultural and Forest Meteorology, 110(1): 27-43.

Law, B.E., Sun, O.J., Campbell, J., Van Tuyl, S. and Thornton, P.E., 2003. Changes in carbon storage and fluxes in a chronosequence of ponderosa pine. Global Change Biology, 9(4): 510-524.

Law, B.E., Thornton, P.E., Irvine, J., Anthoni, P.M. and Van Tuyl, S., 2001c. Carbon storage and fluxes in ponderosa pine forests at different developmental stages. Global Change Biology, 7(7): 755-777.

Law, B.E., Van Tuyl, S., Cescatti, A. and Baldocchi, D.D., 2001d. Estimation of leaf area index in open-canopy ponderosa pine forests at different successional stages and management regimes in Oregon. Agricultural and Forest Meteorology, 108(1): 1-14.

Maybeck, P.S., 1979. Stochastic Models, Estimation and Control, 1. Academic Press, New York.

Mcbratney, A.B. and Webster, R., 1986. Choosing functions for semi-variograms of soil properties and fitting them to sampling estimates. Journal of Soil Science, 37(4): 617-639.

Murray, F.W., 1967. On the computation of saturation vapor pressure. Journal of Applied Meteorology, 6: 203-204.

Myneni, R.B. et al., 2002. Global products of vegetation leaf area and fraction absorbed PAR from year one of MODIS data. Remote Sensing of Environment, 83: 214-231.

Oijen, M.V., Rougier, J. and Smith, R., 2005. Bayesian calibration of process-based forest models: bridging the gap between models and data. Tree Physiology, 25: 915-927.

Quaife, T. et al., 2008. Assimilating canopy reflectance data into an ecosystem model with an ensemble Kalman filter. Remote Sensing of Environment, 112: 1347-1364.

Running, S.W., 1994. Testing forest-bgc ecosystem process simulations across a climatic gradient in Oregon. Ecological Applications, 4(2): 238-247.

Running, S.W., Nemani, R.R. and Hungerford, R.D., 1987. Extrapolation of synoptic meteorological data in mountainous terrain and Its use for simulating forest evapotranspiration and photosynthesis. Canadian Journal of Forest Research-Revue Canadienne De Recherche Forestiere, 17(6): 472-483.

Runyon, J., Waring, R.H., Goward, S.N. and Welles, J.M., 1994. Environmental Limits on Net Primary Production and Light-Use Efficiency across the Oregon Transect. Ecological Applications, 4(2): 226-237.

Schwarz, P.A. et al., 2004. Climatic versus biotic constraints on carbon and water fluxes in seasonally drought-affected ponderosa pine ecosystems. Global Biogeochemical Cycles, 18(4): GB4007, doi:10.1029/2004GB002234,.

Spadavecchia, L. and Williams, M., In review. Can spatio-temporal geostatistical methods improve high resolution regionalisation of meteorological variables? Agricultural and Forest Meteorology.

Tan, B. et al., 2006. The impact of gridding artifacts on the local spatial properties of MODIS data: Implications for validation, compositing, and band-to-band registration across resolutions. Remote Sensing of Environment, 105: 98-114.

Thiessen, A.H., 1911. Precipitation averages for large areas. Monthly Weather Review, 39(7): 1082-1089.

Thornton, P.E., Running, S.W. and White, M.A., 1997. Generating surfaces of daily meteorological variables over large regions of complex terrain. Journal of Hydrology, 190(3-4): 214-251.

Tobler, W.R., 1970. A computer movie simulating urban growth in the Detroit region. Economic Geography, 46: 234-240.

Van Tuyl, S., Law, B.E., Turner, D.P. and Gitelman, A.I., 2005. Variability in net primary production and carbon storage in biomass across Oregon forests - an assessment integrating data from forest inventories, intensive sites, and remote sensing. Forest Ecology and Management, 209(3): 273-291.

Verbeeck, H., Samson, R., Verdonck, F. and Lemeur, R., 2006. Parameter sensitivity and uncertainty of the forest carbon flux model FORUG: a Monte Carlo analysis. Tree Physiology, 26: 807-817.

Wackernagel, H., 1998. Multivariate Geostatistics: An Introduction With Applications. Springer, Berlin; London, xiv,291p pp.

Williams, M., Law, B.E., Anthoni, P.M. and Unsworth, M., 2001a. Use of a simulation model and ecosystem flux data to examine carbon-water interactions in ponderosa pine. Tree Physiology, 21: 287-298.

Williams, M. et al., 1997. Predicitng gross primary productivity in terrestrial ecosystems. Ecological Applications, 7(3): 882-894.

Williams, M. et al., 2001b. Primary production of an arctic watershed: An uncertainty analysis. Ecological Applications, 11(6): 1800-1816.

Williams, M., Schwarz, P., Law, B.E., Irvine, J. and Kurpius, M.R., 2005a. An improved analysis of forest carbon dynamics using data assimilation. Global Change Biology, 11: 89-105.

Williams, M., Schwarz, P.A., Law, B.E., Irvine, J. and Kurpius, M.R., 2005b. An improved analysis of forest carbon dynamics using data assimilation. Global Change Biology, 11(1): 89-105.

Yang, W. et al., 2006. MODIS leaf area index products: From validation to algorithm improvement. IEE Transactions on Geoscience and Remote Sensing, 44(7): 1885-1898.

6.10 Appendix

In order to derive estimates of mean temperature (T_a), vapour pressure deficit (VPD) and incoming solar radiation (RAD) we implement well tested models from the literature. T_a was derived through the relationship provided in Thornton et al. (1997):

$$T_a = 0.606.T_{\max} + 0.394.T_{\min} \tag{6.2}$$

We derive VPD through a locally calibrated version of Murray's formula (Murray, 1967):

$$\begin{aligned} VPD &= e_s - e_m \\ e_s &= A.\exp\left(\frac{B.T_a}{C + T_a}\right) \\ e_m &= A.\exp\left(\frac{B.T_{\min}}{C + T_{\min}}\right) \end{aligned} \tag{6.3}$$

Where e_s is the saturation vapour pressure, e_m is the ambient vapour pressure, and A, B and C are empirical constants.

RAD was determined using the Allen model (Allen, 1997), which relates the atmospheric transmissivity to daily temperature range and site elevation (through atmospheric pressure):

$$RAD = R_A . K_r (T_{\max} - T_{\min})^{0.5}$$
$$K_r = K_{ra}\left(\frac{P}{P_0}\right)^{0.5} \quad \textbf{(6.4)}$$

Where R_A is the Angot (extraterrestrial) radiation in MJ m^{-2} day^{-1}, P is the atmospheric pressure at the site in kPa, and P_0 is the sea level atmospheric pressure (~101.3 kPa). K_r is an empirical constant, which takes values ~0.17 for inland regions, and values of ~0.20 for costal regions.

7. Edinburgh Space-Time Geostatistics Users Guide

Running Title: Spatio-Temporal Geostatistical Methods

L. Spadavecchia[1*]

[1] School of GeoSciences, Institute of Atmospheric and Environmental Science, University of Edinburgh, Edinburgh EH9 3JN, UK.

* Correspondence to Luke Spadavecchia, L.Spadavecchia@Gmail.com.

KEY WORDS: Spatio-temporal geostatistics, geostatistical simulation, product-sum covariance model

* Corresponding Author

7.1 Declaration

I am the sole author of all text and program code described in the following chapter, although the text draws heavily from sources referenced in the text. All references are cited, and I declare the text to be my own work. Fortran 90 code for the programs described is included in electronic format in an appendix.

7.2 Abstract

We document a set of Fortran 90 programs (the *Edinburgh Space-Time Geostatistics Package*) for the spatio-temporal regionalization of data via geostatistical methods. The programs utilize the product and product sum covariance representations of spatio-temporal data interactions. The code described allows interpolation of a data set over and arbitrarily spaced grid in continuous spatial and temporal coordinate systems. Error analyses are provided via the Jack Knife. The resultant spatio-temporal fields represent the expectation of a random function (RF), conditioned on the observed data and covariance model. The techniques implemented allow production of fields of estimation variance. We also provide code for simulation from the RF, via Sequential Gaussian Simulation (SGS). The SGS technique makes random draws from the RF, and allows the user to quantify the uncertainty of the interpolated field. SGS allows *Monte Carlo* analysis of the regionalisation by ensuring draws from the distribution (described by the expectation and estimation variance) conform to the observed spatio-temporal covariance of the data. The SGS technique is particularly useful in cases where the user intends to parameterise a model with a regionalised field, as the interpolation uncertainty can be propagated through the model to produce appropriate confidence intervals. Instructions for the use of the software are provided, along with sufficient background theory to successfully implement spatio-temporal regionalisation. A section discussing practical aspects of geostatistical modelling is also provided as an aid to first time users.

7.3 Introduction

The Edinburgh Space-Time Geostatistics software is a collection of three programs for the purpose of upscaling observations of a variable of interest to a set of coordinates distributed over some region of interest. The programs allow upscaling of data using the inverse distance weighting method (*IDW.exe*) and Kriging (*Geostats.exe*). Use of the Kriging algorithm generates estimates at unsampled locations using a random function model, specified from the data distribution and a description of the spatio-temporal relationship between observations. Simulations can be drawn from this model using the program *Gaussim.exe*.

The field of geostatistics has been in development since the late 1960s (Cressie 1990), and in the last decade, geostatistical techniques have expanded to encompass spatio-temporal estimation problems (Kyriakidis and Journel 1999, Christakos 2000, De Cesare et al. 2001b, De Iaco et al. 2001). While multi-dimensional implementations existed prior to this, unique challenges of spatio-temporal implementations remained: In particular, describing the space-time autocorrelation structure of the data was problematic (Kyriakidis and Journel 1999, De Cesare et al. 2001a, Gneiting 2002b, Gneiting et al. 2005). In 2001, De Iaco et al. introduced the product-sum covariance model (De Iaco et al. 2001), allowing intuitive and simple construction of spatio-temporal descriptions of autocorrelation, and provided Fortran 77 code for estimation via these techniques (De Cesare et al. 2002).

A wealth of software exists for geostatistical estimation (e.g. Deutsch and Journel 1998, De Cesare et al. 2002) prompting the question, why develop a new set of tools at all? The intention of the current software and documentation is to provide a user friendly and flexible implementation of spatio-temporal geostatistical methods as

described by De Cesare et al. (2001a) with custom built Fortran 95 software, rather than the modified GSLIB (Deutsch and Journel 1998) code implemented by De Cesare et al. (2002): In particular, we wished to allow cross-validation of entire time series, rather than the 'one observation at a time' method implemented by De Cesare et al. (2002), and to provide additional outputs not provided by the GSLIB code.

Theoretical introductions to geostatistical techniques are abundant (Clark 1979, Isaaks and Srivastava 1989, Cressie 1991, Goovaerts 1997, Deutsch and Journel 1998, Wackernagel 1998), and relevant material for spatio-temporal implementations can be found in (Kyriakidis and Journel 1999, De Cesare et al. 2001b, a, De Iaco et al. 2001, Heuvelink and Webster 2001, De Cesare et al. 2002, Gneiting 2002b, De Iaco et al. 2003, Gneiting et al. 2005). It is not our intention to re-cover this material: Whilst we provide a brief introduction to the relevant material necessary to successfully implement the techniques described, we assume some familiarity with the theory behind Kriging, and focus on a more applied description of spatio-temporal estimation techniques as implemented in the accompanying software, in the hope that they may prove useful to others. The program is supplied with the GNU general public license agreement: Please acknowledge the authors when using this software.

7.4 The Random Function Model and the Requirement of Stationarity

Linear geostatistical methods employ a probabilistic approach to upscaling; each data point is conceived of as a draw from a normal distribution, referred to as Gaussian random variable (RV). This collection of RVs are related to each other by some

quantifiable distance metric. This collection of spatio-temporally dependent random variables is known as a random function.

Kriging produces an estimate by calculating the conditional expectation of the random function (RF) for the estimation location, given the observed values. The expectation of the RF is fully defined by the expectation and covariance structure of the RF. Local spatial uncertainty can be explored by repeated draws from the RF *via* sequential simulation (see section 7.9.1.iv). Generally, the statistical description of autocorrelation is provided by the semivariogram, although other choices are possible (see section 7.5.2). We generally infer the covariance structure from the semivariogram.

In order to make inferences about any distributional characteristic (expectation, variance *etc.*) of an RV it is useful to have repeated measurements from its distribution. Therefore, in order to estimate the autocorrelation between (the RVs representing) observations separated by distance h, it is useful to have multiple observations on their joint distribution: Such a set of observations are never truly available, since subsequent samples at any location will be drawn at different temporal coordinates.

In the absence of repeated measures, we may substitute spatial replication for *in situ* repetition. The intention is that by grouping together all observation pairs separated by distance h ($\pm$ some lag tolerance), we can reconstruct the RVs, providing the following condition is met: To ensure that the description of autocorrelation is readily calculable, we require that all RVs in lag h share same distribution. This implies that the mean and variance of the data must be translation invariant (homogenous) across the region of interest, a condition referred to as second order stationarity. However it is sufficient that the mean and variance are homogenous only within the lag h; referred to as intrinsic stationarity. If this condition is satisfied, the similarity of data pairs can be defined purely in terms of their separation distances, greatly simplifying the specification

of the RF. If the underlying function is not intrinsically stationary, it may be possible to model a regionalisation using the relative semivariogram (Cressie 1985b). Further discussion can be found in (Cressie 1991, Goovaerts 1997, Deutsch and Journel 1998).

In order to satisfy second order stationarity in practice, it is often necessary to remove trends from the observations via some model. These trends can either be removed form the data and added back to interpolated estimates of the residuals, or incorporated directly in the interpolation scheme (see sections 7.8.2.i and 7.8.2.iii).

7.5 Initial Data Modelling

7.5.1 Accounting for Global Trends

Geostatistical methods model a RF as a combination of the mean m and a spatially coloured, normally distributed noise process ε. The mean is not necessarily uniform across the domain, and may be defined by some global trend function, whilst ε is defined by a model of autocorrelation. This decomposition of the process into a large-scale trend component and small-scale autocorrelated noise is familiar from time series analysis (Cressie 1991), and forms the rationale of non-stationary geostatistics.

Large-scale trends in the data may cause problems in estimating a model for ε, and may often cause statistics such as the semivariogram to become unstable, tending to infinity as separation distances become large (see section 7.5.2.i). On the other hand, large-scale trends may provide another source of information for constraining estimates, and may provide realistic physical dependencies in the resulting estimates. Furthermore, it is conceptually useful to partition data variation between known, measured trends and dependencies, and a stochastic but structured error component; this latter component reflects the unknown or unknowable latent variables which are either unmeasured, or

effectively too complex to control for in data collection. In either case, it is necessary to account for these trends and appropriately quantify them. Large-scale trends can be effectively modelled either through process-based knowledge of the variable of interest, or empirically through the use of trend surface analysis (Haining 2003) or the median polish (Tukey 1977), as popularised by Cressie (Cressie 1984, Cressie 1991).

All three programs provided in the Edinburgh Space-Time Geostatistics package allow for incorporation of large-scale trends in the estimation procedure. When large-scale trends are present in the data, it is necessary to remove them prior to the calculation of the semivariogram. If the trends are related to secondary variables that are known across the study site, non-stationary methods of geostatistics may be applicable (see sections 7.8.2.i and 7.8.2.iii). However, in the case of linear longitudinal trends or similar, non-stationarity may be accounted for by appropriate choice of kriging neighbourhood (see section 7.8.2.ii), providing local stationarity is achieved for the conditioning data (see Journel and Rossi 1989 for further details).

7.5.2 Accounting for Autocorrelation

7.5.2.i The semivariogram

The semivariogram is a method for summarizing the pattern of spatial or temporal variation (autocorrelation) of an observed phenomenon (Hudson and Wackernagel 1994, Gringarten and Deutsch 2001); describing the way in which similar observation values are clustered in space or time, in accordance with Tobler's first law of geography (Tobler 1970). The semivariogram is therefore a measure of the *dissimilarity* of data pairs as the separation between them increases, and is essentially the inverse of the auto-covariance of the data (Deutsch and Journel 1998).

The term semivariogram is often loosely applied to describe a whole series of possible statistics applied to a set of observations with attached coordinates, but most correctly it applies to Matheron's 'classical estimator' (Matheron 1962) of autocorrelation: For a set of n observations, we may choose any pair of data values, z_i and z_j with associated coordinates u_i and u_j. The dissimilarity of the data pair can then be calculated as half the squared difference between the observed values:

$$\gamma_{ij} = \frac{\left[z(u_i) - z(u_j)\right]^2}{2} \tag{7.1}$$

Plotting the differences γ_{ij} against separation distance results in the variogram cloud. The variogram cloud is typically diffuse, and suffers from pointwise instability (Diggle et al. 2002). By averaging the pairwise dissimilarities over a set of n spatial lags $H = \{h_1,\ldots,h_n\}$ we arrive at the more stable semivariogram, denoted $\hat{\gamma}(h)$:

$$\hat{\gamma}_h = \frac{1}{2N(h)} \sum_{i=1}^{N(h)} \left[z(u_i) - z(u_i + h)\right]^2 \tag{7.2}$$

This is actually the first moment of inertia of the lag (Isaaks and Srivastava 1989), reflecting the width of the scatter of z_u on z_{u+h} from the 45° line, where u is any location in the region of interest and h is a separation vector.[1]

Goovaerts (1997) points out that a generalised semivariogram estimator is possible by changing the power of equation 7.2 from 2 to ω:

$$\hat{\gamma}_h = \frac{1}{2N(h)} \sum_{i=1}^{N(h)} \left[z(u_i) - z(u_i + h)\right]^{\omega} \tag{7.3}$$

[1] **NOTE:** The semivariogram can be used to derive an estimate of the fractal dimension of a process, which relates to the surface roughness of the RF. Fractal dimension can be calculated from the slope of the linear portion of the log-log plot of semivariogram (Palmer 1988, Leduc et al. 1994). An interesting extension is provided in (Gneiting and Schlather 2004).

For $\omega = 2$ we arrive at the 'classical' estimator, but by reducing the value of ω we can reduce the influence of extreme values on the measure $\hat{\gamma}_h$. Values of note are $\omega = 1$ and $\omega = 0.5$, returning the mean absolute deviations, and square root deviations (known as the *madogram* and *rodogram* respectively), and are commonly used alternatives (Deutsch and Journel 1998). These more robust alternatives may help to make inferences about the nature of the autocorrelation of a process when used in conjunction with the semivariogram.

Providing the mean and variance of the observed phenomenon is translation invariant (i.e. identical for any subregion of the domain), the semivariogram is a valid description of the spatial autocorrelation structure of the data (Cressie 1991). If the above condition is satisfied, the difference between any pair of data points at arbitrary separation is purely a function of their separation vector h, and the phenomenon is referred to as a stationary process.

For a stationary process, we generally observe an increase in semivariance with increased separation vector h, up to some threshold distance, referred to as the range. At separation distances greater than the range, the semivariance remains at a constant 'sill' value.

In the case of large-scale trend structures (for example, an East-West gradient), a parabolic structure is commonly observed (Clark 1979), where the semivariance values rise in an unbounded fashion. In this case, the phenomenon is said to be non-stationary (Deutsch and Journel 1998), and some method of trend removal is necessary (see section 7.5.1), before the residual values can be analyzed.

In many cases, the semivariogram will display a discontinuity at the origin. This behaviour is commonly referred to as a 'nugget effect', as it reflects the condition where values of the observation vary abruptly at the microscale. This term was coined in

mining geostatistics, where nuggets contained in samples from gold grades tended to produce this effect. Discontinuous behaviour of the semivariogram at the origin can usually be accounted for by a combination of microscale variability below the resolution of the sampling equipment, and sensor noise.

7.5.2.ii The Covariogram

The covariogram is the covariance between data pairs at each lag. By convention, the first value in the comparison is referred to as the 'tail' value, and the second vale in the pair is called the 'head' value [$tail \xrightarrow{h} head$] (Goovaerts 1997, Deutsch and Journel 1998):

$$c(h) = \frac{1}{N(h)} \sum_{i=1}^{N(h)} z(u_i).z(u_i + h) - m(-h).m(+h)$$

where

$$m(-h) = \frac{1}{N(h)} \sum_{i=1}^{N(h)} z(u_i) \qquad (7.4)$$

$$m(+h) = \frac{1}{N(h)} \sum_{i=1}^{N(h)} z(u_i + h)$$

Where $m(-h)$ and $m(+h)$ are the tail and head value means respectively (lag means).

Whilst the semivariogram is the most common description of autocorrelation used in the practice of geostatistics, in general the covariogram is used in the kriging algorithm, because of difficulties in using the semivariogram representation for simple kriging, and improvements in computational efficiency (Goovaerts 1997). The covariogram is readily obtained from the semivariogram by subtracting the semivariogram from the sill variance (see section 7.5.2.i).

Unbounded models have no covariance counterpart; in this case pseudo-covariance is calculated by subtracting the semivariogram from a sufficiently large constraint, such that the resulting value ≥ 0.

7.5.2.iii The Correlogram

In some cases we may wish to discuss data dependency in terms of autocorrelation, as is common in time series analysis. The correlogram is defined by the correlation between the data values in each lag. It is easily obtained from the covariogram by standardisation:

$$\rho(h) = \frac{c(h)}{\sqrt{\sigma^2(-h).\sigma^2(+h)}}$$

where

$$\sigma^2(-h) = \frac{1}{N(h)} \sum_{i=1}^{N(h)} [z(u_i) - m(-h)]^2 \qquad (7.5)$$

$$\sigma^2(+h) = \frac{1}{N(h)} \sum_{i=1}^{N(h)} [z(u_i + h) - m(+h)]^2$$

Where $\sigma^2(-h)$ and $\sigma^2(+h)$ are the variances of the tail and head values respectively (lag variance).

7.6 Continuous Models of Autocorrelation

Having established the pattern of autocorrelation by calculation of the semivariogram, it is desirable to express this structure in continuous terms. Modelling of the semivariogram is necessary for geostatistical estimation, and allows inference to be drawn on various properties of the autocorrelation, such as its effective range and asymptotic variance (known as the sill).

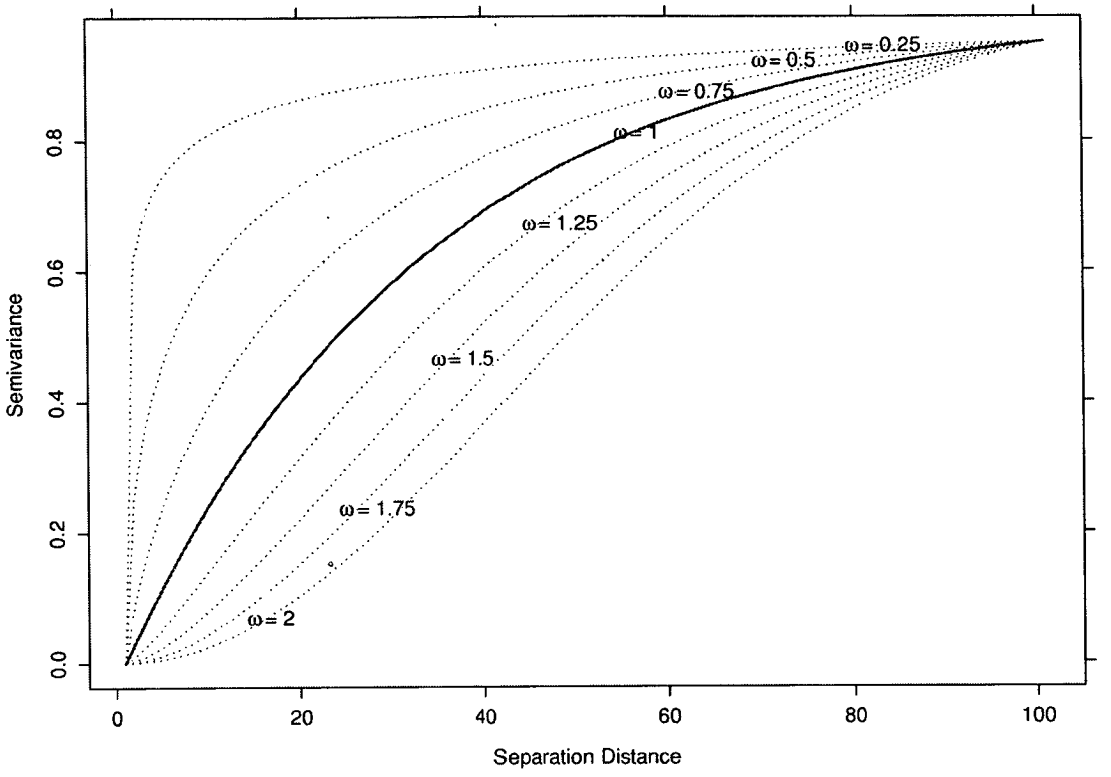

Figure 7.1 Powered exponential model with varying smoothness parameter ω. As ω increases semivarinace increases more slowly at the origin, indicating a very continuous process.

The semivariogram can be modelled with any conditionally negative definite function (Mcbratney and Webster 1986). Rather than testing proposed models for permissibility (e.g. Christakos 1984), it is usual to use one of a set of basic models that are known to be permissible. There are many such models in common use (see Deutsch and Journel 1998), and these basic model structures may be combined in a linear manner to form complex models (Goovaerts 1997).

7.6.1 Permissible Semivariogram Models

The following models are available in the Edinburgh Space-Time Geostatistics programs: Powered exponential, Gaussian, Spherical, Rational quadratic, Power, Hole

effect and dampened hole. These models provide a wide range of functional forms reflecting different surface characteristics. Details of their use and limitations are presented below:

- ***Powered Exponential Model***

$$\hat{\gamma}_h = 1 - \exp\left[-3\left(\frac{h}{\phi}\right)^{\omega}\right]$$

where **(7.6)**

$0 < \omega \leq 2$

Where ω is a smoothness parameter (Figure 7.1). Note that $\omega=0$ is not a valid model. When $\omega=2$ the model is equivalent to the Gaussian model presented below.

- ***Gaussian Model***

$$\hat{\gamma}_h = 1 - \exp\left(\frac{-3h^2}{\phi^2}\right) \quad \textbf{(7.7)}$$

The Gaussian model reflects a very smoothly varying process. It may exhibit unstable behaviour, and is not recommended for use without a nugget effect.

- ***Spherical Model***

$$\hat{\gamma}_h = \begin{cases} 1.5\frac{h}{\phi} - 0.5\left(\frac{h}{\phi}\right)^3 & \text{if } h \leq \phi \\ 1.0 & \text{if } h > \phi \end{cases} \quad \textbf{(7.8)}$$

The spherical model is widely used in the literature. It provides a model with almost linear behaviour near the origin, which abruptly levels to the sill value.

- ***Rational Quadratic Model***

$$\hat{\gamma}_h = h^2 \div \left(\frac{1+h^2}{\phi} \right) \tag{7.9}$$

The rational quadratic model is roughly sigmoidal with moderate smoothness near the origin, having a shorter left hand tail than the powered exponential. It displays linearity at low to intermediate ranges, with a pronounced smooth shoulder towards the sill. Despite its somewhat similar appearance to powered exponential models with high values of ω, the rational quadratic model displays less smoothness at short range and greater stability than the powered exponential.

- ***Power Model***

$$\hat{\gamma}_h = h^{\omega} \tag{7.10}$$

Where ω is the power law, describing the rate of decay in autocorrelation as distance increases; lower values therefore imply a smoother interpolated surface. The power model has no covariance counterpart, as it is unbounded ($\hat{\gamma}_h \rightarrow \infty$ for large h): We implement the model using a pseudo-covariance counterpart (see section 7.5.2.ii). Given that parabolic semivariograms indicate non-stationarity (see section 7.5.2.i), we do not recommend the use of the power model, and include it only for completeness; we recommend de-trending the data (see section 7.5.1) prior to semivariogram modelling to avoid its use.

- ***Hole Effect (Cosine) Model***

$$\hat{\gamma}_h = 1 - \cos\left(\frac{h}{\phi}\pi\right) \tag{7.11}$$

The hole effect describes a periodicity in the underlying features, such as seasonality or diurnal cycling. The range ϕ describes the wavelength of the periodicity. The hole effect is intended for use in nested models (see section 7.6.1.ii). In order for the resulting semivariogram to be valid (positive definite), the hole effect can only be applied in one direction: Therefore its use in time is straightforward. To implement the hole effect spatially, the user should specify an appropriate geometric anisotropy ellipse (see section 7.6.1.iii), with a very large range in the direction perpendicular to the periodicity.

- ***Dampened Hole Model***

$$\hat{\gamma}_h = 1 - \exp\left(\frac{-3h}{d}\right).\cos\left(\frac{h}{\phi}\pi\right) \tag{7.12}$$

The dampened hole effect model decreases the level of periodicity as distance increases. Again, the range ϕ describes the wavelength of the periodicity, whilst parameter d defines the distance at which 95% of the periodicity is removed from the signal.

In all cases h is the lag distance and ϕ is the range over which the data exhibit autocorrelation. Functional forms for all models are presented in Figure 7.2. For the

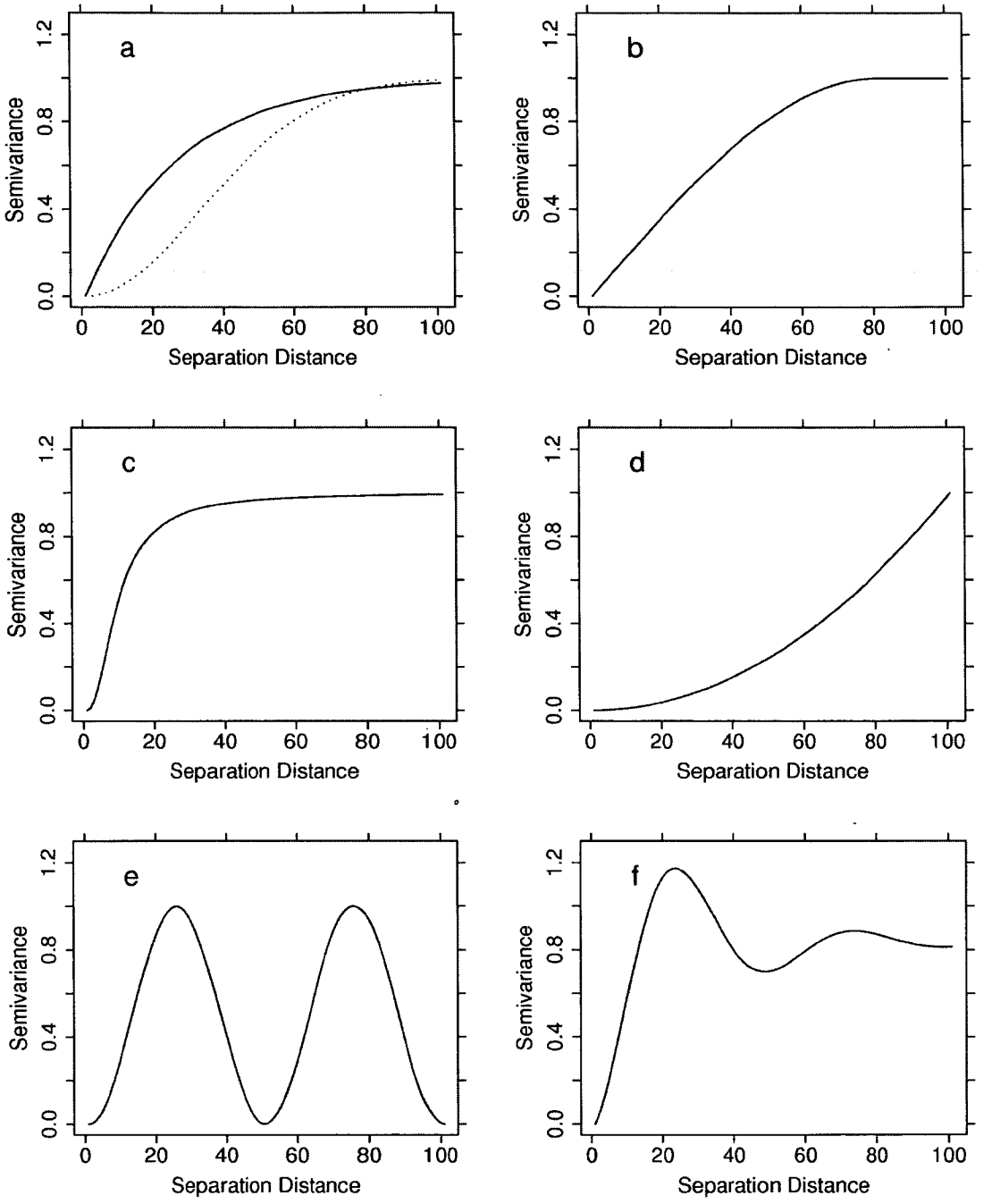

Figure 7.2 Semivariogram models available in Edinburgh Space-Time Geostatistics. (a) Powered exponential model (equation 7.6). The solid line illustrates ω=1, whilst the broken line illustrates ω=2, equivalent to a Gaussian model (equation 7.7). (b) Spherical model (equation 7.8). (c) Rational quadratic (equation 7.9). (d) Power model (equation 7.10). (e) Hole effect (equation 7.11). (f) Dampened hole (equation 7.12).

exponential and Gaussian models ϕ is the effective range, interpreted as the distance at which semivariance reaches 95% of the asymptotic 'sill' variance: The factor of 3 in the numerator solves for effective range[2]. The models are rescaled with a contribution parameter c to reflect the variability of the data set, and may have a 'nugget' discontinuity τ at the origin (see section 7.5.2.i).

It is worth noting that many of these models can be recreated or approximated by the more general Matern class of covariance functions (Wackernagel 1998, p336, Gneiting 2002a).

Although Whittle-Matern type models are very flexible, we chose not to implement them due to their computational expense, which must be undergone twice for every prediction location (once for the observation covariance matrix, once for the estimation covariance matrix; see section 7.9). Although this may seem limiting, significant flexibility can be achieved through the much simpler powered exponential model (Figure 7.1). Detailed notes on semivariogram specification can be found in section 7.11.2.v.

7.6.1.ii Nested models

The choice of permissible models may at first seem restrictive; however, additive combinations of permissible models always give rise to a permissible semivariance function. Hence, any number of semivariogram models can be combined in a linear additive manner to form complex nested models, which considerably increases the range of RF models possible. Although any number of models may be combined, the principle of parsimony is sensible when building a semivariogram model, as more

[2] **Note:** sometimes the exponential model is presented without the factor of 3 in the numerator (e.g. Cressie, 1990, pg. 61), in which case the less intuitive 'integral range' is solved for (Deutsch and Journal, 1998, pg. 25); all programs in the Edinburgh Space-Time Geostatistics package use the effective range convention in their calculations.

complex models do not necessarily improve results, and increase computation time. We recommend that the model should be as simple as possible, and generally comprise of less than three functions, which should preferably relate to the physical characteristics of the variable of interest.

7.6.1.iii Accounting for anisotropy

It is sometimes the case that the range of autocorrelation in a data set varies with the direction of the data pairs under consideration. This situation is referred to as *geometric anisotropy*, and is often observed when the underlying physical processes involved display directionality (e.g. down-wind dispersal of a Gaussian plume). Similarly it is possible to find a variation in the sill value of the semivariogram with direction; a situation referred to as *zonal anisotropy*. Whilst zonal anisotropy is not impossible *per se*, it is rarely encountered in practice, and often is apparent in cases where the sample space does not adequately cover the range of variation in all directions (Isobel Clark, *personal communication*). Zonal anisotropy can be incorporated by setting a very large range on the major axis of variation, such that the effect of the covariance structure is essentially nil perpendicular to the minor axis.

Anisotropy is dealt with by deforming the coordinate system such that all ranges appear equal (Figure 7.3). This is achieved by an affine transformation of the separation vector h:

$$h' = h + h|\sin(\theta)\psi|$$

where (7.13)

$$\psi = \frac{\phi_{\min}}{\phi_{\max}}$$

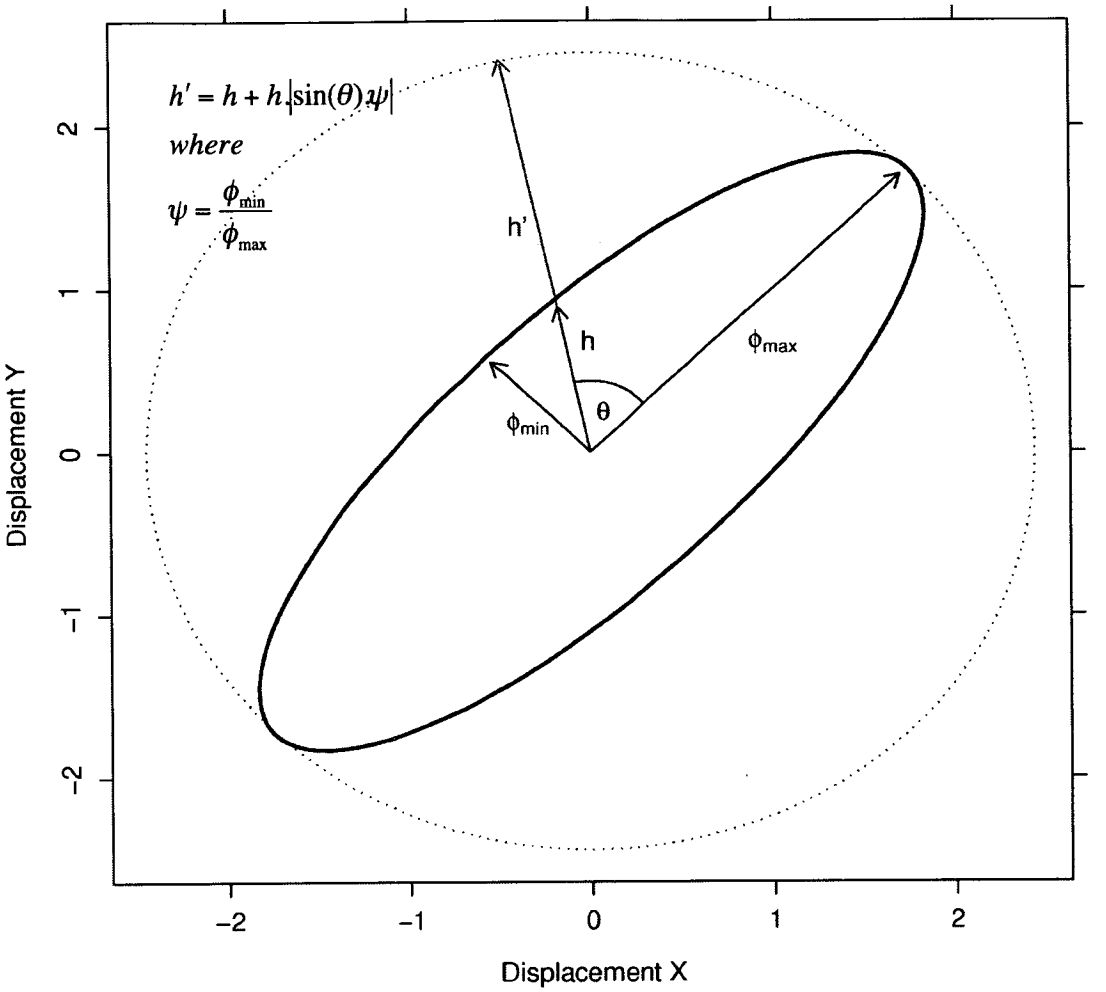

Figure 7.3 Affine transformation of anisotropy ellipse to isotropic coordinate system h'. The minor axis of variation is stretched until it is equivalent to the major axis using equation 4.8. The degree of stretching is dependant on the angle θ subtended by the distance vector h and the major semi-axis of variation, and the eccentricity of the anisotropy ellipse ψ.

The value ψ is the ratio between the minimum range and the maximum range of the semivariogram, and describes the eccentricity of the anisotropy ellipsoid. θ describes the angular difference between the coordinate vector and the direction of the axis of maximum variation ϕ_{max}. The new distance in the transformed coordinate system h' is then used to construct the covariance arrays for estimation.

7.6.1.iv Model Fitting

The method by which these models should be fit is subject to some dispute (see Goovaerts 1992, Diggle et al. 2002 for contrasting views); one school of thought is to fit the model by eye, so that the model appears visually satisfactory. Others use automated fitting procedures, either by least squares (Cressie 1985a) or likelihood based procedures (Diggle et al. 2002).

Whilst least squares (LS) methods provide a fit which is generally visually pleasing, fits may be sensitive to outliers, and in general the sensitivity of the semivariogram to changes in the conditioning data (as assessed by random draws from simulated surfaces) indicates that excessive 'trust' in the data points may produce misleading results (Diggle et al. 2002). Fitting by maximum likelihood (ML) generally requires some notion of the data error distribution, and although such approaches allow balancing of model fit and data uncertainty, they are open to criticism for subjectivity in the choice of distribution parameters, functional form for the prior error model etc.

Kriging estimates can be fairly resilient with respect to changes in the semivariogram specification (Cressie and Zimmerman 1992), although the estimation (Kriging) variances are sensitive to such changes. As a rule of thumb, LS fitting approaches work well when the purpose of the study is estimation, whilst ML based methods are more appropriate when inferences on the parameters of the spatio-temporal distribution are of more interest. We leave decisions on model fitting procedures to the discretion of the user, but urge against 'black box' fitting methods and favour a more interactive approach.

7.7 Modelling a Space-Time Regionalization

So far we have only discussed modelling of semivariograms in terms of spatial or temporal coordinates. Combining the spatial and temporal autocorrelation structures to form a complete model for the regionalisation has been an active area of research in the past decade, and comprehensive reviews can be found in (Kyriakidis and Journel 1999, De Cesare et al. 2001a, Gneiting 2002b, Gneiting et al. 2005). Strategies for combining spatial and temporal autocorrelation structures (which are generally discussed in their covariance form) can be broadly divided into *separable* and *non-separable* classes of models.

The earliest attempts at producing spatio-temporal covariance functions made use of separable models, with somewhat simplistic assumptions about the nature of spatio-temporal variability; either combining spatial and temporal covariance in an additive or multiplicative manner. The separable construction is tantamount to ignoring spatio-temporal interactions, and stating that spatial and temporal covariance display complete independence (Kyriakidis and Journel 1999). Few observed processes behave in this manner, and considerable effort has been made in seeking alternative non-separable representations.

Development of non-separable covariance functions began with metric models (Dimitrakopoulos 1994), whereby spatial and temporal separation units were converted to some common metric, and standard three-dimensional zonal anisotropy techniques used to produce the regionalisation (e.g. as implemented in GSLIB: Deutsch and Journel 1998). The attractive simplicity of this approach is somewhat offset by difficulties in specifying a common metric, and the loss of intuitive units to describe autocorrelation.

Subsequent to this, Cressie and Huang developed a set of permissible non-separable space-time covariance functions through Fourier inversion of one-dimensional covariance functions (Cressie and Huang 1999). Gneiting developed this approach to a Fourier free representation (Gneiting 2002b). These developments were an important step forward in spatio-temporal geostatistics, but it was not until the contribution of De Iaco et al. (2001) that these forms of stationary, non-separable covariance functions became generalized and straightforward to implement (see De Cesare et al. 2001a, b).

The product-sum covariance model of De Iaco (2001) allows the linear combination of arbitrarily complex covariance structures (including zonal and geometric anisotropy) in space and time, with full interaction. The product-sum representation incorporates the Cressie-Huang family of covariance functions and provides new, non-integrable forms that cannot be obtained through the Cressie-Huang representation (De Iaco et al. 2001). Due to the simplicity and ease of use of the product-sum representation, it is the representation of choice for non-separable covariance specification in all programs in the Edinburgh Space-Time Geostatistics package.

Non-stationary space-time covariance structures have been discussed (Kyriakidis and Journel 1999, 2001a), and generally rely on treatment of semivariogram parameters themselves as Gaussian RFs for the region of interest. Kiriakidis and Journel provide an interesting example of this hierarchical RF implementation for European pollution data (Kyriakidis and Journel 2001b). Although this implementation is powerful, it requires multiple regionalisations in order to build the nonstationary RF model, and requires a considerable investment of time in terms of semivariogram modelling and computational load. If such models are required, initial regionalisations may be

undertaken with the existing software, whilst final implementation is possible with minimal modification to the code.

In the discussion of models spatio-temporal covariance structures the following notational conventions will be used: Whenever referring to a property concerning patterns of spatial covariance, a subscript u will be applied. For properties of the covariance structure concerning time, a subscript t is applied. As in previous sections, h denotes separation distance, whilst $\hat{\gamma}$ indicates the semivariance, C denotes covariance, and the definitions of the semivariogram parameters (φ and τ) remain the same (see section 7.6.1). We denote the spatiotemporal semivariogram $\hat{\gamma}_{u,t}$, and refer to subsets of $\hat{\gamma}_{u,t}$ by indicating the range of separation distaces parenthetically, for example $\hat{\gamma}_{u,t}(h_u, h_t = 0)$ is the subset where all temporal separations are zero, i.e. only the spatial element of $\hat{\gamma}_{u,t}$.

7.7.1 Separable Space-Time Covariance: The Product Model

The simplest way to arrive at a permissible space-time covariance function is the product model, which is simply a scaled product of the separate spatial and temporal covariance models. An example of a product semivariogram model is provided in Figure 7.4. Fitting of this model proceeds as follows:

- First, only the simple spatial and temporal semivariograms are considered ($\hat{\gamma}_{u,t}(h_u, h_t = 0)$ and $\hat{\gamma}_{u,t}(h_u = 0, h_t)$ respectively), where h_u and h_t are the spatial and temporal separations. Valid semivariogram models must be fit to them (see section 7.6.1), estimating the spatial and temporal 'partial' ranges (φ_u, φ_t) and sills ($sill_u$, $sill_t$), and adding a 'nugget' discontinuity (τ_u, τ_t) at the origin to reflect spatial uncertainty if required.
- Having described the spatial and temporal behaviour separately, we examine the values of the semivariogram beyond the spatial and temporal ranges ($\hat{\gamma}_{u,t}(h_u > \phi_u, h_t > \phi_t)$) to find the global sill ($sill_g$).
- Calculate the weighting parameter k:

$$k = \frac{sill_g}{sill_u . sill_t} \tag{7.14}$$

- The full covariance model is then arrived at as follows:

$$\begin{aligned} &C_{u,t}(h_u, h_t) = k.C_u(h_u).C_t(h_t) \\ &where \\ &C_u(h_u) = sill_u - \hat{\gamma}_{u,t}(h_u, h_t = 0) \\ &C_t(h_t) = sill_t - \hat{\gamma}_{u,t}(h_u = 0, h_t) \end{aligned} \tag{7.15}$$

7.7.2 Non-Separable Space-Time Covariance: The Product-Sum Model

In order to fit a product-sum covariance model, we proceed as described by De Iaco et al (2001):

- First, only the simple spatial and temporal semivariograms are considered ($\hat{\gamma}_{u,t}(h_u, h_t = 0)$ and $\hat{\gamma}_{u,t}(h_u = 0, h_t)$ respectively), where h_u and h_t are the spatial and temporal separations. Valid semivariogram models must be fit to them (see section 7.6.1), estimating the spatial and temporal 'partial' ranges (φ_u, φ_t) and sills ($sill_u$, $sill_t$), and adding a 'nugget' discontinuity (τ_u, τ_t) at the origin to reflect spatial uncertainty if required.
- Having described the spatial and temporal behaviour separately, we examine the values of the semivariogram beyond the spatial and temporal ranges ($\hat{\gamma}_{u,t}(h_u > \phi_u, h_t > \phi_t)$) to find the global sill ($sill_g$).
- We then check the validity of the fitted model, using the values of $sill_u$, $sill_t$ and $sill_g$ via the diagnostics detailed in De Cesare et al (2001), to ensure the resulting space-time semivariance function is conditionally negative definite. We calculate three diagnostic values k_1, k_2 and k_3 as follows:

$$k_1 = \frac{sill_u + sill_t - sill_g}{sill_u . sill_t}$$
$$k_2 = \frac{sill_g - sill_t}{sill_u} \qquad \textbf{(7.16)}$$
$$k_3 = \frac{sill_g - sill_u}{sill_t}$$

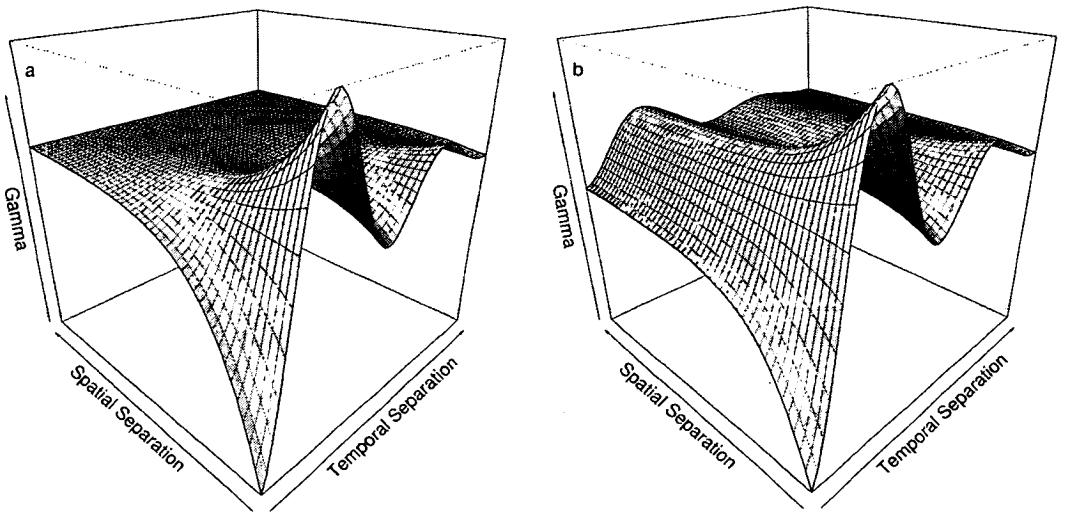

Figure 7.4 Comparison of spatiotemporal semivarogram representations: (a) product model (7.7.1). (b) product-sum model (7.7.2). Note the increased interaction in the product-sum model. Both plots share the same structures and parameters, and differ only in the spatiotemporal combination method.

- To ensure conditional negative definiteness of the resultant semivariogram is in necessary that $k_1 > 0$, $k_2 \geq 0$, and $k_3 \geq 0$. If the above diagnostic constraints are met, the RF model is permissible and may be used for estimation/simulation purposes.
- The full covariance model is then arrived at as follows:

$$C_{u,t}(h_u,h_t) = k_1.C_u(h_u).C_t(h_t) + k_2.C_u(h_u) + k_3.C_t(h_t)$$
$$\textit{where}$$
$$C_u(h_u) = sill_u - \hat{\gamma}_{u,t}(h_u,h_t = 0) \qquad (7.17)$$
$$C_t(h_t) = sill_t - \hat{\gamma}_{u,t}(h_u = 0,h_t)$$

A comparison of the product-sum and product representations is provided in Figure 7.4.

7.8 Spatio-Temporal Estimation

All of the interpolation methods implemented in the Edinburgh Space-Time Geostatistics package produce estimates through weighted linear combination of a subset of the data $Z = \{z_1(u,t)...z_n(u,t)\}$, selected on the basis of spatial and temporal distance from the estimation datum. Spatial effects are decomposed into a global trend m, and a high frequency autocorrelated residual component, formed from a weighted linear combination of the residuals. Therefore the only difference in the prediction algorithms is the method by which the weights (λ) are derived:

$$z^*(u,t) = m(u,t) + \sum_{i=1}^{n} \lambda_i(u,t)[z_i(u,t) - m(u,t)] \qquad \textbf{(7.18)}$$

7.8.1 Inverse Distance Weighting

Inverse distance weighted averages produce estimates of the variable of interest by linear combination of the observations, such that data points closer to the estimation location are ascribed more prominence than those further away. Weights are ascribed to a subset of the total data pool, such that the conditioning data follow a spatial power law. The weights are rescaled such that they sum to one, preventing the estimation exceeding the range of the conditioning data. Any power ω can be used, but most commonly an inverse squared power law is encountered in the manner of Newton's Gravity model; hence the alternative moniker 'Spatial Gravity Models'. Estimates are calculated as follows:

$$z^*(u,t) = \sum_{i=1}^{n} w_i(u,t).z_i(u,t)$$

where **(7.19)**

$$w_i(u,t) = \frac{1/d_i^{\omega}}{\sum_{i=1}^{n} 1/d_i^{\omega}}$$

Where w are the weights, and d_i is the separation distance between $z_i(u,t)$ and z^*. If the estimation location is coincident with an observation, the estimate takes the value of the observation. In the case of global trends, residual data may be interpolated, and the trend added back in after interpolation.

Currently *IDW.exe* does not incorporate temporally adjacent data into the conditioning data; estimates are produced one time step at a time from the available spatial neighbours.

7.8.2 Kriging Methods

Kriging refers to a set of is a multiple linear regression procedures by which the best linear unbiased estimate of an unobserved datum value is arrived at by the weighted linear combination of surrounding observations, such that the prediction error is minimized. A good introductory text is provided by Isaacs and Srivastava (1989);for a historical perspective, see Cressie (1990). The weights ascribed to each observation take into consideration the clustering of the data locations, and the proximity of each observation to the prediction location. These spatial effects are included via reference to the autocorrelation structure of the data set, as summarized by the semivariogram. The result of considering distances between the conditioning data is that points from over-sampled locations are down weighted.

Kriging is a regression procedure of the form $y = mx + c$. In standard notation, we write:

$$z^*(u,t) = \lambda(Z - m) + m \qquad \textbf{(7.20)}$$

Where z^* is the value of an unobserved spatio-temporal location u,t to be estimated, λ is the vector weights, Z is the vector of observations and m is the mean. Typically we work with a sub-set of observations, say the $n = 12$ closest observations to $z^*(u,t)$. In this case, m is the local mean m^*. Thus $z^*(u,t)$ is predicted by the sum of the local mean, plus the spatially autocorrelated deviation from that mean. Differences between Kriging methods reside in the m^* term of equation 7.20. An excellent summary of all Kriging methods described is included in Goovaerts (1999).

7.8.2.i Simple Kriging

Simple Kriging is used in the situation where the mean of the variable of interest m is known across the whole study region. This mean need not be the same at all locations, but the assumption is that the sampling design is sufficient to ensure that calculation of the mean is not affected by data clustering. The mean is subtracted from the observations prior to estimation, and the residual values are used to correct the estimation surface, by the addition of spatially coloured noise. The local correction is a function of the data locations (clustering) and the distance between the conditioning data and the estimation datum, imposed through the Kriging weights λ. The weights are arrived at by solving the following system of linear equations:

$$z^*(u,t) = m(u,t) + \sum_{i=1}^{n} \lambda_i(u,t).[z(u_i,t_i) - m(u,t)]$$

$$\sum_{i=1}^{n} \lambda_i(u,t).C[z(u_i,t_i) - z(u_j,t_j)] = C[z^*(u,t) - z(u_i,t_i)] \quad where \quad j = 1,...,n$$

(7.21)

Here $C[z(u_i,t_i)\text{-}z(u_j,t_j)]$ and $C[(z^*(u,t)\text{-}z(u_i,t_i)]$ are the covariance between observations, and the covariance between observations and the prediction location u,t respectively. These values are obtained by looking up the separation distance h against the semivariogram model. In the case of an underlying trend across the region of interest, the m can take the value of the deterministic trend, which is calculated in advance for each estimation datum.

7.8.2.ii Ordinary Kriging

In the case that the mean value is known in advance, we proceed by Simple Kriging (SK), and m takes the known value of the mean. However, more often the mean is unknown, or is not easily calculated in advance due to data clustering: Estimation then proceeds by ordinary Kriging (OK), where the unknown mean m must be estimated simultaneously with the autocorrelated residual component.

Usually we condition on a subset of n available data, and thus $m^*(u,t)$ represents the local mean of the variable of interest. Given that we only require constant mean and variance within the neighbourhood of the selected data, such moving window approaches allow some degree of robustness to the assumption of stationarity. The OK estimate is thus arrived at by solving the following system of equations:

$$z^*(u,t) = \sum_{i=1}^{n} \lambda_i(u,t).z(u_i,t_i)$$

$$\begin{cases} \sum_{i=1}^{n} \lambda_i(u,t).C[z(u_i,t_i) - z(u_j,t_j)] + \mu = C[z^*(u,t) - z(u_i,t_i)] \\ \sum_{i=1}^{n} \lambda_i(u,t) = 1 \end{cases} \quad \text{where} \quad j = 1,\ldots,n \qquad (7.22)$$

As before $C[z(u_i,t_i)\text{-}z(u_j,t_j)]$ and $C[(z^*(u,t)\text{-}z(u_i,t_i)]$ are the covariance between observations, and the covariance between observations and the prediction location u,t respectively. These values are obtained by looking up the separation distance h against the semivariogram model. The main difference between SK and OK is in the system of equations governing the calculation of λ. Equation system 7.21 is modified by the addition of a Lagrange multiplier μ, necessary to satisfy the un-biasness constraint that the weights sum to one.

7.8.2.iii Kriging With an External Drift

A more complex spatio-temporal regression model can be formulated by extending the framework established in equation 7.20 to include extra covariates in m^*. This leads to a family of Kriging systems referred to as Kriging with a trend (KT). Here m^* contains more terms than the intercept only solutions illustrated above: The m^* component of a KT system contains an intercept b_0, and k slope parameters $b_1 \ldots b_k$. This generalisation allows fitting of linear, polynomial, or Fourier type basis functions combined in arbitrarily complex trend models. However, in practice k typically ≤ 5, and trend models are restricted to low order polynomials (Deutsch and Journel 1998). This partitioning of the data into a large-scale trend component, and a stationary, spatially autocorrelated residual component is the rationale of non-stationary geostatistics:

$$z^*(u,t) = \lambda(Z - m^*) + m^*$$

where (7.23)

$$m^* = b_0 + \sum_{k=1}^{K} b_k S_k$$

Where z^* is value of the unobserved datum location u to be estimated, λ is the vector weights, Z is the vector of observations, b_0 is the intercept, b_k are slope parameters and S_k are vectors of auxiliary variables recorded at all observation and prediction locations $S_k = \{s_i^k(u,t)...s_n^k(u,t)\}$.

Universal Kriging (UK) is the simplest form of KT system, where m is a function of the coordinates, allowing large scale gradients to be dealt with by the Kriging system (i.e. non-stationary problems can be solved). The ordinary Kriging system can be seen as a special case of UK, where $k=0$ (Goovaerts, 1999).

Kriging with an external drift (KED) refers to the case where we use secondary covariates 'external' to the semivariance calculation for our data. Here we require that the variation of the secondary data be smoothly and linearly related to the variable of interest (Deutsch and Journel, 1998). The covariates must be sampled at all observation and all prediction locations.

Typically KED systems are restricted to a single covariate, although theoretically, any number of covariates may be included. The idea is that the extra covariates inform the interpolation, so that more easily available data, such as remote sensing observations, can be used to improve interpolation skill. The method may also be used to impose known physical trends on the interpolation, for example, the decrease in temperature with increased elevation (Hudson and Wackernagel 1994), or as a form

of model-data fusion, using model output as the external drift (e.g. Wackernagel 1998 p297).

Again, we usually condition on a subset of n data points, with $m^*(u,t)$ returning the local trend. Estimation proceeds by solving the following system of equations:

$$z^*(u,t) = \sum_{i=1}^{n} \lambda_i(u,t).z(u_i,t_i)$$

$$\begin{cases} \sum_{i=1}^{n} \lambda_i(u,t).C[z(u_i,t_i) - z(u_j,t_j)] + \mu_1(u,t) + \mu_2(u,t).s(u_j,t_j) \\ = C[z^*(u,t) - z(u_i,t_i)] \\ \sum_{i=1}^{n} \lambda_i(u,t) = 1 \\ \sum_{i=1}^{n} \lambda_i(u,t).s(u_i,t_i) = s(u,t) \end{cases} \quad \textit{where} \quad j = 1,\ldots,n \qquad \textbf{(7.24)}$$

Here we add a further constraint to equation system 7.22, requiring an extra Lagrange multiplier μ_2. This ensures that the dot product of the weights (λ) and the vector of secondary variable (S) equals the observed value of the secondary variable at the prediction location. It is possible to retrieve local values of the intercept and slope parameters with simple modifications to equation system 7.24 (see section 7.9.1.iii). This is particularly useful in the model-data fusion case, where model efficiency can be assessed locally by tracking deviations from $b_0 = 0$ and $b_1 = 1$.

Addition of extra trend terms would require an additional Lagrange multiplier for each term, involving minor code modifications. Further details and examples can be found in Wackernagel (1998).

7.9 Practical Aspects of Kriging

7.9.1.i Calculating Kriging weights

For all Kriging algorithms implemented, the solution of the linear equations to derive λ follows the same general pattern. An illustration of the technique in matrix formulation highlights the similarities between the various algorithms.

In order to retrieve λ from the observed data values, we first produce two distance tables OO_h and OE_h. Matrix OO_h is the square n by n distance matrix for the conditioning data, whilst vector OE_h contains the distances between the conditioning data and the estimation datum:

$$OO_h = \begin{bmatrix} h(z_1,z_1) & h(z_2,z_1) & . & h(z_n,z_1) \\ h(z_1,z_2) & h(z_2,z_2) & . & h(z_n,z_2) \\ . & . & . & . \\ h(z_1,z_n) & . & . & h(z_n,z_n) \end{bmatrix} OE_h = \begin{bmatrix} h(z_1,z^*) \\ h(z_2,z^*) \\ . \\ h(z_n,z^*) \end{bmatrix} \quad \textbf{(7.25)}$$

These distances are easily converted to covariances, by reference to the semivariogram model (see section 7.5.2.ii): Matrix OO is now the observation covariance matrix, and vector OE is the observation-estimation covariance vector. To calculate simple Kriging weights, we invert matrix OO, and multiply by vector OE:

$$\begin{bmatrix} \lambda_1 \\ \lambda_2 \\ . \\ \lambda_n \end{bmatrix} = \begin{bmatrix} C(z_1,z_1) & C(z_2,z_1) & . & C(z_n,z_1) \\ C(z_1,z_2) & C(z_2,z_2) & . & C(z_n,z_2) \\ . & . & . & . \\ C(z_1,z_n) & . & . & C(z_n,z_n) \end{bmatrix}^{-1} \times \begin{bmatrix} C(z_1,z^*) \\ C(z_2,z^*) \\ . \\ C(z_n,z^*) \end{bmatrix} \quad \textbf{(7.26)}$$

In the case of SK weights, the vector $\Lambda = \{\lambda_1 ... \lambda_n\}$ sums to zero. However, in the case of OK or KED, we require that the weights sum to one. The problem is one of

minimisation with a constraint, which can be achieved by *via* the use of Lagrange multipliers. The Lagrange multipliers allow us to solve for m simultaneously with the solution for the weights.

For each extra term in m, we require a Lagrange multiplier $\mathrm{M} = \{\mu_1 ... \mu_k\}$, where k is the number of model terms. In the case of simple Kriging $k=0$, whilst for ordinary Kriging $k=1$: We solve for the intercept only (null model) by adding an extra row and column to OO and OE in which all values equal one, except the bottom right element of OO which contains a zero. An additional row on the weights vector then accommodates the Lagrange multiplier:

$$\begin{bmatrix} \lambda_1 \\ \lambda_2 \\ . \\ \lambda_n \\ \mu \end{bmatrix} = \begin{bmatrix} C(z_1,z_1) & C(z_2,z_1) & . & C(z_n,z_1) & 1 \\ C(z_1,z_2) & C(z_2,z_2) & . & C(z_n,z_2) & 1 \\ . & . & . & . & . \\ C(z_1,z_2) & C(z_2,z_n) & . & C(z_n,z_n) & 1 \\ 1 & 1 & 1 & . & 0 \end{bmatrix}^{-1} \times \begin{bmatrix} C(z_1,z^*) \\ C(z_2,z^*) \\ . \\ C(z_n,z^*) \\ 1 \end{bmatrix} \qquad \textbf{(7.27)}$$

For more complex regression models $k>1$, and we implement the KED algorithm. Addition of terms follows the same pattern as above, augmenting OO and OE with extra rows and columns for the additional Lagrange multipliers. Retrieving λ for an arbitrarily complex regression model KED is then:

$$\begin{bmatrix} \lambda_1 \\ \lambda_2 \\ . \\ \lambda_n \\ \mu_1 \\ . \\ \mu_k \end{bmatrix} = \begin{bmatrix} C(z_1,z_1) & C(z_2,z_1) & . & C(z_n,z_1) & s_1^1 & . & s_1^k \\ C(z_1,z_2) & C(z_2,z_2) & . & C(z_n,z_2) & s_2^1 & . & s_2^k \\ . & . & . & . & . & . & . \\ C(z_1,z_n) & C(z_2,z_n) & . & C(z_n,z_n) & s_n^1 & . & s_n^k \\ s_1^1 & s_2^1 & . & s_n^1 & 0 & . & 0 \\ . & . & . & . & . & . & . \\ s_1^k & s_2^k & . & s_n^k & 0 & . & 0 \end{bmatrix}^{-1} \times \begin{bmatrix} C(z_1,z^*) \\ C(z_2,z^*) \\ . \\ C(z_n,z^*) \\ s_*^1 \\ . \\ s_*^k \end{bmatrix}$$

(7.28)

Where k is typically less than five. S^1 is normally a vector of ones, to solve for the intercept, whilst S^2 to S^k are vectors of secondary variables, which are linearly related to the variable of interest (see section 7.8.2.iii). Again, the bottom right section of OO is filled with zeros.

Sometimes a multiple intercept model is desirable, e.g. to impose different means by vegetation or soil type. In this case, vectors S^1 *to* S^k contain dummy variables, with binary coding for the factor levels. Mixed effects models are readily incorporated by combination of the above techniques. The only limit to the complexity of the model is the need to invert matrix OO, a time consuming and not always stable process: As the complexity of the model increases, the likelihood of producing a singular (degenerate) matrix OO increases. Again, the principle of parsimony is a good guiding rule.

Currently, the programs in the Edinburgh Space-Time Geostatistics package only allow for simple linear models with $k<2$. However, more complex models are possible with minor alteration to the code.

7.9.1.ii Kriging Variances

One of the major attractions of the Geostatistical method is the ability to retrieve estimation variances. Kriging variances are easily obtained by subtracting the dot product of the observation-estimation covariance vector OE and the weights vector Λ from the global sill ($C_{0,0}$). In the case of OK or KED, the full augmented vectors are used, so the resulting variance takes into account the uncertainty associated with the trend model m:

$$\sigma^2(u,t) = C_{0,0} - \begin{bmatrix} \lambda_1 \\ \lambda_2 \\ . \\ \lambda_n \\ \mu_1 \\ . \\ \mu_k \end{bmatrix}^T \times \begin{bmatrix} C(z_1,z^*) \\ C(z_2,z^*) \\ . \\ C(z_n,z^*) \\ s_*^1 \\ . \\ s_*^k \end{bmatrix} = C_{0,0} - \sum_{i=1}^{n} \lambda_i C(z_i,z^*) - \sum_{j=1}^{k} \mu_j s_*^j \qquad (7.29)$$

7.9.1.iii Parameter Retrieval and Filtering

In the case of OK and KED, it is often desirable to retrieve the local parameters $\mathbf{B}^* = \{b_0^* ... b_k^*\}$ from equation 7.23. In the case of OK, we may be interested in declustered local mean of the n conditioning data; in this case we must filter off the high frequency autocorrelated noise ε to obtain the value m. This is easily achieved by modification of the Kriging weights (equation 7.27) to ignore the effect of the conditioning data. We filter ε by setting the first n elements of OE to zero:

$$\begin{bmatrix} \lambda_1 \\ \lambda_2 \\ . \\ \lambda_n \\ \mu \end{bmatrix} = \begin{bmatrix} C(z_1,z_1) & C(z_2,z_1) & . & C(z_n,z_1) & 1 \\ C(z_1,z_2) & C(z_2,z_2) & . & C(z_n,z_2) & 1 \\ . & . & . & . & . \\ C(z_1,z_2) & C(z_2,z_n) & . & C(z_n,z_n) & 1 \\ 1 & 1 & . & 1 & 0 \end{bmatrix}^{-1} \times \begin{bmatrix} 0 \\ 0 \\ . \\ 0 \\ 1 \end{bmatrix} \qquad (7.30)$$

The value of m is then Kriged with the modified vector Λ.

In the case of KED, the value m is retrieved as above, by setting elements $OE_{1:n}$ to zero, and $OE_{n+1:k}$ to ones. Individual KED parameters $\mathbf{B}^* = \{b_i^* ... b_k^*\}$ can be retrieved by substituting OE for the Kronecker delta function ($\delta_{n+i,j}$) centred on the i^{th}

trend parameter, which is one for OE'_{n+i} and zero otherwise; i.e. OE' contains a binary coding for the parameter we wish to retrieve:

$$OE' = \delta_{n+i,j} \begin{cases} 1 & if \quad j = n+i \\ 0 & if \quad j \neq n+i \end{cases} \quad where \quad j = 1...n+k \tag{7.31}$$

7.9.1.iv Exactitude of Kriging

In general, discussions of Kriging specify the nugget variance at $h=0$ as zero, and τ elsewhere (Goovaerts 1997). This formulation ensures that the Kriging estimate for a location at which a conditioning observation exists is exactly equal to the observed value. In this sense, Kriging is referred to as an 'exact interpolator'. This is desirable if we believe our data is infallible, and assumes the primacy of the data over the specified RF model. This approach leads to very 'spiky' surfaces where observations are collocated with grid nodes, due to the discontinuity in the semivariogram model.

In reality, we are faced with imperfect data and an imperfect model representation; whilst the observations correct the local model m in the kriging estimate, we may also wish m to correct the observations when z^* is collocated with a conditioning datum. If we allow the nugget variance to equal τ for all h we no longer strictly honour the observations, and the estimate z^* at an observation location is equivalent to a spatio-temporal assimilation of the observations with m. In this case the estimate at an observation location will be heavily weighted towards the observed value, but the estimate will be drawn towards a value concurrent with the surrounding observations (subject to the semivariogram) and any additional external variables included in the trend model. The degree to which surrounding observations and m correct the data is specified by the magnitude of τ.

It is our contention that the model data fusion approach resultant from allowing a non-zero nugget effect when $h=0$ confers a considerable advantage for the poorly or pseudo-replicated data sets generally used in upscaling studies, and from which the intrinsic stationarity assumption arises (see section 7.4). As such, all semivariance models in the Edinburgh Space-Time Geostatistics package are implemented with a nugget effect equal to τ for all separation distances.

7.10 Assessing Spatio-Temporal Uncertainty

When simple estimation is the goal of a study, evaluation of the RF at a set of locations via Kriging provides an unbiased estimate of the variable of interest, and a Kriging variance, reflecting the uncertainty associated with the draw from the RF. The Kriging variance reflects our prior conception of the data; that it is normally distributed, intrinsically stationary, and autocorrelated with a known and accurately described covariance structure, as inferred from the semivariogram.

Although values derived from Kriging provide optimal estimates in the least squares sense, the results tend to be smoothed, losing the extremes of the data distribution. This smoothing is non-uniform, and occurs mainly at locations separated by large distances from the conditioning data; thus local variability appears (non-intuitively) greater where more observations are present (Goovaerts 1997). Furthermore, the semivariogram is only honoured if we compare observation locations with estimation locations, although short scale variation may be smoothed by the Kriging algorithm: In general Kriging estimates do not reproduce the semivariogram globally, although these effects may be mediated to some degree by *post-hoc* processing (Olea and Pawlowsky 1996).

Whilst Kriging variances appropriately describe model uncertainty, they do not directly relate to error in the sense of model data divergence. In fact, the Kriging variances are arrived at by reference only to the spatio-temporal arrangement of data values, and ignore the data values entirely. In this sense the Kriging vaiance is essentially a ranking score of the data configuration (Journel and Rossi 1989). This is not entirely satisfactory if the goal of the study is to make inferences on the errors associated with estimation of the variable of interest, e.g. when the resulting estimated fields are to be used as inputs to a model; a common application of upscaled surfaces. In this case, a set of random draws from the spatio-temporal RF *via* simulation is more appropriate. One such method of drawing realisations from the RF is *Sequential Gaussian Simulation.* Discussions of alternatives can be found in (Deutsch and Journel 1998).

7.10.1 Sequential Gaussian Simulation

Sequential Gaussian simulation can be employed in order to produce estimates of local error which reflect the data values, and globally preserve the 'texture' of the data variability. The procedure is very similar to the Kriging methods outlined above, with one critical difference: Upon estimation, a draw from the RV $z^*(u,t)$ is added to the data heap used to condition subsequent estimates. Thus as we step through the estimation locations, the size of the conditioning data pool increases, and each estimate is conditionally dependant on all other values in the estimation field. The algorithm functions as follows:

1. Initialise a random visiting schedule for the grid of G locations, with a data heap of n observations $Z = \{z_1(u,t)...z_n(u,t)\}$. Initialise with $i=1$.
2. Visit the i^{th} node of the grid and estimate the expectation and variance *via* Kriging conditioned on the values in the data heap.

3. Draw a random value from the Gaussian distribution of the node, defined by the Kriging estimate (mean) and Kriging variance. The resultant value was the SGS estimate z^*_i.
4. The realization z^*_i was then treated as an observation for subsequent estimates, and added to the data heap ($n+i$ conditioning data).
5. Iterate from 2 until all grid locations were visited ($i=G$).

As in all geostatistical techniques, it is possible to incorporate covariates into the simulations. Randomisation of the visiting schedule ensures each field simulated from the RF will be a unique realisation of the spatio-temporal model, whilst conditioning on all values in the heap ensures reproduction the semivariogram globally.

Sequential Gaussian simulation is available in the Edinburgh Space-Time Geostatistics package using the *Gaussim.exe* program.

7.11 Program Notes and Instructions

7.11.1 IDW.exe

7.11.1.i Data format

All input and output to *IDW.exe* is handled via tab delimited text files. Data are supplied with a strict format: The first line contains a heading in inverted commas. The second line contains, seven column names, and subsequent lines contain the sequence of observations. Missing data flags are not supported. Each data table entry must contain a unique observation ID, a station ID, a sequence of three spatio-temporal coordinates, an observation value and a secondary mean/trend value. Observation Ids

(OID) identify each unique datum, whilst station IDs (SID) identify the time series to which each observation belongs:

"3164 January temperature observations from 112 sites across Oregon, USA"

OID	SID	EAST	NORTH	TIME	TEMP.C	MEAN.C
1	1	633717.8	4878503	1	7.778	3.429
2	1	633717.8	4878503	2	6.110	1.836
3	1	633717.8	4878503	3	6.672	3.319
...						
3163	112	614058.7	4921431	30	-4.693	1.940
3164	112	614058.7	4921431	31	6.679	4.661

7.11.1.ii Notes

The mean is removed from the observations by the program prior to interpolation then added to the estimates before output. As such, the observation values should be raw.

7.11.1.iii Grid file

IDW.exe requires a list of the estimations coordinates for interpolation. Coordinates should be supplied as a tab delimited text file containing a header followed by a list of spatiotemporal coordinates and a mean function. The file must be in the following format:

EAST	NORTH	TIME	MEAN
562618	4903722	1	3.429
563618	4903722	1	3.429
564618	4903722	1	3.429
...			
661618	5003722	31	4.661
662618	5003722	31	4.661

The secondary data may contain the (local) mean or the values of a trend model.

7.11.1.iv Parameter file

IDW.exe is parameterised with a tab delimited text file laid out in strict format:

```
FILENAMES [Data,Grid,Output]:
~/ED_ST_Geostats/Data/Data.txt
~/ED_ST_Geostats/Data/Grid.txt
~/ED_ST_Geostats/Outputs/IDW_out.txt

WEIGHTING FUNCTION:
2

MODE [0=Debug,1=Default,2=Jack-knife]:
1

SEARCH STRATEGY [Neighbours]:
16
```

- Lines 2:4 contain the path and filename of the data file, grid file and output file respectively.
- Line 7 contains the power to use for inverse distance weighting
- Line 10 contains a mode switch, selecting between debug, default or jack-knife modes:
- Debug: Returns a screen prompt containing information on the conditioning data and interpolation result for each point in the grid file. This is a good way to experiment with parameterisation of the program. Results are stored in the output file.
- Default: Interpolates each point in the grid file in turn with minimal output to screen. Results are stored in the output file.
- Jack-knife: Temporarily excludes one data point at a time from the observations, and estimates its value from the remaining data set. This is a good way to assess the interpolation skill given the selected parameters. Results are stored in a modified output file.

- Line 13 contains the number of conditioning data to use in the estimation: the *n* data points closest to the estimation grid coordinate are selected.

7.11.1.v Output file

IDW.exe returns a tab delimited text file containing various pieces of information on the interpolation, depending whether the program was run in debug/default or Jack-knife mode. Standard output contains the following columns:

- Columns 1:3 contain the spato-temporal coordinates of the datum.
- Column 4: The IDW estimate.
- Column 5: The supplied trend value.
- Column 6: The interpolated residual value (estimate minus the trend).
- Column 7: The nearest neighbour distance.
- Column 8: The mean distance of the conditioning data.
- Column 9: The SID of the nearest conditioning datum.

When running in Jack-knife mode, the following columns are returned:

- Column 1: The SID of the Jack-knifed observation.
- Columns 2:4 contain the spato-temporal coordinates of the datum.
- Column 5: The IDW estimate.
- Column 6: The supplied trend value.
- Column 7: The interpolated residual value (estimate minus the trend).
- Column 8: The observed value.
- Column 9: The error (observed minus estimated).
- Column 10: The nearest neighbour distance.
- Column 11: The mean distance of the conditioning data.

- Column 12: The SID of the nearest conditioning datum.

7.11.2 Geostats.exe

7.11.2.i Data format

All input and output to *Geostats.exe* is handled via tab delimited text files. Data are supplied with a strict format: The first line contains a heading in inverted commas. The second line contains, seven column names, and subsequent lines contain the sequence of observations. Missing data flags are not supported. Each data table entry must contain a unique observation ID, a station ID, a sequence of three spatio-temporal coordinates, an observation value and a secondary value. Observation Ids (OID) identify each unique datum, whilst station IDs (SID) identify the time series to which each observation belongs:

"3164 January temperature observations from 112 sites across Oregon, USA"

OID	SID	EAST	NORTH	TIME	TEMP.C	MEAN.C
1	1	633717.8	4878503	1	7.778	3.429
2	1	633717.8	4878503	2	6.110	1.836
3	1	633717.8	4878503	3	6.672	3.319
...						
3163	112	614058.7	4921431	30	-4.693	1.940
3164	112	614058.7	4921431	31	6.679	4.661

7.11.2.ii Notes

In the case of SK the mean is removed from the observations by the program prior to interpolation, then added to the estimates before output. As such, the observation values should be raw, and the secondary value should contain the (local) mean.

SK can be used to incorporate complex trend models or remotely sensed products with the data; in this case the secondary data values should contain model

predictions for each datum. Again, raw observations of the primary variable should be supplied.

In the case of OK, the secondary data value is redundant. However, the program will encounter an error if the column is not filled; a reference value may be included, or zero padding employed.

If global trends are present and the user wishes to interpolate the residuals with OK, trends should be removed from the data prior to analysis with *Geostats.exe* and added into the estimates manually.

In the case of KED, the secondary value can be any auxiliary data linearly related to the primary variable. Again, raw observations of the primary variable should be supplied.

7.11.2.iii Grid file

The *Geostats.exe* grid file is identical in format to that of *IDW.exe*. However, in the case of *Geostats.exe*, the purpose of the secondary data changes with the Kriging method selected.

In the case of SK, the secondary data values are used in an identical fashion to *IDW.exe*, i.e. the interpolated residuals are added to the grid secondary data value to form the estimate.

In the case of OK, the secondary data value is redundant. However, the program will encounter an error if the column is not filled; a reference value may be included, or zero padding employed.

In the case of KED, the secondary data value contains the auxiliary variable, which must be known at all observation and grid locations.

7.11.2.iv Parameter file

Parameters are supplied to *Geostats.exe* in a tab delimited text file with strict format:

```
FILENAMES [Data,Grid,Output]:
~/ED_ST_Geostats/Data/Data.txt
~/ED_ST_Geostats/Data/Grid.txt
~/ED_ST_Geostats/Outputs/KED_out.txt

METHOD [0=SK,1=OK,2=KED]
2

MODE [0=Debug,1=Default,2=Jack-knife]:
1

SEARCH STRATEGY [Neighbours,Window]:
32      7

STRUCTURES [Spatial,Temporal]:
2        1

TAU [Spatial,Temporal]:
0.02    0.0

GLOBAL SILL:
32.46

COVARIANCE MODEL [0=Product,1=Product-Sum]:
1

Spatial             ]---------------- Theta -----------------[  Rotation
=============================================================================
Spherical              3.01         9.67          9.67      0.0       0.0
Exponential            6.99        196.55        196.55     0.0       0.0

Temporal             ]------------ Theta ------------[
=====================================================
Exponential           23.13         6.6           0.0
```

- Lines 3:4 specify the data file, grid file and output file names respectively
- Line 7 contains a mode switch to select between the Simple Kriging (SK), Ordinary Kriging (OK) and Kriging with an External Drift (KED) algorithms.

- Line 10 contains a mode switch, selecting between debug, default or jack-knife modes:
    - Debug: Returns a screen prompt containing information on the conditioning data and interpolation result for each point in the grid file. This is a good way to experiment with parameterisation of the program. Results are stored in the output file.
    - Default: Interpolates each point in the grid file in turn with minimal output to screen. Results are stored in the output file.
    - Jack-knife: Temporarily excludes one temporal vector at a time from the observations, and estimates its values from the remaining data set. This is a good way to assess the interpolation skill given the selected parameters. Results are stored in a modified output file.
- Line 13 parameterises the search strategy: it should consist of two integer values enumerating the number of data values to select from each time step, and the size of the temporal window to use.
    - Neighbours specifies the number of values to select from each window increment; the total number of conditioning data is therefore *neighbours+(neighbours*window)*.
    - Window specifies the number of timesteps to include in the search. The strategy is ± *window*, so a value of 7 will incorporate data from a one fortnight window.
- Line 16 contains two integer values specifying the number of semivariogram structures (not including the nugget) to implement in space and time respectively.

- Line 19 contains the nugget variances for the spatial and temporal semivariograms respectively.
- Line 22 contains the global sill.
- Line 25 is a binary switch to select between the separable product, or non-separable product-sum covariance models.
- Lines 29 onwards specify the semivariogram models in space and time.

7.11.2.v Semivariogram specification

- ***Spatial model specifictaion***

Each line of the semivariogram specification should contain six elements: a structure name, a vector of four parameters, and a rotation parameter.

- Structure name: Linear, Power, Exponential, Spherical, Gaussian, Quadratic, Hole or Dampened Hole (see section 7.6.1).
- Theta1 specifies the contribution of the structure, and can take any non-zero real value.
- Theta2 and Theta3 are the ranges of the minor and major semi-axes of the anisotropy ellipse respectively. In the case of the linear and power models, these values are redundant, and can be zero padded.
- Theta4 is an auxiliary parameter required by some models, taking on the following values:
- The power value ω for the powered exponential and power models.
- The dampening length for the dampened hole model.
- Rotation: A rotation parameter to specify the direction of the major axis of variation in degrees from north (north = 0).

- ***Temporal Model Specification***

Each line of the temporal model specification should contain a list of four elements: A structure name, and a sequence of three parameters.

- Structure name, as above.
- Theta1 is the contribution of each structure of the model.
- Theta2 is the range of the structure.
- Theta3 contains auxiliary parameters, required by some models: See above.

7.11.2.vi Output file

Geostats.exe returns a tab delimited text file containing various pieces of information on the interpolation, depending whether the program was run in debug/default or Jack-knife mode. Standard output contains the following columns:

- Columns 1:2 contain the spatial coordinates of the datum.
- Column 3: The supplied secondary value.
- Column 4: The temporal coordinate.
- Column 5: The local mean *m*.
- Column 6: The Kriging estimate.
- Columns 7:8 contain the Kriging variance and standard deviation respectively.
- Column 9:10 contain the retrieved intercept and slope parameters when using KED.
- Column 11: The nearest neighbour distance.
- Column 12: The mean distance of the conditioning data.
- Column 13:The mean secondary value of the conditioning data.

- Column 14: The SID of the nearest conditioning datum.

When running in Jack-knife mode, the following columns are returned:

- Column 1: The SID of the Jack-knifed temporal vector.
- Columns 2:3 contain the spatial coordinates of the datum.
- Column 4: The supplied secondary value.
- Column 5: The temporal coordinate.
- Column 6: The observed value.
- Column 7: The local mean m.
- Column 8: The Kriging estimate.
- Columns 9:10 contain the Kriging variance and standard deviation respectively.
- Column 11:12 contain the retrieved intercept and slope parameters when using KED.
- Column 13: The Jack-knife error (observed value – Kriging estimate).
- Column 14: The nearest neighbour distance.
- Column 15: The mean distance of the conditioning data.
- Column 16: The SID of the nearest conditioning datum.

7.11.3 Gaussim.exe

Input and output formats for *Gaussim.exe* are identical to those of *Geostats.exe.*

7.11.3.i Parameter File

```
FILENAMES [Data,Grid,Output]:
~/ED_ST_Geostats/Data/Data.txt
~/ED_ST_Geostats/Data/Grid.txt
~/ED_ST_Geostats/Outputs/Simulation

METHOD [0=SK,1=OK,2=KED]
2

MODE [0=Debug,1=Default,2=Jack-knife]:
1

SEARCH STRATEGY [Neighbours,Window]:
32      7

STRUCTURES [Spatial,Temporal]:
2        1

TAU [Spatial,Temporal]:
0.02    0.0

GLOBAL SILL:
32.46

COVARIANCE MODEL [0=Product,1=Product-Sum]:
1

SIMULATIONS
1000

Spatial             ]---------------- Theta -----------------[  Rotation
=============================================================================
Spherical              3.01         9.67          9.67       0.0       0.0
Exponential            6.99        196.55        196.55      0.0       0.0

Temporal            ]------------ Theta ------------[
=====================================================
Exponential           23.13         6.6           0.0
```

The file is identical to the *Geostats.exe* parameter file, with the addition of the SIMULATIONS heading on line 27. The desired number of realisations from the specified RF should be entered on line 28. The program will automatically append the simulation number and a *.txt* file extension to the filename specified on line 4.

7.12 Acknowledgements

I would like to thank Pierre Goovaerts and Hans Wackernagel for their helpful comments and insights when writing the software.

7.13 References

Christakos, G. 1984. On the problem of permissible covariance and variogram models. Water Resources Research 20:251-265.

Christakos, G. 2000. Modern Spatiotemporal Geostatistics. Oxford University Press, Oxford; New York.

Clark, I. 1979. Practical Geostatistics. Applied Science Publishers, London.

Cressie, N. 1984. Median polish kriging. Biometrics 40:1187-1187.

Cressie, N. 1985a. Fitting variogram models by weighted least-squares. Journal of the International Association for Mathematical Geology 17:563-586.

Cressie, N. 1985b. When are relative variograms useful in geostatistics. Journal of the International Association for Mathematical Geology 17:693-702.

Cressie, N. 1990. The origins of kriging. Mathematical Geology 22:239-252.

Cressie, N., and H. C. Huang. 1999. Classes of nonseparable, spatio-temporal stationary covariance functions. Journal of the American Statistical Association 94:1330-1340.

Cressie, N., and D. L. Zimmerman. 1992. On the Stability of the geostatistical method. Mathematical Geology 24:45-59.

Cressie, N. A. C. 1991. Statistics for Spatial Data. Wiley, New York; Chichester.

De Cesare, L., D. E. Myers, and D. Posa. 2001a. Estimating and modeling space-time correlation structures. Statistics & Probability Letters 51:9-14.

De Cesare, L., D. E. Myers, and D. Posa. 2001b. Product-sum covariance for space-time modeling: an environmental application. Environmetrics 12:11-23.

De Cesare, L., D. E. Myers, and D. Posa. 2002. Fortran programs for space-time modeling. Computers & Geosciences 28:205-212.

De Iaco, S., D. E. Myers, and D. Posa. 2001. Space-time analysis using a general product-sum model. Statistics & Probability Letters 52:21-28.

De Iaco, S., D. E. Myers, and D. Posa. 2003. The linear coregionalization model and the product-sum space-time variogram. Mathematical Geology 35:25-38.

Deutsch, C. V., and A. G. Journel. 1998. Gslib: Geostatistical software library and user's guide. Oxford University Press, New York.

Diggle, P. J., P. J. Ribero, and O. F. Cristensen. 2002. An introduction to model based geostatistics. *in* J. Møller, editor. Spatial Statistics and Computational Methods. Springer-Verlag, New York.

Dimitrakopoulos, R. E. 1994. Geostatistics For the Next Century: International Forum: Selected Papers. Kluwer Academic.

Gneiting, T. 2002a. Compactly supported correlation functions. Journal of Multivariate Analysis 83:493-508.

Gneiting, T. 2002b. Nonseparable, stationary covariance functions for space-time data. Journal of the American Statistical Association 97:590-600.

Gneiting, T., M. G. Genton, and P. Guttorp. 2005. Geostatistical space-time models, stationarity, separability and full symmetry. University of Washington, Washington.

Gneiting, T., and M. Schlather. 2004. Stochastic models that separate fractal dimension and the Hurst effect. Siam Review 46:269-282.

Goovaerts, P. 1992. Factorial kriging analysis - a useful tool for exploring the structure of multivariate spatial soil information. Journal of Soil Science 43:597-619.

Goovaerts, P. 1997. Geostatistics for Natural Resources Evaluation. Oxford University Press, New York; Oxford.

Goovaerts, P. 1999. Geostatistics in soil science: state-of-the-art and perspectives. Geoderma 89:1-45.

Gringarten, E., and C. V. Deutsch. 2001. Variogram interpretation and modeling. Mathematical Geology 33:507-534.

Haining, R. P. 2003. Spatial Data Analysis: Theory and Practice. Cambridge University Press, Cambridge, UK; New York.

Heuvelink, G. B. M., and R. Webster. 2001. Modelling soil variation: past, present, and future. Geoderma 100:269-301.

Hudson, G., and H. Wackernagel. 1994. Mapping temperature using kriging with external drift - theory and an example from Scotland. International Journal of Climatology 14:77-91.

Isaaks, E. H., and R. M. Srivastava. 1989. Applied Geostatistics. Oxford University Press, New York; Oxford.

Journel, A. G., and M. E. Rossi. 1989. When do we need a trend model in kriging. Mathematical Geology 21:715-739.

Kyriakidis, P. C., and A. G. Journel. 1999. Geostatistical space-time models: A review. Mathematical Geology 31:651-684.

Kyriakidis, P. C., and A. G. Journel. 2001a. Stochastic modeling of atmospheric pollution: a spatial time-series framework. Part I: methodology. Atmospheric Environment 35:2331-2337.

Kyriakidis, P. C., and A. G. Journel. 2001b. Stochastic modeling of atmospheric pollution: a spatial time-series framework. Part II: application to monitoring monthly sulfate deposition over Europe. Atmospheric Environment 35:2339-2348.

Leduc, A., Y. T. Prairie, and Y. Bergeron. 1994. Fractal dimension estimates of a fragmented landscape - sources of variability. Landscape Ecology 9:279-286.

Matheron, G. 1962. The theory of regionalized variables and its application. Centre de morphologie mathematique, Eisle National Superieure des Mines de Paris, Paris.

Mcbratney, A. B., and R. Webster. 1986. Choosing functions for semi-variograms of soil properties and fitting them to sampling estimates. Journal of Soil Science 37:617-639.

Olea, R. A., and V. Pawlowsky. 1996. Compensating for estimation smoothing in kriging. Mathematical Geology 28:407-417.

Palmer, M. W. 1988. Fractal geometry - a tool for describing spatial patterns of plant communities. Vegetatio 75:91-102.

Tobler, W. R. 1970. A computer movie simulating urban growth in the Detroit region. Economic Geography 46:234-240.

Tukey, J. W. 1977. Exploratory data analysis. Addison-Wesley, Reading, Mass. ; London.

Wackernagel, H. 1998. Multivariate Geostatistics: An Introduction With Applications, 2nd completely rev. edition. Springer, Berlin; London.

8. Discussion

The primary aim of this thesis was to examine and reduce the sources of uncertainty for the estimation of regional to catchment scale carbon budgets. We initially partitioned this task into the influence of the parameterisation of the exchange surface (primarily quantified by LAI), and uncertainties in meteorological driving variables. An investigation of these issues was followed by an analysis of the relative magnitude of uncertainties in the C budget attributable to parameterisation and driver errors respectively. We demonstrated that the dominant source of uncertainty in the final analysis of the C budget was land surface parameterisation, although issues of bias in driver upscaling remain to be resolved.

Land surface parameterisation must be improved to make reliable estimates of C budgets on a regional scale. In Chapter 3 we report persistence of the functional form and approximate error magnitude for LAI NDVI relationships at multiple scales (Williams et al., 2008). However, despite this promising result we demonstrate that it is insufficient to rely on EO derived vegetation indices to provide land surface parameterisations, with weak but significant relationships between key ecosystem variables (LAI) and NDVI (chapters 3 and 4).

On a global scale, DGVMs tend to parameterise the land surface based on a vegetation classification of plant functional types (PFTs) (e.g. Woodward et al., 1995). Results from chapter 4 seem to bear out the validity of this approach. However, the clear variation within PFTs evident in chapter 4 indicates that community dependent topographic relationships may play an important role in regional land surface parameterisation.

Approaches based on topographic predictors of LAI were examined in Chapter 4, and appear to offer stronger relationships than EO based approaches. We report at ~50% stronger relationship between LAI and topography than LAI and NDVI. In particular, scale dependent relationships between elevation and shelter (as quantified by TOPEX) are good predictors of LAI.

It is important to remember the dictum that correlation does not imply causation, and whilst statistical relationships between LAI and topography may be useful in a descriptive sense, it is important to develop a mechanistic understanding of the ecophysiology at work in order to successfully implement these findings in an operational sense. It is likely that the large-scale elevation trend is related to temperature, whilst the microscale relationship between LAI and exposure may be explained by local variations in snow accumulation, thaw dates and hence soil nutrient distributions (Wielgolaski et al., 1975). Further experimental work at Abisko is necessary to build process-based understanding of these issues for future modelling work.

We compared various methods of regionalising LAI in the Arctic tundra, to see if statistically optimal interpolation techniques such as Kriging could outperform simpler and computationally cheaper regression techniques. We report broadly similar interpolation skill for various Kriging techniques, inverse distance weighting (IDW) and linear regression, despite the utilisation of different combinations of data streams.

Despite results in chapter 3, where geostatistical methods provided no improvement in interpolation skill over simpler upscaling techniques, geostatistics are likely to remain an important part of any regionalised modelling activity. A common misconception about geostatistical methods is that they are limited to smoothly varying Gaussian fields with a constant mean: Geostatistical methods exist to deal with non-normality (Armstrong and Matheron, 1986a; Armstrong and Matheron, 1986b), discrete

boundary transitions (Goovaerts and Journel, 1995; Heuvelink and Webster, 2001) and secondary covariates (Goovaerts, 2000; Hudson and Wackernagel, 1994).

Geostatistics provide the ability to assimilate autocorrelated observations into arbitrarily complex regression models, making the techniques an ideal choice for future studies combining PFTs derived from EO vegetation classifications, radiance derived vegetation indices and topographic trends. Mixed effect type models (Pinheiro and Bates, 2000) are readily specified with slight modifications to the standard geostatistical methodologies (see chapter 7.8.2 and 7.9.1.i), providing a framework for the integration of such disparate data sources. Thus geostatistics remain a relevant research area given the significant advantage of offering spatial estimates of parameter variance, which is a key step to developing the potential for spatial data assimilation.

In the second section of the thesis, we turned our attention to problems of upscaling meteorological driving variables. There is a long tradition of such interpolation work in the literature (Ashraf et al., 1997; Hudson and Wackernagel, 1994; Running et al., 1987; Thiessen, 1911; Thornton et al., 1997), although in general this has been attempted at coarser spatio-temporal resolutions (Fuentes et al., 2006). Regionalising precipitation fields is considerably more problematic at fine temporal resolution (Thornton et al., 1997), and we report consistently poor regionalisation of rainfall fields (chapter 5). Geostatistics have previously been reported to provide slight improvements over other methods of regionalisation, and we find broadly similar results to those previously published (Diodato and Ceccarelli, 2005; Goovaerts, 2000): Although geostatistical methods provide an improved analysis over IDW approaches, the relative improvement may be small (Thornton et al., 1997); for example in the case of precipitation our geostatistical analysis provided worse results than IDW.

We implemented state of the art spatio-temporal geostatistical techniques to investigate potential improvements to high-resolution meteorological fields over simpler Kriging techniques that ignore temporal autocorrelation. In every case we report a poorer interpolation skill for the spatio-temporally explicit regionalisations (chapter 5). As such, one may question the merit of geostatistical techniques given their perceived complexity, computational cost and marginal improvement in interpolation skill. However, we reiterate the importance of attaching estimates of uncertainty to regionalised variables, which Kriging and its variants (geostatistical techniques subsume spline fitting methods (Matheron, 1981; Serra, 1987)) are uniquely able to achieve.

We examined the effect of *post hoc* temporal data aggregation on estimated fields of meteorology, and report a decrease in error as the size of temporal window increases. This led us to hypothesise that the somewhat large interpolation errors may cancel out over time in the model structure. Specifically, we hypothesised that integrating processes in the model structure would 'smooth out' errors, whilst rapid processes which react instantaneously to driving variables would display greater error (chapter 6). We report that temperature was the largest component of the meteorological uncertainty, supporting the hypothesis that instantaneous effects dominate the uncertainty of the NEE trajectory. Despite precipitation having the largest uncertainty and poorest r^2 when compared with observations, the resultant impact on NEE uncertainty was minimal. We demonstrated the temporal buffering of uncertainty attributable to precipitation, and suggest this is because the effect of precipitation on vegetation is manifested through drought; an integrative effect related to soil texture and water holding capacity.

The second aim of the thesis was to compare the magnitude of the effects of parameterisation and driver uncertainty on the total C budget. In chapter 6 we present an analysis with significant novelty, being the first study to implement an Ensemble

Kalman Filter (ENKf) to provide constrained parameter uncertainty distributions for a C dynamics model. Furthermore it is the first study to implement spatio-temporal geostatistical simulation *via* the product-sum covariance model (De Cesare et al., 2001) to provide an ensemble of probable meteorological scenarios. We report that despite sizable uncertainties in driver fields, only small NEE uncertainties were attributable to meteorology. This was true even under extreme data scarcity, simulated by ignoring all available data <100 km from the study site. Conversely, the uncertainties associated with parameterisation accounted for up to 50% of the total NEE predicted by the model.

The ability of data assimilation to correct parameters based on incoming data streams was demonstrated in Chapter 6, indicating that the tools necessary to constrain and reduce the uncertainties associated with the exchange surface are already in place. The ability of DA techniques to reduce model uncertainty has been proven elsewhere (Evensen, 1994; Quaife et al., 2008; Williams et al., 2005), and such model correction is likely to continue to be important with the arrival of new EO data streams e.g. NASAs Orbiting Carbon Observatory (OCO) (Crisp and Johnson, 2005), and ESAs forthcoming Earth explorer mission (e.g. BIOMASS) (Bensi et al., 2007). It is the opinion of the author that geostatistical and DA technologies are amongst the most promising and relevant areas of C cycle science at present, and are worthy of considerable attention in the future.

8.1 References

Armstrong, M. and Matheron, G., 1986a. Disjunctive kriging revisited 1. Mathematical Geology, 18(8): 711-728.

Armstrong, M. and Matheron, G., 1986b. Disjunctive kriging revisited 2. Mathematical Geology, 18(8): 729-742.

Ashraf, M., Loftis, J.C. and Hubbard, K.G., 1997. Application of geostatistics to evaluate partial weather station networks. Agricultural and Forest Meteorology, 84(3-4): 255-271.

Bensi, P. et al., 2007. A new Earth explorer the third cycle of core Earth explorers. ESA Bulletin, 131: 31-36.

Crisp, D. and Johnson, C., 2005. The orbiting carbon observatory mission. Acta Astronautica, 56: 193-197.

De Cesare, L., Myers, D.E. and Posa, D., 2001. Estimating and modeling space-time correlation structures. Statistics & Probability Letters, 51(1): 9-14.

Diodato, N. and Ceccarelli, M., 2005. Interpolation processes using multivariate geostatistics for mapping climatological precipitation mean in the Sannio mountains (southern Italy). Earth Surface Processes and Landforms, 30: 259-268.

Evensen, G., 1994. Sequential data assimilation with a non-linear quasi-geostrophic model using Monte Carlo methods to forcast error statistics. Journal of Geophysical Research, 99: 10143-10162.

Fuentes, M., Kittel, T.G.F. and Nychka, D., 2006. Sensitivity of ecological models to their climate drivers: Statistical ensembles for forcing. Ecological Applications, 16(1): 99-116.

Goovaerts, P., 2000. Geostatistical approaches for incorporating elevation into the spatial interpolation of rainfall. Journal of Hydrology, 228(1-2): 113-129.

Goovaerts, P. and Journel, A.G., 1995. Integrating soil map information in modeling the spatial variation of continuous soil properties. European Journal of Soil Science, 46(3): 397-414.

Heuvelink, G.B.M. and Webster, R., 2001. Modelling soil variation: past, present, and future. Geoderma, 100(3-4): 269-301.

Hudson, G. and Wackernagel, H., 1994. Mapping temperature using kriging with external drift - theory and an example from Scotland. International Journal of Climatology, 14(1): 77-91.

Matheron, G., 1981. Splines and Kriging: Their Formal Equivalence. In: D.F. Merriam (Editor), Down-to-Earth Statistics: Solutions Looking For Geological Problems: Syracruse University Geological Contributions, pp. p.77-95.

Pinheiro, J.C. and Bates, D.M., 2000. Mixed-Effects Models in S and S-PLUS. Statistics and computing. Springer, New York, xvi, 528 p. pp.

Quaife, T. et al., 2008. Assimilating canopy reflectance data into an ecosystem model with an ensemble Kalman filter. Remote Sensing of Environment, 112: 1347-1364.

Running, S.W., Nemani, R.R. and Hungerford, R.D., 1987. Extrapolation of synoptic meteorological data in mountainous terrain and Its use for simulating forest evapotranspiration and photosynthesis. Canadian Journal of Forest Research-Revue Canadienne De Recherche Forestiere, 17(6): 472-483.

Serra, J., 1987. Comments on "Geostatistics: Models and tools for the Earth sciences" by A. G. Journel. Mathematical Geology, 19(4): 359-355.

Thiessen, A.H., 1911. Precipitation averages for large areas. Monthly Weather Review, 39(7): 1082-1089.

Thornton, P.E., Running, S.W. and White, M.A., 1997. Generating surfaces of daily meteorological variables over large regions of complex terrain. Journal of Hydrology, 190(3-4): 214-251.

Wielgolaski, F.E., Kallio, P. and Rosswall, T., 1975. Fennoscandian Tundra Ecosystems: Part 1 Plants and Microorganisms. Ecological studies; v. 16-17, 1. Springer-Verlag, Berlin.

Williams, M., Bell, R., Spadavecchia, L., Street, L.E. and van Wijk, M.T., 2008. Upscaling leaf area index in an Artctic landscape using multi-scale reflectance observations. Global Change Biology: DOI: 10.1111/j.1365-2486.2008.01590.x.

Williams, M., Schwarz, P.A., Law, B.E., Irvine, J. and Kurpius, M.R., 2005. An improved analysis of forest carbon dynamics using data assimilation. Global Change Biology, 11(1): 89-105.

Woodward, F.I., Smith, T.M. and Emanuel, W.R., 1995. A global primary productivity and phytogeography model. Global Biogeochemical Cycles, 9: 471–490.

9. Conclusions

The dominant source of uncertainty for regional scale C models is the parameterisation of the land surface. Critically, LAI and foliar N (which may be closely coupled to LAI) must be adequately specified at the working scale to produce reasonable estimates of NEE. EO data sources alone are inadequate to characterise the rapid transitions in LAI typical of Tundra ecosystems and apparent in high-resolution studies. The use of topographic indices derived from high quality DEMS such as those derived by LIDAR may go some way to improving land surface parameterisation. Despite issues of bias in meteorological upscaling, driver uncertainty contributes only marginally to the net uncertainty in C, even in cases of extreme data scarcity. We therefore conclude that future studies should concentrate resources on improving regionalisation of land surface parameters, although an analysis of driver uncertainty is advisable. State of the art spatio-temporal interpolation techniques did not improve driver surface accuracy over those that ignore temporal autocorrelation. We conclude that simpler solutions to upscaling are preferable in terms of computational cost and quality of output. Geostatistical techniques are essential for the calculation of surface error statistics, which are a key step towards regional scale DA implementation; we therefore suggest that regression based techniques or IDW are unsuitable for such studies. DA techniques have proven useful in the correction of model parameterisation, and are likely to provide improvements in model uncertainty in the future, especially if undertaken in 'online' mode such that assimilated observations can adjust parameter trajectories over time.